UNIVERSITY OF ROME TOR VERGATA

XXXIV Cycle of PhD in Computer Science, Control, and Geoinformation

DEVICES AND METHODS FOR LOCAL- AND REMOTE-PROCESSING BODYCENTRIC INTERNET OF THINGS SYSTEMS

Giulio Maria Bianco

A.A. 2021-2022

Academic Advisor: Prof. Gaetano Marrocco

Industrial Advisor: Dr. Abraham Mejia-Aguilar

Coordinator: Prof. Francesco Quaglia

A dissertation submitted in partial fulfillment of the requirements

for the degree of Doctor of Philosophy in Computer Science, Control and Geoinformation

of the University of Rome Tor Vergata

I certify that I have read this dissertation and that, in my opinion, it is fully adequate in scope and quality as a dissertation for the degree of Doctor of Philosophy.

_____

(Prof. G. Marrocco)   Principal Co-Advisor

I certify that I have read this dissertation and that, in my opinion, it is fully adequate in scope and quality as a dissertation for the degree of Doctor of Philosophy.

_____

(Dr. A. Mejia-Aguilar)   Co-Advisor

I certify that I have read this dissertation and that, in my opinion, it is fully adequate in scope and quality as a dissertation for the degree of Doctor of Philosophy.

_____

(Prof. A. Buffi)

I certify that I have read this dissertation and that, in my opinion, it is fully adequate in scope and quality as a dissertation for the degree of Doctor of Philosophy.

_____

(Prof. S. Tedjini)

Approved for the University Committee on Graduate Studies.

_____

Devices and Methods for Local- and Remote-processing Bodycentric Internet of Things Systems

Giulio Maria Bianco

10th April 2022

Contents

II Remote Processing B-IoT – Bodycentric LPWAN for Search and Rescue 99

4 On-body LoRa(WAN) Low-Power Wide-Area Network 101

Appendixes

List of Abbreviations   261

List of Author's Publications   307

Acknowledgements   315

Introduction - Bodycentric Internet of Things (B-IoT)

Motivation

The Internet of Things (IoT) is an increasingly widespread paradigm based on the pervasive presence of *things* that are empowered to communicate and interact with each other in order to achieve a common goal [1]. IoT systems are present in a big part of everyday lives, ranging from the automatic inventory in warehouses to smart houses. In particular, IoT systems working in close proximity to the human body are currently under study for a wide array of applications. This recently introduced type of systems can be referred to as *bodycentric IoT* [2, 3] (hereafter, B-IoT; also known as *body-area IoT*, or body-area network *(BAN)-IoT* [4]), which can be defined as *the set of all IoT systems that include body-worn wireless connected things*. In other words, the B-IoT systems are all the IoT systems involving wireless wearable devices. The B-IoT is defined by the utilized hardware and position, unlike other application-based classifications, for example, the healthcare IoT (H-IoT) or the internet of trees (IoTr) [5]. Since wearable devices are increasingly widespread, B-IoT is also more and more common and investigated for healthcare, safety and defense (Fig. 1).

The B-IoT systems can be categorized into two classes based on their data processing: *local* and *remote*. Local systems exploit short-range wireless protocols having radio ranges in the order of tens of meters as BLE (Bluetooth low-energy) and RFID (radiofrequency identification), whereas remote systems employ ranges of hundreds of meters or more, eventually combined with short-range wireless technologies (Fig. 2). In this last case, the long-range protocol is exploited to transmit data gathered locally; an example of such a B-IoT application is the telemonitoring through wearable diagnostic devices to a concentrator via a long-range protocol (Fig. 3).
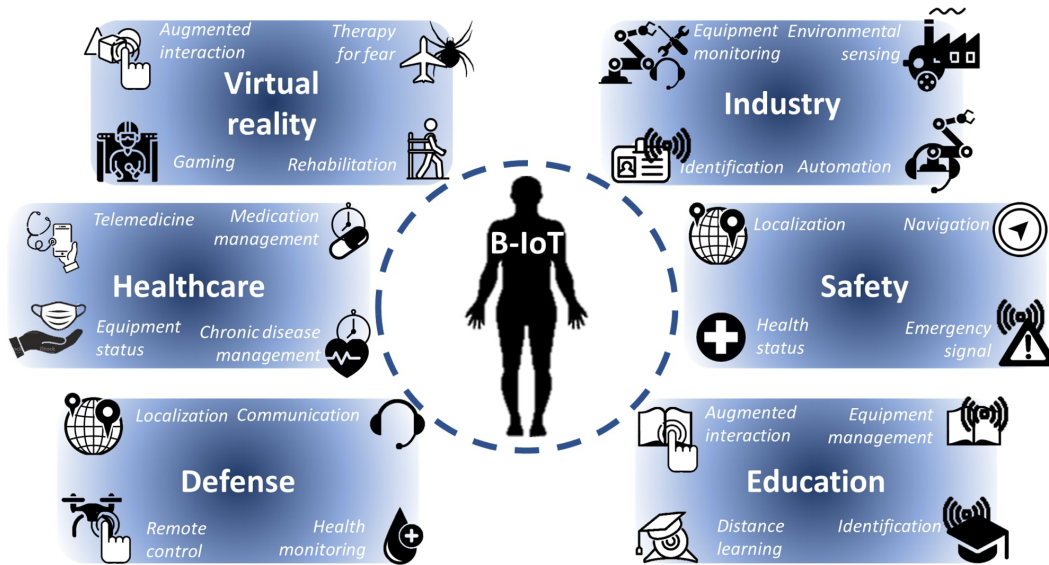
Figure 1: Application examples of B-IoT devices.
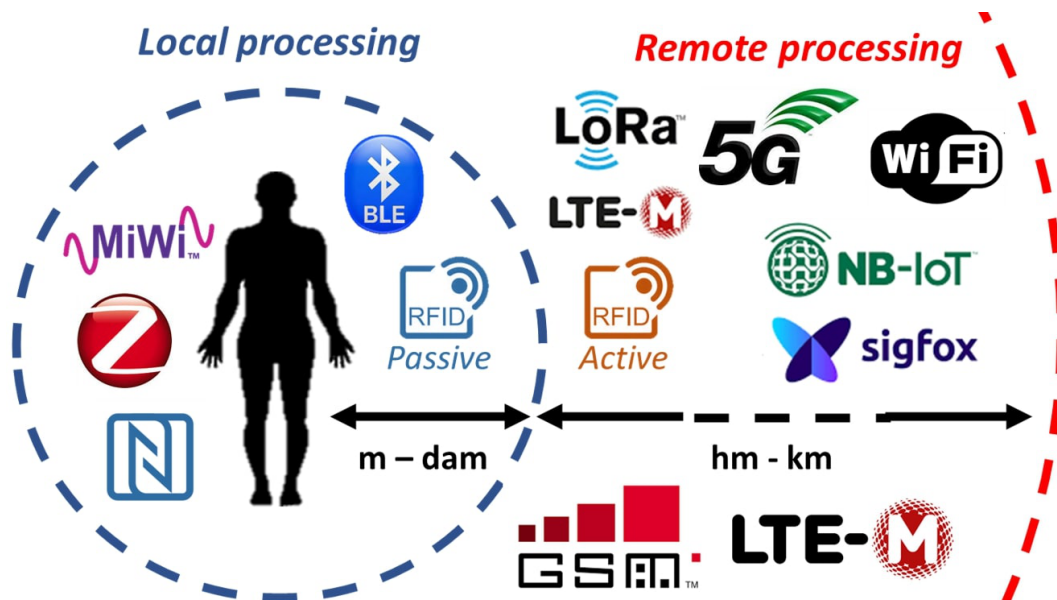
Figure 2: Some wireless protocols employed for local and remote-processing B-IoT.
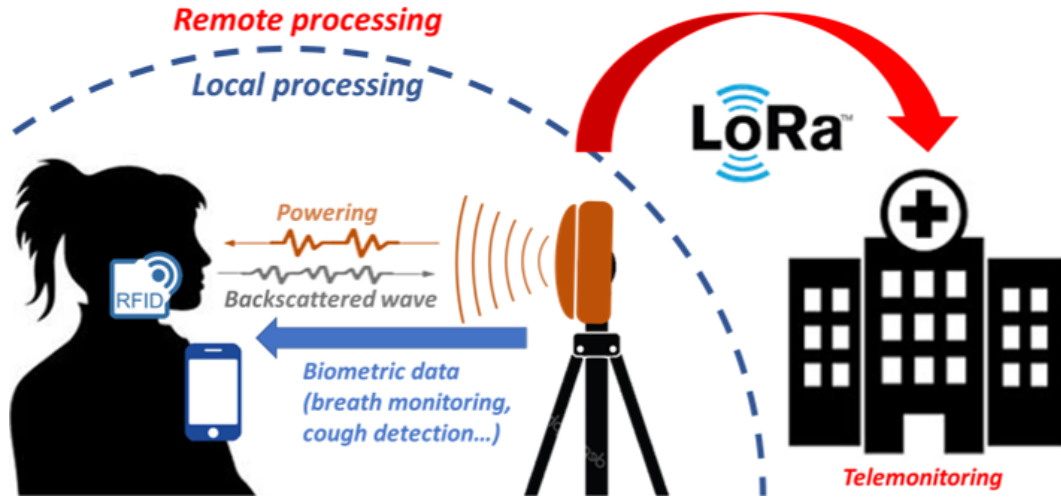
Figure 3: An example of a B-IoT system exploiting both local and remote processing. The biometric data are returned to the user and forwarded to a control center for infectious diseases control.

However, the classic application-defined approach to the IoT overlooks many characteristics that are typical of the B-IoT, such as the size and comfort requirements or the powering issue. An overview of B-IoT as a whole is complex and currently missing, whereas the in-depth analysis of the B-IoT could greatly help designing future devices since the issues to be faced are closely related.

This dissertation aims to analyze the B-IoT class of devices regarding both local and remote processing systems. Two technologies are considered: RFID (radiofrequency identifications) for local and LPWANs (low-power wide-area networks) for remote processing. Particularly, this work focuses on passive RFID tags and the Long-Range (LoRa) LPWAN protocol. By considering the literature on the uses and case studies of both technologies, the bodycentric links of B-IoT are comprehensively analyzed.

Challenges

The presence of the human body is known to be one of the main challenges when designing wireless connected B-IoT devices. The high power absorption caused by the body tissues can compromise the remote interaction with body-worn devices. Other historical challenges are posed by the size and input power, which are constrained by the comfort and the specific absorption rate (SAR) regulations, respectively. The wearable device must not hinder any user action, be potentially worn for a long time, and not cause any harm to the wearer. Moreover, body-worn antennas undergo de-tuning caused by the body movements and are sensitive to the different points of application that can shadow the electromagnetic wave up to hindering any communication.

The de-tuning could be the result of inter- and intra-user unpredictable variability in the body morphology and electrical features. State-of-the-art (SoA) antennas face this issue through a user-dependent fine-tuning of a general layout. The recently-introduced self-tuning (or auto-tuning) integrated circuits (ICs) can modify their equivalent radiofrequency (RF) impedance to compensate for some mismatch between the antenna's and IC's impedance so to successfully face the de-tuning problem. From another point of view, the de-tuning could simultaneously carry information on physical phenomena to be monitored, and the self-tuning ICs could also be exploited for sensing even when a dedicated sensor is absent. However, this technology is little known and has yet to be used optimally. Advances in the theoretical analysis are needed to exploit the IC fully.

Instead, body shadowing is one of the most critical expected body effects on the radio wave propagation from on-body antennas. These off-body links are still under-investigated. Link models need to be developed accounting also for the body postures foreseen in the

actual link use, and the models have to be experimentally validated. Generally, the on-body antenna design and radio wave propagation issues can be present simultaneously.

Lastly, the new long-range links involving the LoRa LPWAN protocol are largely unexplored. They are commonly handled through experimental models. In contrast, the LoRa-based B-IoT link design should also be based on theoretical models to design systems and applications. As it is evident, the challenges posed by the holistic analysis of B-IoT electromagnetic links require to span a broad set of knowledge fields.

Novelty

This work analyzes the B-IoT whole set, comprising both short- and long-range bodycentric links. Accordingly, the following specific novelties are here introduced.

- *Local sensing by auto-tuning ICs*. Through the auto-tuning ICs, it is possible to achieve RFID sensor-tags whose components are only the microchip and the antenna. By mastering the self-tuning mechanism and optimizing the RFID tag antenna, it is possible to simultaneously exploit it for communication and sensing purposes. This work introduces an engineering technique that can be applied for both on-body and off-body sensing regardless of the electromagnetic coupling between the antennas of the reader and the tag (near-field or far-field). This new kind of sensor-less sensing is fundamentally different from current commercial sensor tags that are composed by inlays connected to external, dedicated sensors[1].

- *Off-body LoRa radio links modeling*. Statistical and deterministic link modeling accounting for the presence of the body is introduced and applied to mountain search and rescue (SaR) operations. The precise link models can be used for the localization of the target to be rescued based on the received signal strength (RSS) through classical RSS-based localization algorithms. This dissertation also describes a novel RSS-based algorithm that can be utilized for localizing an on-body transmitting antenna.

The common-mode between the novelties is the human body non-negligible presence, which is properly modeled depending on the link and the considered scenario.

---

[1]For instance, see the RFID tag EVAL01-FENIX-RM by Farsense, embedding a dedicated temperature and pressure sensor (datasheet available at the time of writing at `http://www.farsens.com/wp-content/uploads/2018/09/DS-EVAL01-FENIX-RM-V04.pdf`).

Outline

The dissertation is divided into two parts, devoted to the local (Part I) and remote (Part II) processing B-IoT. Part I focuses on wearable and epidermal RFID antenna design for H-IoT applications, whereas Part II deals with the off-body LoRa links with particular applications to mountain SaR.

Chapter 1 reviews the RFID-based B-IoT for healthcare applications. Several examples of local-processing devices and systems are provided to detail the SoA and current limitations. Chapter 2 introduces the design technique to optimally exploit self-tuning ICs. After reviewing the classic model of the self-tuning mechanism, the permittivity-sensing is detailed and exploited for on-body sensing. A wearable RFID tag for monitoring the humidity of a filtering facepiece respirator (FFR) is engineered to continuously check the FFR filtering capability. Off-body sensing is the focus of Chapter 3, where an epidermal on-finger antenna is exploited for dielectric sensing. This tag is near-field coupled with the reader's wearable antenna and part of a *radiofrequency finger-augmented device* (R-FAD), a hand-worn system originally developed to aid people unable to correctly sense the temperature.

The second part of the dissertation starts with the description of the LoRa protocol and the radio links exploiting this LPWAN, including some bodycentric links (Chapter 4). Then, the off-body LoRa terrestrial links in mountain scenarios (snowy plains and mountain canyons) are investigated to validate the use of LoRa-based B-IoT for mountain SaR (Chapter 5). The off-body ground-to-air links are instead studied in Chapter 6 to utilize the body-UAV (unmanned aerial vehicle) links, which could greatly speed up SaR operations. Lastly, Chapter 7 describes a range-based algorithm for localizing through

RSS. The off-body links and the algorithm could be employed together in a B-IoT system to effectively address SaR problems.

Part I

Local Processing B-IoT – Bodycentric RFID Systems for Healthcare Applications

Chapter 1

RFID in Healthcare B-IoT

Among the several technologies contributing to the IoT, the RFID stands out as one of the most important. The RFID was identified as one of the ten greatest contributory technologies of the 21st century [6] thanks to its adaptability to process- and user-scale systems; moreover, it is nowadays one of the pillars of the H-IoT [7]. H-IoT systems with RFID usually employ transceivers in the body-area such as wearable [8] and epidermal [9] RFID tags, constituting the base of many local processing B-IoT systems

This Chapter presents an overview of the RFID technology and its recent advances in B-IoT systems, focusing on the healthcare applications that will be investigated in-depth in this dissertation. After detailing the basic principles (Section 1.1) and the general use and classification of RFID systems in the H-IoT (Section 1.2), the main H-IoT applications of RFID are introduced and categorized based on the sensed physical parameter, and, then, a literature review on said bodycentric sensors is drawn (Section 1.3) to analyze the local processing B-IoT to be considered. In the review, the sensing is divided into two categories: sensing of a measurand onto the wearer's body is named *on-body sensing*, whereas a parameter not related to the user is measured through *off-body sensing*. Section 1.3.1 deals with the former sensing category, and Section 1.3.2 with the latter.
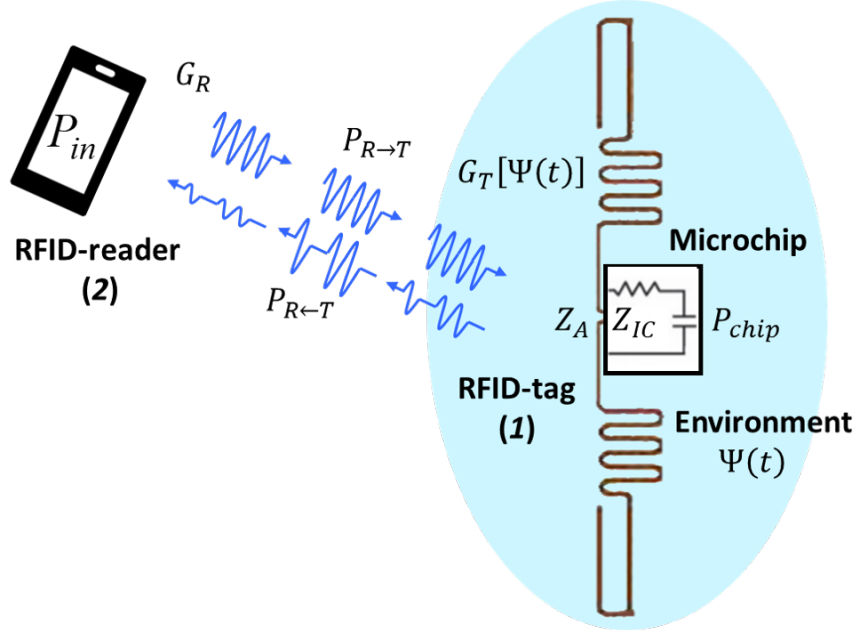
Figure 1.1: Principle scheme of RFID systems. A reader interrogates a tag that is influenced by the time-varying physical parameter $\Psi(t)$.

1.1 Basic Principles of RFID

1.1.1 Fundamentals of RFID systems

RFID systems comprise two key components (Fig. 1.1): a *reader* and a *tag*. The reader can query tag through an EM (electromagnetic) wave. The input power of the reader P_{in} is correlated with the actual power collected by the tag antenna $P_{R \to T}$ by the radiations gain of the antennas of both the reader (G_R) and the tag (G_T). The tag harvests power from the reader's EM wave and utilizes it to energize an IC hosted by the tag's antenna. The power delivered to the IC is proportional to the *power transmission coefficient* τ

$$\tau = \frac{4R_C R_A}{|Z_C + Z_A|^2} \leq 1, \tag{1.1}$$

which is maximum when the impedances of the tag's antenna $Z_A = R_A + jX_A$ and of the IC $Z_C = R_C + jX_C$ are complex conjugate each other, namely when $Z_A = Z_C^*$ being * the complex conjugate operator. When the collected power is higher than the IC sensitivity

24
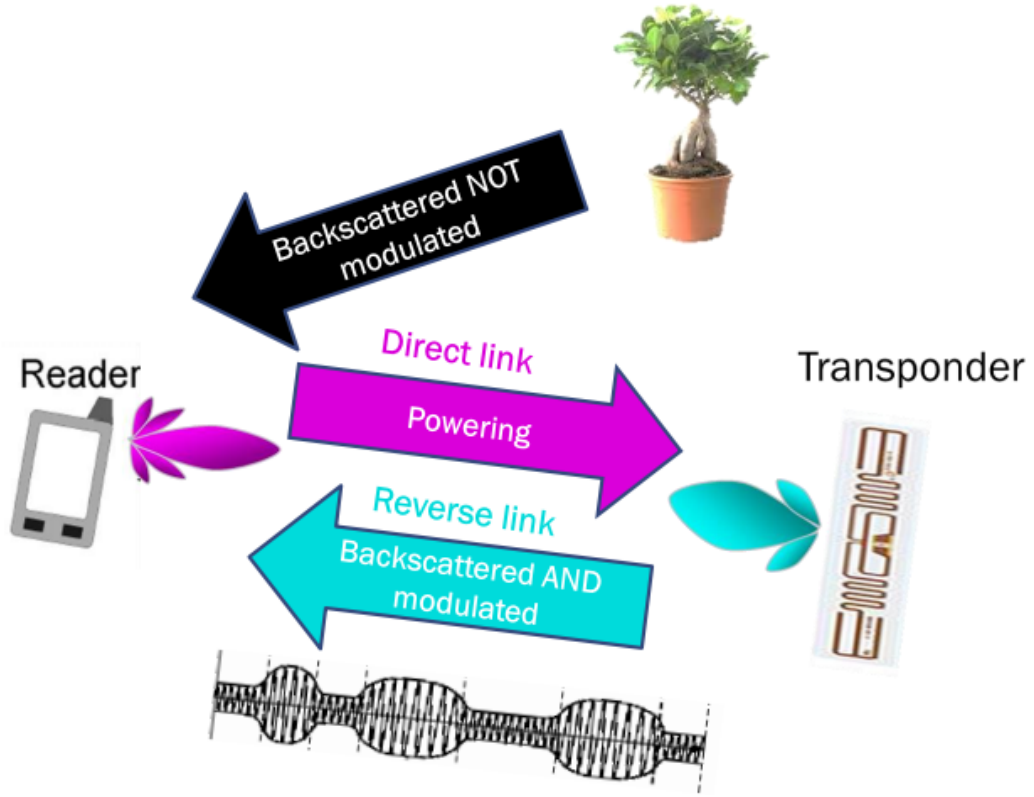
Figure 1.2: The backscattering communication between the RFID reader and the tag.

P_{IC}, the microchip transponder acts as a programmable switching device between a low impedance and a high impedance state to modify the reflectivity of the tag and hence the strength of the reflected field $P_{R \leftarrow T}$. The load switching allows the reader recognizing the tag's response and exchanging information with it (Fig. 1.2). Thus, the backscattering communication involves a *forward link* (from the reader to the tag), which is responsible for the powering of the IC, and a *reverse link*, which is used to gather information from the tags. It is straightforward that every physical parameter Ψ, which unequivocally affects the radiation properties of the tags, can be sensed based on the reflected field solely.

The backscattering communication scheme applies for frequencies ranging from LF (low frequency) to microwaves. Systems operating at LF and HF (high frequencies) exploits the magnetic coupling, whereas from the UHF (ultra-high frequency) the electromagnetic coupling is used. Moreover, the tags can be powered only by the EM wave
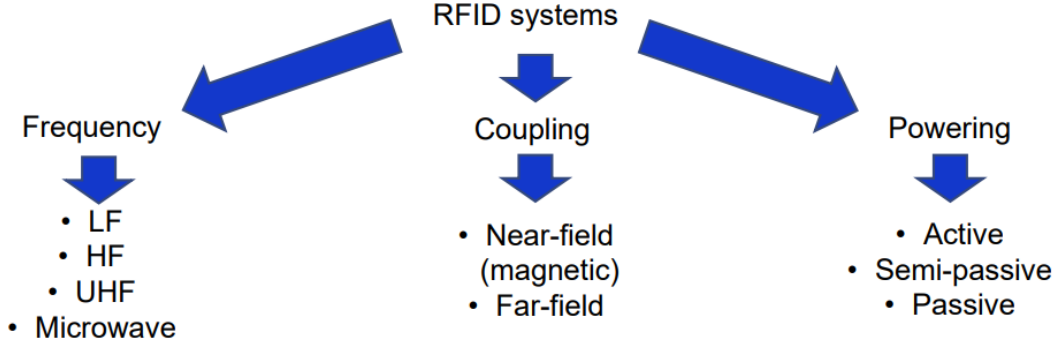
Figure 1.3: A basic taxonomy of RFID systems.

of the reader (*passive tags*), can have a power-source to energize external sensors (*semi-passive tags*, a.k.a. *battery assisted passive*, BAP) or communicate only when fed by an autonomous power supply (*fully active*). Fig. 1.3 depicts a simple taxonomy of the existing RFID systems.

In electromagnetic couplings, when the antennas of the reader and the tag are in the each other's far-field, the powers $P_{R \to T}$ and $P_{T \leftarrow R}$ are returned by the *Friis transmission's formula*

$$P_{R \to T} = \left(\frac{\lambda}{4\pi d} \right)^2 P_{in} G_R G_\tau \eta \tag{1.2}$$

and the *radar equation*

$$P_{R \leftarrow T} = \frac{1}{4\pi} \left(\frac{\lambda}{4\pi d^2} \right)^2 P_{in} G_R^2 \eta^2 \rho, \tag{1.3}$$

respectively, where λ is the wavelength, d is the reader-tag distance, $G_\tau = G_T \tau$ is the realized gain of the tag, η is the polarization loss factor (PLF), and ρ is the radar cross-section

$$\rho = \frac{\lambda^2}{4\pi} G_T^2 \left(\frac{2R_A}{|Z_C + Z_A|} \right)^2. \tag{1.4}$$

The maximum read range can be obtained as the minimum d evaluated by reversing (1.2) and (1.3).

The data most commonly shared between the reader and the tags are:

- *Electronic Product Code* (EPC) and *User memory*, that constitute the unique ID name assigned to the tag. They can be writable and password-protected.

- *Received Signal Strength Indicator* (RSSI), an arbitrary-scale indicator proportional to the power backscattered to the reader.

- *Turn-on power*, the minimum power P_{in} the reader has to give to the antenna to have the tag responding.

- *Phase*, the phase of the EM wave backscattered by the tag.

Nowadays, COTS RFID provided with sensing capabilities are available with integrated sensors and programmable I/O ports for connecting general-purpose micro-controllers and sensors. Regarding the frequency, RFID UHF in the EU are allowed to work only in the band 865.6-867.6 MHz [10].

However, in the literature, the term RFID is sometimes employed also to indicate systems not exploiting the backscattering modulation. For example, references [11, 12, 13] investigated contact tracing using active beacons as [14]. Although the systems are labeled as RFID because an RF ID is assigned through the beacons, those systems do not employ the backscattering modulation, and the tag-beacon can communicate with the reader-beacon autonomously even without being previously queried. Another extended use of the RFID term regards the NFC (near-field contacting) protocol, which is a peer-to-peer 13.56 MHz protocol developed from HF RFID systems. The NFC uses the backscattered modulation, but the distinction between tag and reader is not valid anymore, and it is replaced by the roles of the *initiator*, which starts the communication, and the *target*, which is different from the initiator just because communicates later but can still generate its own EM field if a power source is available.

A comprehensive taxonomy of the several kind of RFID systems and their use is out of the scope of this dissertation. Instead, it is of interest specifying that this works details RFID-based B-IoT systems employing UHF passive tags.

1.1.2 Sensing by RFID tags

RFID tags can act as sensors and monitor given measurands in space. When the RFID tag is used also as sensor, it is usually named *sensor-tag*. The sensor-tags can be divided into two classes based on the presence or absence of a dedicated sensor connected to the tag's antenna.

- *Sensor-tags with dedicated sensors.* This first class of sensor-tags is the widest and most common one. It is composed by a dedicated sensor connected to a standard RFID tag. Commercial sensor-tags use dedicated sensors, with a few exceptions.

- *Sensor-tags without a dedicated sensor.* This second class of sensor-tags does not exploit dedicated sensors and utilizes the tag's antenna as the sensor itself so that a given measurand is measured by variation of a proper antenna's parameter like the radiation gain or the input impedance. This kind of sensing is often referred to as "sensor-less" sensing.

Some examples of commercial sensor-tags embedding dedicated sensors are depicted in Fig. 1.4, and they are:

- EVAL01-RMeter-RM, tag with an ADC for measuring the resistance, to be used together with a resistive sensor (`http://www.farsens.com/en/products/eval01-rmeter-rm/`);

- EVAL01-X5-R, contact detection tag for monitoring the status (open or closed) of a maximum of 5 circuits (`http://www.farsens.com/en/products/eval01-x5-r/`);

- EVAL01-Stella-R, tag provided with a LED as a light actuator. It does not perform sensing properly (`http://www.farsens.com/en/products/eval01-stella-r/`);

- PQS-SR-01, tag embedding a temperature-sensor for on-metal applications (`https://www.pqsense.com.tw/products.html#sensor`);

Figure 1.4: Examples of commercial sensor-tags employing dedicated sensors. Green tags at the upper-left: sensor-tags by Farsense (tag models, from top to bottom: EVAL01-RMeter-RM; EVAL01-X5-R, and EVAL01-Stella-R). Yellow tags at the bottom-left: sensor-tags by PQsense: bolt mount sensors PQS-SR-01. Black tags on the right: AS321X tag evaluation kit (including the following tags: AS3212-EVAL-Pressure, AS3213S-EVAL-Strain, AS3213C-EVAL-Motion, AS3213L-EVAL-Light, AS3212-EVAL-Magnetic, AS3212-EVAL-Analog, AS3213RH-EVAL-Humidity, AS3212-EVAL-Humidity, AS3213C-EVAL-Ext-Cap, and AS3211-EVAL-Temperature).

- AS3212-EVAL-Pressure, tag embedding a pressure sensor (`https://asygn.com/shop-as321x-evaluation-kit/`);

- AS3213S-EVAL-Strain, tag embedding a strain sensor (`https://asygn.com/shop-as321x-evaluation-kit/`);

- AS3213C-EVAL-Motion, tag embedding a motion sensor (`https://asygn.com/shop-as321x-evaluation-kit/`);

- AS3213L-EVAL-Light, tag embedding a light sensor (`https://asygn.com/shop-as321x-evaluation-kit/`);

- AS3212-EVAL-Magnetic, tag embedding a magnetic field sensor (`https://asygn.com/shop-as321x-evaluation-kit/`);

- AS3212-EVAL-Analog, tag admitting analog inputs (voltage or current; `https://asygn.com/shop-as321x-evaluation-kit/`);

- AS3213RH-EVAL-Humidity and AS3212-EVAL-Humidity, tags embedding a humidity sensor (`https://asygn.com/shop-as321x-evaluation-kit/`);

- AS3213C-EVAL-Ext-Cap, tag for the integration of capacitive sensors (`https://asygn.com/shop-as321x-evaluation-kit/`);

- AS3211-EVAL-Temperature. tag embedding a temperature (`https://asygn.com/shop-as321x-evaluation-kit/`).

All the sensor-tags listed above use dipoles as tag's antenna aside from PQS-SR-01, which employs a patch for on-metal application. Many temperature sensors, as in the case of the PQS-SR-01, are even embedded in the IC of the tag.

Table 1.1: Classification of H-IoT RFID applications.

RFID in H-IoT

Non-B-IoT	B-IoT
Healthcare supply chain	Hand hygiene compliance
Medical wastes disposal	Access Control
Indoor microclimate monitoring	Patients identification and management
	Contact tracing
	On-body signals measurement
	Assistive devices

1.2 RFID Use in H-IoT

During the last decade, the RFID use in healthcare quickly rose from the management of hospitals' inventories to the labeling of the patients and sensing. The main RFID application tested and envisaged in the literature can be classified and divided in B-IoT and non-B-IoT as follows (Table 1.1).

- Non-B-IoT applications.

  1. *Healthcare supply chain management* regarding the inventory [15], asset tracking [16], and anti-counterfeit [17].

  2. *Monitoring the disposal of medical wastes* to ensure their correct disposal [18] and reduce the environmental footprint [19].

  3. *Indoor microclimate checks* by measuring the temperature [20] and relative humidity (RH) [21] of the rooms, as well as the air exchange [22].

- B-IoT applications.

  1. *Ensure the compliance with hand hygiene procedures* by identifying [23] and monitoring [24] the healthcare workers who have to perform the hand hygiene.

  2. *Access control* by verifying the identity [25] and confirming or negating the access to individuals based on parameters like the body's temperature [26].

  3. *Patient identification and management* by labeling [27] and possibly tracking [28] the patients.

4. *Contact tracing* [29] and *interpersonal distancing* via proximity detection [30] to limit the transmission of infectious diseases.

5. *Measuring on-body signals* like biosignals as body temperature [31], electrocardiogram (ECG) [32], and electromyography (EMG) [33] for medical assessment, or the humidity of the dresses to assess the thermo-hygrometric comfort of the wearer [34].

6. *Assistive devices* for impaired people, like guides for blinds through a body-worn reader [35] and prosthesis [33].

Less common healthcare applications of RFID can be found in the several reviews on the topic, e.g. [36, 37, 38, 39, 40, 41, 42, 43]. Clearly, most of H-IoT applications involve B-IoT systems since body-worn tags are often necessary, and overall both on-body and off-body sensing are employed.

Naturally, also the RFID tags employed can be categorized based on their positioning in the body-area and their manufacturing [44], leading to the four following categories.

- *Off-body tags* not positioned near to the human body.

- *Wearable tags* that are placed onto the body but are not epidermal.

- *Epidermal tags*, ultra-thin, soft tags adhering directly to the human skin and mechanically imperceptible for the user [45].

- *Implantable tags* implanted inside the human body.

Typical values of realized gain and the corresponding achievable read ranges (RFID UHF band) are resumed in Table 1.2. In the same way, the on-body antennas can be classified as wearable, epidermal and implantable depending on their placement. Given the low reading distances achievable by on-body RFID tags, they can only support local B-IoT systems without the support of any other protocol. Because of the power absorption caused by the human body, the more the antennas are close to the body's lossy tissues, the lower will be the antennas' radiation gains and the communication distances.

Table 1.2: Typical realized gains and maximum reading ranges (assuming $P_C = -22$ dBm, 3.2 equivalent isotropic radiated power emitted by the reader) for the three RFID tags kind [44].

Placement	Realized gain	Read range
Free-space	$0 \div 3$ dBi	$10 \div 19$ m
Wearable tag	$-10 \div 0$ dBi	$4 \div 10$ m
Epidermal tag	$-20 \div -8$ dBi	$10 \div 19$ m
Implanted tag	< -20 dBi	< 1 m

1.3 RFID-based Healthcare B-IoT for Sensing

RFID B-IoT system are widely investigated for healthcare for several applications, and RFID-based sensors are a key component of the most advanced systems. In this Section, the literature on said sensing is reviewed to select representative case studies to be comprehensively investigated.

The first useful sensing categorization can be based on the type of the measurand, viz. an on-body or an off-body measurand. Wearable sensors can adhere directly to the wearer's skin or be worn on a wearable support like pieces of clothing. Such sensors are usually employed for biosignals measurements because of their positioning [46]. The measurement of a physical parameter onto the wearer's body (i.e., generated by the body itself or on it as the wetness of a piece of clothing) can be referred to as *on-body sensing*. These sensors can be used for sensing parameters of objects in the environment, too, as for example the temperature of objects touched by the wearer [47]. This second sensing type can be defined as *off-body sensing* (Fig. 1.5).

A literature review on the RFID-based B-IoT sensors from the year 2005 to the year 2021 is shown in Table 1.3 and is here discussed. Since a single infrastructure can support multiple RFID application simultaneously, some works fall in more than one category like [56, 68].

1.3.1 On-body Sensing

Wearable RFID system for on-body sensing is a promising research topic which is increasingly investigated from the last ten years, mainly because of the low-cost of the sensor-tags

Table 1.3: RFID healthcare B-IoT systems for on-body and off-body sensing.

Sensing type	Type of signal	Scope	Measurand	References
On-body signal	Biosignals	Clinical symptoms monitoring	Body temperature	[31][48][49] [50][51][52] [53][54][55] [56][57]
			Cough	[58]
		Respiratory assessment	Respiratory rate, depth, cycle, and effort	[59][60][61] [62][63][64] [65][66][67] [68][69][70] [71][72]
			Blood oxygen saturation	[73]
		Cardio-vascular status	ECG, Hearth rate	[32][74][68] [75][56][76] [77][78]
			Blood pressure	[68]
		Psycho-physical stress	Sweat	[79][50][80] [81]
			Sleep disorder	[72][63][69] [55][82][83] [84]
		Prostheses	EMG	[33][85]
	Clothing condition	Medical assessment	Humidity	[34][86]
Off-body sensing	External physical parameter	Presence of other tags for activity-based applications	Back-scattered EM wave	[30][87][88]
		Assistance of sensorially impaired patients	Temperature of the touched object	[47]

34
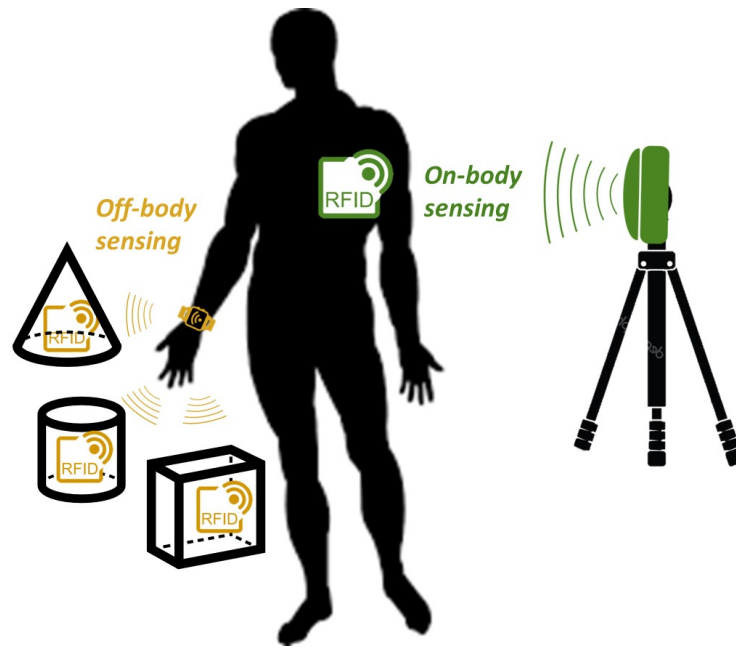
Figure 1.5: Examples of an- and off-body sensing through RFID: a body-worn sensor-tag and an RFID reader inside a bracelet sensing the presence of tags in the surroundings.

and the possibility to read the sensor from the distance, two features of RFID that are extremely useful for the treatment of illnesses from the preventive healthcare to the domestic monitoring and the eventual hospitalization. Accordingly, significant effort was directed to the biosignals measurements, which make up the bulk of the literature. With the same aim, a different approach is to monitor the wearer's clothing to infer indirect information on the wearer's health status.

Next, the RFID sensors are divided and analyzed by the measurand as in Table 1.3.

1.3.1.1   Body Temperature

The body temperature is among the first biosignals measured through RFID. During the SARS outbreak in 2006, an experiment at the Taipei Medical University Hospital demonstrated that the automatic and real-time temperature tracking reduces the risk of staff infections by limiting the interpersonal contacts [52].

Consequently, RFID epidermal thermometers adhering to the human skin through transpiring bio-compatible membranes [57] have been recently designed to be increasingly
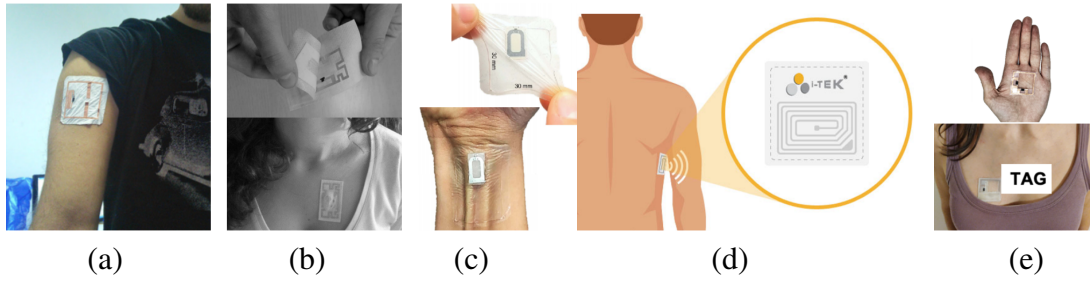
Figure 1.6: On-skin temperature RFID sensors for sensing the body temperature. (a) Worn prototype of the epidermal RFID temperature sensor [57]. (b) Flexible epidermal RFID thermometer [53], [55]. (c) Flexible and conformable RFID thermometer [49]. (d) i-TEK's body temperature monitoring system [89]. (e) Dual-chip flexible epidermal RFID temperature device [48].

conformable [55], low-visual-impact [49], and small [31] (Fig. 1.6). The fabrication costs and the environmental footprint were also considered [54]. New studies are currently developing and testing multi-chip RFID tags to evaluate more accurately the core temperature of the user, which has to be evaluated from the skin temperature actually measured by the RFID IC [48]. Such RFID thermometers were recently experimented in a hospital ward [53] and resulted a viable option. Furthermore, BAP tags can moreover act as data-loggers [50], allowing for the continuous monitoring of the body temperature [51].

1.3.1.2 Cough

The cough monitoring is a biosignal useful for monitoring many respiratory illnesses like the COVID-19 [90]. RFID-based cough detection sensors are still little investigated, though. A wearable RFID tag provided with simple inertial switches can detect coughing fits thanks to the different backscattered field strength caused by the chest movements [58].

1.3.1.3 Respiratory Rate, Depth, Cycle, and Effort

Current instruments for breath monitoring are intrinsically intrusive, as nasal probes and chest bands [91], therefore the RFID solutions were vastly investigated.
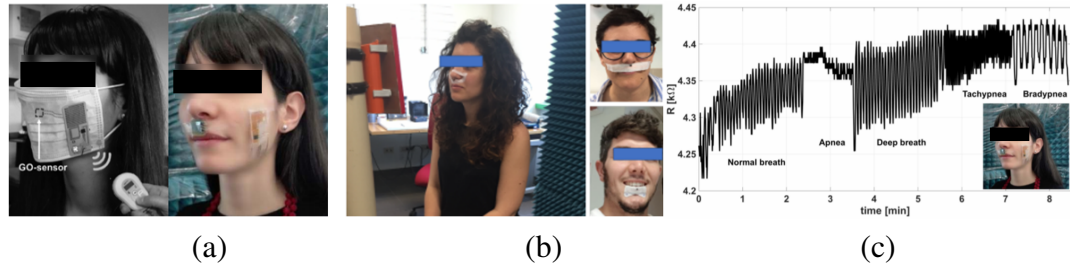
Figure 1.7: RFID sensors for *direct* respiratory function assessment. (a) RFID breath humidity sensors for integration into a facemask (left) and over the skin (right) [66, 64]. (b) Different prototypes of RFID skin-attachable breath temperature sensors [65]. (c) Recording of a respiratory pattern [64].

The breath monitoring can be achieved through graphene-oxide external sensor which can monitor the moisture emitted during the breathing. The external sensor can be connected to a wearable tag adhering to a facemask [66] or an epidermal tag [64] in order to monitor the different respiratory patterns. To reduce the cost of the single RFID sensor, the use of a simpler temperature sensor was proposed and preliminary tested in [65] although the validation of the temperature-based breath monitoring was achieved three years later with the comparison with standard clinical equipment [60] (Fig. 1.7); the validation confirmed that the air flow temperature allows for an accurate measurement of the breath rate but not the breath depth. Moreover, two epidermal tag can be used for the bilateral breath monitoring which can be useful due to nasal septum deviations and the nasal cycle [60].

The measurement of the torso expansion and contraction by placing regular RFID tags on the abdomen or onto the bed can be exploited for breath monitoring as well [72]. In this case, the variations of the RSSI [63, 67, 68] and phase [62, 69, 59] are used to infer the breathing pattern. The apnea and respiration rate can be observed through RFID tags worn on the abdomen [59, 63, 69], eventually in array configuration [62]. This tags placement is suitable for overnight monitoring through a bedside RFID reader and medical examination-like situations [61, 67] (Fig. 1.8). The integration in the garments of RFID tags can also allow an estimation of the respiratory effort by correlating the registered breathing and cardiovascular data [68].
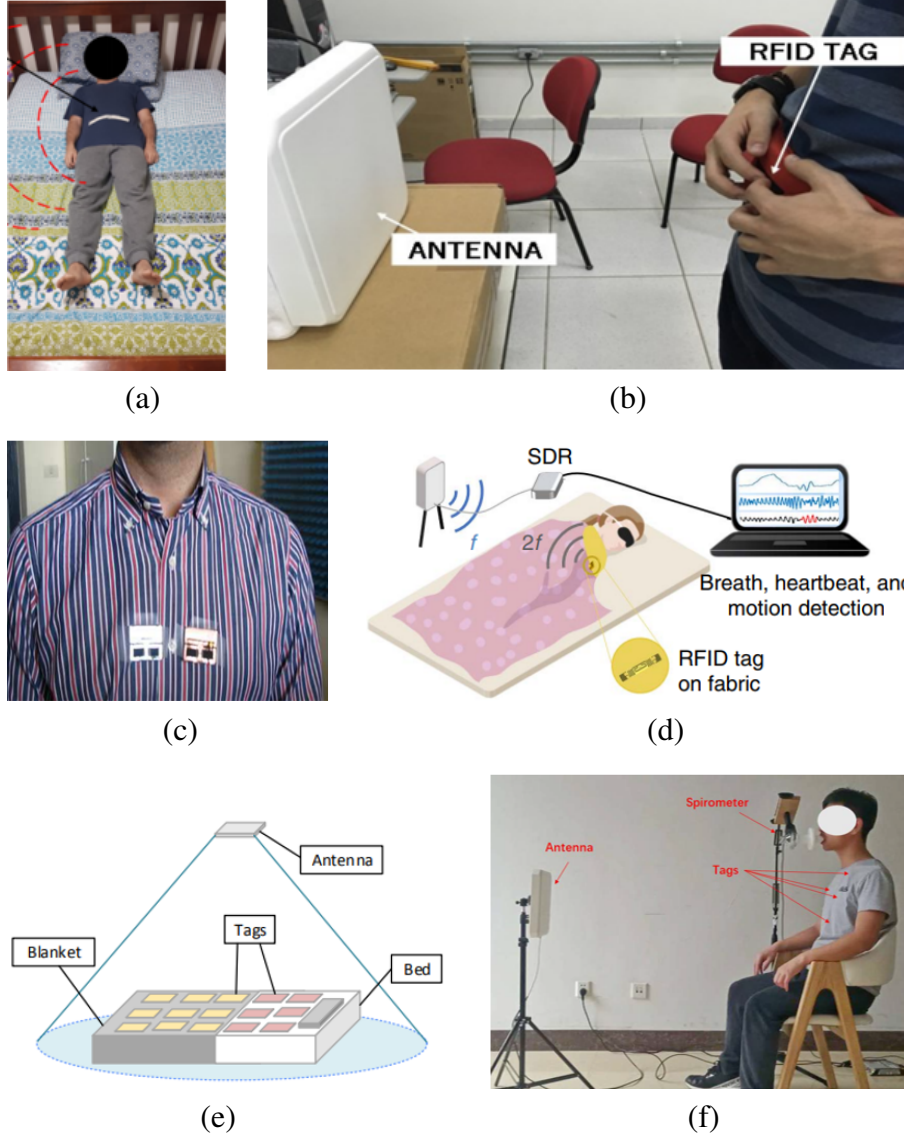
Figure 1.8: RFID sensors for *indirect* respiratory function assessment. (a) Sleep respiration monitoring system with passive COTS RFID tags [63]. (b) RSSI-based respiratory monitoring system with passive RFID tags [67]. (c) Motion inertial based cough monitoring RFID sensor [58]. (d) Fabric-integrated RFID tag for respiratory assessment during sleep [69]. (e) Non-invasive sleep monitoring system based on bed-integrated RFID [72]. (f) Measurement setup of an RF system for sensing abdomen's movements [59].
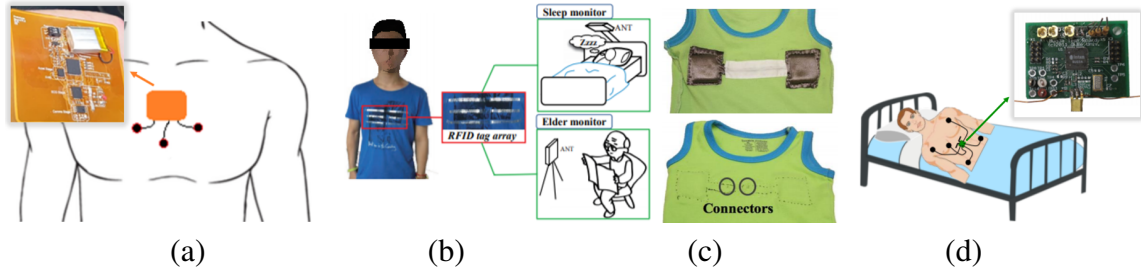
Figure 1.9: RFID sensors for cardiovascular evaluation. (a) Epidermal ECG RFID device [32]. (b) RF-ECG system with an array of COTS RFID tags [74]. (c) Fabric-integrated hearth rate RFID device [75]. (d) Battery-free multichannel ECG sensor [78].

1.3.1.4 Blood Oxygen Saturation

The pulse oximetry can be achieved by standard complementary metal-oxide semiconductor (CMOS) technology and a reflection sensor. After a simple data processing involving an amplifying and a band-pass filter circuit, the data can be transmitted by an active RFID to a reader achieving a comfortable wearable sensor [73].

1.3.1.5 ECG, Hearth Rate

The ECG data can be collected by standard clip electrodes currently used in the clinical practice, and then communicated to the reader by an ultra-low-power RFID BAP tag [32, 77]. The heart rate variability can instead be evaluated similarly to the breath with COTS RFID tags attached to or sewed into the clothes [74]. The hearth rate estimated through this RSSI and phase processing is sensitive to both the movements caused by the heartbeat and the respiration but can reliably estimate the hearth rate anyway. Regarding infants, the hearth rate can be estimated through ECG-enabled RFID sensors sewn onto the front bodice of a baby bodysuit [75, 76]. A multi-electrode wearable ECG harvesting power by the incoming EM wave was also proposed [78], and it could be connected to an RFID tag for data transmission.

1.3.1.6 Blood Pressure

The blood pressure can also be monitored through the amplitude and the phase of the EM wave backscattered by body-worn tags [68]. Since the signal phase is sensitive to minimal
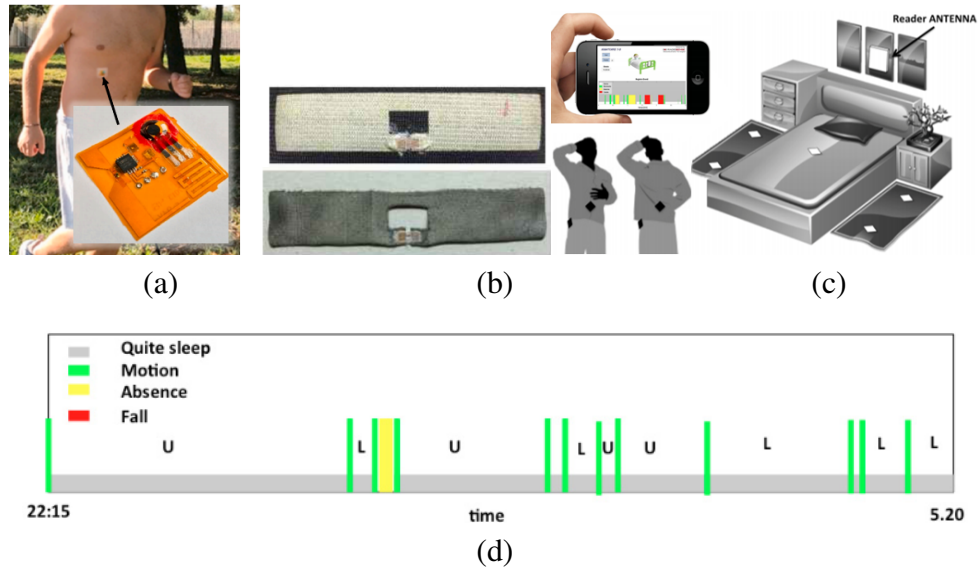
Figure 1.10: (a,b) RFID sensors for sweat monitoring. (a) Epidermal RFID device for pH sweat monitoring [79]. (b) Textile-integrated RFID sweat rate sensor tags [81]. (c) *NightCare* system for sleep monitoring [82], [83]. (d) Classification of sleep quality and different body postures [83].

movements while the amplitude is not, it is possible to process the data to properly isolate the different biosignals as the blood pressure and the chest movements due to the breathing. Particularly, the blood pressure is estimated through the pulse transit time, which in turn is extracted from the proximal and distal arterial waveforms registered by different tags.

1.3.1.7 Sweat

The sweat is a precursor of psychological diseases because of the variations in its chemical composition [92]. A flexible RFID tag for sensing the pH index utilizing an electrochemical printed Iridium-oxide sensor is detailed in [79]. The presence of altered electrolytes can hence be measured in battery-less mode or in data-logging BAP mode [50], and the monitoring can be performed even in motion [80], as in the case of hectic nurse activity. Another interesting biosignal is the sweat rate, which can be evaluated through electro-textiles and the changes in their characteristics when absorbing sweat [81].

1.3.1.8 Sleep Disorder

The sleep disorders can seriously diminish the well-being of a person. For instance, the sleep quality was identified as a pivotal health parameter during the COVID-19 pandemic [93]. The *NightCare* system [82, 83, 84] quantitatively evaluates the phenomenology and quality of sleep utilizing a set of passive tag adhering to the sleeper's clothes and disseminated in the environment, viz. in the bed and nearby carpets. The temperature monitoring overnight can be exploited, too, for illnesses comporting fever [55].

1.3.1.9 EMG

Electromyography through RFID sensors has been recently introduced to pilot arm prostheses [85, 33]. The EMG signal is collected with COTS EMG sensors connected to an epidermal RFID tag for data transmission to the reader. The antenna design is the main investigated topic, as the prostheses has to gather the EMG signal in real-time and without data loss. Although this research topic is very recent, the preliminary results are encouraging, and the transmission of complete EMG tracks were achieved.

1.3.1.10 Humidity of the Pieces of Clothing

Wearable textile tags were investigated for moisture sensing for medical and healthcare applications but they were not tested on the human body. Basically, the sensor exploits the absorption of liquids by the texture and the consequent change in the tag radiation performance to infer information on the user health condition. The liquids to be monitored could be the sweat due to physical exercise [86] or urine to detect bed-wetting [34], for instance, in health residence for the elderly. The considered EM performance can be the peak read range frequency [86] or a scattering parameter [34] since those parameters were proven to be sensitive to the moisture presence.

1.3.2 Off-body Sensing

The RFID-based B-IoT for off-body sensing is much rarer than the on-body. It consists of wearable or epidermal RFID utilized to sense a physical parameter in the surrounding

environment external to the human body. Two proposed healthcare applications are the sensing of interactions with other objects through the backscattered EM wave, and assistive device for individual having a sensory impairment by measuring the temperature of the touched object.

1.3.2.1 Backscattered EM Wave

Tracking the interaction between peoples and objects could be extremely useful to monitor the correct execution of procedures by medics and nurses, as well as to help teaching to junior medical staff. The first systems proposed to this purpose were body-worn readers [88, 87]. The *iGlove* is a reader integrated in gloves, and was tested by medical students to track the correctness of medical procedures [88]. Although the system successfully detected and tracked the procedures, the testers felt uncomfortable in wearing the gloves for a prolonged time. To minimize the discomfort, a similar, less cumbersome *iBracelet* was developed. Reference [87] utilizes the phase of the wave backscattered by the tagged objects to sense and classify the different activities with the objects. Differently from the body-worn readers, the *Sense-a-Tag* device does not directly query the tags, but can sense the backscattered EM wave [30]. The activity recognition can be carried out with integration the Sense-a-Tag in a wristband.

1.3.2.2 Temperature of the Touched Object

Peripheral nephropathy is a common pathological condition which can have many causes, as Multiple Sclerosis, obesity, or aging [94]. Among the great variety of symptoms the patients experience there are the tactile and thermal hypoesthesia, i.e., a sensory impairment consisting in a reduced or even absent sensitivity to tactile or thermal stimuli, respectively. Clearly, such sensory impairment can significantly lower the life quality and the patients can inadvertently cut or burn themselves. An RFID hand-worn system composed by a reader worn onto the wrist and a temperature-sensing fingertip tag was developed and tested to assist patients suffering from thermal hypoesthesia [47]. The system can reliably estimate the temperature of the touched object after a 0.5-s-long touch.

1.4 Conclusion

In this Chapter, the working principles of RFID systems are introduced, and their most common uses in healthcare are resumed to identify the local processing B-IoT case studies to analyze. The most advanced system heavily employ RFID sensor, and a literature review on the topic is presented. From the literature review emerges the importance of an accurate antenna design, which in turn implies a detailed human body model. The antenna design is crucial, especially in the case of sensor-less sensing, namely the tags that do not utilize additional external sensors but gather information based only on the variations of the radiation properties of the antenna in the reaction of local changes. The sensing can be further divided into on-body and off-body sensing, depending on if the measurand is onto the tag wearer's body or not. Epidermal and wearable sensor-tags are employed for both sensing types.

Accordingly, to have an insight on the local processing B-IoT, it is necessary to consider the two types of utilized tags and the two sensing types; thus, in the following Chapters, a wearable tag for the on-body sensing and an epidermal tag for the off-body sensing are investigated whose applications regard the condition of a piece of clothing and the assistance to sensory-impaired individuals, respectively.

Chapter 2

Self-tuning ICs and On-body RFID Sensing

In this Chapter, the self-tuning theory is introduced (Section 2.1), and a design technique to optimally exploit it for sensing is detailed (Section 2.2). Then, the healthcare application of the design technique to monitor the FFR's effectiveness (Section 2.3) is described as a case study of an RFID-based B-IoT device for on-body sensing.

2.1 Self-tuning (Auto-tuning) Theory

The self-tuning theory describes the behavior of the self-tuning (or auto-tuning) ICs that are provided with an internal variable capacitance to be maximized for optimizing the matching condition with the environment.

2.1.1 Self-tuning Mechanism

As discussed in the previous Chapter, the power collected by the IC is the EM power harvested by the RFID antenna multiplied for the power transmission coefficient τ (1.1). The power transmission coefficient is unitary and maximum if and only if $Z_C = Z_A^*$. Consequently, when the operating conditions of a sensor-antenna changes, the power delivered to
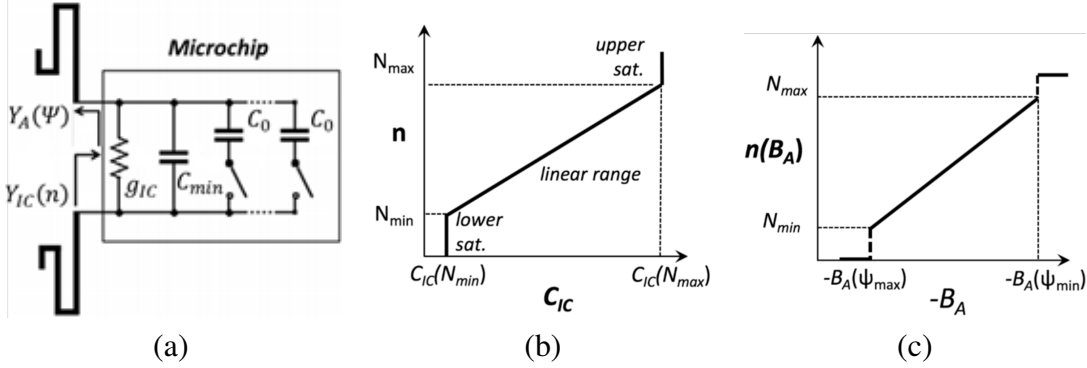
Figure 2.1: (a) Modeling of self-tuning ICs. (b) Linear and saturation ranges of the SC. (c) Mapping of the SC on the antenna's susceptance.

the IC and the communication performance decrease significantly. To overcome this limitation, a new class of ICs named *self-tuning* (a.k.a. *auto-tuning*) was recently introduced on the market. An auto-tuning microchip can dynamically change its internal RF impedance to match that of the hosting antenna and maximize the power transmission coefficient. Accordingly, it can compensate for changes in the operating environment and preserve the antenna's radiation performance. The IC can also return a digital metric, generally named sensor code (SC), which is proportional to the retuning effort and can be employed to sense variations in the boundary conditions. Therefore, auto-tuning-based sensors use the SC for sensing while achieving stable communications thanks to automatic impedance matching.

ICs provided with the auto-tuning feature can be modelled as a resistor connected in parallel with a switchable network of capacitors [95] [Fig. 2.1(a)]. Accordingly, the equivalent input admittance of the microchip is given by a fixed conductance and a variable susceptance

$$Y_{IC} = g_{IC} + j\omega C_{IC} \tag{2.1}$$

where $Y_{IC} = Z_C^{-1}$, g_{IC} and C_{IC} are the admittance, the conductance and the capacitance of the chip, respectively. The variable capacitance $C_{IC}(n) = C_{min} + nC_0$ can span from a minimum value C_{min} to a maximum value through an incremental step C_0. It is evident that the sensor code is correlated with the number of capacitors n, even if the relationship $SC(n)$ can be approximated in multiple ways. The basilar approach approximates $SC \simeq n$, but a more precise approximation is described next.

The number of equivalent connected capacitors n varies to compensate the antenna's admittance seen by the IC (Y_A) according to the following self-tuning equation [95]

$$|B_A + B_C| = 0 \tag{2.2}$$

where $B_A = \text{Im}(Y_A)$ and $B_C = \text{Im}(Y_C)$ are the susceptance of the antenna and the IC, respectively. It is worth noticing that the admittance $Y_A = Z_A^{-1}$ accounts for the entire environment seen by the IC that, in free-space, reduces to the sole hosting antenna whereas in more complex cases it is substituted by the embedded impedance, as discussed next. Therefore, the self-tuning equation achieves the perfect susceptance matching and optimizes the power transmission coefficient. Because of nonlinearities in the real self-tuning ICs, the self-tuning equation holds only in a microchip-specific range named *linear range* whereas saturation effects happen outside it [Fig. 2.1(b)]. The saturation zones are named upper and lower if the SC is too high or too low to work according to (2.2), respectively. Because of the saturation zones, the SC can be evaluated from B_A from two different formulas, namely [95]

$$SC(B_A) = \text{nint}\left[-\frac{1}{C_0}\left(C_{min} + \frac{B_A}{\omega}\right)\right] \tag{2.3}$$

where $\omega = 2\pi f$, nint symbolize the nearest integer operator and the saturation zones are neglected, and

$$SC(B_A) = N_{min} + \text{nint}\left[-\frac{1}{C_0}\left(C_{min} + \frac{B_A}{\omega}\right)\right] \tag{2.4}$$

when they aren't; obviously, the incremental step C_0 is evaluated from the capacitance range and the (N_{min}, N_{max}) pair accordingly. When evaluating the capacitance step, the (N_{min}, N_{max}) values are usually approximated with the saturation SC reported on the IC's datasheet.

The auto-tuning antennas can be used for sensing purposes by exploiting the relationship between the antenna admittance and the physical parameter Ψ to monitor, provided that the auto-tuning IC works in the linear range. However, the antenna susceptance B_A is unknown; thus, the relationship $SC(\Psi)$ must be experimentally determined through a

calibration curve. Application- and IC-specific baselines can be removed by calibrating the SC w.r.t. a reference condition SC_0 introducing the Differential Sensor Code ΔSC

$$\Delta SC\left(\Psi\right) = SC_0 - SC\left(\Psi\right). \tag{2.5}$$

In other words, the SC_0 value is the SC value measured in any reference condition starting from whom variations of the measurands are sensed. The SC is also called "raw SC" to ease the distinction between the SC and the ΔSC. As a consequence of the transduction mechanism, self-tuning antennas are highly susceptible to changes in the electric properties of the tagged object, e.g. conductance or permittivity.

Theoretically, auto-tuning antennas can also be exploited to simultaneously sense two physical parameters, provided that they independently affect the antenna's conductance and susceptance [95]. While the auto-tuning perfectly compensates the susceptance variation, the conductance mismatch causes a reduction of the realized gain G_τ. In this case, the SC and the RSSI will be used to sense a parameter each. The antenna exploitation as a transducer can be further engineered by resorting to additional transduction mechanisms onboard the antenna, e.g., a humidity-dependent capacitance and a thermal-dependent resistance. However, this multi-parameter sensing has never been experimented.

2.1.2 Assessing Communication with Self-tuning ICs

The formulas employed to asses the communication performances of the RFID antennas modify to account for the self-tuning mechanism. When the RFID is designed to communicate in the far-field, the realized gain is employed, whereas the transducer power gain is utilized for designing near-field communications.

2.1.2.1 Realized Gain with Self-tuning

From Fig. 2.1(b) and (2.2), the admittance of the self-tuning ICs can be written as a piece-wise function

$$C_{IC} = \begin{cases} C_{IC}(N_{min}) & \text{if } -\omega C_{IC}(N_{min}) < B_A \\ -B_A/\omega & \text{elsewhere} \\ C_{IC}(N_{max}) & \text{if } -\omega C_{IC}(N_{max}) > B_A \end{cases} \qquad (2.6)$$

Consequently, the power transmission coefficient from (1.1) becomes

$$\tau = \begin{cases} \dfrac{4g_{IC}g_A}{|g_{IC}+j\omega C_{IC}(N_{min})+Y_A|^2} & \text{if } -\omega C_{IC}(N_{min}) < B_A \\ \dfrac{4g_{IC}g_A}{|g_{IC}-B_A+Y_A|^2} & \text{elsewhere} \\ \dfrac{4g_{IC}g_A}{|g_{IC}+j\omega C_{IC}(N_{max})+Y_A|^2} & \text{if } -\omega C_{IC}(N_{max}) > B_A \end{cases} \qquad (2.7)$$

Accordingly, the realized radiation gain is obtained by multiplying the antenna's gain by (2.7). Since the self-tuning mechanism enormously extends the frequency bandwidth of the power transmission coefficient, the radiation performance of the RFID antenna will be stable in the whole auto-tuning range given by the interval between $C_{IC}(N_{min})$ and $C_{IC}(N_{max})$.

2.1.2.2 Transducer Power Gain with Self-tuning

If the reader's and the tag's antenna are not in the radiating far-field of each other, the radiation gain can not be evaluated and the communication performance can be analyzed through the *transducer power gain* G_T, which is defined as the ratio between the power delivered by the network to the load (here the IC) and the available power from the generator. This parameter is a feature of the whole link and it is therefore more general than the realized gain of an antenna as it also accounts for the mutual interaction among the transmitting and receiving antennas as well as for the effect of the nearby environment.

The transducer power gain can be employed to model links which happen in the radiating near-field (also known as mid-field, i.e. the region comprised between the Fresnel and the Fraunhofer limits). It is derived by two-port models [96] (Fig. 2.2) where, in RFID links, one port includes the reader's generator and antenna and the other one the microchip of the tag. The two-port model can employ the impedance ($\mathbf{Z}$), scattering ($\mathbf{S}$), or admittance ($\mathbf{Y}$) matrixes, denoted with bold letters: if the $\mathbf{Z}$ or the $\mathbf{S}$ matrixes are used, the equivalent Thevenin circuit of the antennas are employed, if the $\mathbf{Y}$ matrix is used instead, the Norton
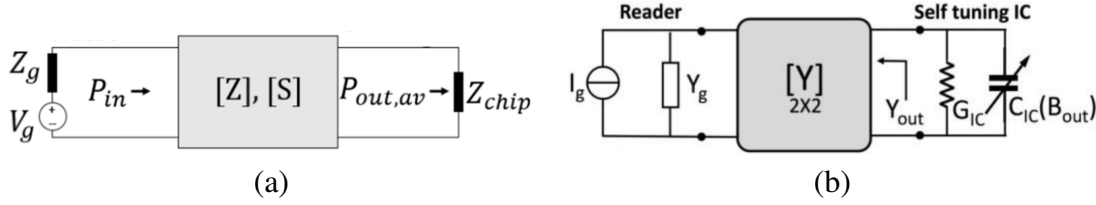
Figure 2.2: Two-port models of near-field RFID links. The port 1 is the reader (subscript *g*) and the second port is the integrated circuit (subscript *chip* or *IC*).The antennas and the environment between them are modeled through (a) Thevenin equivalent circuits and $(\mathbf{Z}, \mathbf{S})$-matrix, or (b) Norton equivalent circuit and $\mathbf{Y}$-matrix, respectively. In (b), the port 2 includes the model of a self-tuning IC.

circuits are drawn. The power entering the two-port network is P_{in}, whereas the power de-livered to the IC is $P_{out,av}$. Accordingly, the embedded admittance seen by the IC, i.e. the input admittance seen by port 2 in Fig. 2.2, is Y_{out}.

The transducer power gain formula is derived from the $\mathbf{Z}$ matrix in [96] as

$$G_T = \frac{P_{R \to T}}{P_{av,R}} = \frac{4 R_{IC} R_g |Z_{21}|^2}{\left| (Z_{11} + Z_g)(Z_{22} + Z_{IC}) - Z_{12} Z_{21} \right|^2} \tag{2.8}$$

where Z_{ij} is the (i, j)-th element of the impedance matrix. It is a significant detail that Orfanidis draws two demonstration of (2.8) in [96], one through matrix calculation and one through a T-equivalent topology. The demonstration by T-equivalent topology needs the hypothesis of a reciprocal network, as to say, a symmetric two-port matrix, to draw the T-equivalent circuit itself. Consequently, the transducer power gain obtained through this last demonstration is a particular case of (2.8) when the impedance matrix is symmetric.

By assuming a reciprocal network and substituting the T- with a Π-equivalent topology, the embedded antenna admittance Y_{out} is

$$Y_{out} = G_{out} + j B_{out} = Y_{22} - \frac{Y_{12}^2}{Y_{11} + Y_g} \tag{2.9}$$

and, therefore, the susceptance to be used to evaluate the IC capacitance of self-tuning IC with (2.6) is B_{out} instead of B_A. Afterwards, by applying the dual formulation than in [96], the transducer power gain formula is

50

$$G_T = \frac{4G_{IC}G_g \left|Y_{12}\right|^2}{\left|(Y_{11} + Y_g)(Y_{22} + Y_{IC}) - Y_{12}^2\right|^2}. \tag{2.10}$$

Obviously, G_T as function of $\mathbf{Y}$ can be obtained also with matrix calculation to obtain the dual formulation than (2.8).

The **S**-matrix is used to evaluate the *system gain* sys_g, which is defined as the transducer power gain when both the port are perfectly matched:

$$sys_g = \frac{\left|S_{21}\right|^2}{\left(1 - \left|S_{11}\right|^2\right)\left(1 - \left|S_{22}\right|^2\right)} \tag{2.11}$$

The system gain is usually employed to compare different antenna layouts independently from the actual IC considered [97].

When using self-tuning ICs, the $\mathbf{Y}$ representation is the most appropriate and the model of the microchip is at the RFID port of the two-port network as shown in Fig. 2.2(b). The variable IC capacitance is considered by inserting (2.6) in (2.10), leading to the following piece-wise function

$$G_T = \begin{cases} \dfrac{4G_{IC}G_g|Y_{12}|^2}{\left|(Y_{11}+Y_g)(Y_{22}+G_{IC}+j\omega C_{IC}(N_{min})) - Y_{12}^2\right|^2} & \text{if } -\omega C_{IC}(N_{min}) < B_{out} \\[2mm] \dfrac{4G_{IC}G_g|Y_{12}|^2}{\left|(Y_{11}+Y_g)(Y_{22}+G_{IC}-jB_{out}) - Y_{12}^2\right|^2} & \text{elsewhere} \\[2mm] \dfrac{4G_{IC}G_g|Y_{12}|^2}{\left|(Y_{11}+Y_g)(Y_{22}+G_{IC}+j\omega C_{IC}(N_{max})) - Y_{12}^2\right|^2} & \text{if } -\omega C_{IC}(N_{min}) > B_{out} \end{cases} \tag{2.12}$$

where the incremental step of the IC's capacitance is assumed infinitesimal so that, in the linear range, $-\omega C_{IC}(N_{min} \leq n \leq N_{max}) = B_{out}$.

2.2 Constrained Design of Self-tuning RFID Sensors

The sensing through auto-tuning antennas is possible only if the IC works in given conditions. Even in the linear range of the self-tuning mechanism, if the power delivered to the antenna is excessive, the relationship between the SC and the measurand will be distorted

by nonlinear effects that can hinder the sensor effectiveness. Therefore, aside from the distinction between the linear range and the saturation zones, there's difference also between the linear and nonlinear regimes with reference to the incoming power [98]. Because of this further issue, self-tuning ICs return to the reader an additional metric named *RSSI-on-chip* ($RSSI_{oc}$) that quantifies the power delivered to the IC.

While the nonlinearities respect to the delivered power can be relatively easy to manage by adjusting the incoming power based on the $RSSI_{oc}$, the SC should be not only in the linear zone, but it should be perfectly mapped in the whole linear range to maximize the sensitivity of the antenna to the measurand [Fig. 2.1(c)]. A design technique should thus be applied when designing sensor antennas with self-tuning to simultaneously maximize the tag sensitivity to the measurand and the read range. The rationale of the design is to consider the effects of the different boundary conditions on the returned SC and the reader-tag propagation link.

The tag antenna layout optimization is therefore a constrained design problem which can be formulated as the minimization of a penalty function. Let $\mathbf{a} = \{a_1, \ldots, a_m\}$ be the vector (denoted by bold letters as matrixes) of geometrical parameters of the tag antenna to be optimized for matching the envisaged constraints. Then, the penalty function to be minimized $U(\mathbf{a})$ can be written as

$$U(\mathbf{a}) = \sum_i w_i u_i(\mathbf{a}) \tag{2.13}$$

being w_i normalized weight so that $\sum_i w_i = 1$ and u_i sub-penalties function. The sub-penalty functions enforce the communications and sensing requirements. At least two sub-penalties are required to optimize the antenna for sensing, i.e. the $n(\psi_{min}) - N_{min}$ and the $N_{max} - n(\psi_{max})$ conditions where all the measurand's Ψ states foreseen are comprised in $[\psi_{min}; \psi_{max}]$, ψ_{min} returns the lowest SC in the $[\psi_{min}; \psi_{max}]$ range and ψ_{max} returns the highest. Both the differences must be greater than zero to avoid the lower and the upper saturation zones of the SC, respectively. Moreover, if the differences are both zero, the sensitivity to the measurand will be maximum, as in the linear zone the sensor's response is roughly linear and the sensitivity S can be approximated as

$$S(\psi) \simeq \frac{SC(\psi_{max}) - SC(\psi_{min})}{\psi_{max} - \psi_{min}}. \tag{2.14}$$

Accordingly, these overall penalty function depends on

$$\Delta B_{out}(\Psi) = |B_{out}(\psi_{max}) - B_{out}(\psi_{min})| \tag{2.15}$$

and, in the simplest case, the optimal layout is the one maximizing $|\Delta B_{out}(\Psi)|$. A third sub-penalty tern can be inserted in (2.13) to maximize the realized gain or the transducer power gain if the communication link happens in the far-field or the near-field, respectively.

2.3 Application to On-body Moisture Sensor to Monitor the FFRs' Effectiveness

Thanks[1] to the possibility of sensing measurands while avoiding external components in addition to the antenna, the self-tuning RFID tags allows for miniaturized sensors even at UHF frequencies and are extremely interesting for B-IoT applications. The design and experimentation of a wearable RFID tag for on-body sensing is discussed in this Section. An application related to the COVID-19 pandemic which is still raging all over the world at the time of writing is considered, namely the monitoring of the FFRs humidity which is related to their effectiveness. Ideally, a smart-FFR sensorized with a single RFID tag will serve multiple purposes, like moisture monitoring, the identification of the wearer, and the check of the body temperature (Fig. 2.3).

2.3.1 Filtering Capacity of FFRs Based on Their Humidity

Face protections, like the Filtering Facepiece Respirators (FFRs), can significantly reduce the risk of infection caused by respiratory pathogens [99]. Because of the ongoing COVID-19 pandemic, the World Health Organization advises for the universal masking in health

---

[1]Work in collaboration with following students of the Tor Vergata University of Rome (M.Sc. in Medical Engineering course): Aru, Luisa; De Angelis, Ludovica; Diamanti, Arianna; Fontana, Elisa; Gagliardi, Miriam; Naccarata, Federica; Salvati, Veronica; Tocci, Tiziana; Veltro, Giulia. I supported as supervisor the experimentation of the sensor.

Figure 2.3: Concept of an RFID-sensorized facemask monitoring the mask status and detecting coughing.

facilities, and the FFRs should be replaced as soon as they become damp [99]. However, such widespread use of masks can cause supply shortages, and their use must be optimized. As recommended by the USA National Institute for Occupational Safety and Health [100], the current practice is not to wear the same mask twice and replace it after a maximum of eight hours of continuous use. Indeed, moisture produced by breath causes an increase of the RH of the interior microclimate and some condensation on the internal surface of the FFR. This was reported to decrease the filtering effect [101, 102], although the knowledge on the phenomenon is still limited, as there is no way to monitor the humidity of an FFR without utilizing costly humidity sensors. Moreover, the moisture in the FFR's deadspace (i.e. the volume between the mask and face) is linked to user discomfort [103].

To discriminate a dry or slightly damp mask from a wet one that needs to be replaced, a low-cost moisture sensor could be placed inside the mask to monitor its effectiveness. The moisture sensing could also be useful to optimize the decontamination cycles of the FFRs [104]. FFRs equipped with RFID tags have been recently proposed for managing

the medical supply chains [105], and RFID sensor-tags for humidity can exploit the antenna performance variations, such as frequency shifts [106] or the power collected by the IC [107]. The price to pay for sensing is a degradation of the read-range as humidity and moisture increase. A different approach considers instead a dedicated external sensor connected to the tag [64]. Although the communication performance is preserved, this solution involves higher complexity and cost, making the application into a cheap FFR (costs lower than 1 USD per unit) rather impractical.

Thus, a facemask-integrated wearable moisture sensor working with the auto-tuning ICs could effectively address the problem. The tag has to be embedded in an N95 FFR and the constrained design can optimize the sensitivity to the moisture inside the deadspace.

2.3.2 Design of the Self-tuning Sensor in the Mask

To design the self-tuning sensor-tag, as first thing the vector of geometrical parameters **a** has to be determined. As antenna geometry, we selected a symmetric loop-matched [108] meandered dipole [Fig. 2.4(a)] that is connected to an Axzon S3 Magnus auto-tuning IC [109] with parameters $N_{min} = 80$, $N_{max} = 400$, $G_{IC} = 462$ mS, $C_{min} = 1.9$ pF, $C_{max} = 2.9$ pF and microchip sensitivity $P_{IC} = -16.6$ dBm. Accordingly, the resulting IC susceptance can retune in the range 10.3 mS $\leq B_{out} \leq$ 15.8 mS at the working frequency of 866 MHz, and the corresponding middle-range impedance is $Z_{IC} = 2.8 - j76.1$ Ω. The tag antenna is placed on a textile substrate suitable for integration inside the facemask and sensitive to both the moisture and the RH. The sensitive substrate to collect the moisture produced by the breath is an inexpensive twill woven fabric made of natural and synthetic fibers (50% cotton, 50% nylon) of size 70 mm × 25 mm × 1 mm. The textile has hydrophilic and hygroscopic properties [110] and absorbs liquid due to both the RH and condensation.

The geometrical parameters of the antenna are optimized through numerical simulations (by CST Microwave Studio 2018) assuming it is attached on an N95 FFR wholly made of polypropylene ($\varepsilon_r = 2.2$, $\tan\delta = 0.002$ [111]). The simulations accounted for the human head by an anthropomorphic homogeneous numerical phantom ($\varepsilon_r = 42.7$, $\sigma = 0.99$ S/m [112]) which is obtainable by combining the publicly available[2] (at the time of writing)

---

[2]Models available at https://grabcad.com/library/helmet-184 (human head model) and https://grabcad.com/library/n95-mask-covid-19-1 (FFR model).
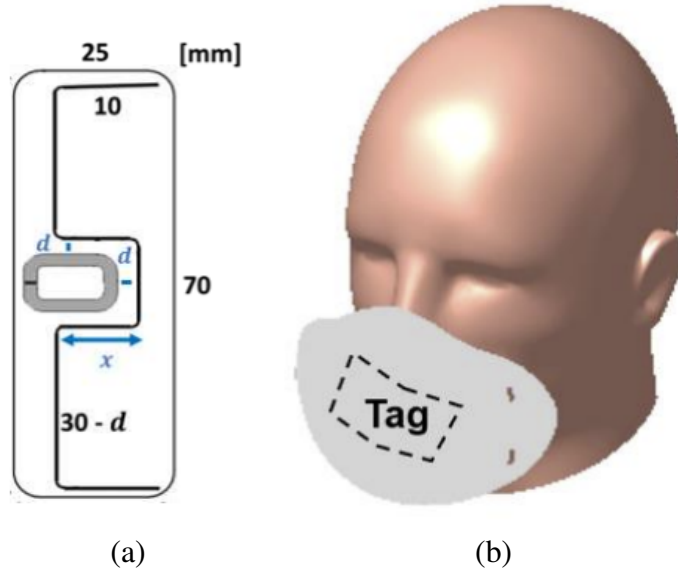
Figure 2.4: Humidity-sensing tag for sensorizing FFRs. (a) Antenna layout with the parameters to be optimized highlighted in blue, and (b) the numerical model utilized for the on-body RFID sensor.

models. The placement of the sensor tag is the core region of the FFR [Fig. 2.4(b)], which is expected to be the wettest portion of the internal surface [113]. The added surface covers a small part of the mask, and the only expected consequence on the FFR's effectiveness is a slightly improved filtering capability.

Accordingly, the set of geometric parameters of the meander line loop-matched dipole are $\mathbf{a} = \{x, d\}$ being x the part of the dipole lying along the major axis of the excitation loop and d the loop-dipole fixed distance [Fig 2.4(a)]. The excitation loop is taken from the RFM-3200 COTS tags by Axzon [114] whereas the meanderline dipole is made of a thin copper wire (diameter 80 μm). The bending of the antenna is simulated with a trapezoidal substrate and the sensorized FFR is placed on the numerical phantom of the human head (Fig. 2.5). The composed numerical phantom is then modified to simulate the extreme boundary condition to monitor, as to say a dry and a wet facemask.

The FFR wetness is quantified by weight, but the weight increase to be monitored is little known; in the literature, a FFR's weight increment of 260 ± 100 mg after 4 hours of continuous use [115], no weight difference after 1 hour of use [116], and little quantity of condensed water due to the respiration [113] are reported. As boundary conditions,
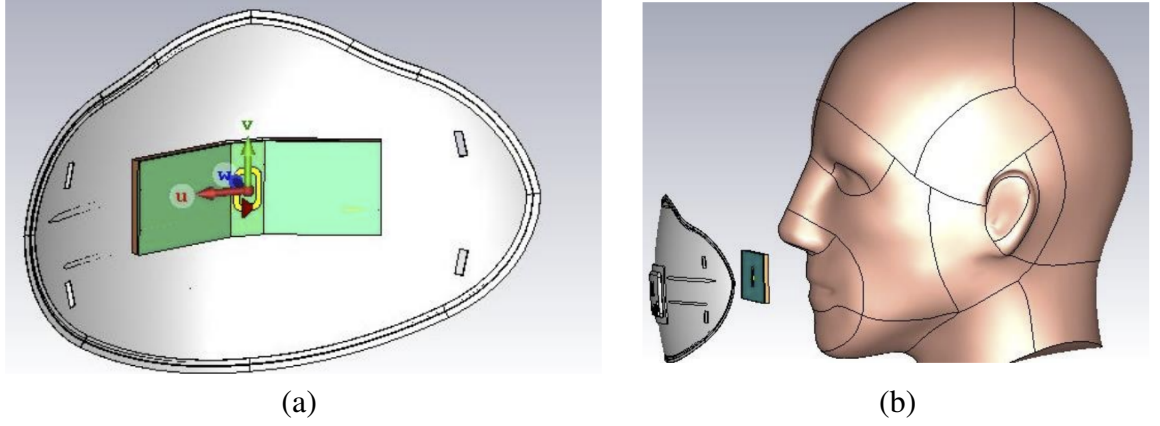
Figure 2.5: Numerical model of the facemask tag. (a) The bent tag inserted in the FFR, and (b) the wearable sensor placed on the numerical phantom of the human head.

we choose the 0% (dry air) and the 100% (saturated air) RH conditions since it is a first approximation of the phenomenon to be sensed. These two condition cause the relative permittivity of the textile substrate to increase from $\varepsilon_{r,min} = \psi_{min} = 2$ to $\varepsilon_{r,max} = \psi_{max} = 2.4$ [110]. Accordingly, the permittivity of the substrate is varied between these two conditions. Since the tag should be read in the far-field by an operator or a fixed station and the G_τ is approximately the same in both the conditions, the tag can be designed by simply maximizing the $|\Delta B_{out}(\Psi)|$ as detailed above. The resulting optimal parameter's vector is $\bar{\mathbf{a}} = \{x = 11.5 \text{ mm}, d = 0.5 \text{ mm}\}$, namely the maximum x and the minimum d possible to manufacture (Fig. 2.6). Even after the optimization procedure, the ΔB_{out} is as small as 0.34 mS given the little variation in the ε_r.

The final antenna form factor constrains the input susceptance inside the IC's tuning range [the shadowed region in Fig. 2.7(a)] for 830 MHz $\leq f \leq$ 980 MHz. The achieved realized gain is higher than $G_{\tau,min} = -15$ dBi along the direction of the nasal septum [Fig. 2.7(b)]. We also plotted the antenna's admittance on the Y-chart of Smith, and observed that the IC is represented with a line per frequency due to the self-tuning mechanism (Fig. 2.8). Thanks to the auto-tune property of the IC, G_τ exhibits the typical nearly-flat profile over a broad band. By assuming the reader emits not less than 22 dBm (low-cost handheld device) a read distance longer than 40 cm is expected. In this way, an operator with arms' length longer than 60 cm [117] could monitor a third-person facemask's status while keeping a

57
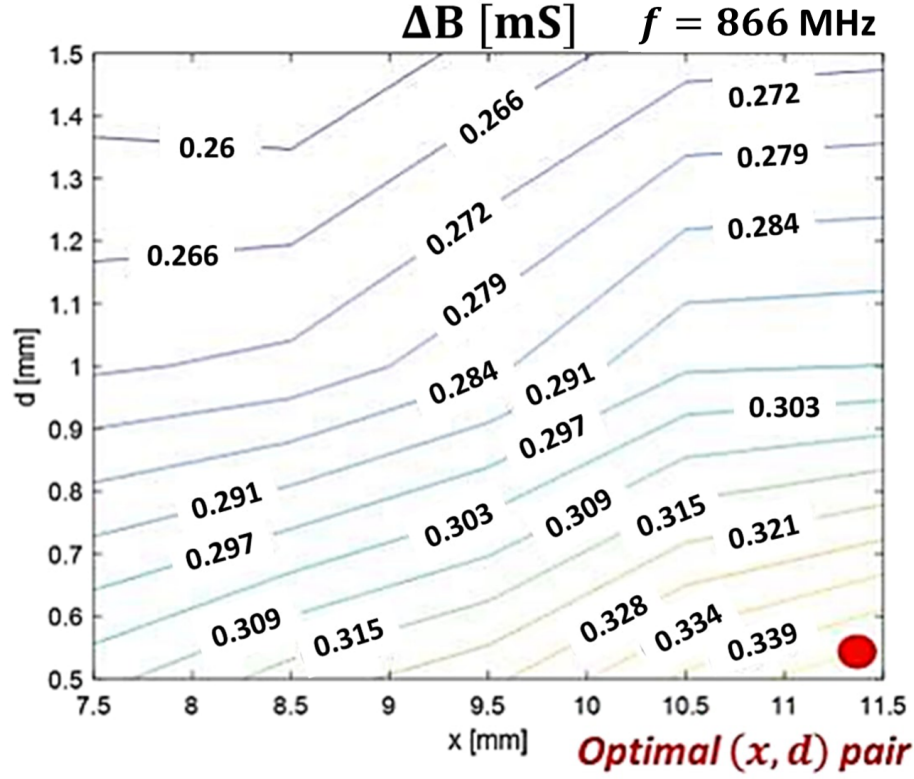
Figure 2.6: The contour plot of ΔB_{out} vs x and d. The optimal layout is returned for minimum d and maximum x possible to manufacture.

(a)   (b)
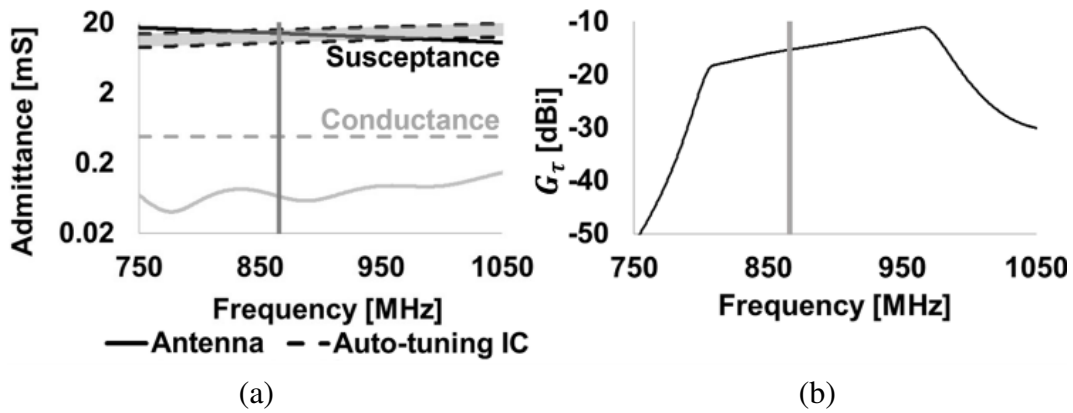
Figure 2.7: Simulated performance of the tag's antenna. The EU unlicensed $865 - 867$ MHz band is highlighted in grey. (a) Admittances of the tag's antenna and the IC. The shadowed region indicates the dynamic range of the susceptance that the auto-tuning IC can match. (b) Realized gain of the sensor-tag along the nasal septum direction.
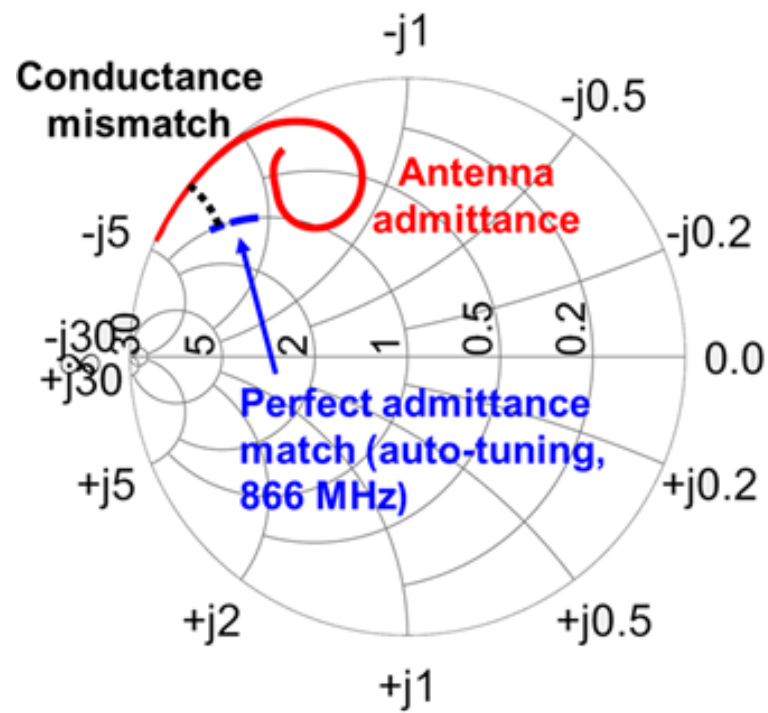
Figure 2.8: Smith chart of admittances representing the impedance mismatch of the RFID tag. The antenna's admittance between 600 MHz and 1100 MHz and the IC admittance at 866 MHz are reported.

<center>(a)   (b)</center>
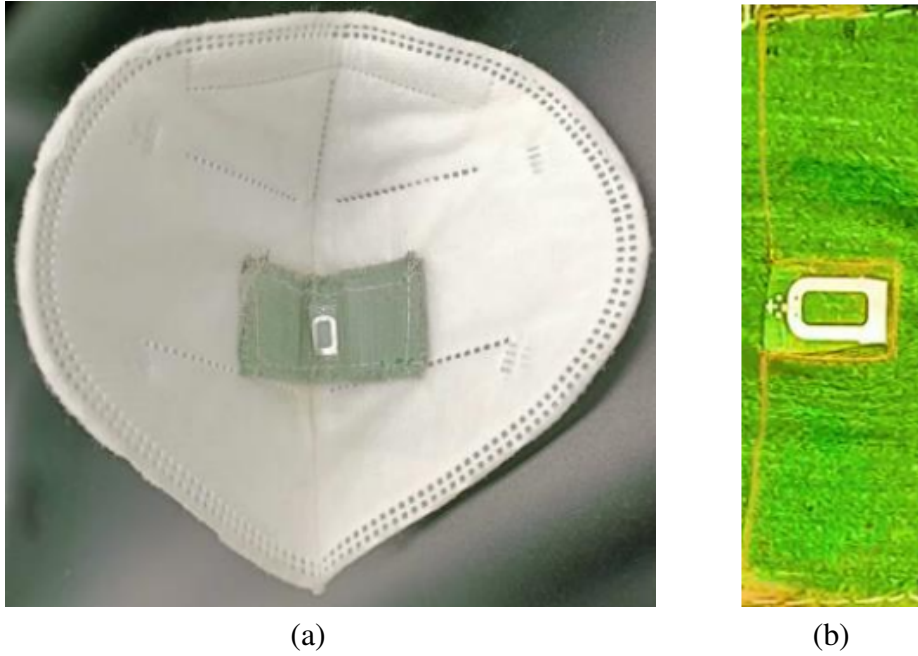
Figure 2.9: (a) Prototype of a facemask tag glued inside an N95 FFR. (b) Zoomed-in view of one tag prototype.

safety droplet-free distance of at least 1 m [99]. Moreover, as previously demonstrated in [64], this arrangement will be fully compliant with SAR regulations.

2.3.3 Protyping and Experimentation

The designed RFID sensor is experimented in different conditions to asses its effectiveness.

2.3.3.1 Test in Controlled Conditions

Some tag's prototypes were manufactured by fixing the dipole, made of a thin copper wire, onto the fabric substrate through a semi-permeable, transparent polyvinyl chloride film (Tegaderm, thickness 25 μm). The boundaries of the resulting tags were then glued inside N95 FFRs (Fig. 2.9). Three volunteers wore a prototype each, and the realized gain was measured in the direction of the nasal septum by through a Voyantic Tagformance Pro station. The measured data (Fig. 2.10) compare well with the simulations, and the average difference is just 1 dB. The three prototypes were then placed inside a Binder MKF 56 cli-

<center>60</center>
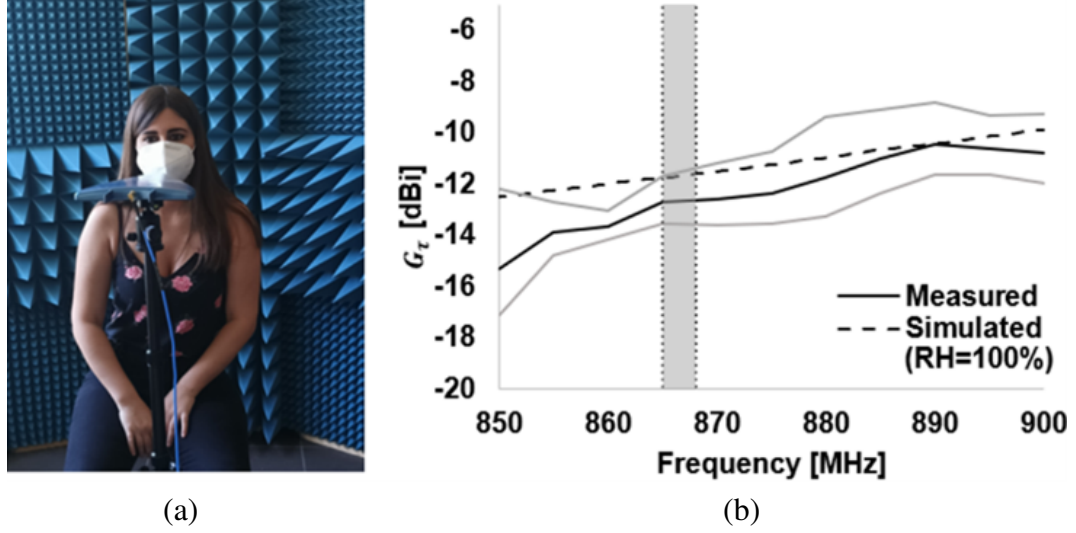
Figure 2.10: Measurement of the electromagnetic performance of the tagged FFRs. (a) Arrangement in a semi-anechoic space and (b) average measured and simulated (RH=100%) realized gain over the three prototypes each worn by a different volunteer. Grey lines indicate the average measured values plus and minus the standard deviations. The EU unlicensed 865-867 MHz band is highlighted in grey.

matic chamber to perform a test on the returned SCs when the ambient humidity is firstly kept at 10%, then raised to 100% and kept for 10 minutes. The ΔSC was measured by ensuring a fixed value of $RSSI_{oc} = 15$ to avoid nonlinearities of the self-tuning mechanism due to fluctuations in the incoming power. The calibration value SC_0 is the sensor code returned by the facemask tag when the facemask is totally dry, i.e., before the mask is wet. The measured ΔSC is slightly higher than the simulated one [Fig. 2.11(a)], probably due to the approximated model of auto-tuning ICs and the effects of condensation of moisture on the tag, not accounted for in the simulations. The sensor's response time is evaluated by stimulating the step response through a sharp exposure of 200 mg of physiologic solution sprayed inside a sensorized dry facemask [Fig. 2.11(b)]. The SC was continuously measured before, during and after the event. The discontinuity was nearly instantaneously detected with just 0.8 s settling time, corresponding to a single sample.

(a)   (b)
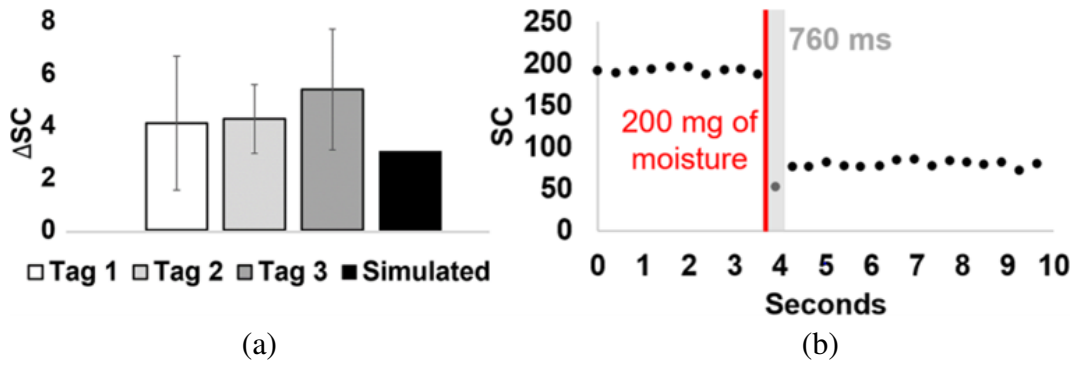
Figure 2.11: (a) Measured and simulated ΔSC after 10 minutes in the climatic chamber. (b) Step response of the tagged facemask when 200 mg of a physiologic solution are sprayed over its interior surface.
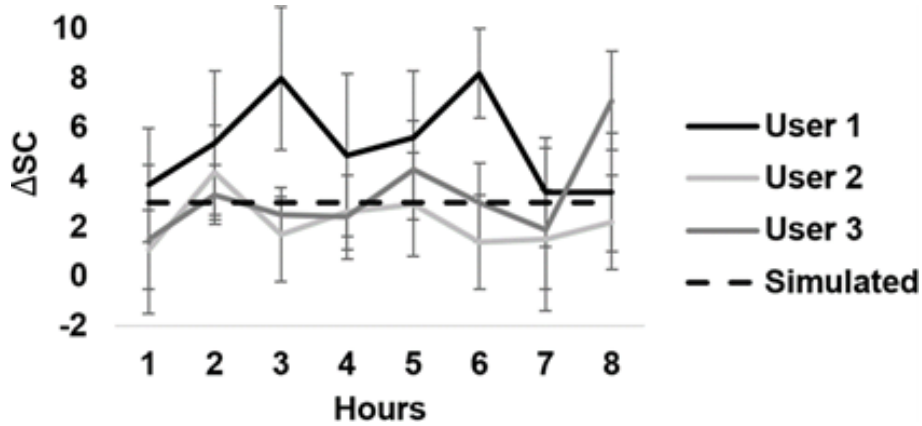
Figure 2.12: Measured ΔSC during 8 hours of continuous use of the tagged facemasks during everyday activities, compared with the simulated value.

2.3.3.2 Test in Everyday Conditions

The volunteers wore the three N95 FFRs for one 8-hours working shift. They interacted with computers and performed several non-challenging physical tasks, like walking to a shop. The FFRs were occasionally removed for less than ten consecutive minutes, and the ΔSC was always checked before and after the removal to be sure that the measurements had not been affected. Three measurements per hour were performed by using a Caen qID mini handheld reader. The resulting ΔSCs (Fig. 2.12) fluctuated in the (-2, 10) range depending on the environment and the performed tasks. In particular, there is a cyclic profile with a 3-hours periodicity in the three cases that is probably due to the balance
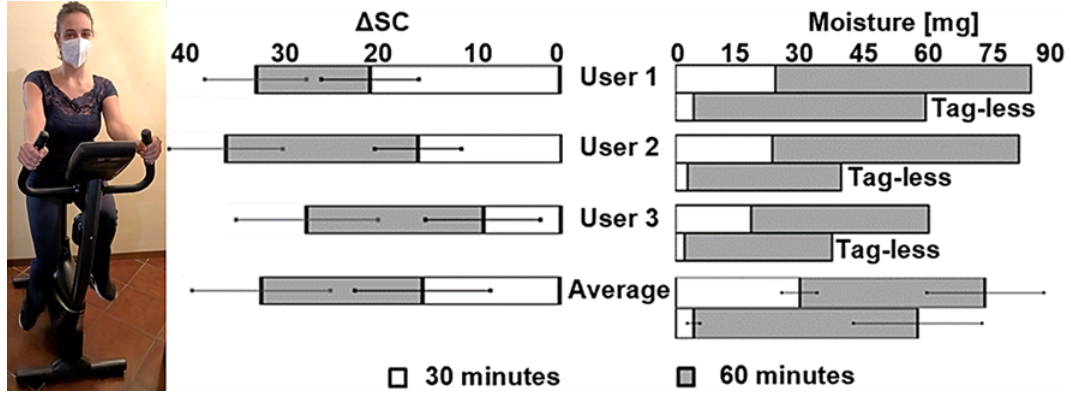
Figure 2.13: Measured ΔSC after 30 and 60 minutes of physical exercise with a stationary bike and the corresponding measured water moisture collected by the tagged and tag-less FFRs.

between cyclic generation and evaporation of the condensed moisture inside the FFRs' deadspaces. Consequently, the effective variation of the SC in regular use is modest and does not permit to discriminate relevant events. A more significant behavior was instead appreciated in stressful conditions, as described in the next Section.

2.3.3.3 Test with User under Physical Stress

The volunteers were asked to perform an intense physical exercise while continuously wearing the FFRs. They had to ride a stationary bike for an hour (maximum resistance, speed 16 km/h, indoor temperature 27 °C). The test was repeated with regular masks without the RFID sensors to evaluate the absorption capability of the sensor's substrate. In both tests, the masks were weighted after 30 minutes and then after 60 minutes of exercise. The weight increments of the tag-less N95s, as measured during the second session, are consistent with values reported in [115, 116, 118]. In comparison with the tag-less masks (Fig. 2.13), the properties of the tag substrate allowed the sensorized masks to collect an additional quantity of moisture (in average, an extra 27% of water after 1 hour of physical exercise), especially during the first 30 minutes. Therefore, the sensitivity to breath is amplified, and the capability of predictive monitoring of the mask status is improved. The corresponding measured ΔSCs are up to four times higher than in the previous experiment involving a weaker activity. Values look correlated with the weight of absorbed moisture,

63
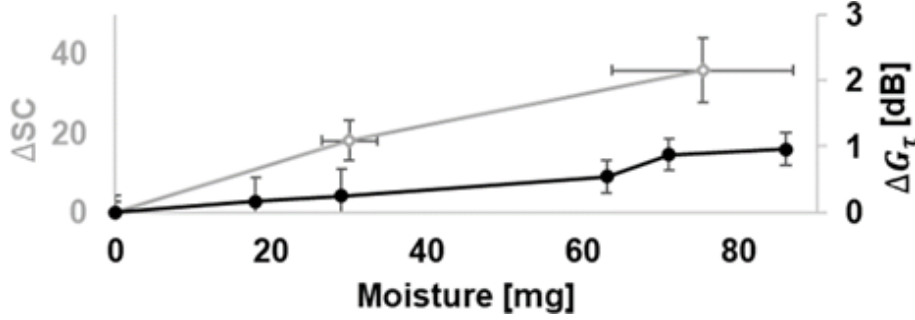
Figure 2.14: Measured ΔG_τ and ΔSC vs. the moisture collected by the mask.

as shown in Fig. 2.14. There is a detectable difference between the two states which are well identified in all the cases. The ΔSC (Ψ) profile (averaged over the three users) is nearly linear, and the estimated sensitivity is $S(\psi) \approx 0.35$ units per mg of moisture. Finally, the reduction of realized gain (ΔG_τ) vs. the condensed moisture during the exercise was of the order of just 0.1 dB per 10 mg. The maximum degradation in the extreme condition is 1 dB that converts in a 10% reduction of the read distance, at most. Accordingly, the electromagnetic performance stays almost stable during the increasing humidification of the mask.

2.4 Conclusion

In this Chapter, the self-tuning theory is recalled, and a piece-wise formula for evaluating the transducer power gain in RFID links with self-tuning ICs is derived, and the design of self-tuning RFID sensors by penalty functions is discussed. Then, a wearable tag design to sense the FFR's wetness is investigated as a case study of local processing on-body sensing B-IoT. A textile integrated moisture sensor-tag based on an auto-tuning RFID IC is designed for application onto an N95 facemask and tested by volunteers in realistic conditions. The tags discriminated the use of the FFRs during an ordinary working day ($\Delta SC \leq 10$) from a more demanding physical activity ($\Delta SC \geq 15$). Hence, the sensor could help to identify excessively wet FFRs to be replaced. Despite the optimization procedure, only half of the SC nominal range is exploited, and there is a margin to improve the sensitivity by further optimizing the antenna layout. It is worth mentioning that we tested the

64

utilized Magnus S3 IC also for cough monitoring by a sensorized facemask through the embedded temperature sensor after the moisture sensor experimentation [119]. Thus, the multi-purpose smart-facemask described above is feasible.

As shown by this case study, the local-processing B-IoT systems are heavily affected by the human body presence, which has to be accounted for in the on-body antenna design by an appropriate numerical phantom of the body itself. Consequently, when designing a sensor-antenna, every boundary condition must include the body presence. The significant inter-subject differences affect the EM performance of the on-body sensor as well as the phenomenon to be measured, with significant variations in the measurand placed onto the human body. Accordingly, the on-body sensing is likely to be more affected by inter- and intra-subject variabilities than the off-body sensing because of the two combined effects: the subject variability on the EM performance and sensing mechanism and on the phenomenon to be measured.

Chapter 3

RFID-based B-IoT for Off-body Sensing

In this Chapter, we investigate dielectric-sensing radiofrequency finger augmentation devices (R-FADs) as a case study of local processing B-IoT systems for off-body sensing. The SoA R-FADs are introduced in Section 3.1, and the first of a dielectric-sensing device is tested. Then, the constrained design of a fingertip tag with self-tuning and its experimentation (Section 3.2) are discussed. Lastly, a multi-channel system is developed, and the benefit for sensing are analyzed (Section 3.3).

3.1 R-FADs Dielectric Sensors

In the following, we introduce the R-FADs and our proof of concept of a dielectric-sensing device

3.1.1 Radiofrequency Finger Augmentation Devices

Finger augmentation devices (FADs) are electronic tools worn on the hand and defined as "*finger-worn devices with an additional augmentation other than their form, that provide a supplemental capability for one or more fingers using the finger itself as a central element*" [120]. Two examples of FADs are an on-nail display [121] and a touch-sensitive pad [122]. The main limitation of the FADs is their powering since wires hinder the free-hand gestures, resulting in discomfort for the wearer. Instead, wireless FADs usually are paired with an
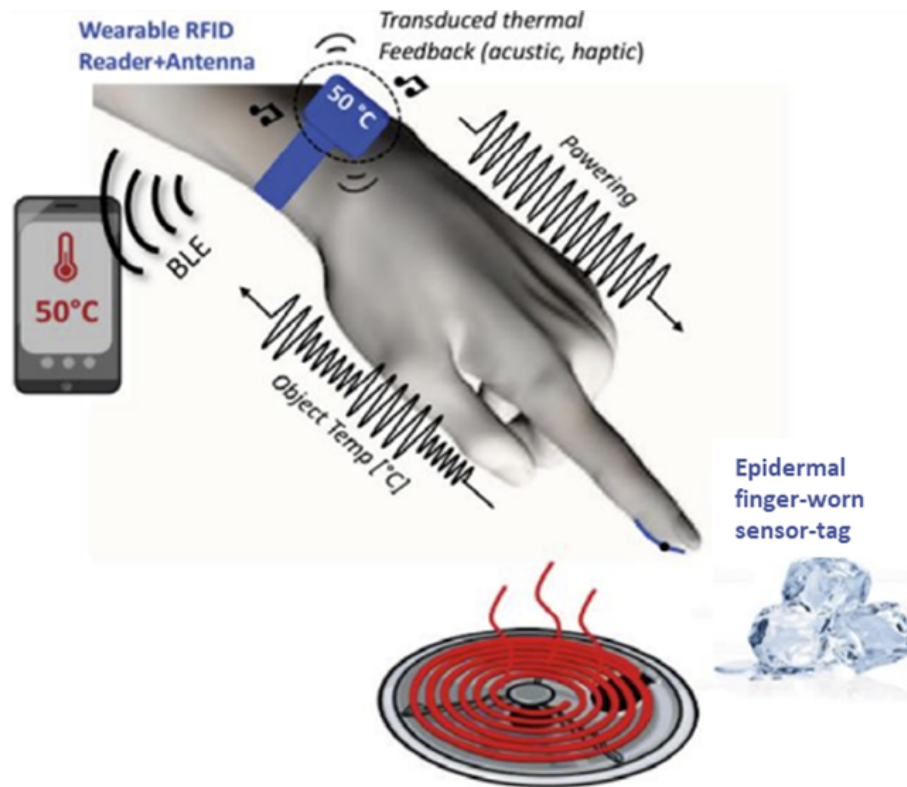
Figure 3.1: Sketch of aN R-FAD for temperature-sensing.

off-body companion device, and the resulting system is not wearable as a whole [120]. More comfortable fingertip devices can be fabricated by resorting to epidermal electronics, i.e. ultra-thin, soft electronics adhering directly onto the human skin and mechanically imperceptible for the user [45].

The on-body powering issue was overcome by combining FADs with the radiofrequency identification (RFID) paradigm, creating a new class of systems, the R-FADs. Although many RFID-based FADs were proposed (e.g., [123, 124, 125, 126]), the term R-FAD specifically refers to a system composed of finger-worn tags (hereafter called *fingertags* and *fingersensors*) provided with sensing capabilities that communicate with a reader antenna placed on the wrist. The system is powered by a portable reader source that utilizes a processing unit to give feedback to the user (Fig. 3.1). The EM wave generated by the reader's antenna energizes the fingertip sensor, which, in turn, modulates and backscatters the wave towards the reader. In this way, there is no wire connected to the

68

fingertips, the system is wholly wearable, and natural free-hand gestures are preserved. Current R-FADs communicate through UHF (860-960 MHz) links; nonetheless, the ongoing research on 5G RFID systems [127] allows envisaging 5G R-FADs in the near future with highly promising applications for the Tactile Internet [128]. While the 5G technology becomes more mature, current UHF R-FADs can be exploited in the short term to test and study the wrist-finger links through backscattering modulation. Moreover, R-FAD systems could also provide the wearer with sensorial *ultrability*. R. Shilkrot in [129] firstly used this term to describe new types of perception, not inherent to the natural human capabilities and obtained through an artificial interface. As a practical example, a dielectric-sensing R-FAD can provide the wearer with the ultrability of sensing the electric permittivity of the touched material. This ultrability can be obtained through the self-tuning ICs as shown next.

The wrist-worn reader communicates via backscattering with the fingertip sensors in the R-FAD architecture. Thus, the EM challenge consists of establishing a robust fingertip-wrist link in the presence of the lossy human body and during natural gestures. Reference [97] introduces and analyzes the wrist-finger links. There are several challenges in establishing such links. Since a wearable battery-fed reader is needed for a fully wearable R-FAD, the available power is reduced with respect to a fixed interrogation station. The direct contact between the antennas and the wearer's skin generates high power losses. The wrist-finger channel is significantly time-variant due to the free-hand gestures, which continuously change the mutual arrangement of antennas. The EM interactions occur near both the antennas and the human body.

Multiple sensors can be used simultaneously by placing them on different fingers [97]; hence the inter-sensor coupling could further complicate the interaction. Since the antennas' arrangement are dependent on the morphology of the user's hand and on the gesture performed, the link is characterized by inter-subject (user-dependent) and intra-subject (no user-dependent) variabilities. The complex wrist-finger communication operates in the mid-field and can be analyzed through a two-port model and the link quality can be assessed with the transducer power gain G_T that account for everything between the reader's antenna feeding port and the IC. If multiple tags are simultaneously worn, the inter-tag coupling can be assessed with the scattering matrix **S** [97]. Moreover, the hand size of the

69
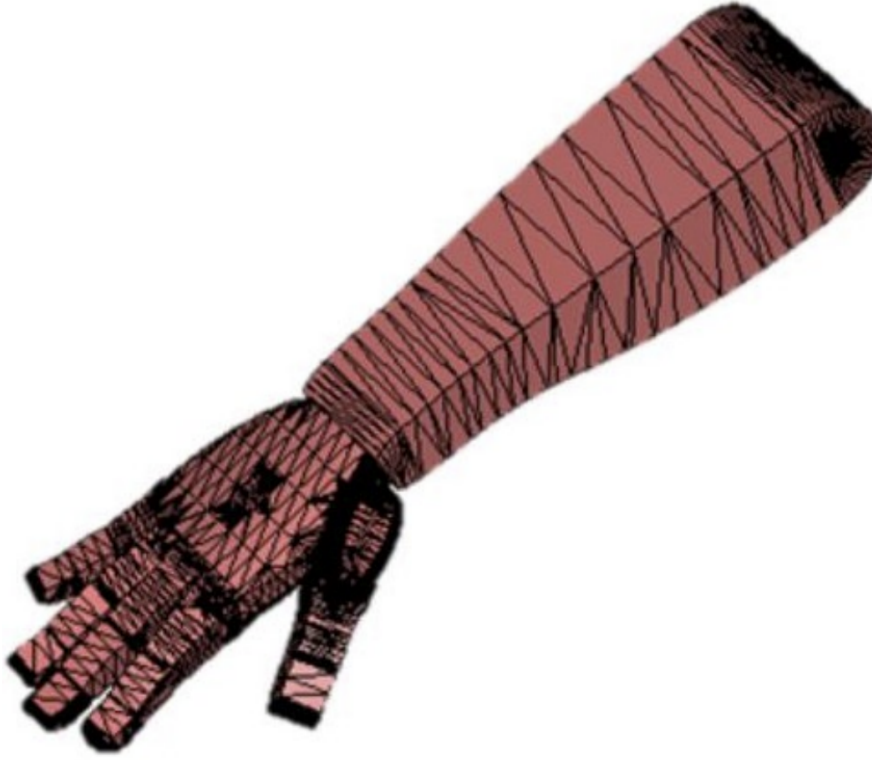
Figure 3.2: Numerical arm's phantom employed in the R-FADs design.

wearer is known to significantly affect the wrist-finger link since the higher the hand the greater the power losses caused by it.

R-FAD systems are designed employing a homogeneous arm's numerical phantom ($\varepsilon_r = 41.2$, $\sigma = 0.95$ S/m; Fig. 3.2) firstly presented in [47]. Since the arm is a different body part, the homogeneous phantom's electric properties vary from those of the head's phantom reported in the previous Chapter. The R-FADs are powered by a portable reader with a wrist-worn folded-patch antenna [47, 130] worn on the wrist using cloth bracelets directly contacting the human skin and hosting the reader module as well (Fig. 3.3). Their substrate is a slightly stretchable low-permittivity closed-cell polyvinyl-chloride foam ($\varepsilon = 1.55$, $\sigma = 6 \cdot 10$ S/m) [97], which can moderately bend to conform to the user's wrist morphology. The most appropriate placement of the reader's antenna when considering both the communication link and the user's comfort is the top side of the wrist.

Figure 3.3: R-FAD bracelet hosting the portable reader and the folded patch.

Naturally, the R-FADs are compliant with the SAR regulations, and the significant power losses caused by the human body greatly change depending on the gestures performed [97].

R-FADs can successfully estimate the temperature of a touched object but the wrist-finger communication is interrupted during the contact because of the impedance mismatch in the fingertag [47]. Moreover, the SC can be used simultaneously for sensing of the permittivity so providing to the user a ultrability and enabling applications related to the materials recognition. As detailed in the following, the self-tuning IC Magnus-S3 embedding a temperature sensor can achieve both the goals through the design technique introduced in the previous Chapter.

3.1.2 R-FADs for Dielectric-sensing

Dielectric-sensing R-FADs can estimate the permittivity of the touched object by exploiting the self-tuning mechanism to recognize the touched material. They could be useful to aid visually impaired people that find it hard to recognize the objects they are interacting with [131]. Another medical condition which could be relieved by a dielectric sensing R-FADs is the Peripheral Neuropathy that provokes a loss or decrease of tactile sensitivity and can cause problems in common tasks like finding a switch in the dark or sensing humidity of hairs after a shower [94]. Aiming at creating a new assistive device, we preliminary experimented dielectric-sensing R-FAD using a simple 33-mm-long T-matched dipole as fingertag. The size of the bio-silicone layer under the antenna is experimentally determined to minimize the turn-on power [Fig. 3.4(a)], and the dipole is stuck onto the fingertip by

71

(a)   (b)
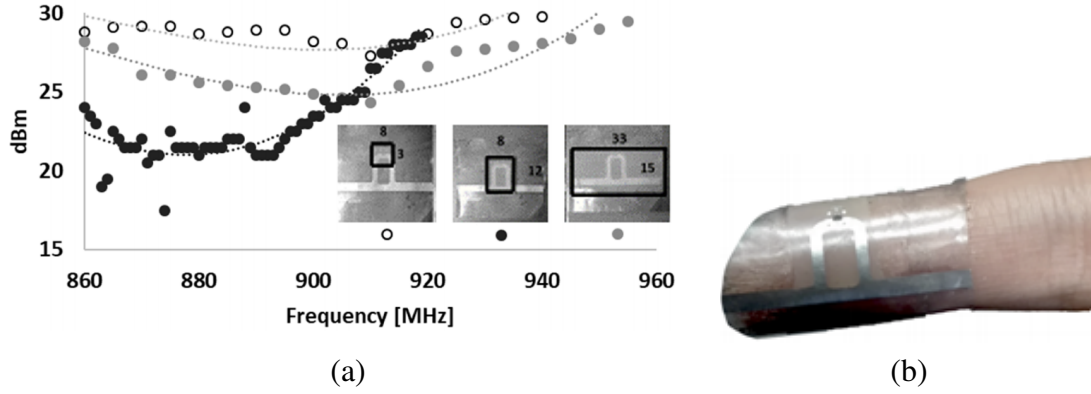
Figure 3.4: (a) Turn-on power of several configurations of the fingertip antenna for different size of the insulating silicone layers. Continuous lines are for the least square interpolation of measured (circular markers) measured data. (b) A prototype of the self-tuning tag attached to the fingertip by means of a 5 μm breathable polyurethane film and insulated in the middle by a 1 mm thick silicone layer.

Table 3.1: Dielectric constants of the materials utilized to test R-FADs [130].

Material	ε_r	Material	ε_r
Air	1	Milk	70.9
Olive Oil	3.1	Wine	75.2
Sugar	3.5	Water	78
Salt	3.8	Vinegar	79
Ethyl alcohol	17		

a breathable tape [Fig. 3.4(b)]. The SC metric returned by the auto-tuning IC is highly sensitive to the permittivity of the touched object throughout the mismatch of the fingertip antenna that the self-tuning IC tries to compensate. The raw SC is tested to recognize different materials inside PET (polyethylene terephthalate) bottles, find a light switch on the wall and sense the filling level of a bottle (Fig. 3.5 and Table 3.1).

In another test, a volunteer touched his hairs before and after wet them, and the returned raw SC was 161 and 54, respectively. Unfortunately, in R-FAD applications, guaranteeing a stable RSSI-on-chip as done in the facemask case is not possible as the interaction with surroundings and the body-shadowing are unpredictable as well as dominant. For this reason, no condition on the RSSI-on-chip is assumed in the remainder of this Chapter. The
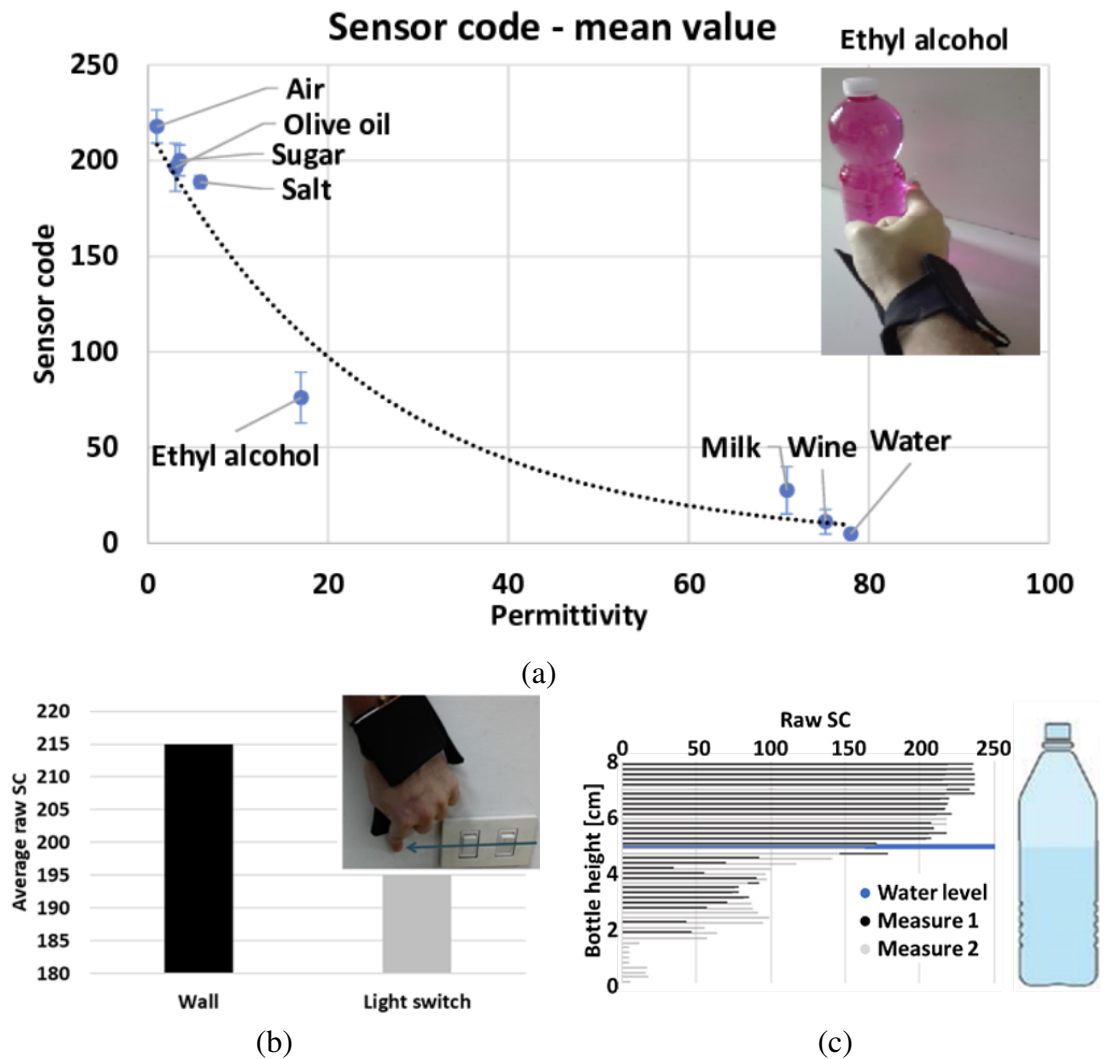
Figure 3.5: (a) Sensor code returned at 868 MHz by the self-tuning fingertip antenna when touching a PET bottle filled with different liquids and powders. Mean SC value over five measurements. (b) Raw SC returned when contacting a wall and a light switch, and (c) when contacting twice a bottle half-filled with water from the top to the bottom.

non-linear effects caused by the variable harvested power are instead taken into account by evaluating the overall uncertainty of the measurements.

Following this proof of concept the dielectric-sensing R-FAD is deemed feasible and promising. A fingertag for dielectric sensing has to be designed to fully exploit the self-tuning mechanism and to reduce the external size. Moreover, more than a single finger should be sensorized to gather more information. In the following of this Chapter we address these issues.

3.2 Constrained Design for the Dielectric-sensing Fingertip Antenna

The fingertag for dielectric sensing is optimized with a three term penalty function and preliminary tested.

3.2.1 Penalty Function Minimization

The design of the R-FADs will be constrained to make the on-hand link reliable independently of the interactions performed by the wearer. This reliability is possible by resorting to temperature-sensing ICs capable of self-tuning. When considering a self-tuning fingertip sensor, the two-ports model of the wrist-finger link must account for the variable IC capacitance as detailed in Section 2.2.

Let us assume that all the J expected interactions are fully characterized by a set of values $\blacksquare = \{\psi_1, ..., \psi_J\}$ of a physical parameter ψ. Let us now consider the case when all the interactions can be wholly characterized by the dielectric constant so that $\psi = \varepsilon_r = Re(\varepsilon_C)$, where ε_C is the complex permittivity of the touched material. Then, the vector $\psi = \varepsilon_r = \{\varepsilon_{r,1}, ..., \varepsilon_{r,J}\}$ represents the boundary conditions wherein the fingertip sensor must work. The optimal design of the sensor must ensure a reliable wrist-finger link in the above boundary conditions and, to optimally utilize the self-tuning feature of the IC, the antenna susceptance $B_{out}(\varepsilon_r)$ has to be exactly mapped in the linear range of the IC. Therefore, to activate the RFID link, the turn-on power P_{to} (i.e. the minimum power the reader has to emit to activate the remote tag) must be lower than the maximum value $P_{av,max}$ that is

74

available by the transmitter, even in the worst-case scenario concerning the parameter ψ. P_{to} is proportional to the power sensitivity (p_{IC}) of the IC through G_T. The communication constraint is, therefore:

$$P_{to}(\varepsilon_r) = \frac{p_{IC}}{G_T(\varepsilon_r)} \leq P_{av,max}, \qquad \text{for } \varepsilon_{r,min} \leq \varepsilon \leq \varepsilon_{r,max} \tag{3.1}$$

where $G_T(\varepsilon_r)$ from (2.12) accounts for the self-tuning IC. Moreover, to exploit the full self-tuning capability of the IC, the antenna susceptance

$$B_{out}\left(\varepsilon_{r,min} \leq \varepsilon \leq \varepsilon_{r,max}\right)$$

has to be exactly mapped within the whole linear region of the self-tuning IC for the possible values of the boundary conditions. The following design constraints have to be accordingly matched:

$$n(\varepsilon_{r,max}) \to N_{min}, \qquad n(\varepsilon_{r,min}) \to N_{max} \tag{3.2}$$

since $B_{out}\left(\varepsilon_{r,max}\right) > B_{out}\left(\varepsilon_{r,min}\right)$.

The optimization problem is then formalized as the minimization of the following penalty function:

$$U(\bar{\mathbf{a}}) = \sum_{i=1}^{3} w_i u_i(\bar{\mathbf{a}}) \tag{3.3}$$

where:

$$u_1 = \begin{cases} \left| 1 - \frac{|B_A(\varepsilon_{r,max})[\bar{\mathbf{a}}]|}{\omega C_{IC}(N_{min})} \right| \\ \text{if } C_{IC}\left(N_{min}\right) \leq -\frac{B_A(\varepsilon_{r,max})}{\omega} \leq C_{IC}\left(N_{max}\right) \\ 1 \qquad \text{otherwise} \end{cases} \tag{3.4}$$

$$u_2 = \begin{cases} \left| 1 - \frac{|B_A(\varepsilon_{r,min})[\bar{\mathbf{a}}]|}{\omega C_{IC}(N_{max})} \right| \\ \text{if } C_{IC}\left(N_{min}\right) \leq -\frac{B_A(\varepsilon_{r,min})}{\omega} \leq C_{IC}\left(N_{max}\right) \\ 1 \qquad \text{otherwise} \end{cases} \tag{3.5}$$

$$u_3 = \begin{cases} \dfrac{\max_j[P_{to}(\varepsilon_r)[\overline{\mathbf{a}}]]}{P_{av,max}} & \text{if } \max_j \left\{ P_{to}(\varepsilon_{r,j})[\mathbf{a}] \right\} \leq P_{av,max} \\ 1 & \text{otherwise} \end{cases} \tag{3.6}$$

with $B_A(\varepsilon_{r,j})[\overline{\mathbf{a}}]$ indicating the embedded susceptance of a tag antenna, with sizes $\overline{\mathbf{a}}$, with respect to the boundary condition $\varepsilon_{rj} \in [\varepsilon_{r,min}, \varepsilon_{rmax}]$. The sub-penalties u_1 and u_2 enforce the mapping of tag susceptance over the useful self-tuning range in (3.2), while u_3 enforces the minimization of the activation power. Sub-penalty weights are defined to satisfy the condition $\Sigma_m w_m = 1$.

The fingertip tag to be optimized is a rectangular loop EM coupled to a meandered dipole covering the area of a typical fingertip. As in the antecedent Chapter, the loop consists of a 35 μm aluminum trace, whereas the meandered dipole is made up of a copper wire having 40 μm radius. The loop is stuck onto the fingertip through a 1 mm thick biocompatible silicone layer ($\varepsilon_r = 2.5$, $\sigma = 0.005$ S/m) that is used as a spacer to reduce the interaction with the lossy human body. The touched object is represented as a cylinder (height 200 mm and radius 30 mm) made up of 0.3 mm thick PET ($\varepsilon_r = 2.5$ [132]) filled with air ($\varepsilon_{r,min} = 1$) or distilled water ($\varepsilon_{r,max} = 78$, $\sigma_{max} = 0.05$ S/m [133]) in order to account for two extreme boundary conditions. In the numerical R-FAD model, the fingertip tag touches the cylinder at the height of 80 mm from the bottom (Fig. 3.6). The maximum input power is limited to $P_{av,max} = 27$ dBm that is a typical value of battery-driven RFID readers which are suitable to be integrated within a wrist module.

After having fixed the external size of the meandered dipole (15 x 20 mm^2) so that the tag can fit the area of a typical fingertip, the selected parameters for the optimization are the distance a_1 between the loop and the wire and the major axis a_2 of the loop (Fig. 3.7). $\overline{\mathbf{a}} = \{a_1, a_2\}$ is optimized in the ranges (0.5 mm $\leq a_1 \leq$ 2 mm), and (6.5 mm $\leq a_2 \leq$ 8.2 mm) by minimizing the penalty function as in (3.3). The weights are fixed to $w_1 =$ 0.25, $w_2 = 0.25$, $w_3 = 0.5$ so that the sensing is weighted overall as the communication. The numerical simulations evaluates the admittance matrix $\mathbf{Y}(\varepsilon_r)[\overline{\mathbf{a}}]$ of the entire R-FAD system and the environment, including the arm and the PET bottle filled with the dielectric liquids. The SC is evaluated from the embedded admittance seen by the IC by (2.3).
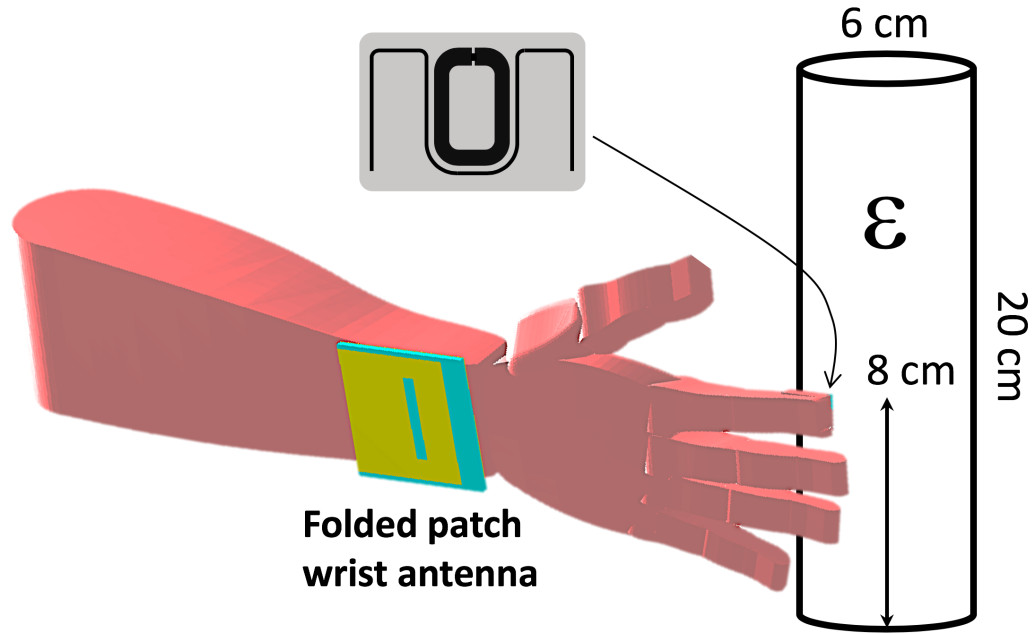
Figure 3.6: Numerical model of the whole R-FAD system.
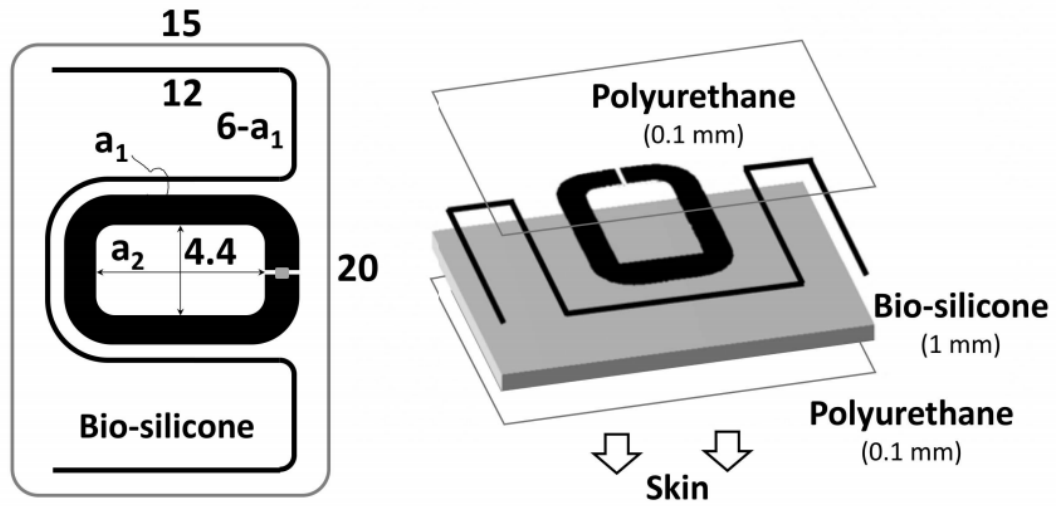
Figure 3.7: Loop match dipole used as fingertip tag over a 1-mm-thick layer of biocompatible silicone. Tag layout (sizes in mm) is on the left, and the exploded view of the multi-layers for application over the skin is on the right.
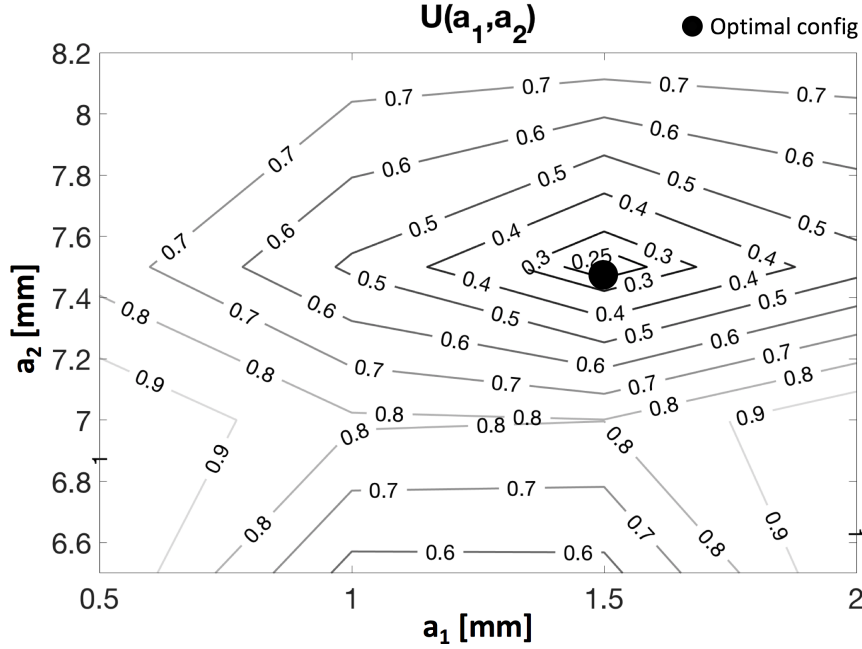
Figure 3.8: Penalty function U with the indication of the optimal couplet $\{a_1, a_2\}$.

Table 3.2: Numerical results: turn-on power and sensor code SC for the optimal configuration.

Simulated values [870 MHz]	Air ($\varepsilon_1 = 1$)	Water ($\varepsilon_2 = 78$)
P_{to} [dBm]	19	22.9
n	339	157

Fig. 3.8 shows the contour plot of the penalty function. The optimal configuration (smallest U) corresponds to the parameters $\bar{\mathbf{a}} = \{a_1 = 1.5 \text{ mm}; a_2 = 7.5 \text{ mm}\}$. The performance of the optimal R-FAD system, namely the required activation powers and the returned SC for two boundary configurations, are listed in Table 3.2. The trade-off imposed by the strict constraints returned a retuning range $|n(\varepsilon_{max}) - n(\varepsilon_{min})| = 182$, meaning that only half of the retuning capability of the IC ($N_2 - N_1 = 340$) is sufficient to match the power requirement. In both the extreme boundary conditions the estimated requested power to be emitted by the interrogator is lower than 23 dBm.

Power transmission coefficient
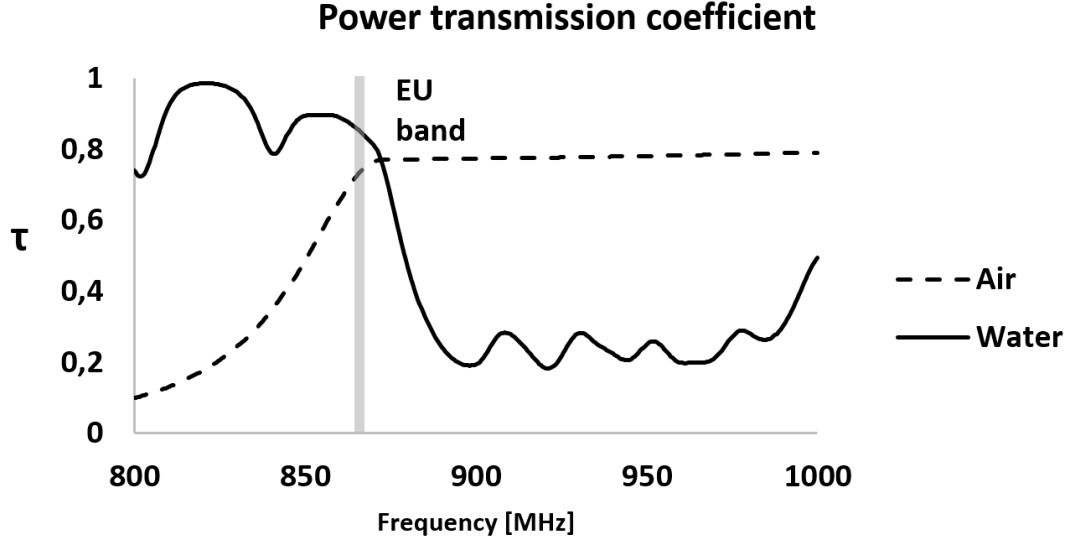
Figure 3.9: Simulated power transmission coefficient τ of the optimized fingertip tag in reference air condition and when it touches a water-filled bottle. The gray area highlights the target ETSI frequency band of the device.

Fig. 3.9 shows the simulated power transfer coefficient of the tag for the two dielectric configurations. Thanks to the self-tuning mechanism of the IC, the power transfer coefficient is $\tau > 0.7$ within the ETSI band ($865 - 868$ MHz) for both cases of air and water, in spite of their huge dielectric contrast. The small differences between the values of τ while contacting air and water are due to variations in the antenna conductance (mainly related to the different conductivity of the two materials), which is not compensated by the self-tuning mechanism.

3.2.2 Experimentation

A prototype of the whole R-FAD systems, including the wrist-mounted patch (Fig.3.10.b) and the optimized fingertip tag, was experimentally characterized. The ThingMagic M6e reader was connected to the wrist antenna and driven by a custom test software running on a notebook. The transducer power gain was derived from the measured turn-on power as $G_T = p_{IC}/P_{to}$ for three configurations: fingertip in air, fingertip touching a PET bottle

(a)   (b)
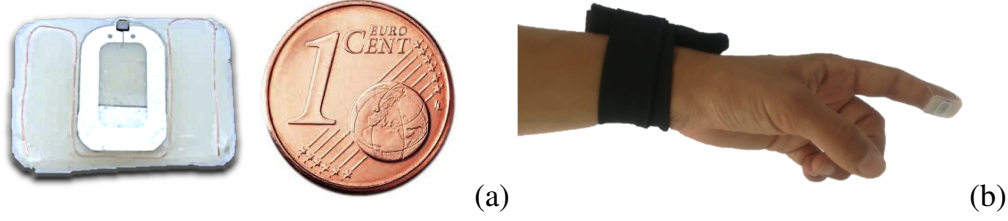
Figure 3.10: (a) Prototype of optimized fingertip antenna. (b) Entire R-FAD system comprising the fingertip tag applied on the index and a folded-patch antenna integrated within a wristband and connected by a coaxial cable to a ThingMagic M6 reader (not visible in the figure) for the measurement of the transducer power gain G_T of the link.

filled with water - as in the previous numerical simulations - plus an intermediate case considering ethyl alcohol ($\varepsilon_r = 17$, $\sigma = 10^{-5}$ S/m [134]) as filling liquid.

The measured power transducer gains and the tuning code SC are compared (Fig.3.11 and Table 3.3) with simulations involving the two-port model of the self-tuning tag. The ± 3 dB shadowed region around the nominal simulated curves accounts for *i*) the unpredictable variability of users' hand form factor and morphology w.r.t. the oversimplified homogeneous hand model [97], *ii*) the approximated deposition of the wire conductor to form the fingertip meandered dipole and *iii*) the real-life fingertip-bottle touch that is far to be sharp (and sweat-free) as in the simulations. Overall, the experimental outcomes reasonably confirm the expected results. It is moreover clear that the measured transducer gain values at 870 MHz are nearly the same ($G_T \cong -39$ dB) for the three considered dielectric boundary conditions. Accordingly, the communication performance of the system can be considered robust and rather insensitive to the variability of the touched object as enforced by the optimization procedure.

Table 3.3: Comparison between simulated and measured values at 870 MHz.

	Air	Alcohol	Water
ε_r	1	17	78
SC, estimated	339	187	157
SC, measured	327 ± 9	185 ± 34	119 ± 24
G_T, **estimated**	$-35,6$ dB	$-35,3$ dB	-39.5 dB
G_T, **measured**	-38 ± 1.7 dB	-39 ± 1 dB	-39 ± 1 dB
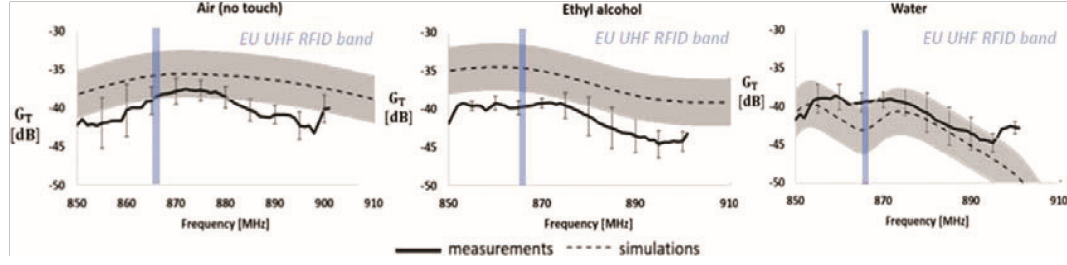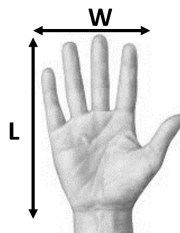
Figure 3.11: Measured and simulated transducer power gains of the optimized R-FAD for three configurations of the fingertip: a) absence of contact, b) touching a bottle filled with water and c) with alcohol. The ± 3 dB shadowed regions account for the approximate hand model w.r.t. real hands, the manufacturing un-perfection of the tag and the not sharp finger touch. The standard deviations of the measurements are related to the repetition of measurements with three prototypes for each configuration.

Table 3.4: Subjects' hand sizes.

Volunteer	Hand length (L) [cm]	Hand width (W) [cm]
Female 1	17	7
Female 2	15.5	6
Male 1	18	7
Male 2	19.5	7.5

Furthermore, the G_T is not affected by the wearer's gestures while not touching anything (Fig. 3.12).

However, the raw SC is affected by very significant inter- and intra-subject variabilities such as the antenna layout, the sensor positioning, the adherence to the human skin, the gesture performed, the specific IC used, and even more. Therefore, the raw SC has low reproducibility and has to be carefully managed. Moreover, the inter- and intra-subject variability has to be analyzed by comparing the R-FAD response over multiple users. An R-FAD system prototype (Fig. 3.13) is therefore tested with three PET bottles filled with dielectric liquids (olive oil, ethyl alcohol and vinegar; dielectric constants in Table 3.1) on four different users (inter-subject variability; sex and hand sizes in Table 3.4) and two different grasp gestures (intra-subject variability; Fig. 3.14).

The volunteers performed the pointing and prehension gestures firstly in air (i.e., without touching any object) and then by touching three bottles. The raw SCs (averaged over

81
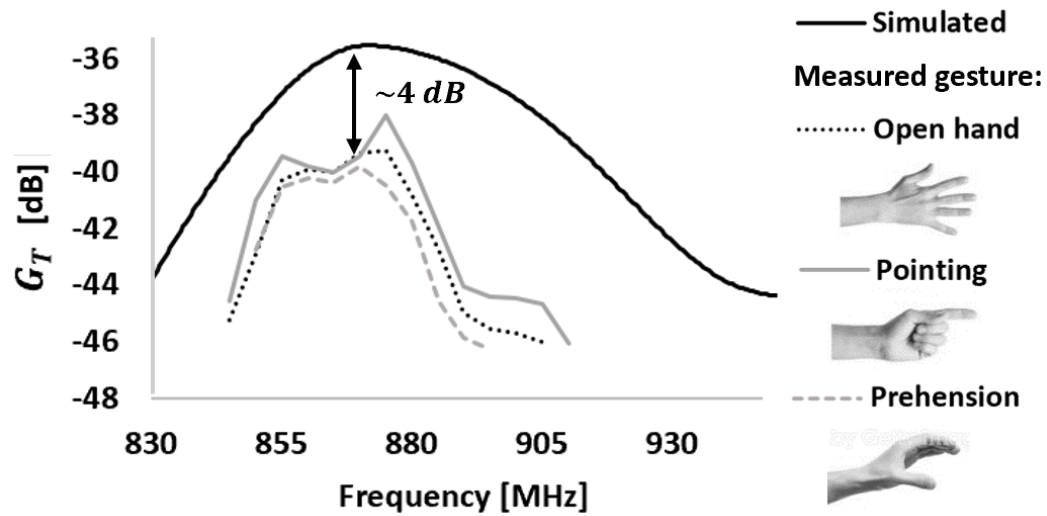
Figure 3.12: The simulated and measured transducer power gain of the R-FAD system for three different hand gestures.
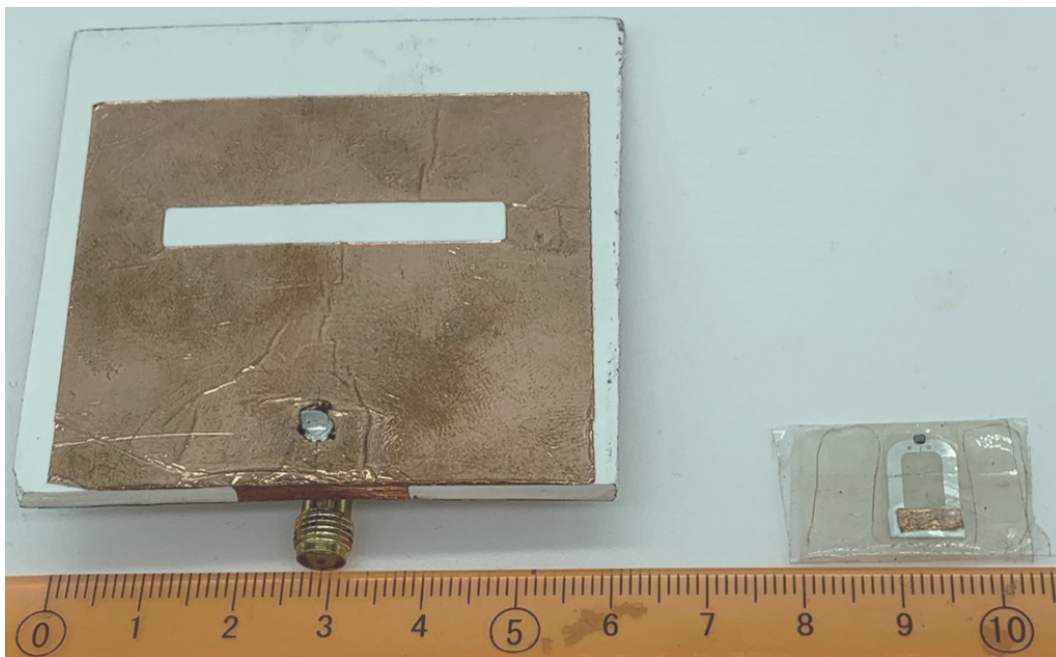
Figure 3.13: Prototypes of the wrist antenna and of the soft fingertip tag.
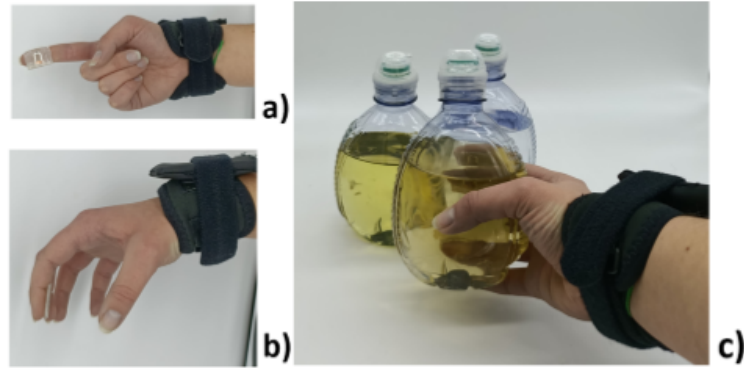
Figure 3.14: Measurement setup for testing. (a) Pointing and (b) prehension gestures. (c) Bottles filled with ethyl alcohol, olive oil and vinegar touched by a volunteer performing the prehension gesture.

five measurements per user, each lasting 3 seconds) are reported in the bar plot in Fig. 3.15. The SC(air) measured in the reference air condition are rather similar (263 ± 7) despite different users and gestures while the SCs for the liquids appear very sensitive to both the specific user and gesture.

In the previous Chapter, the ΔSC was proven to discriminate dielectric contrast even lower than a single unit, therefore a similar effect is expected when using the ΔSC with dielectric-sensing R-FADs. Indeed, the inter-subject variability can be reduced by calibration, and the SCs measured were normalized by subtracting the average SC(vinegar) value measured on the same user and gesture. The resulting ΔSC metric greatly reduces the inter-subject variability (Fig. 3.16) while maintaining significant differences for each material through the volunteers. It is worth noticing that the materials can be recognized even in the most critical situations when considering only the raw SC values would lead to ambiguities, e.g. the raw SC(alcohol) of Female 1 is equal to the average raw SC(vinegar) of Female 2 (see Fig. 3.15 again). Nonetheless, the intra-subject variability caused by the different gestures is still too high to recognize the dielectric independently from the performed gesture although the returned ΔSC while touching the alcohol-filled bottle is very similar in both the prehension and pointing case. A live demo involving dielectric-sensing R-FAD through the ΔSC is currently available online[1].

---

[1] https://www.youtube.com/watch?v=bQZOG3eVgm0
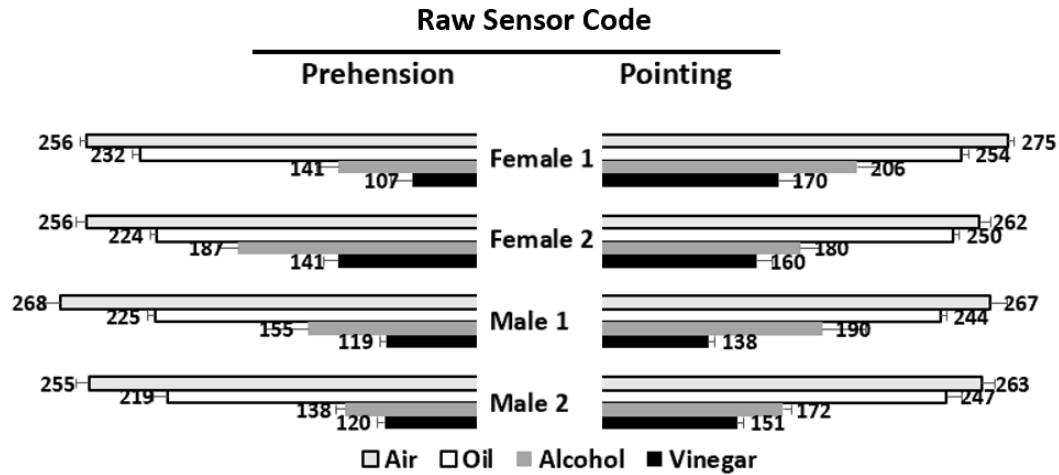
Figure 3.15: Raw measured Sensor Codes over the four volunteers and two different gestures performed while touching different materials.
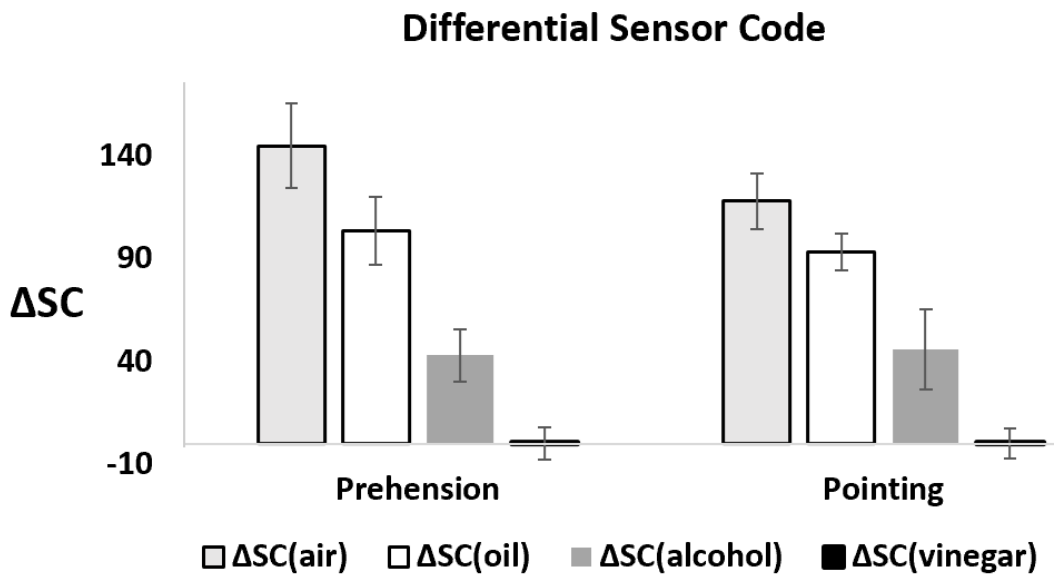
Figure 3.16: Average and Standard Deviation of measured Differential Sensor Code over the four volunteers and two different gestures performed while touching different materials. The average ΔSC of vinegar is null.
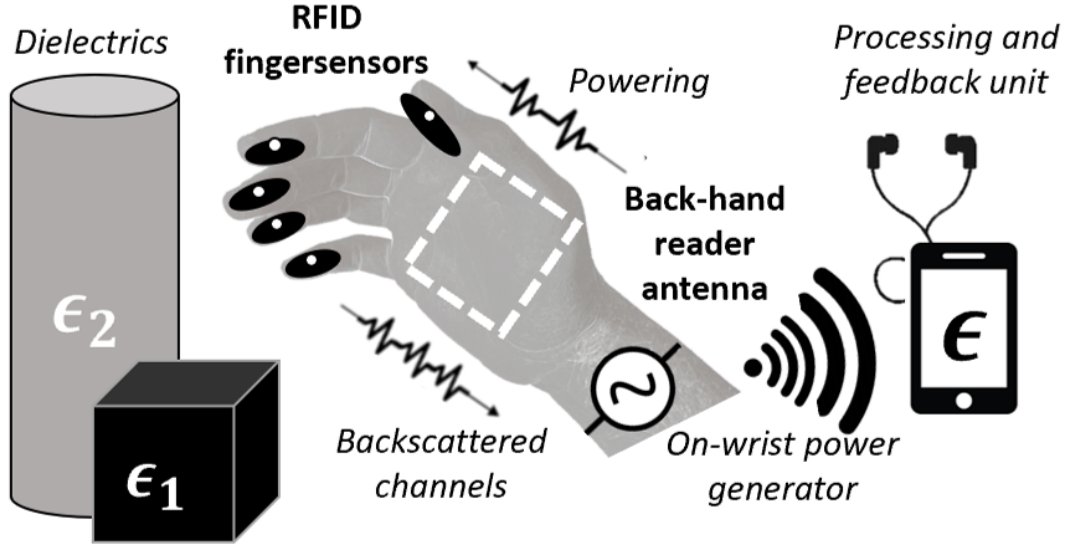
Figure 3.17: Sketch of a multi-channel dielectric-sensing R-FAD.

3.3 Multi-channel Permittivity Sensing R-FADs

In[2] all cases previously discussed, only a single fingertip is sensorized and, hence, the real potentiality of the R-FAD architecture is still mostly under-used. A further improvement on the robustness of sample data and the reliability of the identification of materials can be achieved by multi-channel R-FADs, namely devices wherein all the five fingers are provided with identical sensors simultaneously (Fig. 3.17). The measurement metric is now a *digital fingerprint*, namely the vector of the ΔSC measured by each finger so that different digital fingerprints are observed when touching different dielectric materials.

3.3.1 System and Inter-sensor EM Coupling

The considered finger antennas are the T-matched dipoles soldered to Magnus-S3 ICs (by Axzon) utilized for the proof of concept in Section 3.1.2 and are encapsulated between two layers of Ecoflex$^{\text{TM}}$ 00-30 (by Smooth-On; thickness ~ 0.3 mm each) silicone, which are cured together with a layer of Silbione$^{\text{TM}}$ (by Elkem Silicones; thickness ~ 0.1 mm; Fig. 3.18). The Ecoflex$^{\text{TM}}$ act as coating film for the sensor, whereas the Silbione$^{\text{TM}}$ silicone

---

[2]Work in collaboration with Ms. Federica Naccarata that I supported as adjunct supervisor.
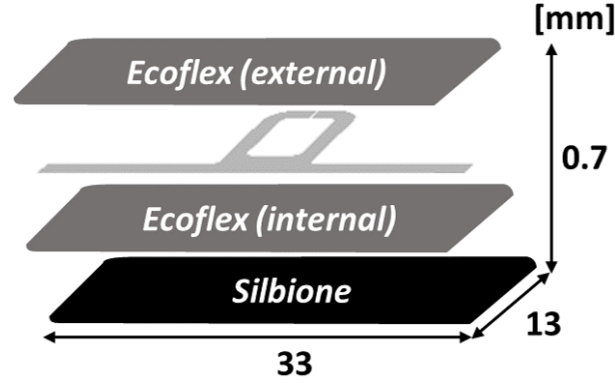
Figure 3.18: Exploded view of the fingersensor.

ensures the adherence to the skin of the finger. The electric properties of the two silicone rubbers were characterized with a two-port ring resonator [135]. The reader folded-patch is placed on the back-hand to properly illuminate all the fingertags. The fingers are labeled with Roman numerals for the sake of conciseness, going from I (thumb) to V (little finger).

The inter-sensor electromagnetic coupling is assessed by numerical simulations. The sensors are positioned on the fingers so that the IC is illuminated by the highest possible E-field. According to the simulations, the fingersensors do not significantly illuminate each others because of the human body tissue power absorption (Fig. 3.19).

3.3.2 Prototypes and Measurement Procedure

3.3.2.1 R-FAD Prototype

A multi-channel R-FAD prototype is then manufactured. The resulting prototype is bio-compatible, soft, gently following the finger's natural bending and can be detached and attached several times, after cleaning. (for instance, when the wearer changes; Fig. 3.20).

The numerical simulations are in agreement with the turn-on power measured when a user wears the five fingersensors or only one of them utilizing a multi-channel R-FAD prototype. The turn-on powers experimentally registered confirm that there is no significant difference in the transducer power gain when a different number of fingersensors is worn [Fig. 3.21(a)] and the sensors are negligibly electromagnetically coupled.
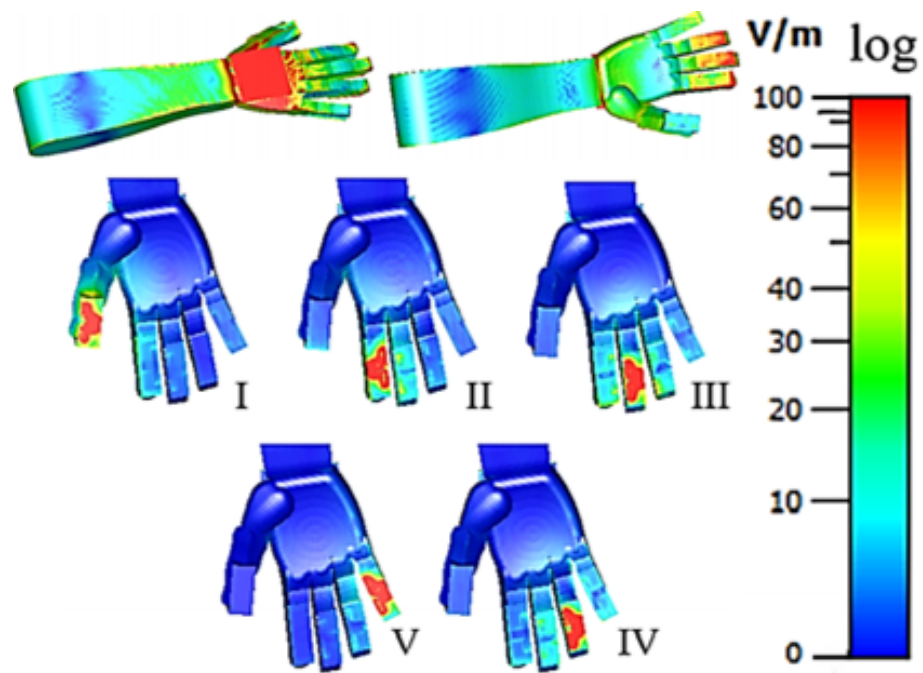
Figure 3.19: Numerical simulations of inter-sensor electromagnetic coupling (E-field) of the multi-channel R-FAD. The normalized E-field when only one of the six ports is fed is shown.
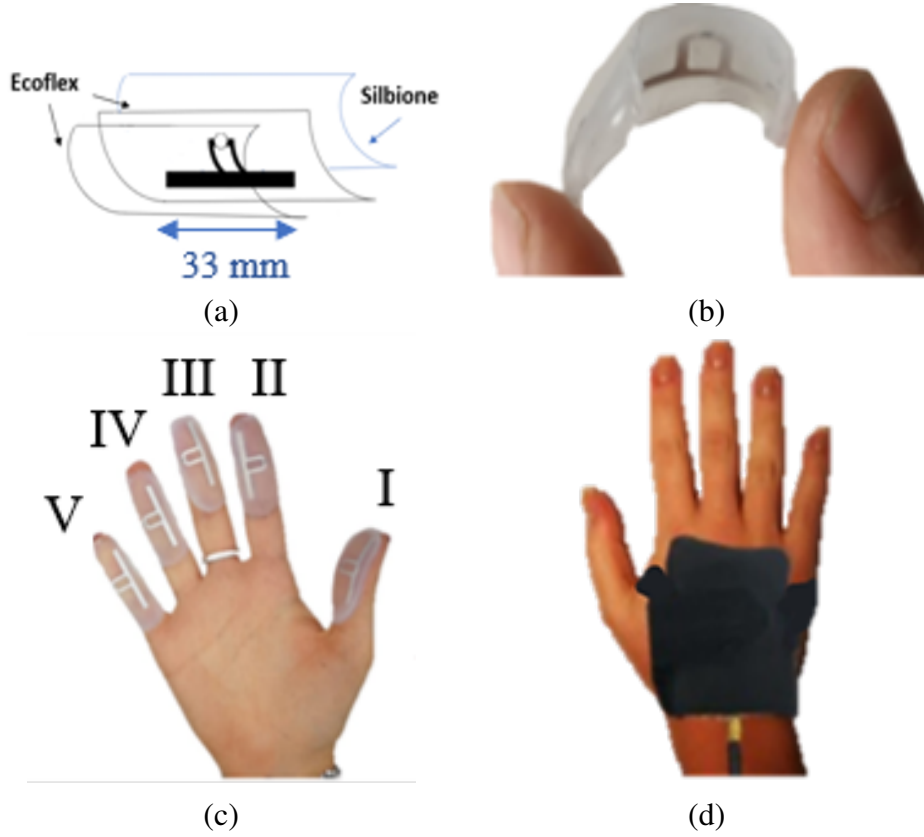
Figure 3.20: Multi-channel R-FAD system: (a) fingertip tag's layout, (b) one flexed tag prototype, (c) placement of tags on the hand, and (d) position of the reader's antenna on the back of the hand.

3.3.2.2 Metrics

Multi-channel R-FADs comprise $2 \leq N \leq 5$ fingertip sensors. When the system wearer touches a dielectric material ε_r, N differential SC are returned to the reader, and the set of ΔSC_i returned by the fingers compose the following digital fingerprint $\mathbf{F}(\varepsilon_{r,m})$

$$\mathbf{F}(\varepsilon_{r,m}) = \left\{ SC(\varepsilon_{r,o}) - SC(\varepsilon_{r,m}), ..., SC(\varepsilon_{r,0}) - SC(\varepsilon_{r,m}) \right\}. \tag{3.7}$$

The reference sensor code $SC(\varepsilon_{r,0}) = SC_0$ is the sensor code returned by the finger in the reference air condition, when the user is not touching anything and is keeping the hand open. As in the single-channel case above, the measurement of the reference SC values (i.e., the calibration of the R-FAD) is performed once at the beginning of the measurement
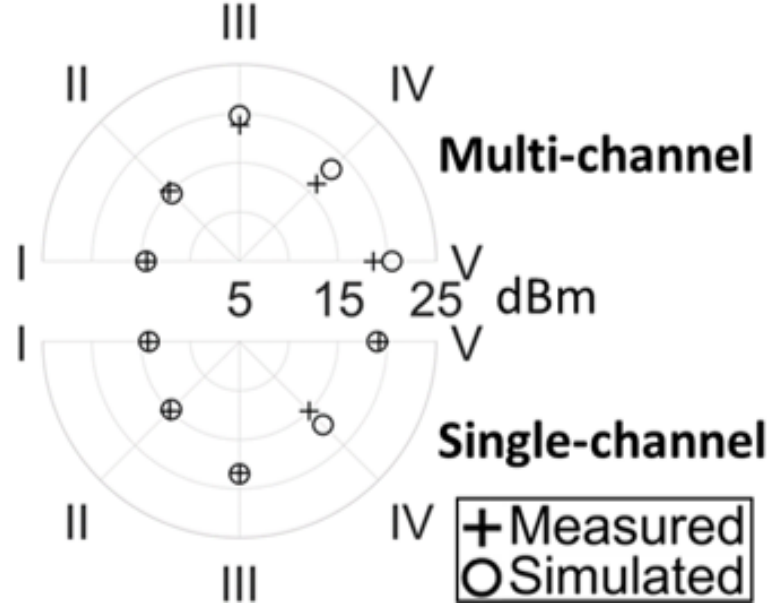
Figure 3.21: Turn-on powers ($f = 867$ MHz) simulated and measured when different fingersensors are worn.

session to evaluate the differential sensor codes when the user is contacting any material. The average over the fingertip sensors' responses is readily evaluated by the companion device

$$\overline{F}\left(\varepsilon_{r,m}\right) = \frac{\sum_{i=1}^{N}\left[\mathbf{F}\left(\varepsilon_{r,m}\right)\right]_i}{N} = \frac{\sum_{i=1}^{N}\Delta SC\left(\varepsilon_{r,m}\right)}{N}. \tag{3.8}$$

If a sensor is not read by the reader, its response is replaced with the mean over the other responsive fingersensors. Thus, the *N*-dimensional fingerprint provides robustness with reference to not-read fingersensors, and it can be visualized through Kiviat diagrams (Fig. 3.26). The following *digital contrast* is hereafter used as the metric to discriminate two digital fingerprints:

$$C_{mn} = \overline{F}\left(\varepsilon_{r,m}\right) - \overline{F}\left(\varepsilon_{r,n}\right). \tag{3.9}$$

For notation simplicity, $\mathbf{F}\left(\varepsilon_{r,m}\right)$ and C_{mn} are extended also for $N = 1$.

89
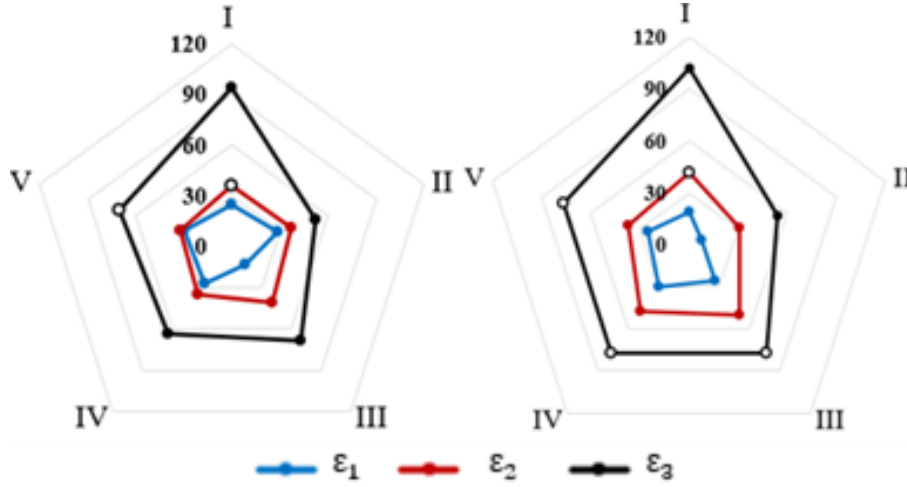
Figure 3.22: Digital fingerprints of two wearers when the multi-sensorized hand is touching bottles filled with three different liquids. Empty circles indicate that there was no response from the tag and the value is interpolated as the average over the other fingers.

3.3.2.3 Measurement Set-up and Window

As experimental set-up, three PET (polyethylene terephthalate) bottles filled with some dielectric liquids are considered. The three liquid selected have a high dielectric contrast, allow to study the sensors' response both in the low-medium and in the medium-high permittivity ranges, and are of common use: the olive oil, the ethyl alcohol and the distilled water [Fig. 3.23(a); electric properties in Table 3.1]. The R-FAD wearer was asked to use a physiological grasp as reference gesture to touch the bottles [Fig. 3.23(b)].

When acquiring a signal, the SC is subject to fluctuations even in fixed boundary conditions and permanent regime [Fig. 3.24(a)], independently from the finger onto whom the sensor is attached and the dielectric material eventually contacted. The time-domain observed fluctuations resemble a sawtooth wave, and the relative signal spectrum exhibits a peak at 0.28 Hz for every material-finger pair, proving that the temporal variations are a property of the self-tuning mechanism.

Moreover, a transient regime is experienced when grasping the bottles, as the sensor passes from the air condition to contact a dielectric material. While the auto-tuning mechanism adapts to changed boundary conditions, the fingersensor does not respond. This
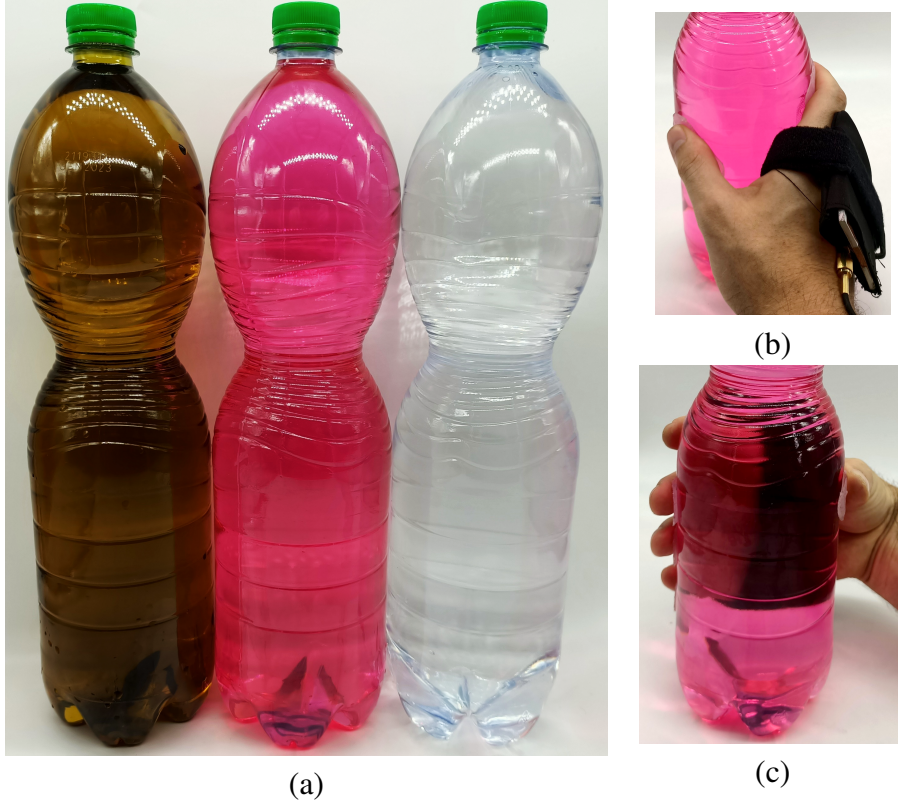
Figure 3.23: Experimental set-up. (a) Three PET bottles filled with the three dielectric liquids. (b,c) The reference grasp gesture performed to touch the bottles.

not-responsive time window lasts about 800 ms [Fig. 3.25(a)] similarly to the time observed when experimenting the facemask tag (see previous Chapter). Then, the fingersensors respond to the reader. The number of samples needed to have a stable metric can be established through the analysis of the convergence error δ, which is defined as [136]

$$\delta\,[\mathbf{M}] = \sigma\,[\mathbf{M}] - \sigma\,[\infty],\tag{3.10}$$

where $\sigma\,[\mathbf{M}]$ is the standard deviation of the $\overline{F}\,(\varepsilon_r)$ samples vector $\mathbf{M}$ collected from the first contact moment t_0 and $\sigma\,[\infty]$ is the asymptotic value. The *minimum* number of samples $\overline{M}$ needed so that $\delta\,[\mathbf{M}] < 1$ is the sample number constituting a stable measurement. Each material is measured thrice to determine the optimal $\overline{M}$. $\overline{M}$ is higher as the material's ε_r increases, and $\sigma\,[\infty] \sim \sigma\,[\overline{M} = 90]$ [Fig. 3.25(b,c,d)]. The physiological variability of the
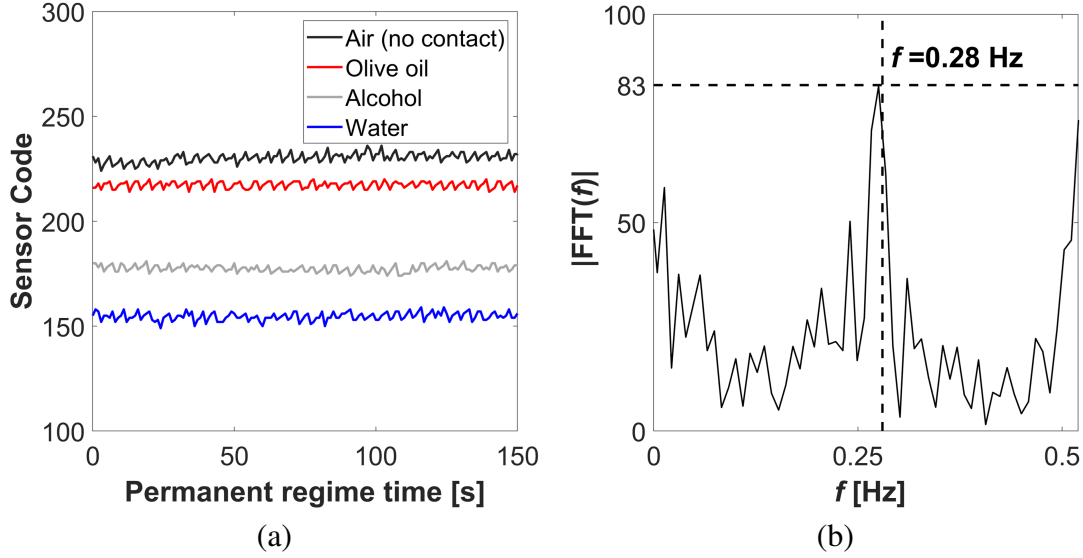
Figure 3.24: (a) Continuous acquisition of the SC signal while the thumb sensor contacts the bottles filled with dielectric material. (b) Amplitude spectrum of one continuous acquisition through Fast Fourier Transform (FFT).

gesture execution causes some variation in the $\delta[\mathbf{M}]$ profiles, so a conservative $\overline{M} = 10$ can guarantee an accurate measurement with the multi-sensor device.

3.3.2.4 Touch Variability

The inter-user and inter-finger variabilities are known to add an unpredictable offset for each contacted material, notwithstanding the $\Delta SC(\varepsilon_r)$ monotonic behavior for a given user and gesture. Additional fluctuations are experienced even for a fixed user-gesture pair due to the pressure applied as it changes the adhesion of the fingersensor onto the object and is expected to modify the sensed effective permittivity which is higher the stronger the pressure.

To quantify the pressure effects, the ΔSC of a fingersensor has to be analyzed when keeping constant every boundary condition but the pressure. A bottle diameter of 8.2 cm and a volunteer finger thickness is 1 cm are considered to asses the uncertainty σ_p caused by the pressure. Three pressures were kept stable by binding the index finger to the bottles with plastic ties having different perimeters: $8,5$ cm for the low-pressure, 8 cm for the

medium and 7.6 cm for the high. The pressures comprehend the physiological variations and range from the barely-fixed to tightly-bound finger.

Consecutive measurements taken when the finger is bound are stable and return the same values. The higher the pressure applied, the better the IC contacts the dielectric, the higher is the ΔSC registered (Fig. 3.26). Over the three pressures, the σ_p reaches a maximum value of 10.5 and a maximum $\sigma_P/\Delta SC$ ratio of 0.3. The $\sigma_P/\Delta SC$ ratio decreases with ε and is always comprised in the range 0.2 ± 0.1. Given the relevant effects of the touch pressure, a conservative uncertainty region $\sigma_p/\Delta SC = 0.3$ is hereafter considered for every physiological measure. Thus, for the law of propagation of uncertainty, the uncertainty over $\overline{F}$ because of pressures is [137, 138]

$$\overline{\sigma}_F = \sqrt{\frac{\sum_{i=1}^{N} \sigma_{p,i}^2}{N^2}} \leq \frac{0.3}{N} \sqrt{\sum_{i=1}^{N} \Delta SC_i^2}, \tag{3.11}$$

being N the number of responsive fingersensors.

3.3.2.5 Comparison between Multi- and Single-sensor R-FADs

Single-channel R-FADs are affected by missed readings caused by the unpredictable wearer-environment interactions. The inter-finger variability can also cause a severely reduced sensitivity of the system to ε_r if only one of the less sensitive fingers is employed. The envisaged benefits from the use of multiple sensors are verified by comparing the multi-sensor and a single-sensor R-FAD in terms of sensitivity.

The sensitivity of R-FADs to the dielectric constant can be evaluated as

$$S = \frac{\partial C}{\partial \varepsilon_r} \cong \frac{C_{mn}}{\varepsilon_{r,m} - \varepsilon_{r,n}}. \tag{3.12}$$

A volunteer is asked to touch the bottle both when all the fingers are sensorized and when only a fingersensor is worn. The most sensitive fingersensor for the specific wearer is the thumb-sensor, which is not read for the ethyl alcohol case and, thus, is not the optimal finger to sensorize (Table 3.5). Instead, the optimal fingersensor for the specified user is the middle-sensor which achieves the highest sensitivity between the sensors responding while

Table 3.5: Digital Contrast measured by the single-channel (when different fingers are sensorized) and multi-channel R-FADs.

	Single-channel					Multi-channel
	I	II	III	IV	V	
C_{21}	25	29	13	27	30	25
C_{32}	-	37	41	35	32	36
C_{31}	94	52	69	64	-	70

touching each material. The multi-channel R-FAD is hence compared with the classic index-sensor R-FAD and the single-channel device sensorizing only the optimal finger.

Remarkably, the multi-channel approach achieves a digital contrast up to two times the classic index-sensor R-FAD (Fig. 3.27), and uncertainty down to 50 % lower thanks to the multiple observations. The multi-channel device compares favorably even when only the optimal finger is sensorized. The multiple, simultaneous observations significantly lower the uncertainty caused by the pressure, which in the middle-sensor R-FAD causes the response for water and alcohol to be superimposed. Overall, the use of multiple fingersensors brings the foreseen advantages for the dielectric sensing.

3.4 Conclusion

After having introduced the R-FADs and detailed the experimentation of the first dielectric-sensing device, we discuss the optimization of the fingertip tag devices through the minimization of a penalty function. The constrained design permits to exploit and master the full potentiality of the new family of self-tuning ICs, even in these complex configurations where the far-field approximation can not be used. The experimental validation of the R-FAD system corroborated the numerical results with a nearly invariant antenna response even when the tag interacts with materials of up to 70 units of dielectric contrast. The differential SC greatly reduces the inter-subject variability, albeit the metric still heavily depends on the performed gesture. Lastly, a multi-channel device significantly improving the sensitivity to the dielectric constant is described.

The R-FAD case study allows for gaining insight into the local-processing B-IoT systems for off-body sensing. Although the measurand is not on the body so that its phenomenology is not heavily affected by the body presence, the effect of the body on the RFID tags is still a major source of uncertainty. Since the same transducing mechanism has been exploited for the on-body sensing in the previous Chapter, it is of interest to directly compare the two case studies. In the on-body sensing case, the permittivity range is limited to some units at most, much lower than the range utilized in the R-FAD experimentation. It is evident that wearable sensors are much less affected by the human body than epidermal sensors. Thus, the on-body sensing by epidermal sensors is the most affected by the inter- and intra-subject variability; in contrast, the off-body sensing by wearable sensors is the least affected by the human body.
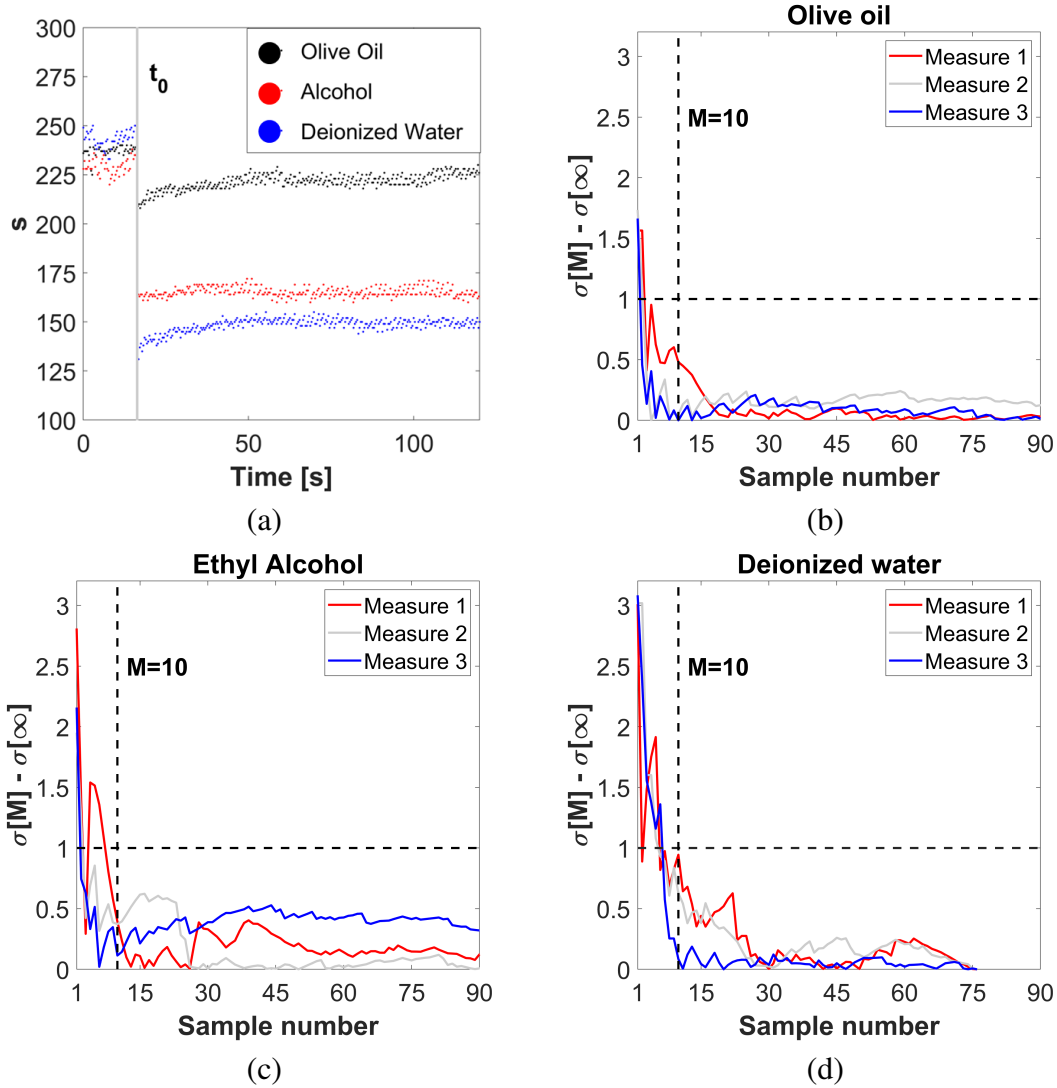
Figure 3.25: (a) Time profiles of *s* when the bottles filled with dielectric liquid are touched. The gray zone is the time window when the fingersensors do not respond. (b,c,d) Convergence error of a multi-channel R-FAD when touching different materials. The sample number start from the first sample after the contact.
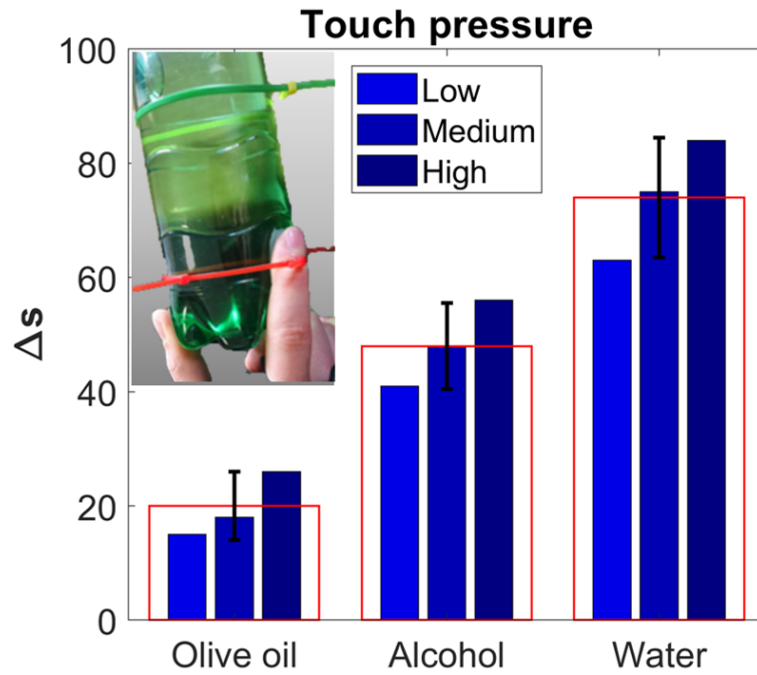
Figure 3.26: Digital fingerprints when keeping different touch pressures.
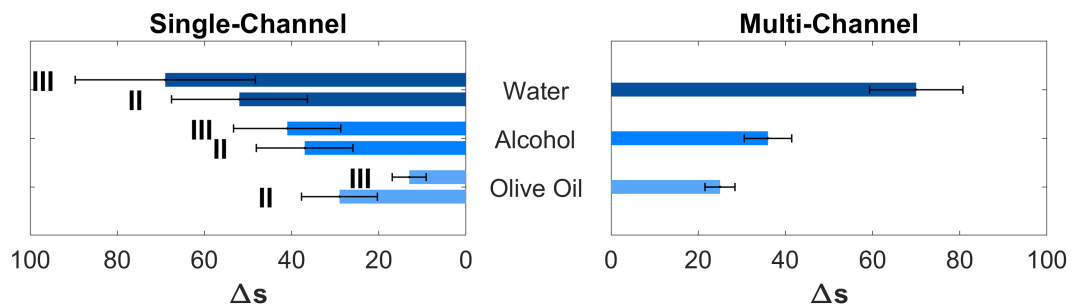
Figure 3.27: Digital contrasts of single-channel and multi-channel R-FAD. The sensorized finger in the single-channel case is the index (II) or the middle (III) finger.

Part II

Remote Processing B-IoT – Bodycentric LPWAN for Search and Rescue

Chapter 4

On-body LoRa(WAN) Low-Power Wide-Area Network

This Chapter introduces the body-worn LoRa devices. LoRa and LoRaWAN are detailed (Section 4.1) focusing on the literature on the bodycentric LoRa devices and its limitations (Section 4.2). The LPWANs are described and their peculiarities analyzed further in Appendix A.

4.1   LoRa, LoRaWAN, and LoRaWAN Networks

An LPWAN is composed by a PHY (physical layer) and a MAC (medium access control). An LPWAN composed by LoRa PHY and LoRaWAN MAC is usually called *LoRaWAN network* [139]. Network utilizing the LoRa PHY but a MAC other than LoRaWAN can be referred to as LoRa networks instead.

The distinction between LoRa and LoRaWAN is not always reflected in the literature on the topic. For instance, Mekki *et al.* [140] refer to LoRa also when considering MAC-defined characteristics as the payload length (Fig. A.3). In this dissertation, we write LoRa, LoRaWAN and LoRa(WAN) to address the PHY, the MAC, and both of them at the same time, respectively. The term LoRaWAN network instead is used to point to a network based on LoRa(WAN).
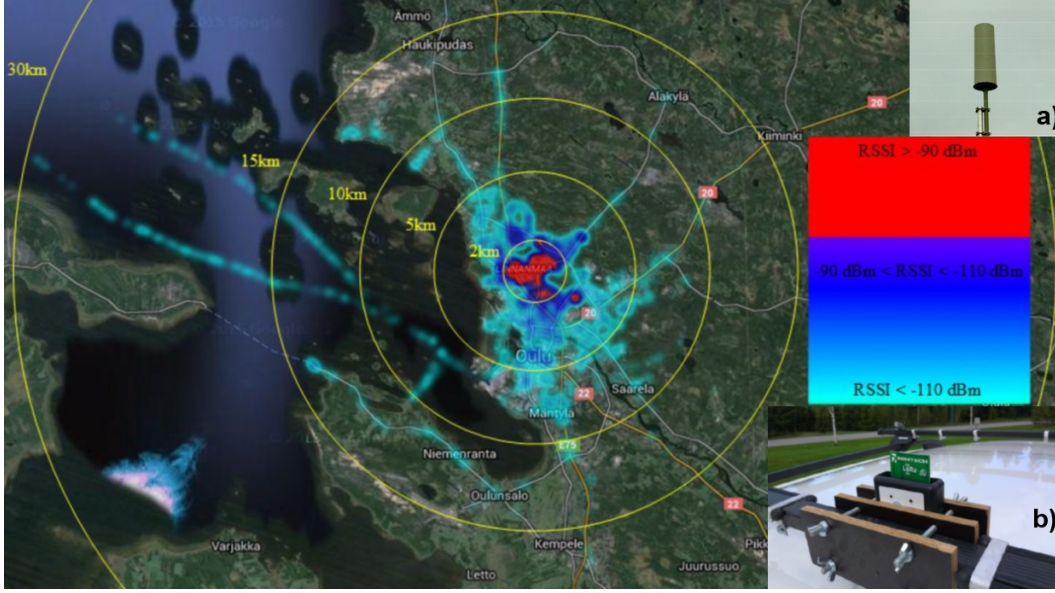
Figure 4.1: RSSI from a mote (b) in different locations in Oulu, Finland, centered at the location of the base station (a). $P_{Tx} = 14$ dBm, $G_{Rx} = 2$ dBi, $R_b = 293$ bps, $h_{Tx} = 2$ m, $h_{Rx} = 24$ m, being P_{Tx} the input power of the mote, G_{Rx} the maximum gain of the receiving biconical dipole gateway, R the set bitrate, h_{Tx} the altitude of the mote, and h_{Rx} the altitude of the gateway [141].

4.1.1 Long Range: LoRa

LoRa is a PHY (physical layer) based on a modulation technique called CSS (chirp spread spectrum). At the time of writing, Semtech holds the intellectual propriety of the LoRa modulation. The LoRa protocol can cover kilometric distances with little transmitting powers. As an example, in Fig. 4.1 is shown the RSSI measured from a mote distant up to 30 km from the base station. LoRa is conceived to operate usually in the unlicensed band, such as 433.050-434.790 MHz and 865-868 MHz ISM (industrial, scientific, and medical) bands in Europe. The PHY performances can be very different depending on the band chosen due to the path losses and the local regulations. A comparison of the performance of LoRa using the 433 MHz respect to using the 866 MHz is in [142] and in [143] (Fig. 4.2). Although the path losses in the 433 MHz band are diminished, the maximum equivalent isotropic radiated power (EIRP) is 10 dBm respect to 14 dBm in 866 MHz band, and since
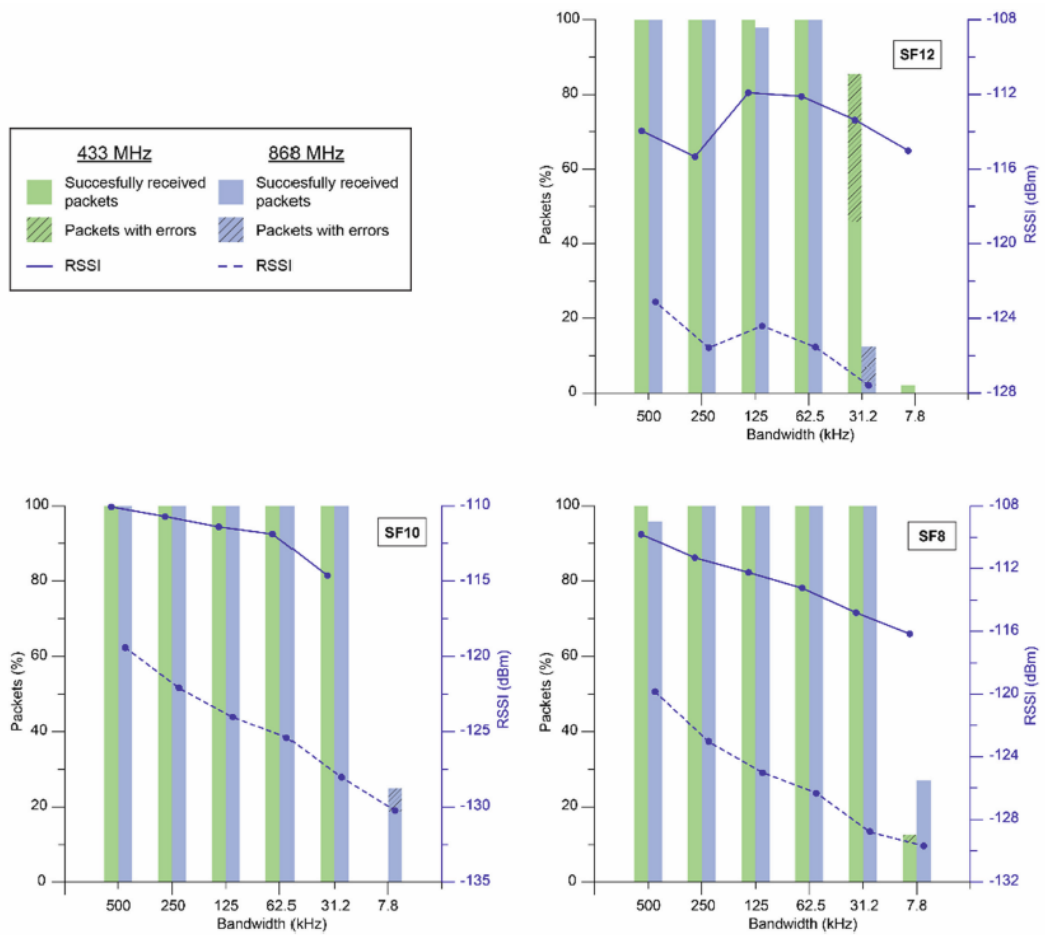
Figure 4.2: Packet delivery ratio vs channel bandwidth using 433 MHz and 866 MHz bands and the same setup [143].

(a) Symbol 1   (b) Symbol 2   (c) FFT output 1   (d) FFT output 2
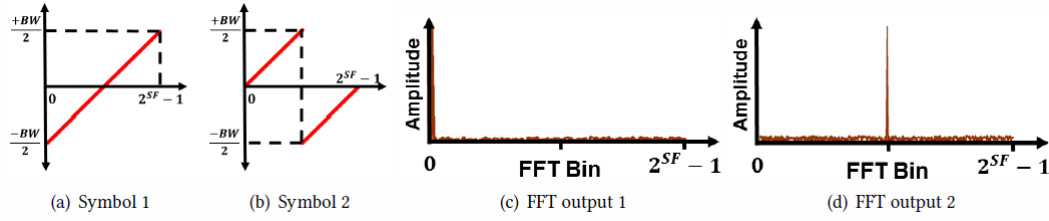
Figure 4.3: An example of CSS signal. BW stands for the bandwidth of the chirp and SF stands for spreading factor (4.1.1.3). (a) Example of baseline up-chirp. (b) Time-shifted up-chirp. (c) FFT output of an incoming baseline chirp (there's a peak is in $t = 0$). (d) FFT output of an incoming up-chirp [145].
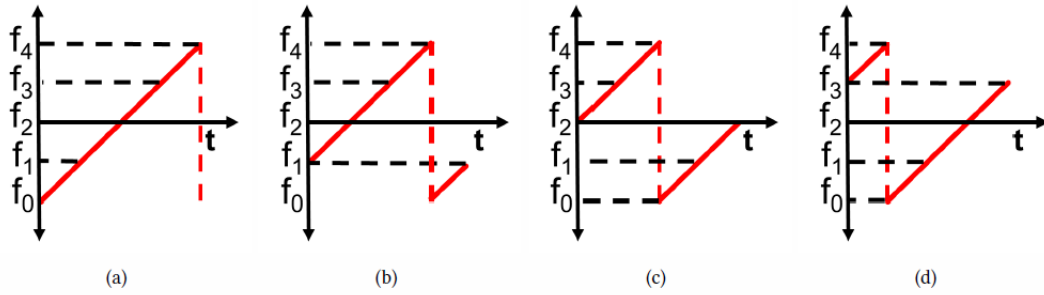
(a)   (b)   (c)   (d)

Figure 4.4: (a,b,c,d) Four different CSS up-chirps with $BW = f_4 - f_0$, $SF = 2$ [145].

the 433 MHz band is narrower fewer communication channels can be created. Moreover, usually, the 433 MHz band is more crowded in Europe than the 866 MHz one.

When the LoRa PHY is used bypassing LoRaWAN MAC so that the signal is broadcasted like an RF beacon, it is often called *raw LoRa* mode or *LoRa-MAC* [144].

4.1.1.1 Chirp Spread Spectrum (CSS) Modulation

CSS uses linear frequency modulated chirp pulses which can be up-chirps (frequency increases with time; Fig. 4.3 and Fig. 4.6) or down-chirp (frequency decreases with time).

A time delay in the chirp signals translates to a frequency shift at the output of the FFT and the CSS encodes data as cyclic time shift in the baseline chirp. The receiver multiplies the incoming signals for the baseline chirp and then performs an FFT. Since multiplication in the time domain is the correlation in the frequency domain, the receiver output is a peak

in the FFT frequency bin corresponding to the time delay in the received chirp (Fig. 4.3). The number of bit per chirp encoded depends on the receiver. If the receiver performs an N point FFT, it can distinguish between N cyclic shift which corresponds to a peak in each of the N FFT bin. Thus, we can transmit $\log_2(N)$ bit per chirp. The number of bit per chirp encoded is called Spreading Factor (SF) so that $N = 2^{SF}$. In other words, a CSS signal with a spreading factor SF can have 2^{SF} cyclic shifts (Fig. 4.4).

CSS has some properties extremely useful in LPWAN applications.

1. It can achieve high sensitivity by using an efficient trade-off between bandwidth and data rates when the signal is drowned in noise (e.g.: Sx1276 Lora receiver can decode CSS packets down to -149 dBm).

2. It is resilient to fading like Doppler noise and in-band/out-of-band interference.

3. Unlike techniques that have a long signal acquisition time at low SNRs (e.g., GPS), CSS has significantly lower acquisition overhead.

4. It doesn't require fine-grained frequency synchronization, because small offsets in the oscillators at the transmitter and receiver result in a frequency offset that which can be corrected during the FFT operation.

In [145] these features are discussed and is described how to create a CSS-modulating backscatter that can synthesize LoRa packets without using any LoRa chip.

4.1.1.2 From CSS to LoRa

The structure of a LoRa packet is shown in Fig. 4.5. A sequence of the repeating chirps constitutes the preamble, whose length can be between 6 and 65535 chirps symbols. The preamble ends with a synchronization window and two and a quarter down-chirp. After the down-chirp there's the (optional) header with information about the bit rate and the symbol rate used (see the following Sub-subsection), then the CSS-encoded payload starts. An optional 16-bit CRC (cyclic redundancy check) can be sent at the end of the packet.

The CSS modulation allows LoRa for achieving extended radio ranges. The measured maximum communication distances were 15 km in urban areas and 30 km in rural ones,
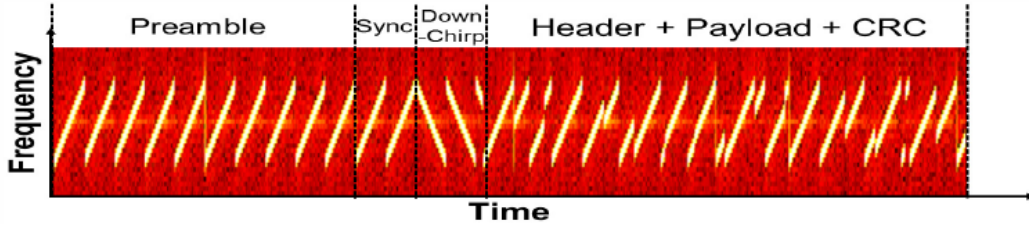
Figure 4.5: The structure of a LoRa packet. Sync is the synchronization window. CRC stands for Cyclic Redundancy Check. [145]

with a success of packet delivery in the rural context of 69% between 15 and 30 km, though the delivered packets in the urban area between 10 and 15 km were only 26% [141]. This is because LoRa is characterized by soft degradation of the signal, as opposed to devices like the avalanche beacons, which are characterized by hard degradation, i.e. an abrupt transition from a signal reception area to an area where no signal is received.

4.1.1.3 Bandwidth, Spreading Factor and Symbol Rate

The bit rate achieved using CSS modulation depends on the following three parameters.

1. Chirp bandwidth (BW): LoRa supports the BW of 7.8 kHz, 10.4 kHz, 20.8 kHz, 31.25 kHz, 62.5 kHz, 125 kHz, 250 kHz and 500 kHz.

2. Spreading factor (SF): LoRa supports SF equal to 6, 7, 8, 9, 10, 11 and 12. The SF and the BW determine the ICs sensitivity [146].

3. symbol rate (or "error coding rate" or "coding rate", CR): LoRa supports CR equal to $\frac{4}{5}$, $\frac{4}{6}$, $\frac{4}{7}$, $\frac{4}{8}$, whereas the payload has always CR=$\frac{4}{8}$.

If the chirp base frequency is f_0 and BW is the bandwidth, the chirp frequency varies linearly between $f_0 - BW/2$ and $f_0 + BW/2$ (Fig. 4.3). The SF is the number of bit per chirp encoded and because a chirp with N samples can encode $\log_2(N)$ bits (Section 4.1.1.1), a chirp with spreading factor SF has 2^{SF} samples. Symbols using different SF are orthogonal each other, which means that they appear as noise each other and there is theoretically no interference (Fig. 4.6), thus it is possible to achieve network separation using two different
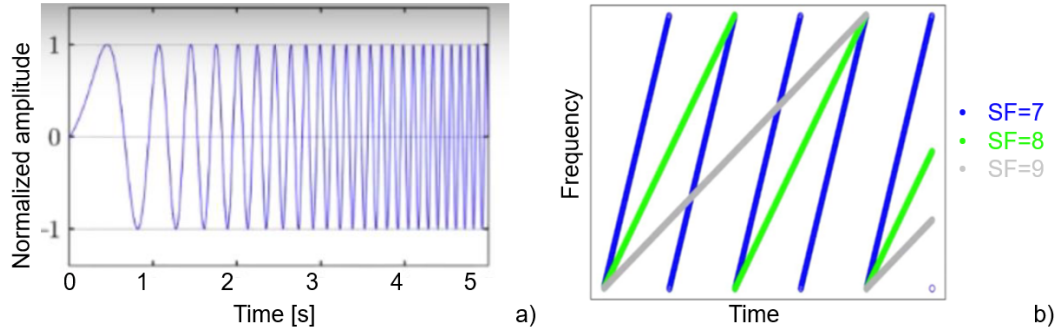
Figure 4.6: a) an up-chirp in the time domain; b) three up-chirp with different spreading factors.

Received Lora signal
Narrowband interferer
LoRa with different SF

Inverse chirp

Decoded symbols
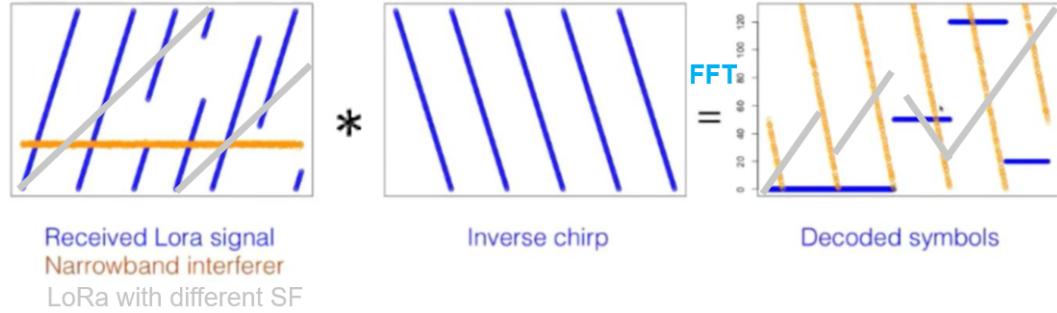
Figure 4.7: The convolution in frequency-domain between the incoming signal and the receiver baseline chirp is shown. The FFT follows the convolution and separates the information from the interference. A LoRa signal having different SF than that of the receiver is not read and doesn't interfere with the communication.

SF (fig. 4.7) [147]. Furthermore, each cyclic shift of the baseline represents a modulated symbol.

The BW and SF of the signal affect both the data rate and the sensitivity (the minimum signal a receiver can distinguish from noise). Indeed, given the BW, the Nyquist sample rate is $\frac{1}{BW}$ samples per second, and given a spreading factor of SF the length of each symbol is $\frac{2^{SF}}{BW}$. Since every symbol encodes SF bits, the bit rate is given by $\frac{BW}{2^{SF}}SF$. Moreover, at the same BW equal to 125 kHz, the sensitivity of the receiver can decrease from -123 dBm for SF 7 to -136 dBm for SF 12 [148].

Because of their relevance and effects, the BW, SF, and CR settings have to be a trade-off solution depending on the application (Table 4.1). The three LoRa parameters can be

Table 4.1: LoRa performance varying BW and SF, compared to FSK modulation ($BW = 125$ kHz) [149].

Mode	Equivalent bit rate (kb/s)	Sensitivity (dBm)	Δ (dB)
FSK	1.2	-122	-
LoRa SF = 12	0.293	-137	+15
LoRa SF = 11	0.537	-134.5	+12.5
LoRa SF = 10	0.976	-132	+10
LoRa SF = 9	1757	-129	+7
LoRa SF = 8	3125	-126	+4
LoRa SF = 7	5468	-123	+1
LoRa SF = 6	9375	-118	-3

independently modified resulting in a total of 224-bit-rate and sensitivity settings between 11 bps and 37.5 kbps [139].

4.1.2 LoRaWAN

The commonest MAC (medium access control) used with LoRa PHY is LoRaWAN, an open standard regulated by the LoRa Alliance, though different MACs are compatible with the LoRa PHY (e.g. Symphony [150]) and it is also possible creating a custom firmware for LoRa PHY.

4.1.2.1 LoRaWAN Specifications

LoRaWAN is an open access MAC protocol regulated by the LoRa Alliance. LoRaWAN is optimized for battery-powered ED and it's the most common MAC used with LoRa PHY although it can include FSK (frequency shift modulation) modulating devices, too [151]. LoRaWAN characteristic and the requirements a LoRa mote has to meet in order to be LoRaWAN compatible are written in the LoRaWAN specification [139].

- LoRaWAN Characteristics

  1. Stars-of-stars topology, in which gateways relay messages between EDs and a central network server. The intermediate elements, the *repeaters* which use LoRaWAN as backhaul, are not described in [139] even if the payload restrictions

for encapsulation overhead are included in LoRaWAN specifications, suggesting future expansions of LoRaWAN.

2. Uplink communication from the EDs to the network server is expected to be the predominant traffic.

3. The LoRa network infrastructure can manage the data rate and RF-output for each end-device individually by means of an adaptive data rate (ADR) scheme.

4. The EDs change the channel in a pseudo-random fashion for every transmission, and the resulting frequency diversity makes the system more robust to interference.

5. Each downlink message is sent by the network server to only one end-device and is relayed by a single gateway. LoRaWAN specification does not describe the transmission of multicast messages from a network server to many end-devices.

6. No payload integrity check is done at this level to keep messages as short as possible with minimum impact on any duty-cycle limitations of the ISM bands used.

7. LoRaWAN uses duty cycle to comply with local regulation. The ED is off depending on the duty-cycle as in equation (equation 4.1).

8. LoRaWAN is an asynchronous ALOHA-based MAC.

An asynchronous ALOHA system is random medium access protocol in which each user communicates to the server in a completely unsynchronized (from one user to another) manner. The network will send a confirmation message to the user when the message is received and decrypted. If the user doesn't receive the confirmation message, the message is sent again [152]. Moreover, although LoRaWAN requests only 3 channels, a maximum of 47 channel a can be created in the EU 863-873 MHz band using a BW of 125 kHz [153].

• LoRaWAN requirements:

1. The ED respects the maximum transmit duty cycle relative to the sub-band used and local regulations.

2. The ED respects the maximum transmit duration (or dwell time) relative to the sub-band used and local regulations.

3. The ED must implement at least the class A functionality and, in addition, they may implement two options named class B and class C. LoRaWAN classes are described in Sub-subsection 4.1.2.2.

4. The ED must implement LoRaWAN default channels.

The time the ED has to be off is evaluated as follows

$$Toff_{subband} = \frac{TimeOnAir}{DutyCycle_{subband}} - TimeOnAir. \qquad (4.1)$$

LoRaWAN networks can work both in confirmed mode (in confirmed mode the gateway sends to the ED a confirmation message, called *acknowledgment message*; ACK) or in unconfirmed mode, in which the ED doesn't wait for the ACK message and deletes the message sent. From (4.1), is possible to see that the duty-cycle limitation is a hard limit for any LoRa network; for example in EU 868 MHz band, a simple message of 10 bytes with a low SF of 7 (as higher SF has a major channel usage) has a ToA of about 40 mS, thus the ED has to be off for about $Toff_{subbsnd} = \frac{0.04 \text{ s}}{0.01} - 0.04 \text{ s} \simeq 4 \text{ s}$ [154]. The formula evaluating the ToA is in [153] and it is implemented by the LoRaTools website [155] hosts a free ToA calculator, which evaluates ToA basing on eight parameters: SF, BW, CR, payload length, preamble length, explicit header (presence/absence), CRC (presence/absence).

4.1.2.2 LoRaWAN Classes

A receive window is a slot of time during which the ED listen to the gateway waiting for a downlink message. The three LoRaWAN classes have a different number of receive windows: class C has more windows than class B which has more windows than class A. In order to be LoRaWAN compatible, a device must implement the class A. Devices implementing more than class A are generally named "higher class end-devices" [139]. In Fig. 4.8 are shown the receiving slots of the three LoRaWAN classes.
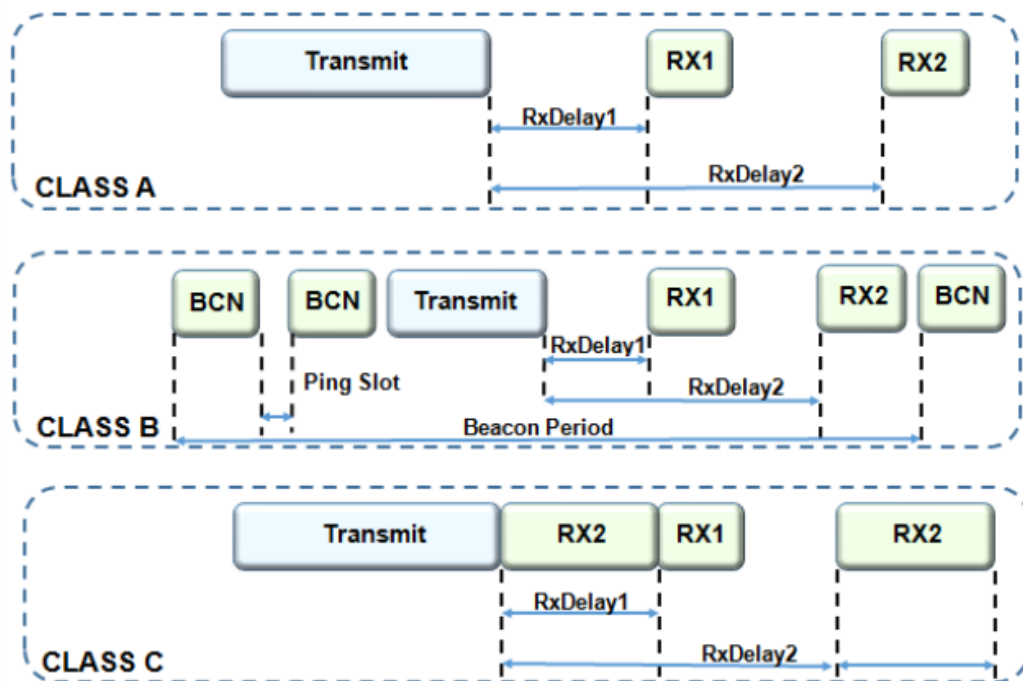
Figure 4.8: LoRaWAN classes receive slots (RX) [156].

LoRaWAN Class A   Implementing LoRaWAN class A is a requirement to be LoRaWAN compatible. End-devices of this class allow for bi-directional communications whereby each end-device's uplink transmission is followed by two short downlink-receiving windows. The transmission slot scheduled by the end-device is based on its own communication needs with a small variation based on a random time basis (ALOHA-type of the protocol). This Class A operation is optimized for applications that only require downlink communication from the server shortly after the end-device has sent an uplink transmission. Downlink communications from the server at any other time will have to wait until the next scheduled uplink. There are two receiving slots named RX1 and RX2 (fig. 4.8). Class A is the class with the lowest power consumption.

LoRaWAN Class B   End devices of Class B open extra receive windows at scheduled times in addition to the Class A random receive windows. The gateway sends to the Class B end device a time-synchronized beacon so that the server knows when the ED is listening.

LoRaWAN Class C   End devices of class C have open receive windows whenever they can so that the windows are closed only when the ED is transmitting (Fig. 4.8). Class C is the most power-hungry class but offers the lowest latency for the server to ED communication.

4.1.3   LoRaWAN Networks

In LoRaWAN networks, LoRa is used solely for the communication between ED and gateway, while the communication between gateway and network uses a backhaul connection different from LoRa (e.g.: Ethernet, Wi-Fi, 4G). The encryption is decided by the network and communicated to the ED so that the gateway of an intruder cannot decrypt the data without the network access. Different studies aim at evaluating the performance of LoRaWAN networks. While the maximum communication distances depend only upon the PHY, the maximum number of nodes depends also on the MAC, and the most conservative estimation evaluate a theoretical maximum of 0.151 payload byte/second per gateway, as to say 1000 motes which transmit 10 messages/day per gateway. In order to transmit an empty payload frame, a LoRaWAN network needs 13 bytes (Fig. 4.9) of header anyway
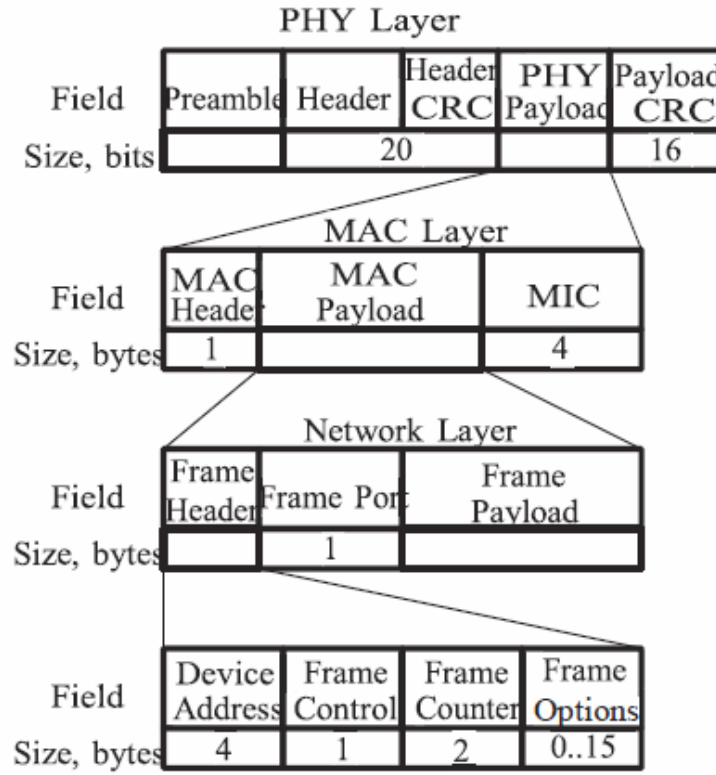
Figure 4.9: The structure of a LoRa packet [157].

[157]. Because of the slow modulation rate, LoRaWAN networks have a maximum payload length for a message of 243 bytes. LoRaWAN networks use a FEC (forward error correction) algorithm to increase the PDR.

4.1.3.1 Transmission Parameters Selection: Data Rate

The performances of a LoRaWAN network depends mainly on the following five transmission parameters [158] that must be comprised in the specified ranges.

1. Transmission power (-4 dBm $\leq TP \leq$ 20 dBm).

2. Carrier frequency (137 MHz $\leq CF \leq$ 1020 MHz).

3. Spreading factor (6 $\leq SF \leq$ 12).
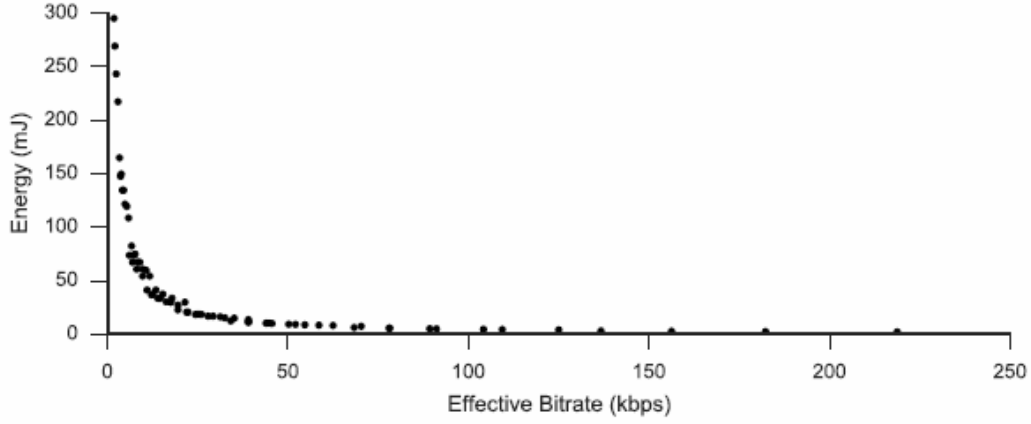
Figure 4.10: Effective bitrate [kbps] vs. energy consumption [mJ] for a packet with a 32-byte payload at TP=14 dBm [158].

4. Bandwidth (7.5 $kHz \leq BW \leq 500\ kHz$).

5. Coding rate (FEC rate; $\frac{4}{8} \leq CR \leq \frac{4}{5}$).

If the value of each parameter is in the aforementioned range, the ED is LoRaWAN compatible. Because of hardware implementation limits, the TP range is often limited to 2 dBm to 20 dBm. The CF is the center frequency that can be programmed in steps of 61 Hz and it is usually set to be in the local unlicensed band (Fig. A.2).

As the PHY, the network performances are very sensible to transmission parameters settings (Fig. 4.10) and over 6720 settings are possible [158]. Currently, no way to determine the best setting exists. Moreover, depending on the setting, the energy consumption can vary from 2.20 mJ to 295 mJ, a factor of 134 [158]. The transmission parameters are divided in given combinations identified by a number called Data Rate (DR; e.g. DR=0 means SF=12 and BW=125). A LoRaWAN network's ED can decide to use the ADR or not, and if not the ED transmission parameters are fixed. The ADR provides a subset of 8 data rate settings and 6 transmission parameter settings and uses the subsets to find the best trade-off between data rate and power consumption. As a side note, it is worth reporting that LoRa, using highest TP, *SF*, and *BW*, and by exploiting both perfect LoS and a strong waveguiding effect, achieved 832 km of range [159].

Table 4.2: Most significant works on bodycentric LoRa.

Reference	Off-body link	On-body antenna
[160]	Body-to-BS, indoor	General purpose
[161]	Body-to-BS, outdoor	General purpose
[162, 163]	Body-to-body, indoor	Wearable
[164]	Body-to-body, outdoor	Wearable
[165]	Body-to-BS, outdoor	Wearable
[145]	Body-to-BS, indoor	Epidermal

4.2 LoRa-based B-IoT

On-body LoRa devices are being studied and tested worldwide to understand the effect of the human body in LPWAN communications since the long-range off-body links could be useful for remote-processing B-IoT systems. Table 4.2 lists the most relevant works on the bodycentric LoRa currently in the literature. Probably due to the duty-cycle limitations, LoRa is deemed not interesting for on-body communication when other communication links (like BLE and RFID) can be more effective.

Naturally, the first works on the topic employed general antennas stuck on the human body to study the off-body links in terms of range and reliability. A commercial LoRa ED fixed on the arm was tested in [160, 161] to analyze body-to-BS links. The researchers observed that the communication between an external gateway and a body-worn ED is reliable over an indoor area of 570x320 m^2 (body-to-BS, indoor) including multiple floors so that a single gateway could cover entire buildings [160]. In outdoor, instead, a Nagakami model provides the best fit model for the RSSI of a body-worn LoRa device, and LoRa can perform better in NLoS than LoS scenarios thanks to multipath channel communication [161].

Given the excellent performances of general LoRa ED (Fig. 4.11) worn on the body, it is possible to perform system design and analyses based on general-purpose nodes. A bodycentric system for tracking mentally-disordered patients was designed [166] and analyzed in terms of power consumption [167]. The system utilizes simple COTS nodes placed on the wrist. Similarly, the LoRa-based wearable device of in [168, 169] relies on simple LoRa motes to perform the communications without any additional analysis. The device
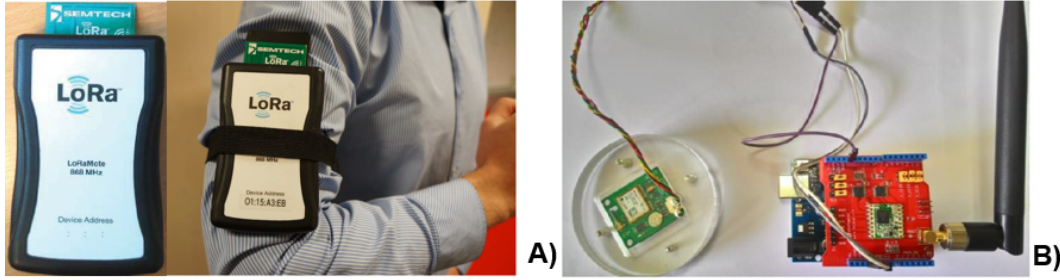
Figure 4.11: General purpose EDs used for studies on off-body LoRa links. (a) ED used in [161] and [160]. (b) ED used in [166] and [167].

called *WeSafe*, is designed to detect possibly harmful environments. It is a heavy bracelet including multiple sensors of CO, CO_2, temperature, humidity, ultra-violet rays, PM_{10} (Fig. 4.12).

Currently, in commerce exist some wearable trackers using general-purpose antennas and LoRaWAN (Fig. 4.13). Gper [170] is a pendant while Lineable [171] is a wristband and WearLOC-2 [172] is a watch. Such commercial LoRa trackers are commonly found in countries which have an extensive LoRa coverage like the Netherlands and South Korea [171].

In contrast to the mentioned work and devices, [162, 163, 164, 165, 173, 174] use the SIW (substrate-integrated waveguide) wearable antenna described in [175]. The antenna is 11 cm × 11 cm and it is worn on the torso. The body-shadowing is proven to cause a fall in the received signal strength (RSS) of about 30 dB [173]. However, in indoor environments, the body shadowing is mitigated by the multiple reflections of the signal [162]. In outdoor environments, the path loss is thought to dominate the propagation up to some hundreds of meters, whereas the multi-path dominates the channel at higher distances [164]. From outdoor body-to-BS measurement campaigns, the Doppler effect is considered negligible even at the body speed of 31 mph, meaning that off-body LoRa links are reliable for cyclists and car drivers, too [165, 174]. Furthermore, the body shadowing can be contrasted by receiver diversity [163]. Regarding the transmission parameters, it is estimated that a subset of 2 or 3 SF values could optimize the off-body LoRa links [163].

Lastly, two epidermal LoRa backscatters that don't use any commercial LoRa chip were presented [145] (Fig. 4.14). Thanks to the backscattering, the bulky LoRa board is
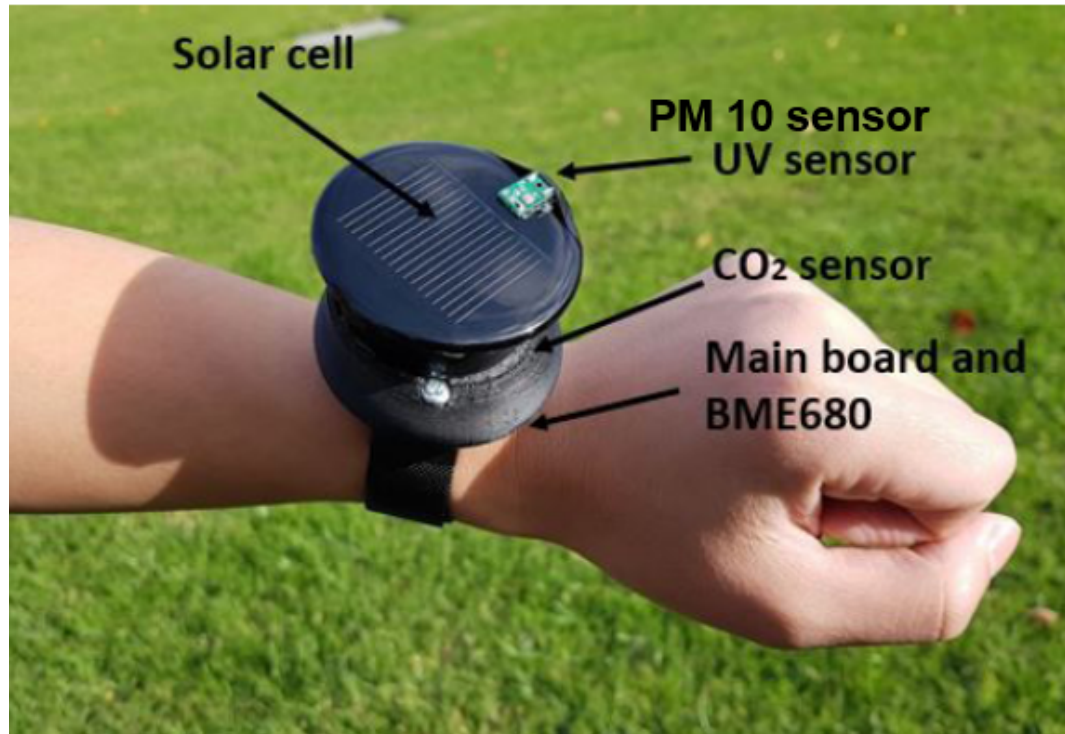
Figure 4.12: A LoRa wearable device sensible to harmful environments [169].

Figure 4.13: Three commercial LoRa trackers: (a) Gper; (b) Lineable; (c) WearLOC-2.
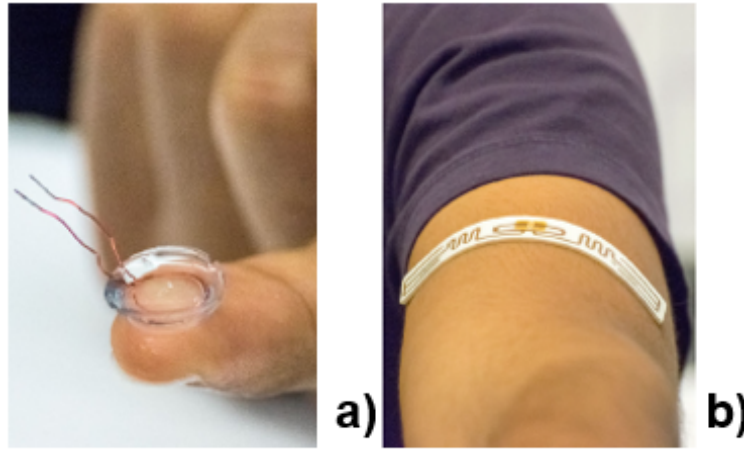
Figure 4.14: Two LoRa epidermal backscatters: (a) a contact lens (b) and a patch [145].

avoided, and the epidermal antenna is included in a wristband or even a contact lens. The CSS modulation allows still for communication over entire large rooms.

4.3 Conclusion

We introduced LoRa, LoRaWAN and the LoRaWAN networks. They are discussed to present the on-body LoRa and the works studying it. The use of commercial LoRa motes as on-body radio is a simple and effective way to implement LoRa B-IoT systems since such radios can still cover radio ranges long hundreds of meters. Wearable LoRa radios were proposed as well as epidermal backscatters.

The literature on bodycentric LoRa systems comprehensively analyzed off-body links in indoor and outdoor urban environments. However, no study in the literature considered off-body links in more challenging environments. The off-body link with a flying BS is another unexplored topic. Furthermore, since our goal is the study of B-IoT systems, the effect of the human body on the system-level design and analyses should be taken into account, too.

To overcome these limitations of the literature on the topic, we consider an unexplored B-IoT application of LoRa and use it as a case study of a remote-processing system. The use of an LPWAN for search and rescue (SaR) operations has never been examined, but

it is expected to be a promising research topic due to the LPWAN's features. Therefore, in the following Chapters, we treat the design of a LoRa-based system for mountain SaR including the off-body links in harsh environments and with a flying BS.

Chapter 5

Off-body Terrestrial LoRa Links for Mountain SaR

In this Chapter, the off-body terrestrial LoRa links for application to mountain SaR operations are investigated for the first time, hence overcoming a significant limitation of the current literature on the topic. The LoRa LPWAN technology is validated for use in this application (Section 5.1). Then, the characterization of the LoRa propagation is detailed (Section 5.2) to derive empirical models in the mountain environments necessary for the design of a LoRa-based B-IoT system for mountain SaR (Section 5.3).

5.1   Performance Evaluation of LoRa for Mountain SaR

The mountain SaR problem and the SoA on the current safety devices are outlined in Appendix B to delineate the open issues. The avalanches beacons (ARVAs) are the current golden standard for mountain SaR operations; they are magnetic dipoles working at 457 kHz and ensure a radio range of about 50 m which can be exploited by a receiving ARVA (rescuer) to localize a transmitting ARVA (target to be rescued; the ARVAs are by default settings in transmitting mode). In this Section instead, the use of LoRa to address the found issues is validated experimentally by comparison with golden standard wireless technologies.
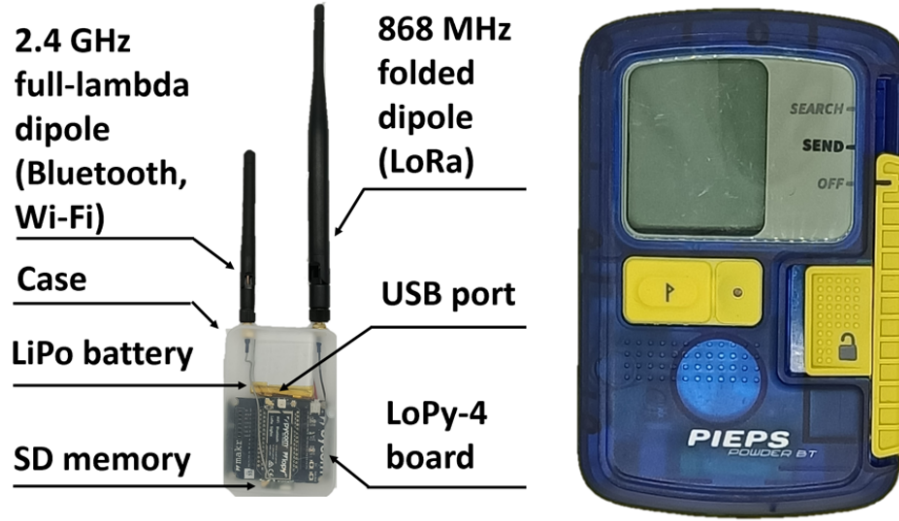
Figure 5.1: (a) LoPy-4 programmable board and (b) PIEPS POWDER BT ARVA.

5.1.1 Hardware Used for the Technology Comparison

The considered hardware for the performance evaluation and the technology comparison consists of two LoPy-4 [176] (firmware 1.20.1.r1; Fig. 5.1.a) programmable boards for LoRa, Wi-Fi and Bluetooth and of two PIEPS POWDER BT [177] for ARVA (Fig. 5.1.b). Since LoRa performances greatly vary depending on the set of selected transmission parameters, the LoRa settings are chosen based on the analyses detailed in the next Section. For comparison, we tested two commonly employed WLAN technologies: the Bluetooth v. 4.2 [178] and the Wi-Fi 802.11 n [179]. The transmitting boards were programmed to transmit the same 5 bytes message every three seconds using one of the three considered protocols: *i*) broadcasting in raw LoRa mode or connecting and communicating via either *ii*) Bluetooth or *iii*) Wi-Fi. The two LoPy-4 expansion boards used hereafter in this Chapter, instead, are equipped with two commercial external antennas: one 868 MHz folded dipole (from [180]; this is the dipole used with the LoRa board in the remainder of this thesis) and one 2.4 GHz full-lambda dipole used to communicate the system with a computer via WiFi. The boards are powered using lithium polymer batteries (LiPo batteries, output voltage 3.7 V, capacity 1100 mAh). The dimensions of the LoRa radio are 295 $mm \times 60$ $mm \times 20$ mm and its weight is 50 g. Thus, this device is suitable as both

as body-worn radio and payload of COTS UAVs.

5.1.2   LoRa Transmission Parameters Selection

Since the LoRa performances greatly vary depending on the selected transmission parameters, based on [158] we selected the following set of parameters: transmission power $P_{Tx} = 14$ dBm; 868 MHz carrier frequency; Spreading Factor (SF) equal to 7; Bandwidth equal to 125 kHz; Coding rate of 4/5. Although the PL in the 433 MHz band is lower than that in the 868 MHz one, the maximum transmitting power in that band is 10 dBm; furthermore, antenna dimensions at 433 MHz are bigger for a stated radiation efficiency; finally, since the 433 MHz band is narrower than the corresponding band at 868 MHz, a lower number of communication channels can be created [143]. The configuration of the LoRa radios described in this subsection are used hereafter in the present and the following chapters to deploy and test LoRa communication links.

1. Transmission Power: the maximum allowed P_{Tx} in the EU $865 - 868$ MHz band compliant with the highest duty cycle (1%) admitted for LoRa device has been selected i.e. $P_{TX} = 14$ dBm.

2. Carrier Frequency (*CF*): the 868 MHz frequency is considered for the following reasons. Even though PL in the 433 MHz band is lower than in 868 MHz, the maximum transmitting power in that band is 10 dBm; furthermore, antenna dimensions at 433 MHz are bigger for a stated radiation efficiency; finally, since the 433 MHz band is narrower than the corresponding band at 868 MHz, a lower number of communication channels can be created [143].

3. Spreading Factor (*SF*): has been set to 7. Although a higher SF results in a lower receiver sensitivity [181], and thus a higher link budget, each unitary increase in SF halves the transmission rate thus doubling the transmission time (so the required time of sleep), energy consumption and the communication channel usage.

4. Bandwidth (*BW*): the BW increase lowers the receiver sensitivity but the data rate is increased because of the time on air reduction. The BW was set at $BW = 125$ kHz.
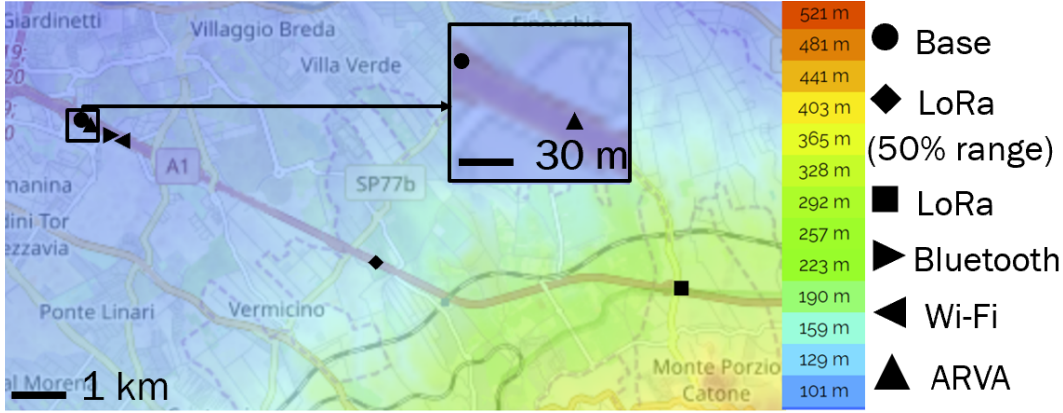
Figure 5.2: Elevation map reporting the measured ranges in Line of Sight condition.

5. Coding Rate (*CR*): *CR* can be set to be either 4/5, 4/6, 4/7 or 4/8. In order to minimize the ToA, we selected $CR = 4/5$.

5.1.3 Performance Evaluation

We considered three key performance indicators useful for SaR: range, battery life, and link robustness to shadowing. Current ARVAs are highly optimized devices in all these three parameters.

5.1.3.1 Range Test

The range measurements were done in Line of Sight (LoS) conditions by placing the transmitters on an overpass above the E821 speedway near Rome, and then by driving on the speedway itself with the receiver placed outside the car. The transmitters were placed at a height of 1 m from the ground in order to reduce the interactions with the environment. Because of the absence of obstacles and the different heights between the point of the last received packet and the base station where the transmitters were placed, the LoS condition was ensured (Fig. 5.2). Distances d_{max} from the base station where the last packets were received are resumed in Table 5.1. Whereas ARVAs are characterized by a hard degradation of the signal, LoRa has a soft degradation as it is possible to see from the range where the Packet Delivery Ratio (PDR) is more than 50%.

124

Table 5.1: Measured max ranges

Technology	d_{max}[m]	Difference in elevation [m]
LoRa	8408	287
LoRa (50 % PDR)	5501	112
Bluetooth	192	-68
Wi-Fi	236	-45
Arva	53	-70

5.1.3.2 Battery Life Test

The battery life of a device is inversely proportional to the current drained from the battery. The average current per transmission $\left(\overline{I_T}\right)$ was evaluated from the battery capacity $\left(C_{battery}\right)$ and from the measured hours of battery life $\left(h_{life}\right)$ according to the following formula:

$$\overline{I_T} = \frac{C_{battery}}{h_{life}N_T} \tag{5.1}$$

where N_T is the number of transmissions sent/received during the h_{life}. From $\overline{I_T}$ and from the output voltage of the battery (V_{out}) the mean power consumption per transmission $\overline{P_T}$ is evaluated as:

$$\overline{P_T} = \overline{I_T}V_{out} \tag{5.2}$$

In order to not consider the power consumption caused by additional tasks performed by the boards (e.g.: storing the currents sampled on the SD memory) we subtracted to $\overline{I_T}$ the current drawn by the LoPy-4 for such tasks, by measuring the hours of life of a LoPy-4 board performing only the additional cyclic tasks and using the (5.1) where N_T was substituted with the number of completed cycles. Then the average power consumptions per transmission, in both transmitting $\left(\overline{P_{Tx}}\right)$ and receiving $\left(\overline{P_{Rx}}\right)$ mode, were evaluated by (5.2), and they are reported in Table 5.2. Unlike the other considered technologies, ARVAs' power consumption is higher in receiving mode than in transmitting mode as indicated by theirs datasheet [177].

Table 5.2: Average power consumption per transmission ($\overline{P}$) in transmitting (Tx) and receiving (Rx) mode during test.

Technology	$\overline{P_{Tx}}$ [μW]	$\overline{P_{Rx}}$ [μW]
LoRa	4.61	1.90
Bluetooth	25.60	25.24
Wi-Fi	44.68	25.09
ARVA	0.05	0.29

Figure 5.3: LoPy-4 board and reference 4 L sealed water bag on the bottom of the ceramic container.
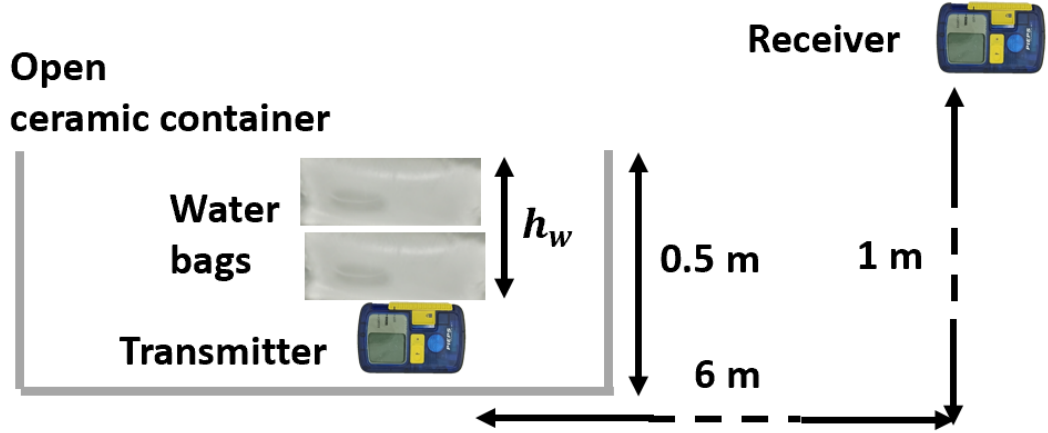
Figure 5.4: Setup for link robustness to shadowing test.

5.1.3.3 Link Robustness

Shadowing occurs when an obstacle is placed between the transmitter and the receiver so that the LoS is negated. In mountains, obstacles, rockfalls and avalanches can shadow the RF transmission. The worst condition is the avalanche since the water of the snow introduces also a very high attenuation, due to the power absorption of the water. To test the robustness to shadowing, the transmitter was activated and placed inside an open ceramic container (length 150 cm, width 70 cm, height 50 cm, ceramic thickness 10 cm). Then sealed plastic bags (length 40 cm, width 15 cm, height 5 cm) filled with 4 liters of water ($T = 20\ ^oC$; $\sigma = 188\ mS/cm$; $\varepsilon = 78$) each were placed onto the transmitter. This experiment is a worst-case scenario respect to the transmitter under snow scenario since the snow is less dense than water. The receiver was then placed at a distance of 6 meters and at a height of 1 meter. The water bags produced a shadowing of the transmissions and a very high power absorption (Fig. 5.3). The ceramic container introduced instead reflection and diffractions, thus a very harsh electromagnetic environment was overall created (Fig. 5.4). The Packet Delivery Ratio for six different water heights h_w (0, 5, 10, 15, 20 and 25 cm) was then measured over 900 transmissions. The PDR can thus be seen as a function of the water height, and the evaluated $PDR(h_w)$ is plotted in Fig. 5.5. Since the ARVA doesn't transmit any packet, an equivalent Pulse Detection Ratio was evaluated as
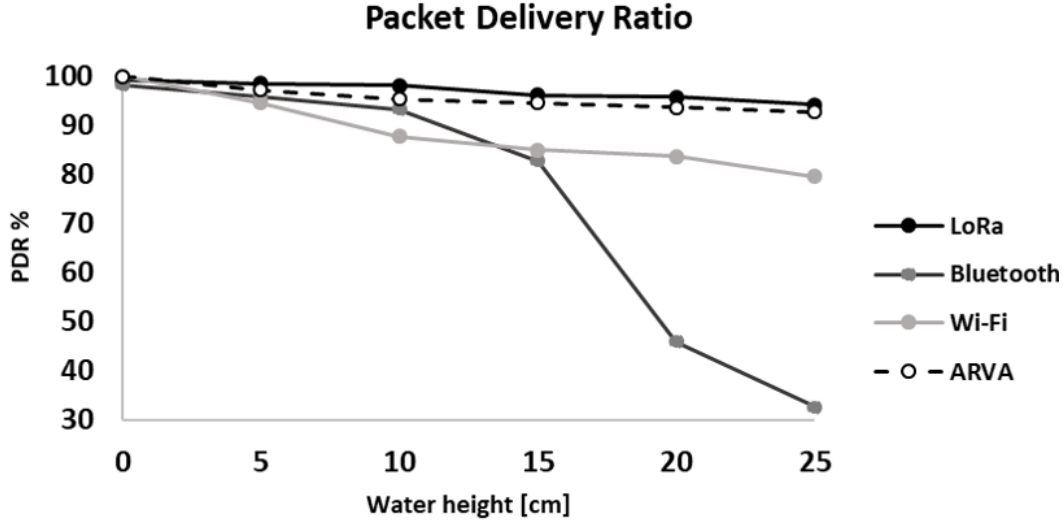
Figure 5.5: Packet Delivery Ratio vs water height measured for LoRa, Bluetooth and Wi-Fi. For the ARVA the Pulse Detection Ratio was considered.

the ratio between the number of pulses detected by the receiving ARVA over the number of transmitted pulses.

5.1.3.4 Technology Comparison Results

A score per test is assigned to each technology. The scores for range (S_R), battery life (S_{BL}) and link robustness (S_{LR}) are evaluated as follows:

$$S_R = log_{10}(d_{max}) \tag{5.3}$$

$$S_{BL} = \left\{ log_{10} \left[max \left(\overline{P_{Tx}}, \overline{P_{Rx}} \right) \right] \right\}^{-1} \tag{5.4}$$

$$S_{LR} = PDR(0) + \sum_{i=1}^{5} PDR(h_{w,i}) * h_{w,i} \tag{5.5}$$

where d_{max}, $\overline{P_{Tx}}$, $\overline{P_{Rx}}$, $PDR(h_w)$ are defined in this Section above. The scores are equalized in the $[0;1]$ range and then represented on a Kiavat diagram (Fig. 5.6) so that if a technology has the best score in every test its area covers the whole plot. In Table 5.3 the equalized scores and the percentages of the plot area covered per technology are reported. Over the

128
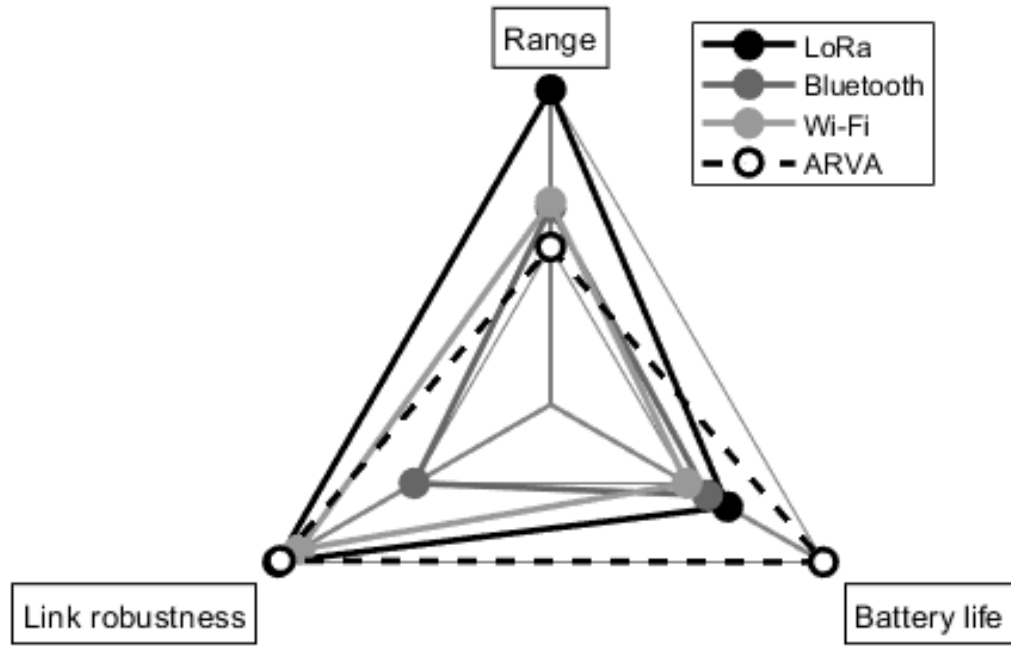
Figure 5.6: Kiavat diagram comparing the performance of the three technologies.

Table 5.3: Area on the Kiavat diagram (Fig. 5.6) for the different technologies tested.

Technology	S_R	S_{BL}	S_{LR}	Area [%]
LoRa	1	0.67	1	76.6 %
Bluetooth	0.58	0.56	0.77	31.6 %
Wi-Fi	0.60	0.53	0.91	42.5 %
ARVA	0.44	1	0.99	65.4 %

three considered parameters, LoRa outperforms both the WLAN protocols, whereas AR-VAs have the highest score in battery life thanks to their extremely low power consumption per transmission. Although LoRa has almost the same robustness to shadowing than ARVA, the extended range greatly outweighs ARVAs' battery life. It is moreover worth noticing that ARVAs cannot transmit any packets, whereas LoRa transmits proper packets which can contain useful information. The scores per technology were then compared using a normalized radar plot. LoRa performed an overall score of 76.6% and outperformed Bluetooth (31.6%), Wi-Fi (42.5%), and ARVA (65.4%) mainly thanks to its extended range, although ARVA's battery life was longer than LoRa's one. Overall, the idea of using LoRa as Body-Area Internet of Things technology for creating SaR networks in mountain areas, properly exploiting its extended range and the possibility to transmit information, is feasible and very promising.

5.2 Characterization of LoRa Radiowave Propagation

To design as system exploiting the LoRa technology for mountain SaR operations the behavior of the protocol in terms of radio range and fluctuations of the signal's power level has to be known. The radiowave propagation modeling of LoRa links is introduced in this Section, whereas the fundamentals of radiowave propagation are reported in Appendix C.

5.2.1 Empirical Characterization of LoRa Propagation

Because of LoRa's characteristics, the path loss modeling is complex: multipath is an important factor to check due to the low sensitivity, and the required data are acquired slowly due to the duty cycle limitation. Although the RF propagation of LoRa was demonstrated to follow the Nakagami distribution for a body-to-base-station link [161], in [141, 182] the following formulas used to model the LoRa path loss from experimental data are introduced and validated:

$$PL = |RSSI| + SNR + EIRP + G_{RX} \tag{5.6}$$

where $EIRP$ is the effective isotropic radiated power of the transmitting antenna and G_{RX} is the gain of the receiving antenna in the direction of the transmitter. It is clear that the

received power is approximated as $P_R = |RSSI| + SNR$; this approximation valid only for very low values of the RSSI and SNR though. Indeed, from the very SNR definition and by assuming that the RSSI is the exact signal power level in absence of noise, the RSSI is incremented by the SNR only if the signal is below the noise level. Accordingly, henceforth a more accurate signal strength approximation is considered

$$P_R = RSSI + 10 \cdot \log_{10} \left(1 + \frac{1}{1 + SNR} \right) \qquad (5.7)$$

where the RSSI is in the dBm scale and is similar to P_R, whereas SNR is in the linear scale. The LoRa hardware employed in this thesis is capable of returning both the RSSI and the SNR so that the RSS P_R can be estimated according to (5.7).

From (5.6) is possible to model the EPL (Estimated Path Loss) using a linear polynomial fit to derive the expected path loss from the measured data with logarithmic link distance. Thus, through a first order fit [162, 183], the empirical PL model is derived

$$EPL = PL(d_0) + 10n \cdot \log_{10} (d/d_0) \qquad (5.8)$$

where B is the PL intercept, n is the PL exponent and d_0 is a reference distance. The EPL obtained in this way is a log-distance path loss propagation model as in eq. (7.46). According to [183], (5.6) can be used to model different channels also for UHF between $2 - 3$ GHz; channel model obtained this way, such as WINNER models in [183], were used for cellular base-station placement.

The deviation between the instantaneous and the mean PL are modeled as a lognormal shadow fading having zero-mean and STD σ_{SF}, so that, if PL_{Meas} is the vector of the measured PLs and EPL_{Corr} is the vector of the corresponding expected PL values,

$$\sigma_{SF} = std \left(PL_{Meas} - EPL_{Corr} \right). \qquad (5.9)$$

Naturally, this common way of modeling signal strength's fluctuations attributes to the shadowing every effect which make the PL deviate from the mean, even if it is not the case [184].

Table 5.4: Log-distance PL models used for LoRa in the literature. The σ_{SF} value is not available for all the models.

Frequency	Environment	$PL(d_0 = 1\text{ m})$	PLE	σ_{SF}
[141] 868 MHz	Sea	59.35 dB	2.32	7.8 dB
[141] 868 MHz	Urban	73.63 dB	1.76	8.0 dB
[143] 868 MHz	Urban	57.25 dB	2.65	-
[143] 433 MHz	Urban	47 dB	2.65	-
[182] 868 MHz	Urban	49.6 dB	2.8	-
[187] 602 MHz	Suburban	36.35 dB	2.49	-
[186] 900 MHz	Mountain (rocky field, no height)	55.75 dB	2.82	8.9 dB
[186] 900 MHz	Mountain (rocky field, 0.5 m height)	27.30 dB	3.94	11.9 dB

This method for modeling the channel and predict the RF propagation under given condition was also validated in subsequent works as [164], and is known as the WINNER + channel model since it is the WINNER II model extended to the 880 MHz band [185].

In Table 5.4 are reported empirical lognormal models used for the LoRa protocol in the literature. For comparison purposes with the derived PL model shown in the following, the reference distance of all the models is set to 1 m. Because of the ground-bounce multi-path, two different log-distance models for LoRa links in mountains are reported by [186].

5.3 Terrestrial Off-body LoRa Links in Mountain Environments

The LoRa radiowave propagation needed to design a SaR system can be experimentally characterized as described in the previous Section. The LoRa terrestrial PL models are derived from data collected during experimental campaigns in mountain environments. Two critical scenarios for SaR operations have been considered: the mountain canyon, which is among the harshest condition for SaR, and the snowy plain, which is a common scenario both because of lost hikers and avalanches (Fig. 5.7). The transmitter is placed on the ground, whereas the LoRa receiver is body-worn (as typical ARVAs) so that the proposed models include the impact of the body on the LoRa radio propagation in such scenarios

<center>(a)   (b)</center>

Figure 5.7: Mountain environments wherein the measurement campaigns were conducted. (a) Bletterbach canyon and (b) Campo Imperatore field, at the top of the Gran Sasso mountain.

(Fig. 5.8). Therefore, during the measurements, the transmitter broadcasts a message every approximatively 3 seconds while a volunteer with a body-worn receiver and a satellite tracker walks away trying to draw a straight line from the receiver. The receiving LoRa radio collects the RSSI and the SNR of the transmitted packets, and records them on an SD memory card.

5.3.1   Mountain Canyon

A range of 51 m was observed for the ARVA devices (Fig. 5.9) inside the canyon. This result is in line with the nominal 60 m range declared by the manufacturers. Instead, the 50% PDR range measured for LoRa was 300 m (point-to-point GNSS observation) namely about six times the ARVA's maximum range. The measured range is lower than the typical values of LoRa systems because the body-worn receiver is working in an extremely harsh environment characterized by body shadowing and reflections, and also by the impedance mismatch of the antenna.

The measured average PL for a 53% PDR was of 135 dB (see Table 5.5) with a relatively small standard deviation. In [182] the estimated RSSI is about of -140 dBm when using $SF = 12$, corresponding to PL$\cong$ 155 dB obtained using (5.6) and (5.7). This PL value is compatible with the measured values. In particular, it should be observed that moving

<center>133</center>
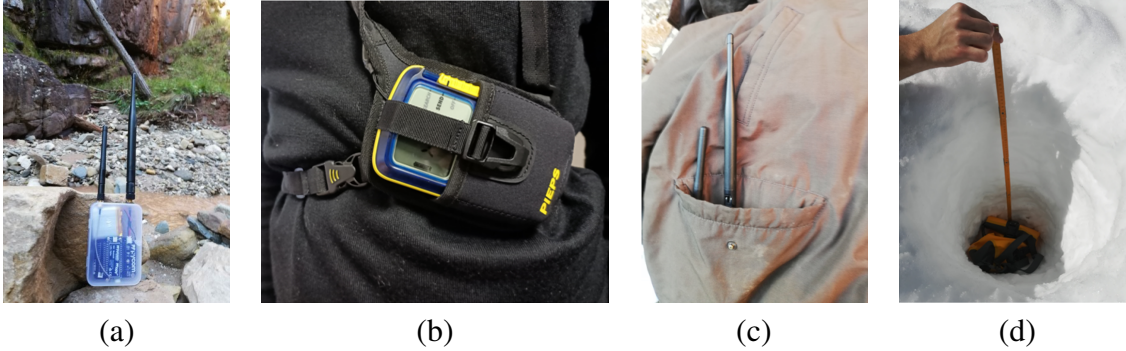
Figure 5.8: Experimental set-up for the characterization of terrestrial LoRa links in mountain settings. (a) Transmitting LoRa radio on the ground. (b) Typical body-worn ARVA. (c) Body-worn LoRa receiver in a pocket of the volunteer's jacket. (d) LoRa transmitter inserted in a watertight bag and buried under 1 m of snow.

from $SF = 7$ to $SF = 12$ leads to 13 dB variations in the receiver sensitivity [181]. From

Figure 5.9: Range measurements in Bletterbach canyon.

the measurements of RSSI and SNR, it was observed that a lognormal PL model for the canyon scenario provides good fitting. Because of the canyon topology, the channel propagation changes when passing from LoS to NLoS at a distance of 163 m. This sudden change does not affect the PL. This is possibly due to a sort of waveguiding effect in the canyon at the considered transmission frequencies. Collected data with the superimposed

Table 5.5: Measured statistics at a distance of 300 m from the transmitter in the canyon.

Distance (radial)	300 m
Average PL	135.4 dB
PL std	0.9 dB
PDR	53%
Number of packets sent	150

PL measurements are shown in Fig. 5.10. Model parameters are reported in Table 5.6 and they are compared to the FS (free-space) model.
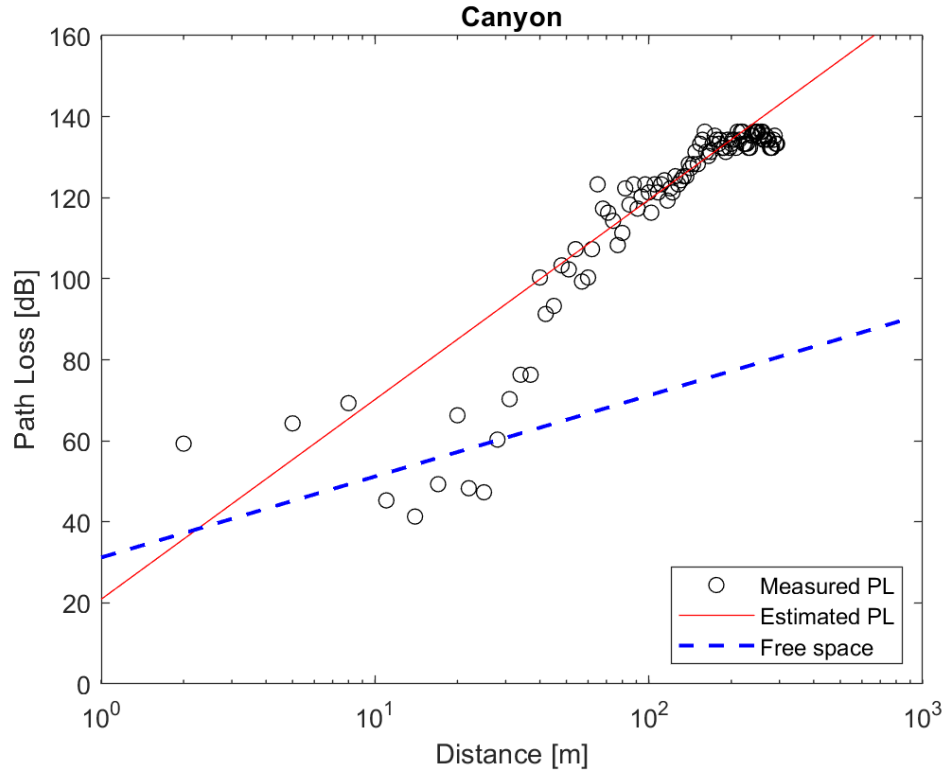
Figure 5.10: LoRa (868 MHz) estimated and measured PL in canyon compared with the free space model.

The standard deviation σ_{SF} of shadowing is high due to the harsh environment. The relatively large value of the PL exponent, which is of the same order of that observed for NLoS propagation in buildings [188], accounts for the presence of obstacles influencing propagation.

Table 5.6: Canyon path loss parameters.

Environment	Canyon	Free Space
EPL exponent (γ)	5.51	2
EPL intercept ($PL(d_0)$) [dB]	0.9	31.2
σ_{SF} [dB]	10.13	-
Number of packets sent	206	-

The model fitting of data in Fig. 5.10 appears to be valid at distances greater than about 20 m, whereas at closer distances the PL measurements appear to be unstable. This is mainly due to the prevalence of body shadowing effects, that affect propagation at smaller distances and can greatly vary depending on the position of the body with respect to the transmitter.

5.3.2   Snowy Plain: Lost Hiker and Avalanche Victim

The second critical scenario after the mountain canyon is the snowy plain, a common mountain SaR scenario because of lost hikers, and avalanches. Particularly, the ARVAs are optimized for the latter kind of SaR operations. To mimic a lost hiker, the LoRa transmitter is placed on the snow assuming an injured non-standing hiker.

The range measured with the ARVA with the transmitter over the snow was 64 m, greater than the nominal range. The measured 50% PDR LoRa range under the same conditions is about 332 m, which is similar to the range measured in the canyon. In this case, it seems the main problems to propagation are due to snow reflections and body shadowing. When the transmitter was buried 1 m under the wet snow, the operating ranges of LoRa and ARVA were more than halved. This fact is shown by the results in Fig. 5.11 and in Table 5.7. It is worth noticing that the 50% PDR range of LoRa is about five times the maximum radio range of ARVA. The range reduction is mainly due to the power losses introduced by the water content of the snow. The average PLs measured at distances corresponding to a PDR of about 50% are reported in Table 5.8 and are consistent with that in Table 5.5. The higher standard deviation of PL measured in the case of LoRa transmitter over the snow is due to snow reflections. From data collected in the case of the receiver just over the buried transmitter (Table 5.8), the 1 m snow layer alone causes around 60 ± 10 dB

Figure 5.11: Range measurements in Campo Imperatore.

Table 5.7: Maximum range measured in Campo Imperatore.

Technology	Max range [m]
LoRa (over snow), 50% PDR	332
LoRa (buried), 50% PDR	152
ARVA (over snow)	64
ARVA (buried)	27

Table 5.8: Statistics at different radials distances when the transmitter is either lying on the snow or buried under 1 m of snow.

Transmitter position	Lying	Buried	Buried
Distance (radial)	332 m	152 m	0 m
Average PL	120.2 dB	134.9 dB	61.2 dB
PL std	9.5 dB	1.4 dB	10.8 dB
PDR	54%	46%	83%
Number of packets sent	150	150	300

of entry loss and decreases the PDR of almost 20%. Collected data with the fitted model corresponding to the case of the LoRa transmitter over the snow are shown in Fig. 5.12, whereas data for the buried transmitter with the corresponding fitted EPL model are reproduced in Fig. 5.13. In Table 5.9 the PL parameters measured in the snowy field are reported. It is worth noticing that the data collected at close distances seem to have very different behavior in the two considered cases: when the transmitter is over the snow the data at close distances are more similar to the FS model, as observed from the canyon measurements (Fig. 5.10); when the transmitter is buried under the snow instead, the single-slope PL model fits well also at close distances, thanks to the PL introduced by the layer of snow. During the measurements three packets having $PL = 128 \pm 0.6$ dB were measured at close distances when the transmitter was placed on the snow, probably due to a malfunctioning of the receiver; those data were not included in the EPL but they are nonetheless reported

in Fig. 5.12 and labeled as outliers. Overall, the values of σ_{SF} measured in the snowy field (Table 5.9) are smaller than those measured in the canyon (Table 5.6). Finally, for the sake of completeness, some measurements of RSSI and SNR are reported as returned by the LoRa receiver (Fig. 5.14); it is evident that the RSSI fluctuates more than the SNR, which, in turn, abruptly decreases after about 100 m due to the challenging environment. This behaviour was observed in all the measurements performed in mountain scenarios that are shown in this thesis.
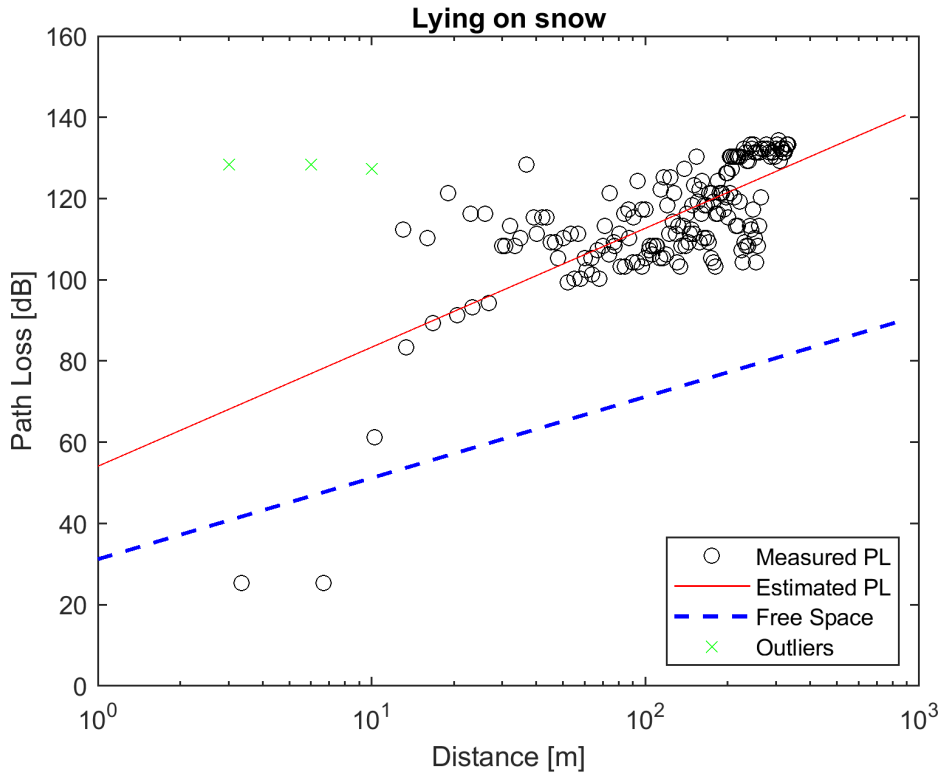
Figure 5.12: LoRa (868 MHz) estimated and measured PL when the transmitter is lying on the snow compared with the free space model.

5.4   Conclusion

The usage of body-worn LoRa transceivers for mountain SaR is validated and analyzed in this Chapter by comparing the LPWAN technology with the current golden standards.
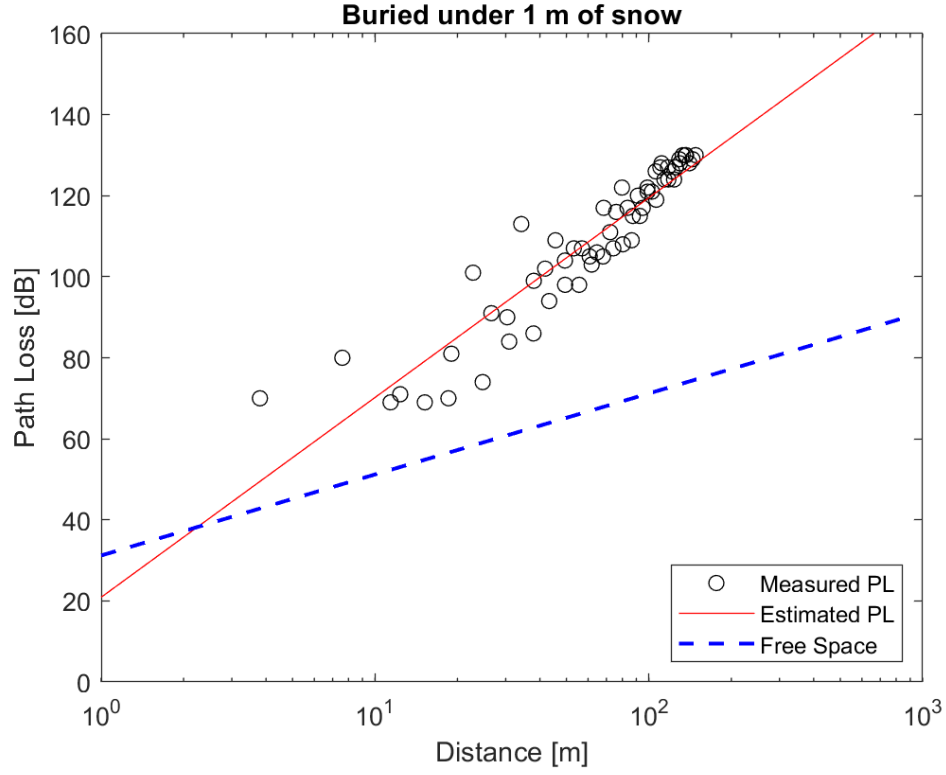
Figure 5.13: LoRa (868 MHz) estimated and measured PL when the transmitter is buried under 1 m of snow compared with the free space model.

Table 5.9: PL statistics measured in the snowy field.

Transmitter position	Lying	Buried	Free space
EPL exponent γ	3,17	4.93	2
EPL intercept $(PL(d_0))$	56.7 dB	18.0 dB	31.2
σ_{SF}	9.95 dB	7.33 dB	
Number of packets sent	198	133	

Then, the radiowave propagation of LoRa is characterized through empirical log-distance path loss models in two critical scenarios: a mountain canyon and a snowy plain. In the latter case, both a transmitter lying on the snow and buried under 1 m of snow are considered. It is observed that the log-distance model well-describes these particular off-body links, although the body shadowing and the harsh environment cause very significant values of shadow fading, which models the signal strength's fluctuations. Aside from the

139
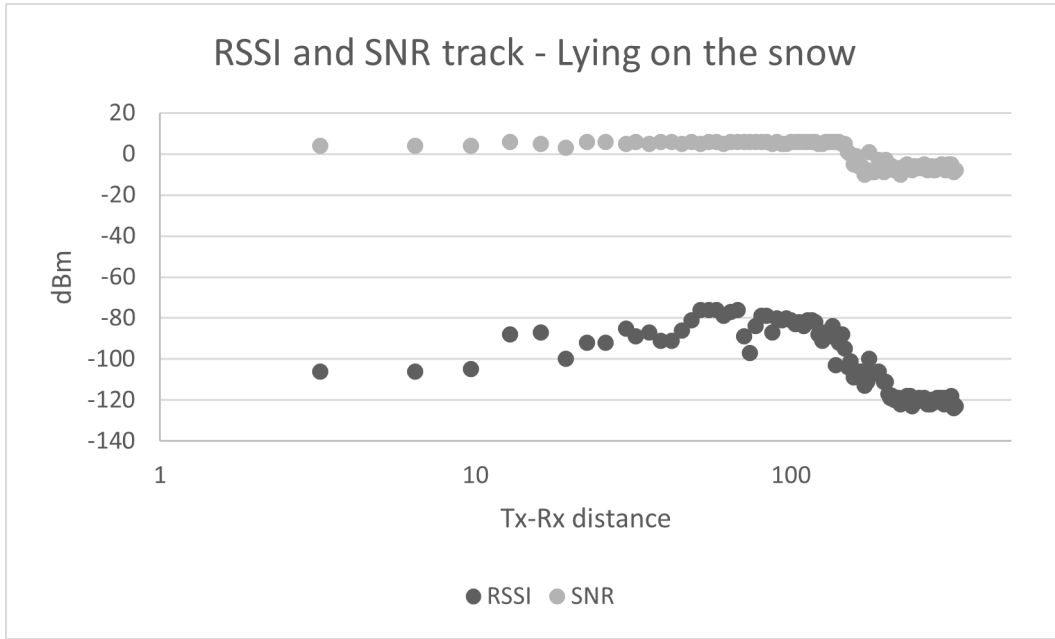
Figure 5.14: RSSI and SNR tracks recorded by the LoRa receiver when measuring the PL (lying on snow case

.

buried transmitter case, the body-shadowing causes the fluctuations for short Tx-Rx distances (up to some tens of meters), whereas the environment dominates further. Instead, if the transmitted is buried under 1 m of snow, the significant entry loss caused by the snow overshadows the body-shadowing. Overall, the RSS observed by a receiver with these off-body links could be exploited for the localization of the transmitter's wearer since the localization of an RF source whose signal follows a log-distance model is a long-investigated research topic, as it is detailed next in Chapter 7.

Chapter 6

Off-body Ground-to-air LoRa Links for Mountain SaR

This Chapter introduces the ground-to-UAV LoRa links for mountain SaR operations. No body-UAV connectivity in a similar environment has ever been investigated. The system exploiting a body-worn transmitting radio and a receiving UAV is introduced (Section 6.1), then it is employed to analyze the RSS profiles in flat lands through a deterministic model (Section 6.2) and in mountain environments with a statistical model (Section 6.3).

6.1 Body-UAV Antenna System for Mountain SaR with LoRa

As written above, an RF source can be localized based on the strength of its signal provided that the radiowave propagation is roughly known. The terrestrial LoRa links in harsh mountain environments are characterized in the previous Chapter, and they are deemed exploitable for localization purposes. However, in mountain SaR scenarios the terrain is usually extremely harsh, the time required to collect the measurements can be high, while the survival chances of the target could drop very quickly, especially in case of avalanches [189]. Instead, a UAV equipped with a LoRa receiver could search a vast area in little span of time while collecting many RSS measurements to speed up the localization through the

ground-to-air off-body link. For this purpose, a system composed of a body-worn transmitting radio and a receiving UAV exploiting the LoRa protocol is used to analyze for the first time this particular kind of links. Specifically, a LoRa UAV-wearable device link [190] has never been neither characterized nor modeled before.

6.1.1 Wearable Transmitting LoRa Beacon

As the transmitting radio, the LoRa radio considered is a LoPy-4 board connected to the COTS $863 - 873$ MHz dipole [180] as in the previous Chapters. Regarding the body placement, most first responders and hikers wear a safety helmet during operations and outdoor activities (like skiing or canyoneering), so a possible placement of the LoRa beacon is the helmet itself. Although the helmet antennas are a topic of research since 1981 for security purposes (military, police, firefighters), the literature on the topic is limited as by searching "helmet antenna" on IEEE Xplore 67 papers are returned by the archive at the date of writing, of whom only 10 are journal articles. Wearable helmet-mounted antennas were mainly proposed for disaster prevention [191] and military forces [192], and the more common helmet antenna types are dipoles, patches, and loops (Table 6.1). However, all the helmet antennas proposed so far are designed to work when the user is vigilant and standing so that effects of the ground when the wearer is unconscious or injured have not been addressed. Instead, if an accident happens, the user is likely lying on the ground, eventually in the presence of snow, and the helmet-UAV link is expected to be greatly affected by the helmet wearer position. Generally, the wearer is can assume four possible positions: standing, lying on the front, side-lying, lying on the back (Fig. 6.1).

The choice of the reference helmet antenna could, in principle, consider both a linearly-polarized (LP) or a circularly-polarized (CP) device as for the receiver onboard the UAV. A CP antenna would permit to minimize the interference due to the ground since the reflection would invert the polarization verse so that the reflected field is filtered out by the receiver antenna having opposite polarization. However, using a CP antenna on the helmet too would introduce some drawbacks since the polarization of the helmet antenna could be seen as reversed by the receiver because of the unpredictable Tx-Rx mutual positions during the UAV flight and the actual posture of the user. Sharp polarization mismatches could

Table 6.1: Examples of helmet antennas in the literature. The types of the antennas are divided into sub-types as the PIFA (planar inverted F antenna), PILA (planar inverted L antenna), and CLA (circular loop antenna).

Type of antenna	Antenna	Type of antenna	Antenna
Dipole	PIFA [193, 191, 194, 195]	**Patch**	Monopolar patch [196]
	PILA [193]		Planar patch [197]
	Folded dipole [198, 199]		Stacked patch [192, 200]
	Planar dipole [201]	**Spiral**	Spiral [202]
Loop	Half CLA [203]	**Microstrip**	Spiral mode microstrip [204]
	Square loop [205]	**Slot**	Slot with metamaterials [206]
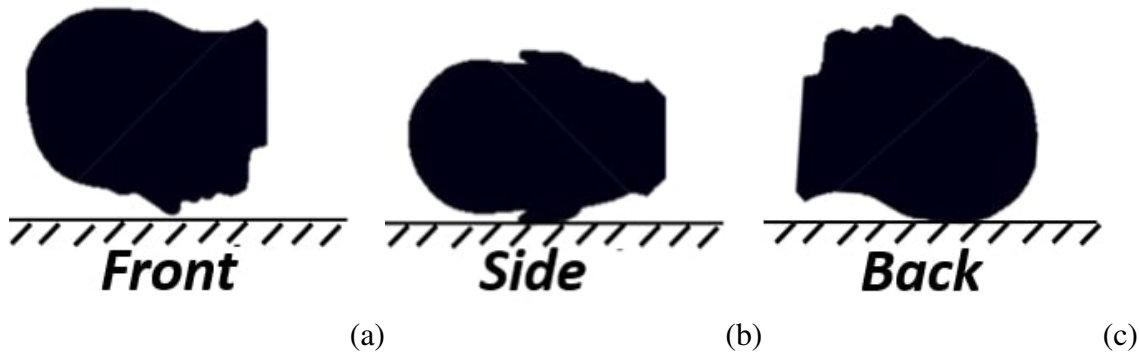
Figure 6.1: The three possible positions of a lying user (a) on the front, (b) on the side, and (c) on the back.

occur hence preventing the establishment of the communication. For the sake of generality, the transmitting helmet antenna is assumed to be a flat dipole (copper trace 35 µm thick) wrapped onto the top of the helmet (Fig. 6.2) according to two possible arrangements (w.r.t. the anatomical planes): along the median sagittal plane (hereafter *sagittal dipole*), and the coronal plane (*coronal dipole*). As shown next in Sub-subsection 6.2.2, this arrangement guarantees a reliable polarization matching in most conditions when the receiving antenna is CP.

The gain G_T of the transmitting antenna is dependent on the working conditions. In particular, when the user is lying, the interaction with the ground is expected to disturb the radiation pattern strongly. To simplify the evaluation of the link budget of the system, the transmitting antenna is taken into account through an equivalent uniform gain pattern whose value is derived from statistical analyses involving the user's possible positions. For this purpose, the radiation performances of all the combinations of antennas and positions are numerically evaluated utilizing the software CST Microwave Studio Suite 2018. The numerical model (open access and available at `https://grabcad.com/library/helmet-184.`) employed for the simulations includes:

- a homogeneous numerical phantom of a human head with average relative permittivity and conductivity $\varepsilon_r = 42.7$, $\sigma = 0.99$ S/m [112] respectively;

- a lossless foamed plastic ($\varepsilon_r = 1.5$ [207]) shell with the dimensions of a typical helmet for mountaineering (derived from the Vayu 2.0 model by Salewa, having perimeter length of 63 cm);

- ground modeled as a conducting plate.

The dipoles were preliminarily tuned at 868 MHz in the standing user case so that the reflection coefficient is $\Gamma_T \leq -10$ dB in the whole LoRa band. The proximity with the PEC ground in the case of a lying user produces a moderate impedance mismatch (Fig. 6.3), nevertheless preserving the same maximum value as before. If the terrain is dry, the reflection coefficients are less affected by the helmet position and are more similar to the standing user case.

By referring to the radiation gain patterns at the zenith (Fig. 6.4), it is clear that the two antenna layouts behave similarly for a standing user. In contrast, relevant differences are

144
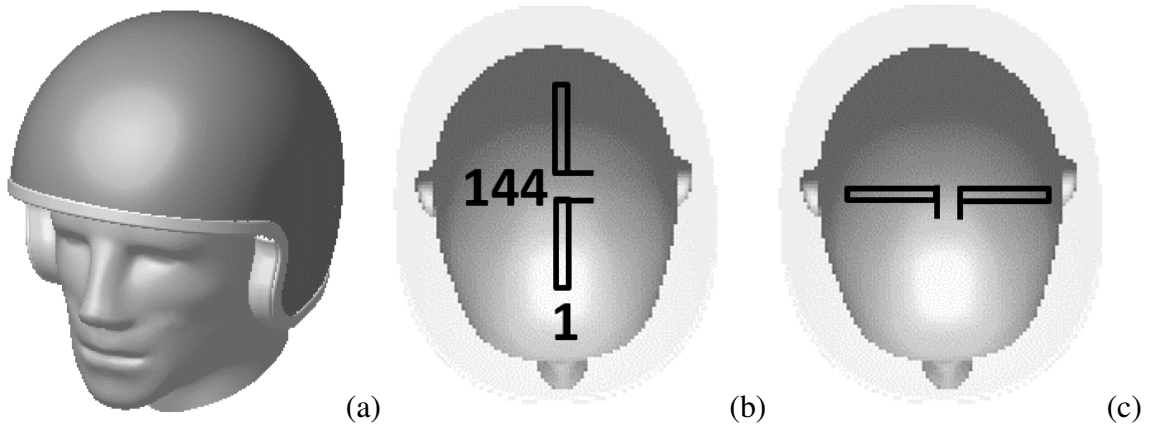
Figure 6.2: (a) Helmet and head numerical phantoms. The flat dipole (size in mm) along (b) the medial sagittal and (c) the coronal planes.
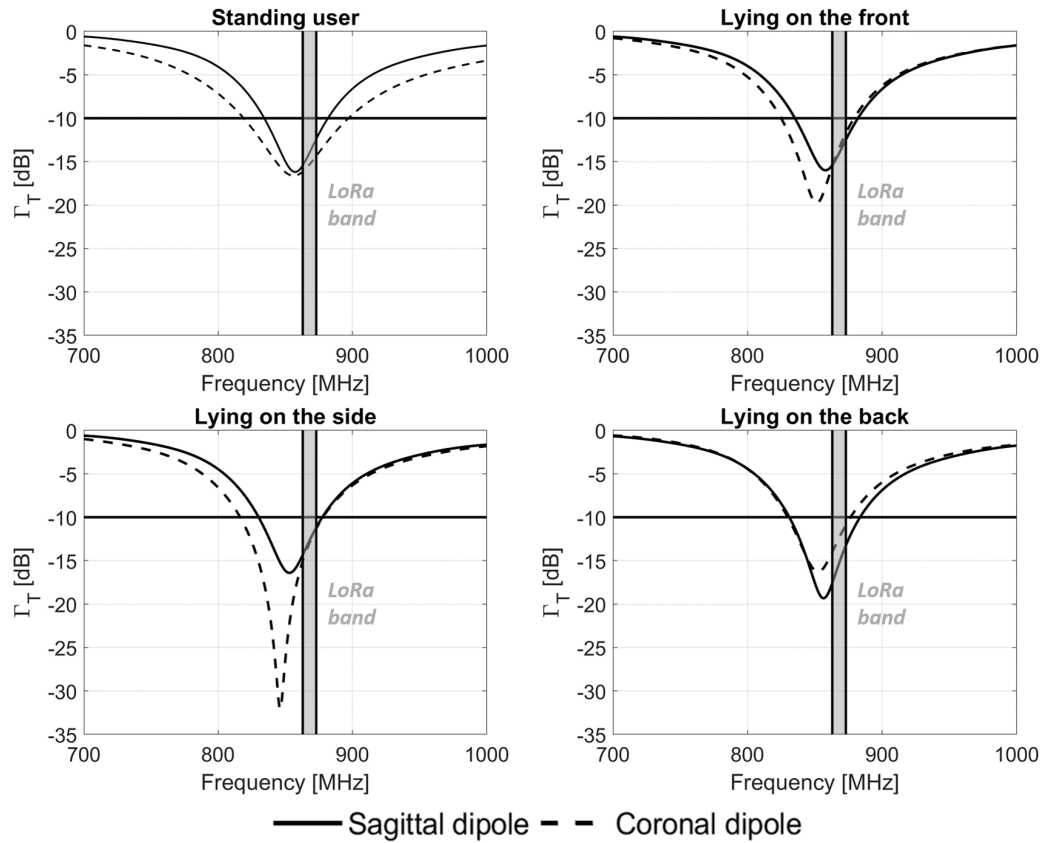
Figure 6.3: Simulated reflection coefficients of the helmet antennas in Fig. 6.2 in four user positions over PEC terrain. The LoRa 863-873 MHz band is highlighted in grey.

Table 6.2: Selected equivalent Tx gain $G_0\,(CCDF = 75\%)$ for different user and terrain conditions.

Standing user	−4.1 dBi	
Lying user	Wet terrain	Dry terrain
	−4.5 dBi	−6.5 dBi

visible in the case of a lying user, with the maximum radiation occurring either along the zenith or the horizon depending on the position of the helmet.

The most appropriate antenna arrangement is the one maximizing the uniformity of the radiation pattern in the upper half-space in all the considered user configurations, especially in the lying ones. The complementary cumulative distribution function (CCDF) for $G_T > G_0$ in the whole half-space is used as a metric (Fig. 6.5), $CCDF(G_0)$ being the percentage of the half-space where the gain of the antenna in all the three lying configurations is more than G_0. Accordingly, the coronal dipole outperforms the sagittal one. By considering, for instance, the threshold value of probability 75%, the corresponding lower bound gain $G_0\,(CCDF = 75\%)$ of the coronal dipole is about 2 dB higher than the corresponding value of the sagittal dipole.

In conclusion, the coronal dipole is hereafter considered the transmitting antenna whose equivalent gain is $G_T = G_0\,(CCDF = 75\%)$, keeping the different values for standing and lying cases and kind of terrain, as summarized in Table 6.2.

6.1.2 Receiving UAV-Mounted Antenna

The UAV is hereafter assumed to be equipped with a circularly polarized patch as in [208]. For CP patches it is possible to derive an approximation of the antenna's radiation gain based on the literature. Indeed, it was demonstrated that an RFID reader equipped with a CP patch has an ellipsoidal reading region having axes [209] [w.r.t. Fig. 6.6(a)]

$$a_y = \frac{\lambda}{8\pi}\sqrt{\chi\frac{EIRP}{\hat{p}_C}} \qquad (6.1)$$

Standing user

Sagittal plane

Coronal plane

Lying user

Front

Transverse plane

Sagittal plane

Side

Transverse plane

Coronal plane

Back

Transverse plane
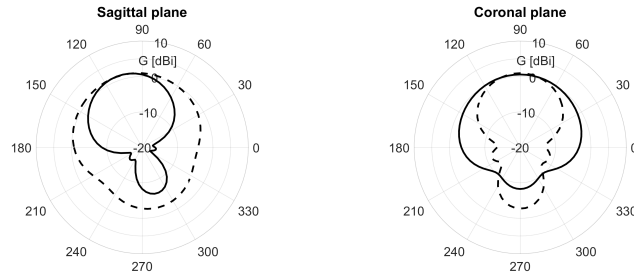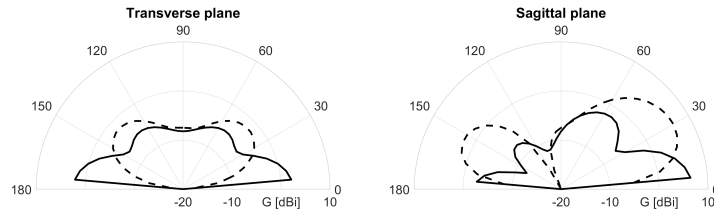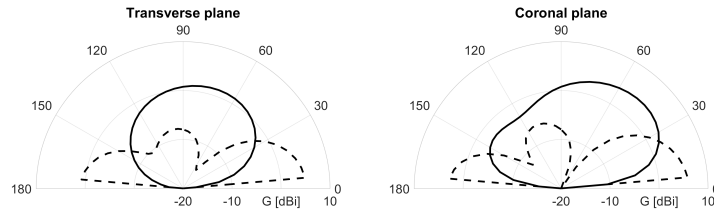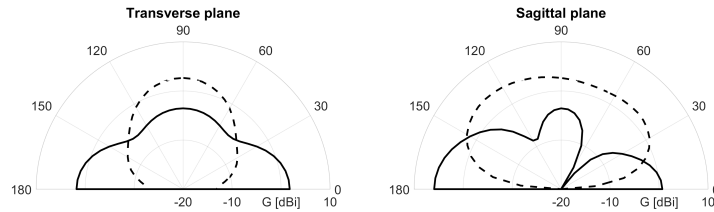
Sagittal plane

—— Sagittal dipole – – Coronal dipole

Figure 6.4: Simulated radiation gain of the helmet antennas (sagittal and coronal dipoles) over planes passing through the zenith. In the case of a lying user, a PEC ground is assumed. The dry terrain case returns the same patterns with an offset of -2 dB.
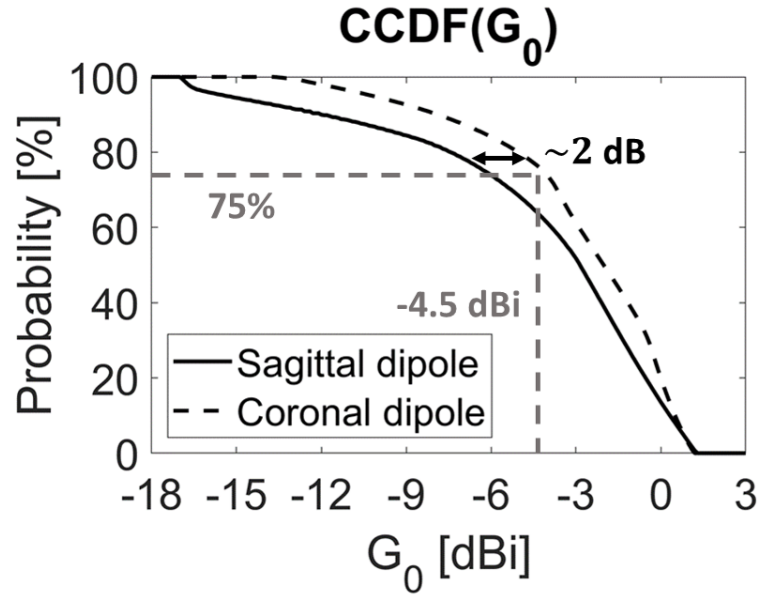
Figure 6.5: Complementary cumulative distribution function $CCDF(G_0)$ for the sagittal and coronal dipoles by taking into account the data of all the three lying positions of the user on a PEC ground (Fig. 6.1).

(a)   (b)
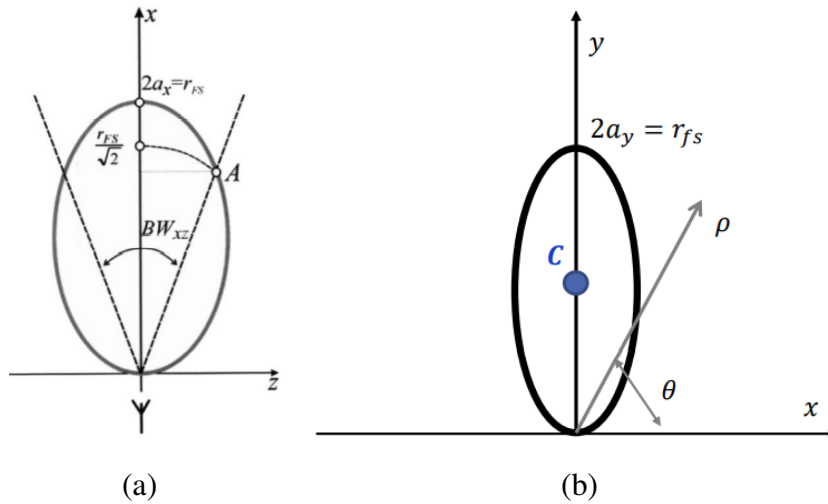
Figure 6.6: (a) Ellipsoidal reading region of an RFID reader equipped with a CP patch [209]. (b) Ellipsoidal approximation of the CP patch's gain $[(x,y)\text{-plane}]$.

$$a_\xi = -a_x \sqrt{\tan\left(\frac{BW_{x\xi}}{2}\right) \frac{\sin\left(\frac{BW_{x\xi}}{2}\right)}{\sqrt{2} - \cos\left(\frac{BW_{x\xi}}{2}\right)}} \tag{6.2}$$

where *EIRP* is the reader's EIRP, $\hat{p}_C$ is the RFID tag's IC sensitivity, χ is the polarization loss factor, ξ is an axes orthogonal to the $x-$axis, and $BW_{x\xi}$ is the half-power beamwidth of the CP patch whose radiation pattern in assumed axially symmetric. By assuming $\xi = y$ without any loss of generality, the ellipsoid equation is

$$\frac{(x - a_x)^2}{a_x^2} + \frac{y^2}{a_y^2} + \frac{z^2}{a_z^2} = 1. \tag{6.3}$$

Let us consider the (x, y)-plane and the ellipsoid's section lying on it without any loss of generality [Fig. 6.6(a)]. The center of the ellipse is the point $C = (0, a_y)$ and its equation is

$$\frac{x^2}{a_x^2} + \frac{(y - a_y)^2}{a_y^2} = 1. \tag{6.4}$$

If G_R is the receiver patch's antenna gain, from the Friis' transmission formula in polar coordinates, we obtain

$$G_R(\theta, \phi) = \left[\frac{4\pi}{\lambda} r_{max}(\theta, \phi)\right]^2 \frac{\hat{p}_C}{\chi EIRP} \tag{6.5}$$

where r_{max} is the maximum communication distance. Thanks to the rotational symmetry, the dependence on ϕ can be dropped out, so $G_R(\theta, \phi) = G_R(\theta)$. Equation (6.4) in polar coordinates becomes:

$$\frac{(\rho \cos \theta)^2}{a_x^2} + \frac{(\rho \sin \theta - a_y^2)^2}{a_y^2} = 1. \tag{6.6}$$

The ellipse (6.6) can also be written as:

$$\rho = \frac{2a_x^2 a_y^2 \sin \theta}{a_y^2 (\cos \theta)^2 + a_x^2 (\sin \theta)^2} \tag{6.7}$$

so by imposing $\rho = r_{max}$ and inserting (6.7) in (6.6), it is obtained

$$G_R(\theta) = \left[\frac{4\pi}{\lambda} \frac{2a_x^2 a_y^2 \sin\theta}{a_y^2 (\cos\theta)^2 + a_x^2 (\sin\theta)^2} \right]^2 \frac{\hat{p}_C}{\chi EIRP}. \tag{6.8}$$

Since [209], being $r_{fs} = \max[r_{max}(\theta)]$,

$$G_{R,max} = \left(\frac{4\pi}{\lambda} r_{fs} \right)^2 \frac{\hat{p}_C}{\chi EIRP}, \tag{6.9}$$

$$a_y = \frac{\lambda}{8\pi} \sqrt{\chi \frac{EIRP}{\hat{p}_C}} = \frac{r_{fs}}{2}, \tag{6.10}$$

and

$$a_x = a_y \sqrt{\tan\frac{BW_{xy}}{2} \frac{\sin\frac{BW:xy}{2}}{\sqrt{2} - \cos\frac{BW_{xy}}{2}}} = r_{fs} f(BW_{xy}) \tag{6.11}$$

where

$$f(BW_{xy}) = \sqrt{\tan\frac{BW_{xy}}{2} \frac{\sin\frac{BW:xy}{2}}{\sqrt{2} - \cos\frac{BW_{xy}}{2}}}. \tag{6.12}$$

Accordingly, starting from the ellipsoid approximation presented in [209], by inserting (6.9), (6.10) and (6.11) in (6.8), the radiation gain of the CP patch is

$$G_R(\theta) = G_{R,max} \left[\frac{f^2(BW_{x\xi}) \sin\theta}{(\cos\theta)^2 + f^2(BW_{x\xi})(\sin\theta)^2} \right]. \tag{6.13}$$

This approximation can be easily evaluated for each θ given the pair $\left(BW_{x\xi}, G_{R,max} \right)$ known from the datasheet of the CP patch. (6.13) draws a drop-curve in the space (6.7).
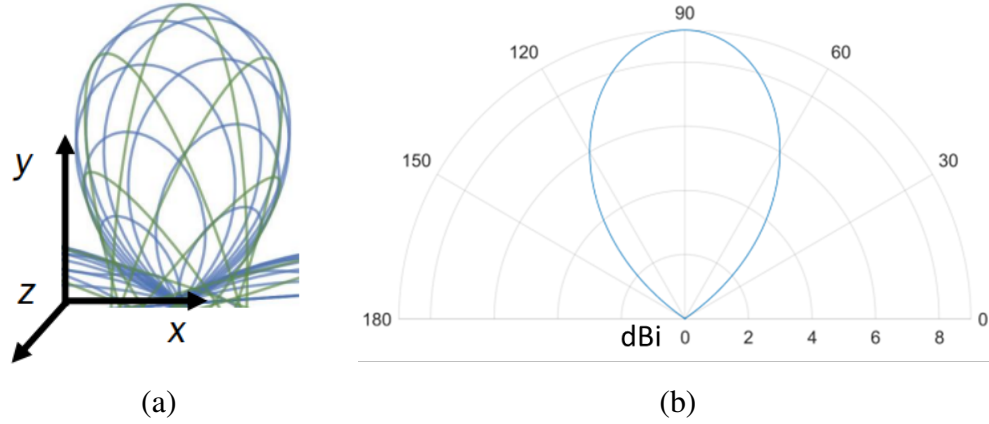
Figure 6.7: Numerically evaluated (with Octave 6.4.0) drop-curve from (6.13) when $BW_{x\xi} = 60^o$ and $G_{R,max} = 9$ dBi. (a) Drop-curve in a tridimensional plot when $G_{R,max}$ lies on the $y-$axis, and (b) section including the pole.

6.1.3 Antenna System Prototypes

The LoPy-4 board [176] is embedded into a typical helmet for mountaineering (Vayu 2.0 by Salewa) utilizing a bi-adhesive tape while the COTS dipole [180] is similarly fixed outside the helmet. The helmet including the board and the wearable antenna (hereafter named *radiohelmet*) can be comfortably worn without causing any discomfort to the wearer. The transmitting board is programmed to broadcast a LoRa packet using the transmission parameters detailed in Subsection 6.11. Two identical radiohelmet prototypes are used to perform the measurements presented in this Chapter (Fig. 6.8).

Similarly, the receiving UAVs carry with them a CP patch with fixed a LoPy-4 board on it. The board stores on an SD memory the timestamp, the progressive number, the RSSI and the SNR of the received packet. The UAV are geolocalized and the packet records are synchronized so that each PL measurement is correlated with the corresponding measurement point. Two different UAVs equipped with a different COTS CP patch each are assembled to analyze the LoRa off-body ground-to-air links:

1. the Prototype A consists of a DJI Phantom 3 Pro quadcopter carrying a Keonn Advantenna p-11 patch ($G_{R,max} = 3.2$ dBic; $BW_{x\xi} = 1.745$ rad [210]) [Fig. 6.9(a)];

151
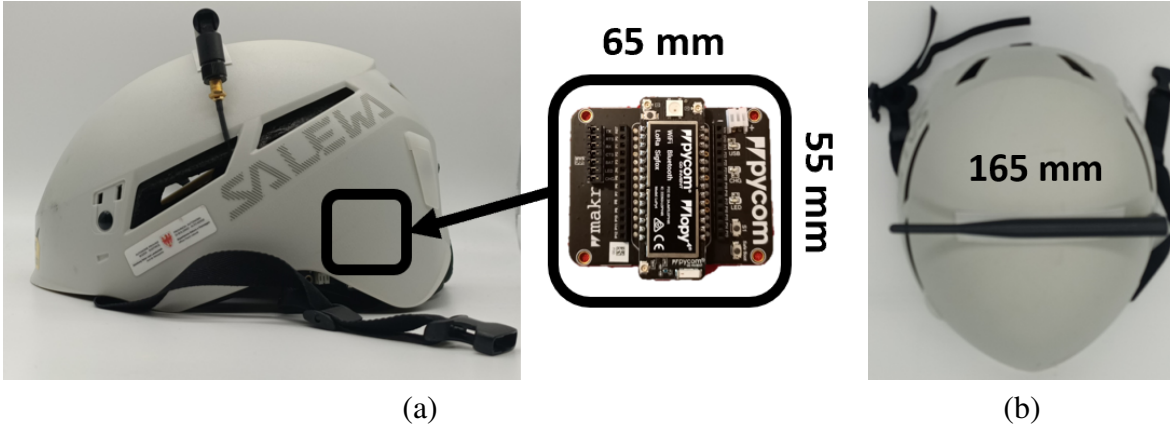
Figure 6.8: A radiohelmet prototype. (a) Side view with an indication of the placement of the LoRa board. (b) Top view with the length of the COTS dipole.

2. the Prototype B consists of a Soleon octocopter for mountain applications equipped with a WANTENNAX005 by CAEN RFID spa ($G_{R,max} = 7$ dBic; $BW_{x\xi} = 1.047$ rad [211]) [Fig. 6.9(b)].

The system prototypes are hereafter used to validate the body-to-UAV links over flat lands (Prototype A) and actual mountain environments (Prototype B).

6.2 Body-to-UAV Links in Flat Lands

The simplest body-UAV links are the ones taking place over flat lands wherein the terrain roughness is negligible and there are no obstacles so that the transmitting and receiving antennas are always in the LoS condition. Consequently, the flat land LoS scenario is the first model of the off-body links considered. Despite the simple approximation, the model can describe several SaR events, for example, *i*) mountaineers in open environments hit by an avalanche, *ii*) lost hikers in some natural parks after fires, *iii*) injured soldiers in desert areas, *iv*) missing citizens and first responders after cataclysms (as earthquakes, tornadoes, tsunami) that destroy obstacles and create mostly flat and homogeneous zones.

Figure 6.9: The two receiving UAVs equipped with CP patches. (a) Prototype A (DJI Phantom3 quadcopter equipped with Advantenna p11 by Keonn). (b) Prototype B (Soleon octocopter equipped with WANTENNAX005 by CAEN RFID spa), where *1*) is the receiving LoRa radio, *2*) is the optical instrumentation (RGB and thermal cameras), and *3*) is the UAV platform.

6.2.1 Body-UAV Link Model and Link Budget

Like every Tx-Rx link, the body-UAV link follow a Link budget equation, namely an equation expressing the relationship between the transmitted power P_T and the received power P_R; the latter is the RSS seen by the UAV, too. In the following, we model the off-body link to a UAV as a function of four variables:

1. R, the terrestrial distance between the radiohelmet wearer and the UAV;

2. H, the flying height of the UAV;

3. h, the transmitter distance from the ground;

4. t, the terrain condition.

Accordingly, the link budget in the dB scale is

$$
\begin{aligned}
P_R(R,H,h,t) = P_T + G_T(R,H,h,t) + G_R(R,H,h) \\
+ \tau_T(h,t) + \chi(R,H,h,t) - PL(R,H,h) + F(R,H,h,t)
\end{aligned}
\tag{6.14}
$$

where P_R is the RSS seen by the UAV, P is the transmitting power whereas χ is the polarization loss factor. The log-distance PL expression is $PL(r) = PL(d_0) + 10 \cdot n \cdot \log_{10}(r/d_0)$, being d_0 a reference distance, n the path loss exponent and r the ray-path. Since LoS ground-to-air channels of low-altitude UAVs can be approximated by the free-space link [212], the conditions $d_0 = \lambda/4\pi$ and $n = 2$ are assumed. Being Γ_T the module of the reflection coefficient of the transmitting antenna, $\tau_T = (1 - \Gamma_T^2)$ is the corresponding power transfer coefficient. The receiving antenna is instead considered perfectly matched to the receiver. The theoretical maximum communication distance is evaluated by imposing P_R equal to the receiver's sensitivity, which depends on the bandwidth and the spreading factor (*SF*) of the LoRa signal as in Table 6.3. Based on [158] and the previous Chapter, a signal bandwidth of 125 kHz and a variable *SF* value are considered for the numerical analyses described next. Finally, the term F is the path-gain factor that accounts for the multi-path in the case of a standing user through the flat-earth two-ray propagation model [214, 212]. With reference to the geometrical parameters in Fig. 6.10

Table 6.3: Sensitivity of the LoRa SX1276 transceiver for different *SF* values at bandwidth 125 kHz. [213]

Spreading Factor	Sensitivity [dBm]	Spreading Factor	Sensitivity [dBm]
12	-136	9	-129
11	-133	8	-126
10	-132	7	-123
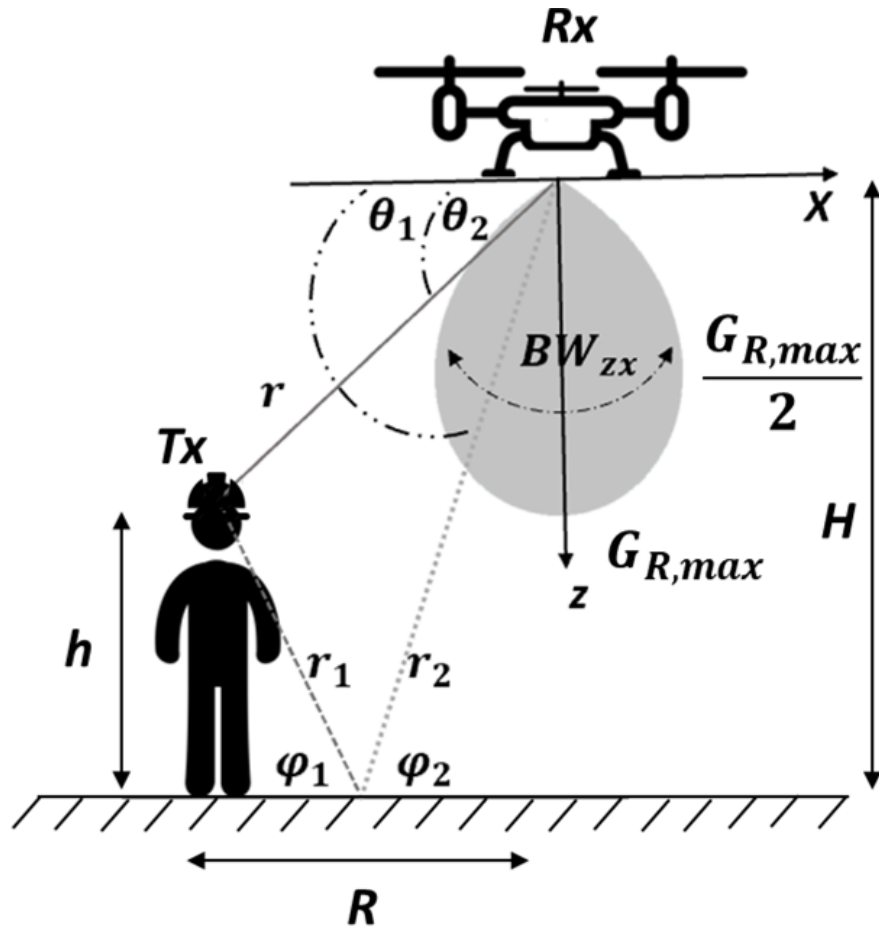
Figure 6.10: Sketch of the radiohelmet-to-UAV link and relevant parameters.

$$F = 20\log_{10}\left[\left|1 + \rho e^{j\psi}\sqrt{\frac{G_T\left(\theta'_1\right)G_R\left(\theta_1\right)}{G_T\left(\theta'_2\right)G_R\left(\theta_2\right)}}e^{-jk_0(r-r_1-r_2)}\right|\right], \tag{6.15}$$

where k_0 is the free-space propagation constant, $\rho e^{j\psi}$ is the Fresnel reflection coefficient, θ_2 identifies the direction of the direct path, and the antennas' gains are in linear scale. By assuming a smooth ground, then $\varphi_1 = \varphi_2 = \varphi$. The Fresnel reflection coefficient for an electromagnetic wave polarized parallelly to the ground is evaluated from the permittivity of the land itself as [214]

$$\rho e^{j\psi} = \frac{\sin\varphi - \sqrt{\varepsilon/\varepsilon_0 - \cos^2\varphi}}{\sin\varphi + \sqrt{\varepsilon/\varepsilon_0 - \cos^2\varphi}}. \tag{6.16}$$

For PEC reflecting surfaces, then $\rho e^{j\psi} = -1$. If the user is lying, the antenna is on the ground, the multi-path disappears, F is dropped out from (6.14), and the ground effect is accounted for in the gain of the helmet antenna as described in the next Section.

The link budget in (6.14) is here parametrized regarding the user's position (through the transmitter gain) and the features of the receiving antenna.

6.2.2 Polarization Loss Factor

Like the antennas' gains, the polarization loss factor heavily varies with the helmet wearer's position and the terrain condition. The loss factor is evaluated from the polarization versors of the transmitter $(\hat{\rho}_T)$ and the receiver $(\hat{\rho}_R)$ as

$$\chi = |\hat{\rho}_T \bullet \hat{\rho}_R^*|^2 \tag{6.17}$$

$|\cdot|$, $*$ and $\bullet$ being the module, the complex conjugate, and the inner product operators, respectively.

To model the polarization effects, the polarization of the receiving CP patch is assumed constant and equal to $\hat{\rho}_R = \sqrt{2^{-1}}(1+j)$, whereas the versor of the transmitting antenna is numerically evaluated when considering all the position-terrain combinations and all the possible observation angles. The polarization of the transmitting antenna is established based on the axial ratio AxR of the observed EM wave:

156
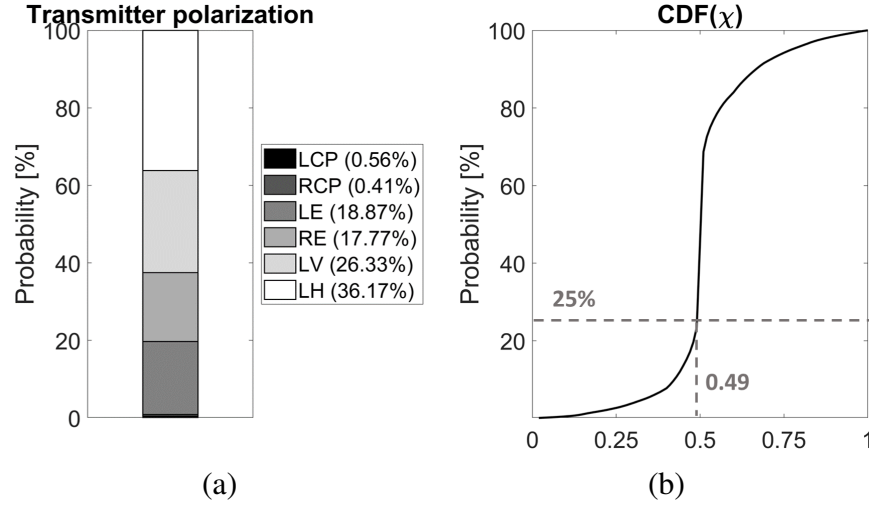
Figure 6.11: (a) Probability that the transmitted EM wave is polarized in a given way over all the direction of observation and user's postures. (b) $CDF(\chi_0)$ for the coronal dipole when considering both the standing and the lying postures.

- if $AxR < 3$ dB, the wave is considered CP, either right-hand (RHCP) or left-hand (LHCP) based on the dominant component returned by the simulator;

- if $AxR > 20$ dB, the wave is considered linearly polarized, either vertically (VP) or horizontally (HP) based on the dominant component returned by the simulator;

- if 3 dB $\leq AxR \leq 20$ dB, the wave is considered elliptically polarized, either right-hand (RHEP) or left-hand (LHEP) based on the dominant component returned by the simulator.

From the simulations, the transmitted wave is linearly polarized 60% of times, and $\chi \geq -3$ dB in 75% of the cases (Fig. 6.11). Accordingly, the assumption $\chi = -3$ dB is considered for the next evaluation of the received power P_R.

Table 6.4: Considered values for the numerical RSS evaluation.

Parameter	Value	Parameter	Value
P_T	14 dBm	R	$[0; 10000]$ m
$G_{R,max}$	3.2 dBi	H	$[5; 120]$ m
$BW_{z\xi}$	100°	h (standing)	1.7 m
χ	-3 dB	h (lying)	0 m
f	868 MHz	τ_T	-0.01 dB

6.2.3 Numerical Analysis

Following the above framework, the radiohelmet-to-UAV link is numerically evaluated to predict the maximum achievable communication range and analyze the two-ray interference through coverage maps. The communication range is expressed as the radio-helmet-UAV ground distance since it is a crucial parameter for most SaR operations. The user-UAV link must be as monotonic as possible to apply range-based location algorithms exploiting the RSS effectively, as analyzed in-depth in the following Chapter.

The RSS is evaluated according to (6.14). The parameters of the receiving antenna to derive $G_R(\theta)$ are referred to the Keonn Advantenna p-11 since the Prototype A of the antenna system is then used for corroboration. The received power at the UAV side is evaluated for a variable flight altitude $5 \text{ m} \leq H \leq 120 \text{ m}$ of the UAV as $H = 120$ m is the highest altitude of a UAV that is compliant with EU regulations on civilian applications (open category) [215]. The corresponding maximum radio range R_{max}, wherein the received power P_R equals the sensitivity of the receiver, is derived consequently. The transmitter must moreover comply with the ERP regulation for LoRa systems. By enforcing the EU constraint [216] over the maximum LoRa irradiation (namely, ERP = 14 dBm at 868 MHz), the maximum transmitter power to insert in (6.14) is $P_T = 14$ dBm. All computations refer to an $h = 1.7$ m tall user. Finally, from Fig. 6.3, $\tau_T(h,t) \simeq \tau_T = -0.01$ dB. The values of the parameters employed in the numerical simulations are resumed in Table 6.2 and Table 6.4.

Although both the lying-user and the standing-user links are in LoS conditions, the evaluated RSS is very different. Firstly, by considering the standing-user case, Fig. 6.12(a) shows the maximum estimated communication distances versus H for dry or wet terrains.

The link range is mostly unaffected by the terrain's wetness, which instead impacts the interference fringes, as shown next. The achievable R_{max} spans from about 3.8 km to 6.5 km, depending on the *SF*. For instance, by increasing *SF* from 7 to 12, the predicted R_{max} for $H = 50$ m lengthens from 2 km to 3 km. Focused coverage maps for $R \leq 500$ m, wherein the interference pattern is highly variable, are depicted in Fig. 6.12(b,c). The RSS is not monotonically related to the Tx-Rx distance, even in the ideal free-space case. The nulls in the RSS patterns are sharp due to the strong interference, especially for short horizontal distances. Regarding the ground's condition, the wetter the terrain is, the stronger the reflected field is and, consequently, the more relevant the fluctuations are. An example of RSS profiles due to different terrain's wetness is shown in Fig. 6.13. When comparing Fig. 6.13(a) with Fig. 6.13(b), it is evident that the fluctuations can be restricted to shorter distances R by lowering H. In particular, for $H = 15$ m, the interference fringes are restricted to $R < 100$ m.

In the case of a lying user, the multi-path is absent so that the RSS decreases monotonically with the Tx-Rx distance (Fig. 6.14). Unlike the previous case, the wetness of the terrain has a significant impact on the maximum range, especially for high *SF* values. Indeed, if the wearer is lying on the ground, the on-helmet antenna's gain improves with the terrain wetness of 2 dB (as in Table 6.2), at most, leading to a 21% higher radio range. The maximum communication range is up to 9.5 km if the terrain is wet, and hence it is more extended than the corresponding distance in the case of a standing user.

6.2.4 Experimental Corroboration

The above numerical achievements are corroborated by preliminary experimentation with a UAV equipped with a LoRa receiver and a typical mountain helmet embedding a transmitter to reproduce the simulated scenarios. Both vertical and horizontal flights are performed to verify the model's prediction.

The input parameter of the helmet-mounted dipole is measured by a portable Vector Network Analyzer (MS2024A by Anritsu) when the volunteer is standing and lying over dry and wet terrains. Overall, despite some frequency shift between standing and fallen positions w.r.t. the nominal LoRa band, as predicted by the simulations (Fig. 6.3), the
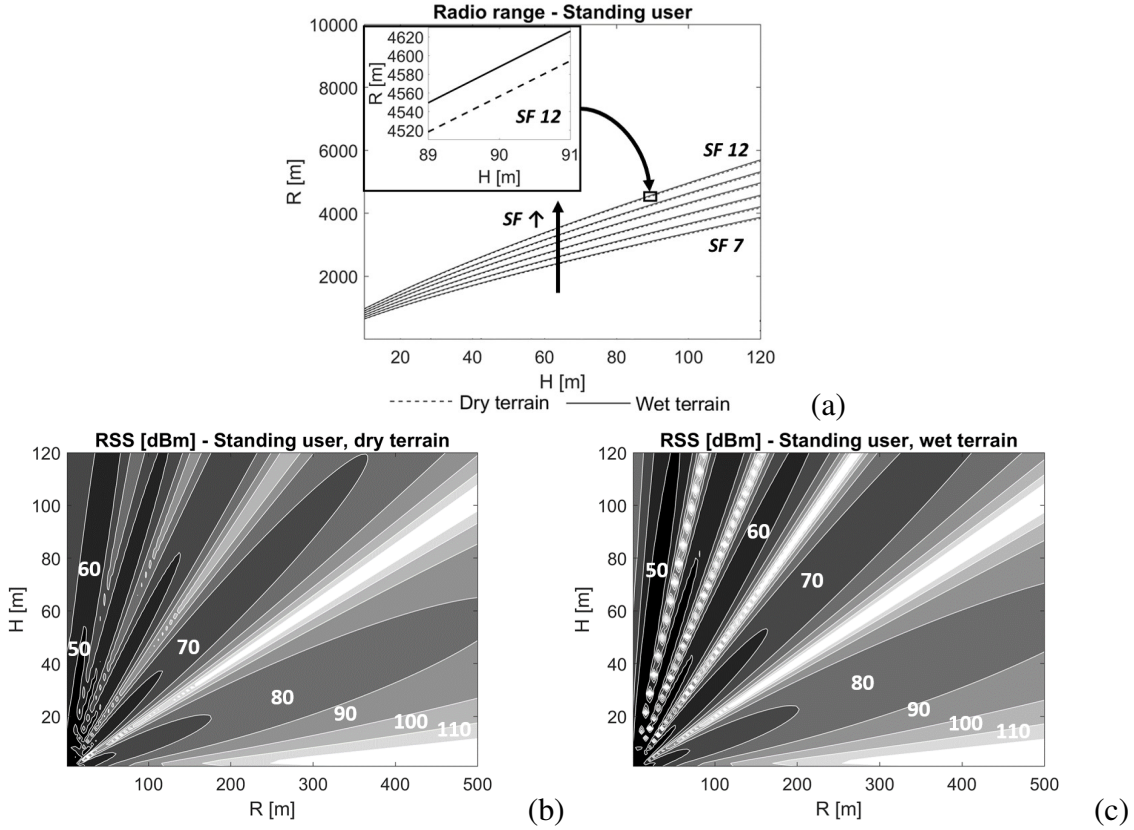
Figure 6.12: Theoretical coverage maps of the LoRa transmitting radio-helmet and the UAV receiver in the standing user case for different flying heights *H* and radial distances *R*. (a) Maximum communication distances versus the UAV height when varying the *SF* value in case of dry and wet terrain. RSS for $R \leq 500$ m in case of (b) dry terrain and (c) wet terrain.
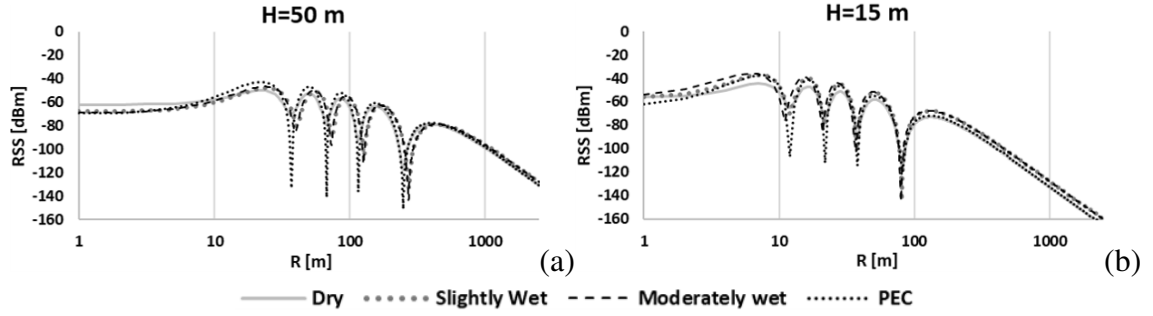
Figure 6.13: Numerically evaluated RSS for $1 \text{ m} \leq R \leq 2500 \text{ m}$ and different terrain's wetness. The assumed intermediate permittivities are $\varepsilon_0 (15 - 0.4j)$ for a slightly wet terrain and $\varepsilon_0 (30 - 0.4j)$ for a moderately wet terrain [217]. Two different flying altitudes are considered (a) $H = 50 \text{ m}$ and (b) $H = 15 \text{ m}$.
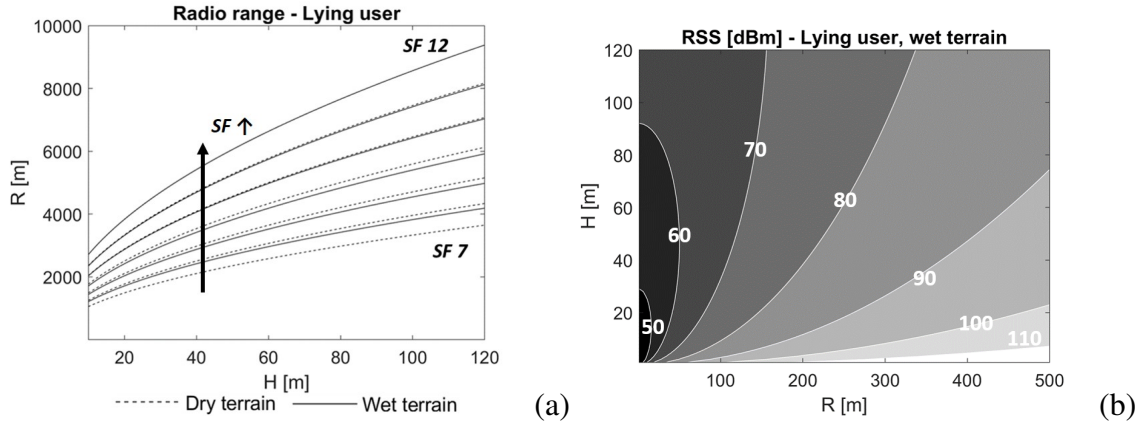
Figure 6.14: Theoretical coverage maps of the LoRa transmitting radio-helmet and the UAV receiver in the lying user case. (a) Maximum communication distances versus the UAV height when varying the *SF* value and (b) RSS for $R \leq 500 \text{ m}$ (wet terrain).

161

Measured Γ_T - Commercial coronal dipole
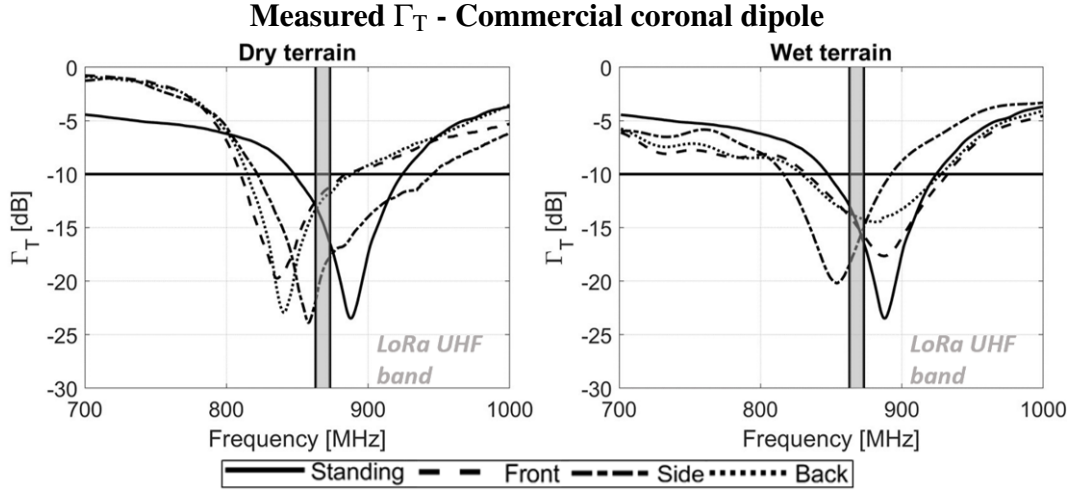
Figure 6.15: The measured reflection coefficient of the coronal dipole installed over the helmet when the wearer is standing and then lying on dry or wet terrain in the three postures.

obtained reflection coefficient (Fig. 6.15) is always $\Gamma_T < 11$ dB at the LoRa upper UHF frequencies, and it is well comparable with the simulated τ_T value in Table 6.4. The maximum observed downward frequency shift is about 55 MHz over all the conditions, so the helmet antenna must thus ensure a frequency bandwidth of at least 65 MHz to cover the whole UHF LoRa band regardless of the wearer's posture.

The RSS measurements are performed during a period of consecutive sunny days over an uncultivated field near Colle Romito whose GPS coordinates are (41.551526, 12.567001) [Ardea, Lazio, Italy; Fig. 6.16(a)]. The field is flat [Fig. 6.16(b)] and covered by bushes. Thus, the test field can be considered dry ground. In the experiments, the UAV is driven at 1 m/s approximate speed along both horizontal trajectories at fixed altitudes and vertical trajectories at a fixed radial distance from the user. The RSS in the dBm scale is estimated from the RSSI (received signal strength indicator) and from the SNR (signal-to-noise ratio) that are returned by the receiver, as

$$P_R = RSSI - 10\log_{10}\left(1 + \frac{1}{SNR}\right) + c_0, \tag{6.18}$$

162
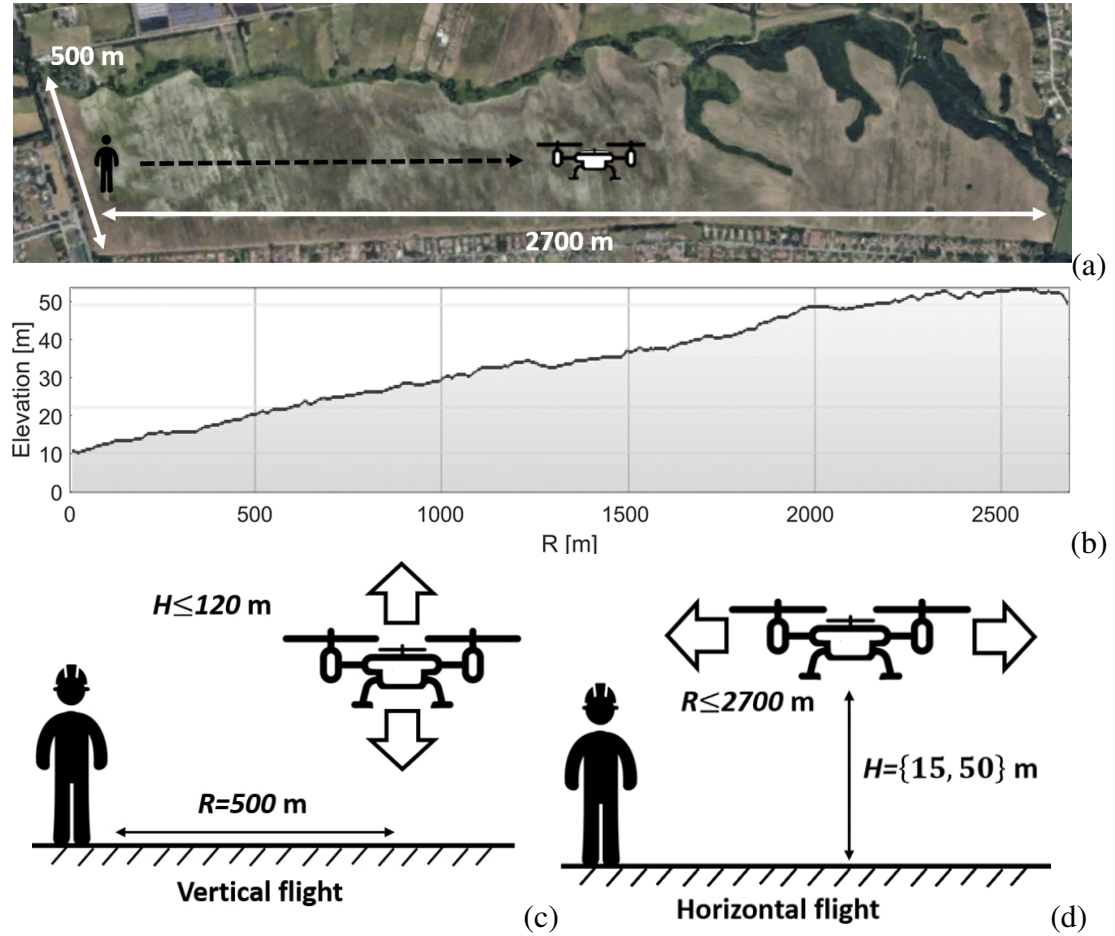
Figure 6.16: (a) Satellite view of the location for the experimental helmet-UAV LoRa link measurement, (b) elevation profile of the field, (c) sketch of the vertical flights, and (d) of the horizontal flights.

where P_R is in dBm scale, the RSSI is in dB scale, the SNR is in linear scale, and c_0 (dBm scale) is a constant parameter obtained from a single-point calibration [213] through the Anritsu MS2711A spectrum analyzer by comparing the measured signal power with the theoretical one at a given distance. The calibration procedure for obtaining c_0 consisted in comparing the measured and numerically-evaluated P_R at a given distance (10 cm) while using the same antennas as in the measurements and the simulations; the difference between measurement and simulations is attributed to losses (cables, nonlinearities...) and it is accounted for by the value c_0. Although the differences between measurements and simulations are not a simple offset, the observed value $c_o = 22.6$ dBm account for most of the effects satisfactorily.

In the first test, the UAV takes off at a distance $R = 500$ m from the volunteer and then flies up vertically up to $H = 120$ m [Fig. 6.16(c)]. In the second test, the UAV flies horizontally at two fixed altitudes $H = \{50 \text{ m}, 15 \text{ m}\}$ for distances $1 \text{ m} \leq R \leq 2700 \text{ m}$ [Fig. 6.16(d)]. During the flights, 1921 data packets are received overall.

The measured RSS profiles are reported in Fig. 6.17 and Fig. 6.18 and compared with the simulated ones for vertical and horizontal flights, respectively. The simulated RSS is computed numerically through (6.14). Interestingly, the RSS is rather insensitive to the lying user's particular position, and the modeling through a numerically evaluated equivalent gain is proven to be effective.

Overall, in spite of some differences, the measurements corroborate the phenomena derived by the numerical model described in this Section (Fig. 6.12 and Fig. 6.14), even in the presence of the significant multi-path in the standing configuration. In detail, simulations overestimate the RSS of just 2 dB on the vertical and horizontal paths shown in Fig. 6.17 and Fig. 6.18(a,b,d). Regarding Fig. 6.18(c), there are some differences with the simulations at the end of the profile, where the model underestimates the RSS. The measured profile follows the flat-earth two-ray model for $R \leq 700$ m but, afterwards, it shows an intermediate behavior between the two-ray and the single-ray propagation. In this condition, the incident rays intercept the ground at grazing angles ($\varphi \leq 1.4^o$) so that slight surface irregularities are no longer negligible [214]. Moreover, the combined effect of the absorption by the low vegetation, scattering, and the earth elevation [Fig. 6.16(b)] can attenuate further the reflected field. The result is a weaker interference and, consequently, a lengthening of

164
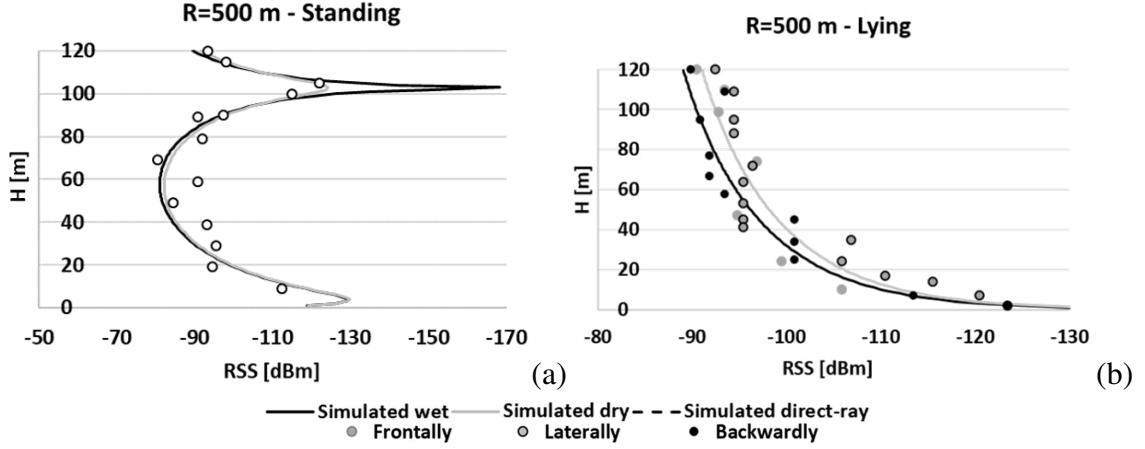
Vertical flights

Figure 6.17: RSS measured by the on-UAV LoRa ($SF = 12$) receiver during the vertical flights at fixed ground distance $R = 500$ m from the transmitter. Measurements for a (a) standing user and (b) lying user.

the link range, benefiting the target identification from long distances. Lastly, the packets having RSS lower than the nominal receiver sensitivity are caused by nonlinear effects of the board that alter the RSSI and the SNR registered by the board.

The Tx-Rx distance slightly affects also the time delay between the transmission and the reception of the packets. In the performed flights, the measured delay ranges between 820 ms (at the shortest helmet-UAV mutual distance) up to 1022 ms (upper bound distance) and is comparable with the values reported in [218]. By considering the typical packet transmission rate (roughly 1 packet every 3 s), the above delays will not cause any loss of the received packet sequence. Accordingly, the observed packet delivery ratio (PDR) in the experiments is of the order of 95% and nearly constant in all the cases. In more complex environments with non-flat grounds, the soft degradation of the LoRa signals will lead to reduced radio ranges with the corresponding decrease of the PDR [219]. Concerning the implications on localization, the time delay could slightly raise the localization errors, especially if the target is moving. In SaR operations, however, the transmitter is mostly stationary since the wearer could be fallen or at most slowly moving within a confined area. The corresponding error in estimating the position of the target is therefore expected

Horizontal flights
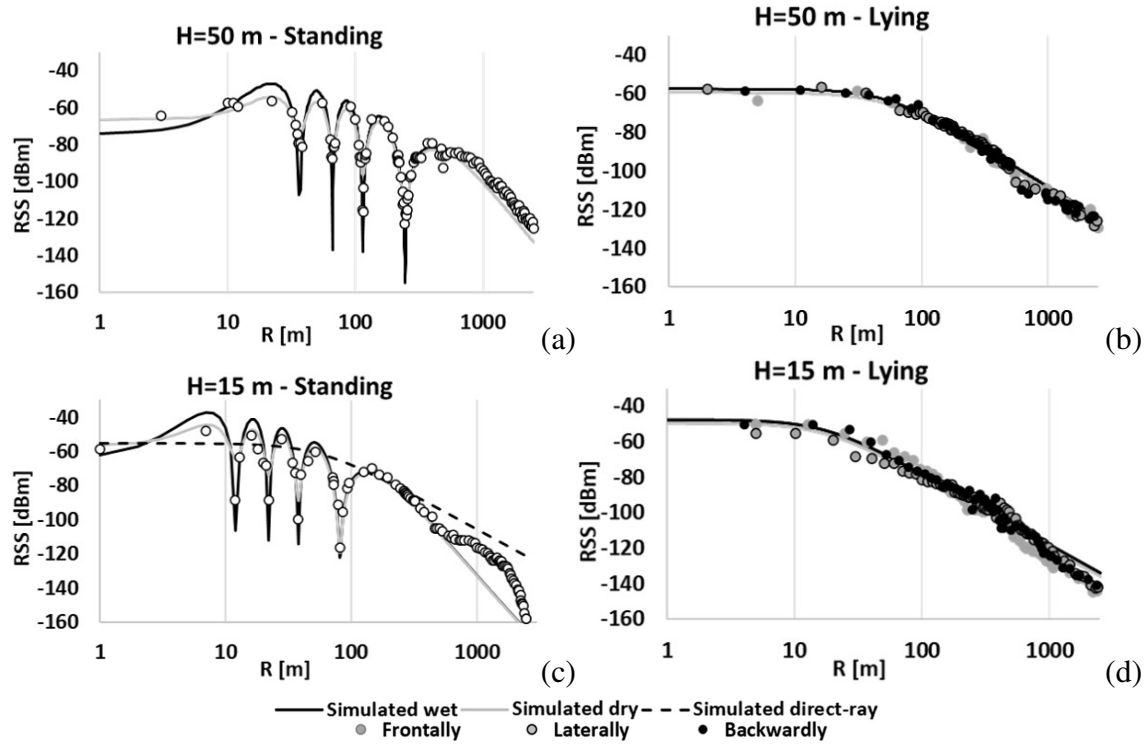
Figure 6.18: RSS measured by the on-UAV LoRa ($SF = 12$) receiver during the horizontal flights at different fixed flying heights H and for different user positions: (a) $H = 50$ m, standing user, (b) $H = 50$ m, lying user, (c) $H = 15$ m, standing user, and (d) $H = 15$ m, lying user.

to be modest. Furthermore, the UAV will generally get closer and closer to the target during SaR procedures so that the time delay reduces, the PDR increases, and the estimation of the target position is progressively refined.

It is worth specifying that, due to hardware constraints and law regulations, the above experimental tests did not allow us to appreciate the complete communication range corresponding to the last received packet. For this purpose, the UAV should have flown up to a much longer horizontal distance ($R > 2700$ m), thus exiting from the test area and over-flying various obstacles (houses, roads, woods). Anyway, the maximum achieved communications of 8.4 km measured in 5.1.1 is in reasonable agreement with the numerical estimations.

6.3 Body-to-UAV links in Mountain Environments

The basic model described in the previous Section can be extended to a more complex radio propagation environment, including non-LoS links. The extension can be quickly drawn if an equivalent log-distance PL model is available by inserting the path loss model and the eventual path-gain factor in the proposed link budget appropriately. However, no empirical model apt to extend the link budget to common mountain SaR scenarios exists in the literature.

6.3.1 Area of Interest: Elevation Profile and Seasonal Variations

The Area of Interest (AoI) selected to analyze the body-UAV links is the same Bletter-bach canyon (Fig. 6.19) used to derive the mountain canyon empirical PL model (Sub-subsection 5.3.1). The GEOPARC Bletterbach is an extremely relevant scenario for mountain SaR since it is one of the Dolomites UNESCO parks and receives $60,000$ tourist visits every year, that are attracted by the geological formations and spectacular landscapes. The AoI undergoes significant seasonal variations since the canyon's walls become covered by ice in the winter season (Fig. 6.20), and is characterized by a complex orography ranging between $1,474$ m and $1,618$ m [Fig. 6.21(a)].
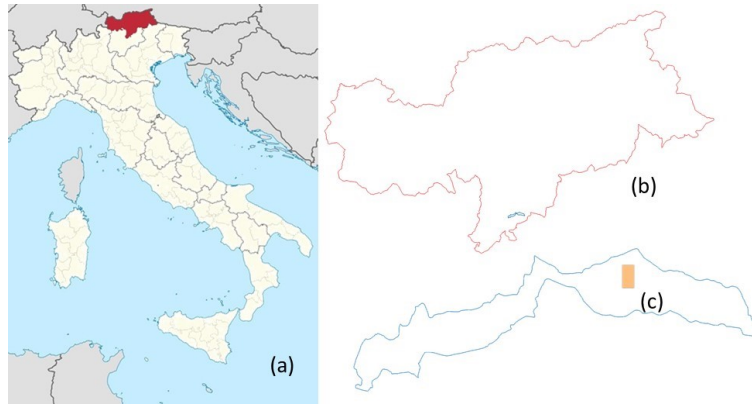
Figure 6.19: Location of the AoI. (a) South Tyrol Province, Italy. (b) Location of the GEOPARC Bletterbach in the municipality of Aldein. (c) AoI highlighted in orange,

Figure 6.20: The Bletterbach canyon in the (a) summer, and (b) winter season.
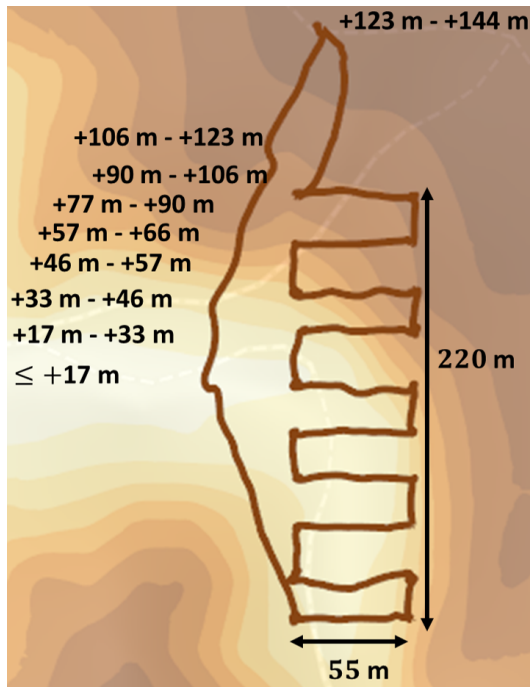
Figure 6.21: (a) The elevation map of the AoI and the flying path employed to characterize the excessive aerial PL. (b) (b) Measurement points P1-P20 in the Bletterbach canyon as registered by the GNSS on-board the Soleon octocopter. The position of the transmitter is also reported.

Figure 6.22: Prototype B at the starting point (near to P20) outside the canyon gorge during the winter campaign.

To experimentally characterize the signal PL, the flying path in Fig. 6.21 is employed where the Soleon octocopter (Prototype B) hovers for a given time in the measurement points P1-P20 [Fig. 6.21(b)], as detailed in the next Sub-subsection. The AoI includes areas over and outside the canyon to assess the signal propagation also in absence of the waveguide effect typical of the in-canyon terrestrial links (Sub-subsection 5.3.1) and the reception of the signal from outside the canyon (Fig. 6.22).

6.3.2 Measurement Campaign and Empirical Model

With reference to Fig. 6.23, the instantaneous ground-to-air PL for low-altitude UAVs can be described through an *angle-based model* as a function of the transmitter-receiver ground distance d and the depression angle θ. Accordingly, the mean terrestrial path loss $PL_{Ter}(d)$
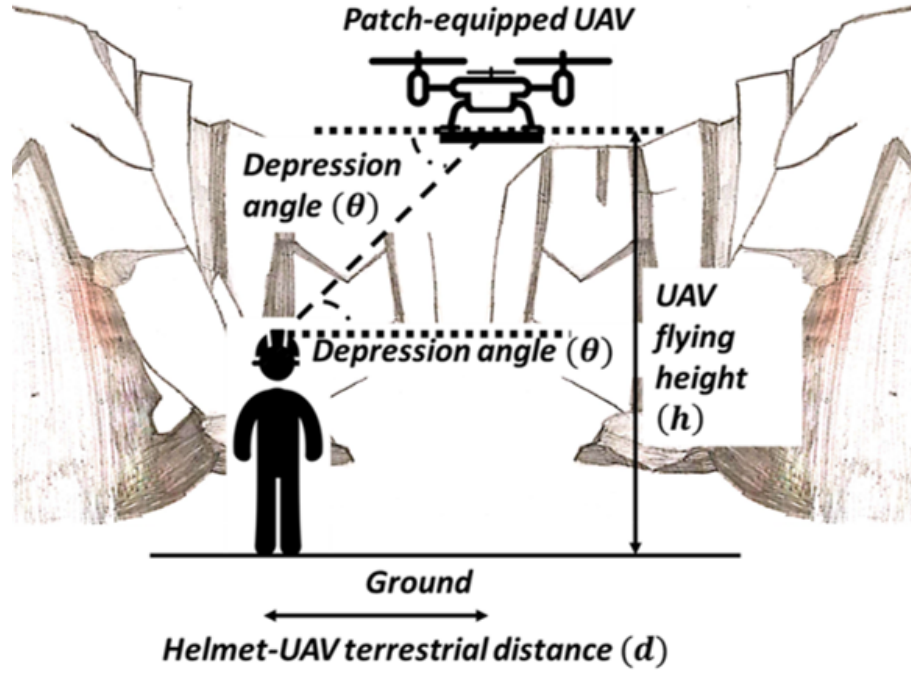
Figure 6.23: Sketch of the radiohelmet-UAV links in a mountain canyon.

is corrected by adding the *excessive aerial PL* $\eta(\theta)$ so that the actual path attenuation $PL(d, \theta)$ is written as [220]

$$PL(d, \theta) = PL_{Ter}(d) + \eta(\theta) + X(\theta) \qquad (6.19)$$

where $X(\theta)$ accounts for the difference between the instantaneous and the mean PL. The terrestrial PL follows the typical narrowband log-distance PL model [221], whereas the excessive aerial PL is an angle-dependent function [220]

$$\eta(\theta) = \eta_0 + A(\theta - \theta_0) \exp\left(-\frac{\theta - \theta_0}{B}\right) \qquad (6.20)$$

where η_0 is the excess PL offset, A is the excess PL scaler, θ_0 is the angle offset, and B is the angle scaler. Finally, $X(\theta)$ can be expressed as the sum of the large-scale fluctuations observed over ten wavelengths or more and the small-scales fluctuations observed over few units of wavelength [221]. The large-scale PL fluctuations are modeled as shadow
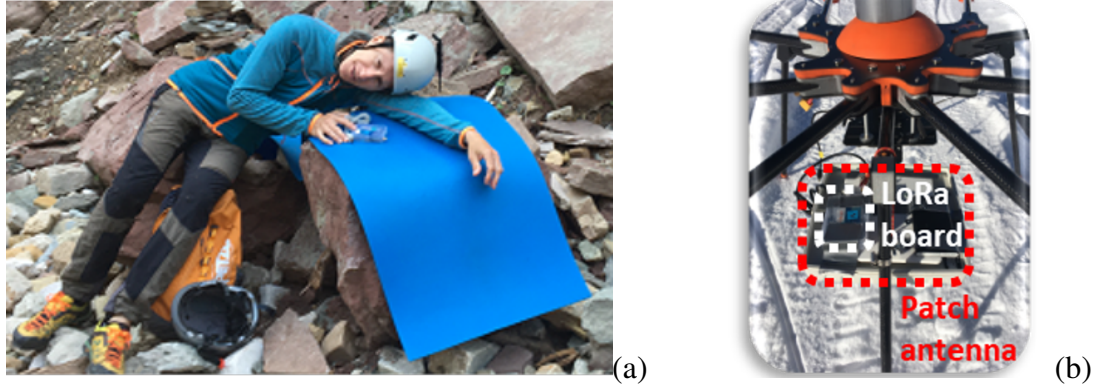
Figure 6.24: (a) Radiohelmet wearer lying on a rock during the spring campaign. (b) LoRa receiving radio mounted on the Soleon octocopter in the Prototype B of the antenna system.

fading [184], which is a zero-mean Gaussian random variable having an angle-dependent standard deviation in ground-UAV links [220]. Instead, the small-scale fading can produce unpredictable variations of the RSS up to 40 dB [221]. Then,

$$X(\theta) = \mathcal{N}(0, a\theta + \sigma_0) + f_{sc}, \tag{6.21}$$

where a (the UAV shadowing slope) and σ_0 (the UAV shadowing offset) are fitting parameters, and f_{sc} symbolizes the small-scale fading. During the measurement campaign, the LoRa-broadcasting radiohelmet with the coronal dipole is worn by a volunteer lying on a rock, emulating the lying target to be localized (Fig. 6.3.2). The PL evaluation is performed as described in Sub-subsection 6.2.4.

Ten packets per measurement point P1-P20 are collected so that the PL is evaluated in each point as the average over the ten packets, and the small-scale fading term is reduced by the averaging [221]. The flying height from the ground of the UAV is kept constant to $h = 20$ m. To assess any major effect on the LoRa propagation caused by the seasonally frozen canyon's walls, the measurements were performed on two different seasons: winter (on the 21st of January) and spring (on the 15th of June) 2021.

As shown in Fig. 6.25, the PL measured in winter and spring are very similar, and the effects of the canyon's walls covered by ice are negligible. No packet is received if the UAV flies relatively far from the canyon due to the canyon's waveguiding effect so that no RSS is
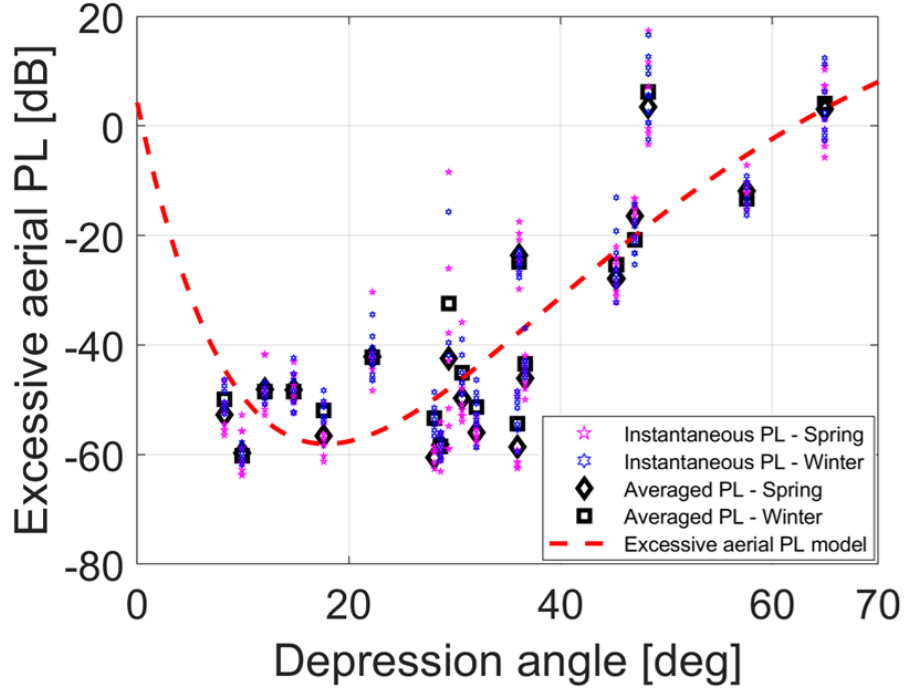
Figure 6.25: Excessive aerial PL model for ground-to-UAV LoRa links in the mountain canyon.

measured at the position P20. Instead, the broadcasted LoRa packets are still received at the points P13-P19 thanks to the UAV flying height, which establishes unobstructed ray-paths. Considering the model geometry (Fig. 6.23), the excess aerial PL model is constrained to be null for $\theta = 0$ rad. The overall PL model's parameters are resumed in Table 6.5, where the terrestrial PL model for the mountain canyon is the Bletterbach model for LoRa exposed in Chapter 5. The statistical validity of the model is verified by evaluating the relative standard error of the mean (RSE) for every bin as [220]

$$RSE_{\hat{\eta}}(\theta) = X(\theta) \left[\sqrt{M(\theta)} \hat{\eta}(\theta) \right]^{-1} \tag{6.22}$$

where $M\left(\overline{\theta}\right)$ is the number of samples collected at the depression angle $\overline{\theta}$, whereas $\hat{\eta}\left(\overline{\theta}\right)$ is the measured instantaneous PL at $\overline{\theta}$. The average evaluated $RSE_{\hat{\eta}}(\theta)$ is less than 4.8%, proving the validity of the sample size.

Table 6.5: PL Model Parameters.

Parameter	Symbol	Value
Reference distance	d_0	1 m
Terrestrial path loss intercept	$PL(d_0)$	0.9 dB
Terrestrial path loss exponent	γ	5.51
Excess aerial path loss offset	η_0	33.92 dB
Excess aerial path loss scaler	A	-12.12 dB
Angle offset	θ_0	-2.8 deg
Angle scaler	B	20.63 deg
UAV shadowing slope	a	0.005 dB/deg
UAV shadowing offset	σ_0	1.55 dB

6.4   Conclusion

The off-body links from a body-worn LoRa beacon to a receiving UAV are experimentally characterized in this Chapter by means of deterministic and statistical models. The investigated system is composed of an on-helmet dipole and a CP patch mounted on the UAV, which is modelled through a new gain approximation derived from the literature. In the simplest cases, namely, on flat-land in LoS conditions, the body-UAV link is a free-space link eventually affected by the ground-bounce multi-path. In more complex environments, as in the mountain canyon case, the PL model is angular-dependent. Therefore, a log-distance model similar to the terrestrial one is achieved only in the case of a lying user on flat land, which is the simplest case albeit an important one. In the other cases, the localization through the RSS measured by the UAV is expected to be way more complex since the model is also dependent on the UAV flying height in an angular way.

The body-UAV links are heavily dependent on the body posture, even more than the terrestrial ones because of the eventual ground-bounce multi-path. However, the envisaged wearers' positions can be effectively accounted for by numerical and statistical analyses. Differently from the terrestrial link case, the body shadowing is always avoided in the body-UAV links thanks to the position of the antenna on the helmet, which allows fully exploiting the LoS improvement given by the flying height of the UAV.

Chapter 7

Signal-based Localization of On-body LoRa Transmitters for Mountain SaR

The on-body LoRa transmitter localization by the off-body EM signal would be extremely useful in SaR operations. In this Chapter, a suitable localization algorithm for mountain SaR is designed based on the analyses of the wearable radio and the radiowave propagation exposed in Chapters 5 and 6. In Appendix D, there is an overview on the basics of the signal-based localization from which the following work starts.

The localization through LoRa signals is reviewed (Section 7.1). Based on the existing works and their limitations, a new algorithm is developed and detailed in Section 7.2, and its application to the mountain SaR is detailed in Section 7.3 through a high-level system design.

7.1 Range-based Localization through LoRa(WAN) RSS

LoRa(WAN) was proposed for wireless localization systems both when used with satellite positioning systems [222, 223] and signal-based localization algorithms [224, 223], especially by fingerprint [225, 226, 227, 228, 229]. The SoA of the RSS-based LoRa localization is of interest to draw the current achievements and limits.

In [230] four RSS localization algorithm are employed in both indoor and outdoor scenarios. The algorithm combines the RSS obtained when different LoRa transmission

parameters are used. The work approximates the RSS with the RSSI and neglects the SNR. The performance enhancement observed when considering the different transmission parameters (the RMSE hoes down to the 16 % its original value) confirms that the SF has a major impact on the returned RSSI. Particular caution has to be posed when localizing a signal source exploiting multiple SF therefore.

Lam *et al.* investigated various clustering methods to identify and discard bad nodes [231, 232, 233]. In [231] two RSS-UDPG algorithms assuming $PL(d_0)$ known and discarding the nosiest anchor point are described and tested. The algorithms are further studied and refined in [232] so to reduce the localization error. In [233] three different RSS-based localization algorithms are proposed and tested. The researchers do not investigate the effects of the PLE nor the noise since they focus on identifying and discarding measurements that carry more noise than information.

A DRSS approach is experimented in [187] wherein different algorithms are experimented through simulated data generated from an experimental log-distance PL model. The DRSS performs similarly to the RSS with known and unknown PL. However, due to the significant RSSI fluctuations, the LoRa technology is outperformed by the BLE.

Table 7.1 resumes the performances of the proposed algorithms according to the key performance indicators of RSS-based localization algorithms. Overall, the literature on the RSS range-based LoRa localization is still in its infancy.

7.2 Grid-based RSS-UDPG Localization Algorithm

From Section 7.1, the following critical points to be overcome are evident.

1. All the works using LoRa neglect the SNR, whereas in mountain environments the measured SNR are significant and even lower than -6 dB at short distances, i.e. about 50 meters.

2. Typical methods to solve the RSS-UDPG are based on nonlinear methods which could not converge to a good estimate in very noisy environments [234, 235] like the characterized mountain scenarios .

Table 7.1: Performances of the experimented signal-based localization algorithm employing LoRa in the literature. When a data is not reported, a backslash is used instead.

Reference	Technique	PLE, measurement number and shadowing	Test area	Mean absolute localization error [m]
[230] (indoor)	RSS-UDPG	$n = \backslash$; $M = 7$; $\sigma_F^2 = \backslash$	37 m × 1 m	∼ 10 m
[230] (outdoor)	RSS-UDPG	$n = \backslash$; $M = 7$; $\sigma_F^2 = \backslash$	3217 m × 1 m	∼ 500 m
[231]	RSS-UDPG	$n = \backslash$; $M = 6$; $\sigma_F^2 = \backslash$	110 m × 64 m	∼ 14 m
[232]	RSS-UDPG	$n = \backslash$; $M = 8$; $\sigma_F^2 = \backslash$	100 m × 100 m	7.5 m
[233]	RSS-UDPG	$n = \backslash$; $M = 6$; $\sigma_F^2 = \backslash$	36 m × 36 m	∼ 10 m
[187]	DRSS, RSS, RSS-UDPG	$n = 1.5$; $M = 6$; $\sigma_F^2 = 36$ dB	69 m × 69 m	∼ 20 m

3. Every RSS-UDPG algorithm assumes a single-slope log-distance model. However, the unpredictable conditions (environment, Tx-Rx angle) could make this assumption not valid [236, 237] hence hindering the localization [238, 239].

Therefore, a new RSS-UDPG algorithm has to be developed to remedy these shortcomings. The algorithm must be able to handle scenarios characterized by multi-slope and/or angular-dependent log-distance PL model.

7.2.1 Grid-based Exhaustive Search Algorithm through PL

The packets having very low SNR values can be accounted for by using the PL measurements to localize the target, whereas nonlinear optimization can be avoided with exhaustive searches. Moreover, complicated multi-slope [240, 241, 242, 243, 244] and/or angular-dependent [245] models can be managed by opportunely partitioning the dataset based on the critical distances $d^{(c)}$ and/or the critical angles $\delta^{(c)}$ so that all and only the measurements corresponding to a given slope are included in the given subset. However, this is possible only if the position of the transmitter is known. A spatial grid superimposed over the search area can be used, as detailed next. After the dataset partition, the minimization of a linear least square cost function can allow estimating the PL of the subset. Even though we analyze only the bidimensional case, the localization procedure can be extended to tridimensional coordinates straightforwardly.

7.2.1.1 Grid-based Exhaustive Search

According to the above reasoning, the localization can be resolved as described in this Sub-subsection. Let us indicate with (x_T, y_T) the unknown position of the transmitter, and assume M PL measurements are taken over the entire area. For each PL measurement, the position of the respective anchor $P_R = \{(x_m, y_m)\}$, $m = 1, \ldots, M$, is known. The PL measurements can be used to estimate the parameters of the mean PL model characterizing the search area's radio propagation and the transmitter's position by minimizing the following weighted least square (WLS) function

178

$$\varepsilon\left(\{L_k\}_{k=1}^K, \{\gamma_k\}_{k=1}^K, \{d_k^{(c)}\}_{k=1}^K, x_T, y_T\right) =$$

$$\sum_{k=1}^{K}\sum_{n=1}^{N_k} w_{kn}\left|\overline{PL}_{kn} - L_k - 10\gamma_k \log_{10}(d_{kn})\right|^2, \tag{7.1}$$

where w_{kn} is the weight of the $\overline{PL}_{kn}$ measure, N_k is the cardinality of the k-th subset, $k = 1, \ldots, K$ of PL measurements in P_R, including the PL values $\overline{PL}_{kn}$ in P_R such that the distance d_{kn} between the receiver and the transmitter is $d_k^{(c)} \leq d_{kn} < d_{k+1}^{(c)}$ for $n = 1, 2, \ldots, N_k$. The weights w_{kn} allow accounting for the quality of the PL measurements in the dataset [231, 232, 233]. We have $M = N_1 + N_2 + \ldots + N_K$, and the partitioning of the M PL measurements into the K subsets to be used in (7.1) varies each time with the assumed transmitter's position.

The cost function (7.1) is a generalization of that in [234], therefore it is non-convex and has multiple local minima. However, it can become convex with respect to γ_k and L_k, $k = 1, \ldots, K$, when fixing the (x_T, y_T) pair. To minimize (7.1) for fixed K and assigned critical distances $d_k^{(c)}$, we first need to partition the available set of M measurements into the K subsets $\{\overline{PL}_{kn}\}$, $n = 1, \ldots, N_k$, $k = 1, \ldots, K$. For this purpose, we start by fixing the position (x_T, y_T) of the transmitter and then evaluate the set of distances $\{d_{mT}\}$, $m = 1, \ldots, M$ between the M measurements points and the assumed transmitter's position. The m-th PL measurement is assigned to the k-th subset if $d_k^{(c)} \leq d_{mT} < d_{k+1}^{(c)}$. At the end of the partitioning process, we reindex with d_{kn} the N_k receivers' distances whose PL measurements have been included in the k-th subset following the previous criterion.

For the given (x_T, y_T) and the corresponding partition of the PL measurements, from (7.1), it can be observed that the optimal values of $\{L_k\}_{k=1}^K$ and the PLEs $\{\gamma_k\}_{k=1}^K$ can be determined in closed-form by solving the following K separated linear systems with two equations

$$\frac{\partial \varepsilon}{\partial L_k} = -2\sum_{k=1}^{K}\sum_{n=1}^{N_k} w_{kn}\left(\overline{PL}_{kn} - L_k - 10\gamma_k \log_{10}(d_{kn})\right) = 0 \tag{7.2}$$

and

$$\frac{\partial \varepsilon}{\partial \gamma} = -20 \sum_{k=1}^{K} \sum_{n=1}^{N_k} w_{kn} \left(\overline{PL}_{kn} - L_k - 10\gamma_k \log_{10}(d_{kn}) \right) \log_{10}(d_{kn}) = 0. \tag{7.3}$$

Then, K system with two equations and variable can be written. When all the measurements are equally weighted, the system can be written as

$$\begin{cases} L_k N_k + 10\gamma_k \sum_{n=1}^{N_k} \log_{10}(d_{kn}) = \sum_{n=1}^{N_k} \overline{PL}_{kn} \\ L_k \sum_{n=1}^{N_k} \log_{10}(d_{kn}) + 10\gamma_k \sum_{n=1}^{N_k} \left(\log_{10}(d_{kn}) \right)^2 = \\ \qquad \sum_{n=1}^{N_k} \overline{PL}_{kn} \log_{10}(d_{kn}), \quad k = 1, \dots, K \end{cases} \tag{7.4}$$

where $d_{kn} = \sqrt{(x_{kn} - x_T)^2 + (y_{kn} - y_T)^2}$, $n = 1, \dots, N_k$. Solving the system, we obtain that for each k, $k = 1, \dots, K$, the corresponding L_k and γ_k are evaluated as

$$\hat{L}_k = \frac{\sum_{n=1}^{N_k} w_{kn} \overline{PL}_{kn} - 10\hat{\gamma}_k \sum_{n=1}^{N_k} w_{kn} \log_{10}(d_{kn})}{\sum_{n=1}^{N_k} w_{kn}} \tag{7.5}$$

and

$$\hat{\gamma}_k = \frac{\sum_{m=1}^{N_k} w_{km} \sum_{n=1}^{N_k} w_{kn} \overline{PL}_{kn} \log_{10}(d_{nk}) - \sum_{m=1}^{N_k} w_{km} \overline{PL}_{km} \sum_{n=1}^{N_k} w_{kn} \log_{10}(d_{kn})}{10 \sum_{m=1}^{N_k} w_{km} \sum_{n=1}^{N_k} w_{kn} \left(\log_{10}(dkn) \right)^2 - 10 \left(\sum_{n=1}^{N_k} w_{kn} \log_{10}(d_{kn}) \right)^2} \tag{7.6}$$

if the measurements are weighted, and

$$L_k = \frac{\sum_{n=1}^{N_k} \overline{PL}_{kn} - 10\gamma_k \sum_{n=1}^{N_k} \log_{10}(d_{kn})}{N_k} \tag{7.7}$$

and

$$\gamma_k = \frac{N_k \sum_{n=1}^{N_k} \overline{PL}_{kn} \log_{10}(d_{kn}) - \sum_{l=1}^{N_k} \overline{PL}_{kl} \sum_{n=1}^{N_k} \log_{10}(d_{kn})}{10 N_k \sum_{n=1}^{N_k} \left(\log_{10}(d_{kn}) \right)^2 - 10 \left(\sum_{n=1}^{N_k} \log_{10}(d_{kn}) \right)^2} \tag{7.8}$$

if they aren't.

180

The K systems (7.4) must not be under-determined, and, in general, the number of available measurements for each one of the K systems needs to be higher than the number of the corresponding PL parameters to evaluate (7.7) and (7.8). In the presence of shadowing, the number of measurements $M \gg 2K + 1$ is required to achieve an accurate estimate of the position.

The previous procedure is based on the implicit knowledge of the transmitter position (x_T, y_T), which is unknown and must be determined to minimize (7.1). Therefore, we assume that (x_T, y_T) can vary over a spatial grid of candidate points, superimposed on the considered area by excluding the eventual positions where the transmitter cannot be. The overall minimization procedure can now be stated as follows, w.r.t. Fig. 7.1:

1. start from M PL measurements taken at known points (x_m, y_m), $m = 1, \ldots, M$ in the area;

2. assign the $K - 1$ critical distances, $d_k^{(c)}$, $k = 2, \ldots, K$;

3. select the candidate point (x_T, y_T) in the grid and evaluate the distances of the anchors d_{mT}, $m = 1, 2, \ldots, M$ from the selected transmitter point in the grid;

4. partition the set of the M PL measurements into the K subsets $\{\overline{PL}_{kn}\}$, $n = 1, \ldots, N_k$ assigning the measure $\overline{PL}_m$ to the k-th subset if the corresponding receiver distance d_{mT} is such that $d_k^{(c)} \leq d_{mT} < d_{k+1}^{(c)}$;

5. for each k, $k = 1, 2, \ldots, K$, calculate L_k and γ_k using (7.7) and (7.8), respectively;

6. evaluate the minimum least square error in (7.1) obtained with the selected (x_T, y_T) and the corresponding L_k and γ_k in (7.7) and (7.8) for $k = 1, \ldots, K$ obtained in the previous step, and store them;

7. repeat the calculation procedure from point 3) by selecting the next candidate transmitter point on the grid until all the points in the grid have been considered;

8. after the examination of all the candidate points, the tuple achieving the minimum least square error in (7.1) provides the best solution for minimizing (7.1).
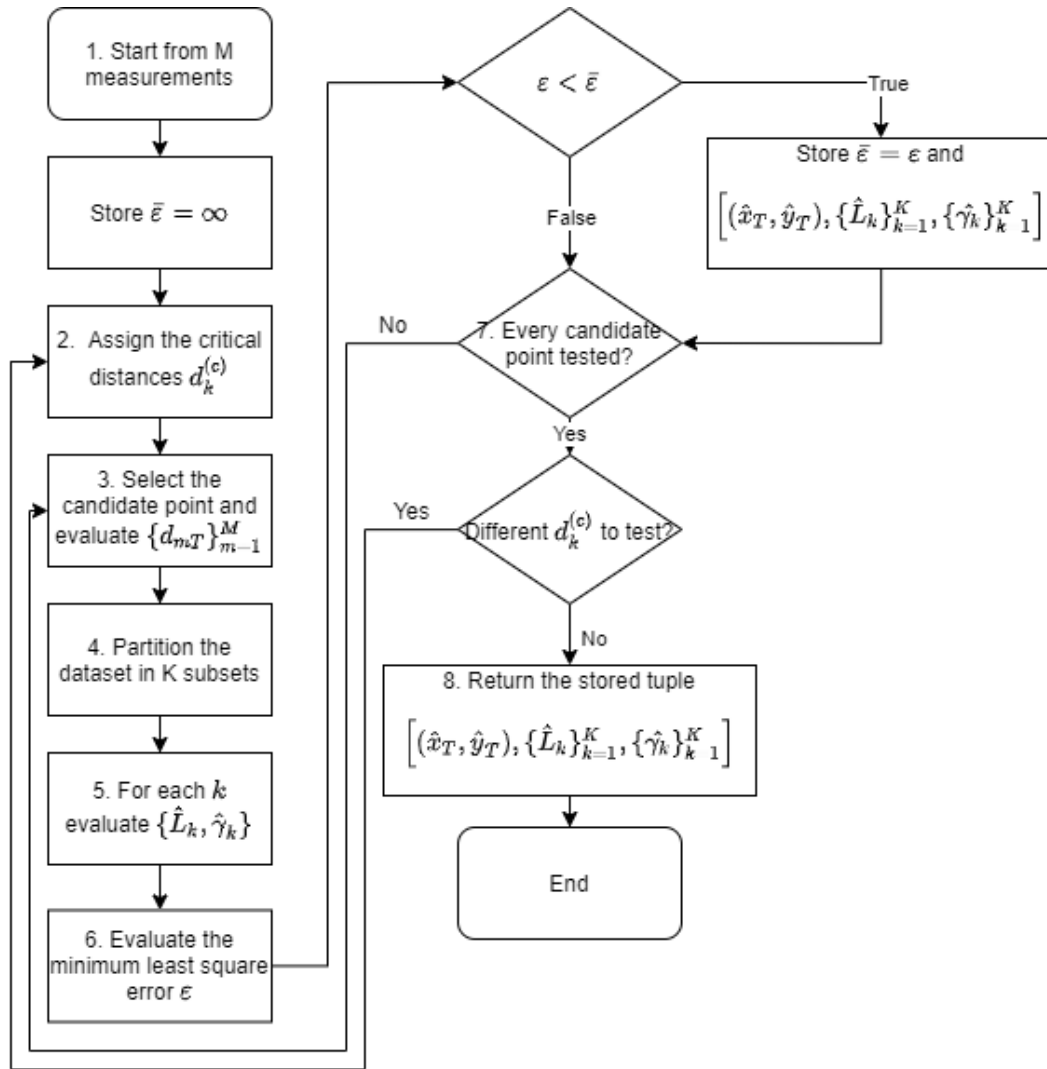
Figure 7.1: Flow chart describing the proposed UDPG-RSS-based localization ESA.

Table 7.2: Terms contributing to the computational complexity.

Operation	Number of Multiplications
$\{\gamma_1, ..., \gamma_K\}$ evaluation	$2M + 7K$
$\{L_1, ..., L_K\}$ evaluation	$3K$
ε evaluation	$4M$
Overall complexity	$\mathscr{O}(Q \cdot n_P \cdot K \cdot M)$

We implicitly assumed the $K - 1$ critical distances $d_k^{(c)}$ and/or angles $\delta_k^{(c)}$ had been set. If $d_k^{(c)}$ are not available, it is possible to repeat the procedure by varying $d_k^{(c)}$ over a set of values. In the more common case when $K = 2$ in multi-slope scenarios, we have one critical distance to determine through this additional exhaustive search. Finally, we select the tuple providing the absolute minimum of (7.1) concerning the configurations of critical distances and/or angles.

7.2.1.2 Computational Complexity of the Algorithm

Let Q be the number of sets of $K - 1$ critical distances and angles to be considered in the position estimation. Let n_P be the number of candidate points on the grid to be analyzed in each algorithm iteration for a given set of critical distances. Calculations from point 3) in Fig. 7.1 are then repeated $Q \times n_P$ times. Accordingly, the evaluation of (7.7), (7.8) and of the corresponding values of the WLS error in (7.1) are carried out $Q \times n_P \times K$ times. In the case of a regular grid of candidate points uniformly spaced by Δ along the x and y axes, the number of grid points can be approximated as $n_P = \lceil A/\Delta^2 \rceil$ where A is the extension of the considered area and $\lceil \cdot \rceil$ is the lowest integer higher than the argument. Thus, in general, the computational complexity of the exposed algorithm is polynomial with the number n_P of candidate points for fixed Q and K. The terms contributing to the computational complexity assuming tabulated logarithms are resumed in Table 7.2.

7.2.2 Hierarchical Search

The computational complexity of the algorithm can be reduced through hierarchical search. Let us consider a regularly spaced grid with points uniformly spaced along the x and y axes
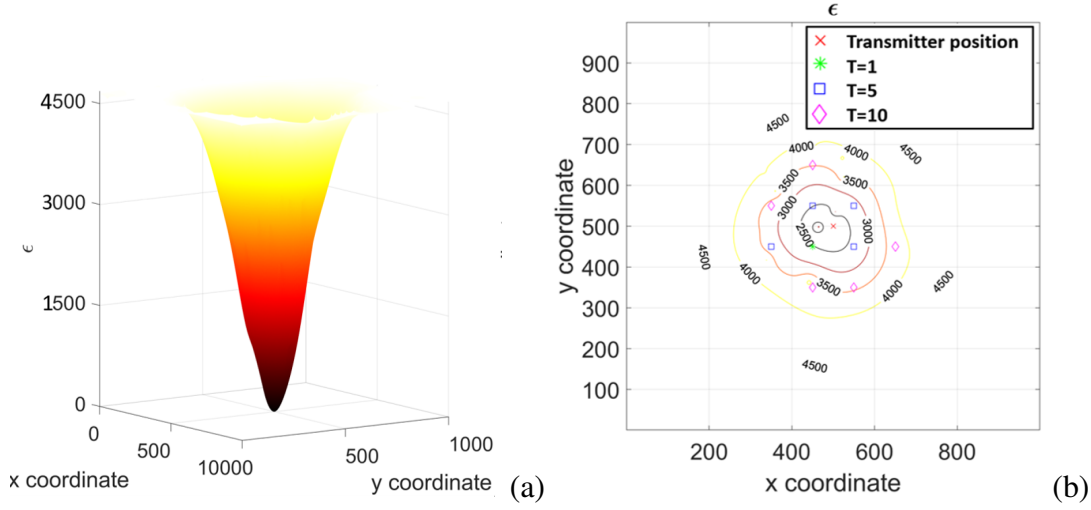
Figure 7.2: (a) Error function ε evaluated from (7.1) when $M = 100$, $\sigma_S^2 = 12$ dB over a 1000 m $\times$1000 m search area (single-slope PL, $\gamma = 2$, $L = 30$ dB), and (b) corresponding contour plot and candidate points when varying T.

by Δ, for a given area A, the total number of points to be tested is

$$n_P = \left\lceil \frac{A}{\Delta^2} \right\rceil. \tag{7.9}$$

The mostly monotonic behavior of (7.1) can be exploited [Fig. 7.2(a)] to reduce the number of candidate points n_P. The search for the best candidate point is carried out with hierarchical search, viz. in a multiple-step search. For the sake of simplicity, we focus on the two-step search since the extension to multiple-steps is straightforward. Accordingly, the procedure starts with a search over a coarse grid with points uniformly spaced with a relatively large step $q\Delta$, where $q > 1$ is an integer. For the same area A, the number of candidate points is now proportional to $A/(q\Delta)^2 < n_P$. After the first search step, we order the WLS errors in (7.1) corresponding to the considered candidate points in ascending order. To start the second search stage, we select the T candidate points achieving the lowest T error values. Then, the search for the best transmitter position proceeds over T smaller grids, each centred around one of the selected T target points [Fig. 7.2(b)]. The spacing of points in these grids is reduced to Δ. For example, considering square grids, we assume each grid extends from $-m\Delta/2$ to $(m-1)\Delta/2$ along the x and y axes, and m is an integer. The value

$m \geq 2q$ is required to not neglect any area's space in the spatial exhaustive search. Now, the second search is carried out over $(m^2 - 1)$ candidate points for each grid. In the exposed two-step hierarchical search, the total number of candidate points can be approximated as

$$\alpha n_P \cong \frac{n_P}{q^2} + (m^2 - 1) \cdot T, \tag{7.10}$$

where $0 < \alpha < 1$.

Even in this simple case with only square grids, the optimal set of parameters (q, m, T) depends on the specific search strategy, on the anchor's topology, on how the grid is superimposed over the search area and on the characteristics of the radio propagation environment. Generally, the lower the α, the higher can be errors caused by the coarse grid step and the possibility of falling in one local minimum. To select the optimal set of parameters, project maps (Fig. 7.3) can be employed. Given a M and an acceptable error value, a satisfying set (m, q, T) is quickly found; such project charts have to be previously drawn through numerical simulations as shown next in this Section.

7.2.3 Cramér-Rao Lower Bound

As detailed above, the CRLB expresses the minimum variance of unbiased estimators of deterministic parameters and it is necessary to assess the algorithm's effectiveness. From the log-distance PL model, the estimator $g_{kn}(\theta)$ can be expressed as

$$g_{kn}(x_n, y_n, \gamma_k, L_k) = L_k + 10\gamma_k \cdot \log_{10}\left(\frac{d_{kn}}{d_0}\right), \tag{7.11}$$

being $\theta = [x, y, \gamma_1, ..., \gamma_K, L_1, ..., L_K]^T$ the unknown parameters vector. From [234], the PL observations $\overline{PL}_{kn}$ have a probability density function

$$f\left(\overline{PL}_{kn}; \theta\right) = \frac{1}{\sqrt{2\pi}\sigma_S} \exp\left\{-\frac{\left(\overline{PL}_{kn} - g_{kn}(\theta)\right)^2}{2\sigma_S^2}\right\}. \tag{7.12}$$
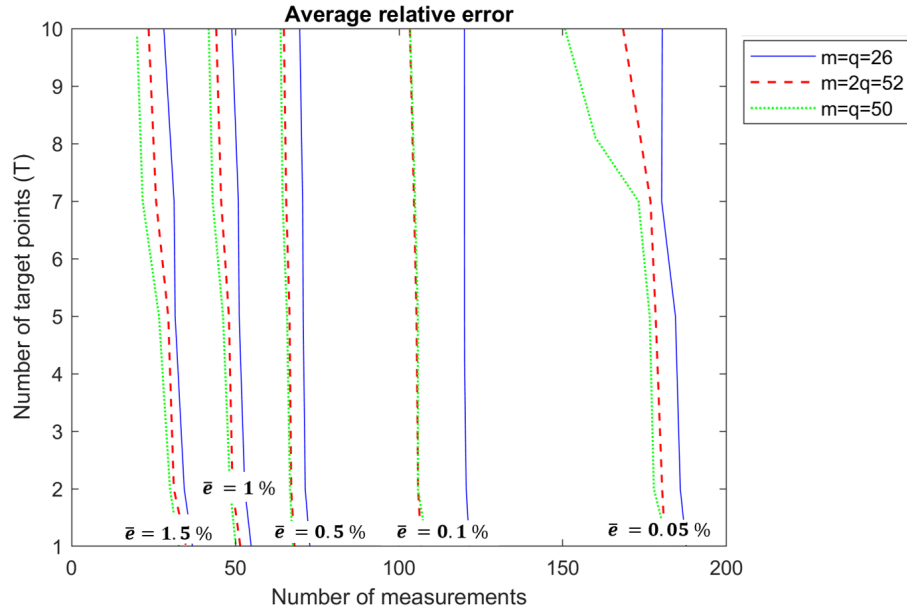
Figure 7.3: Project chart to select the parameters (m, q, T) in a two-step hierarchical search. Single-slope PL model $\gamma = 2$ and $L = 30$ dB. The RMSE is averaged on 1000 distinct anchor's topology generated by Monte-Carlo over a 1000 m$\times$1000 m search area. The RMSE is divided by the area extension so to obtain the relative localization error.

By assuming that the observations are statistically independent, the joint distribution of the observation matrix $\overline{\mathbf{PL}}$ is

$$f\left(\overline{\mathbf{PL}}; \theta\right) = \prod_{k=1}^{K} \prod_{n=1}^{N_k} f\left(\overline{PL}_{kn}; \theta\right). \tag{7.13}$$

where bold symbols denote matrixes. The CRLB is then evaluated from the inverse of the FIM

$$\mathbf{F} = -E\left[\nabla_\theta \left(\nabla_\theta \ln f(\overline{\mathbf{PL}}; \theta)\right)^T\right]. \tag{7.14}$$

Accordingly, the log-likelihood function is

$$l(\theta) = -\frac{1}{2\sigma_S^2} \sum_{k=1}^{K} \sum_{n=1}^{N_k} \left(\overline{PL}_{kn} - g_{kn}(\theta)\right)^2, \tag{7.15}$$

and the FIM can be expressed as

$$[\mathbf{F}]_{ij} = -E\left[\frac{\partial^2 l(\theta)}{\partial \theta_i \partial \theta_j}\right] = \frac{1}{\sigma_S^2} \sum_{k=1}^{K} \sum_{n=1}^{N_k} \frac{\partial g_{kn}(\theta)}{\partial \theta_i} \frac{\partial g_{kn}(\theta)}{\partial \theta_j}. \tag{7.16}$$

The $\mathbf{F}$ can consequently be evaluated from the partial derivatives of the estimator, which are

$$\frac{\partial g_{kn}(\theta)}{\partial x} = \frac{10(x_T - x_{kn})}{\ln(10)} \cdot \frac{\gamma_k}{d_{kn}^2}, \tag{7.17}$$

$$\frac{\partial g_{kn}(\theta)}{\partial y} = \frac{10(y_T - y_{kn})}{\ln(10)} \cdot \frac{\gamma_k}{d_{kn}^2}, \tag{7.18}$$

$$\frac{\partial g_{kn}(\theta)}{\partial \gamma_k} = \frac{10}{\ln(10)} \cdot \ln(d_{kn}), \tag{7.19}$$

$$\frac{\partial g_{kn}(\theta)}{\partial L_k} = 1. \tag{7.20}$$

Finally, the CRLBs on the estimation errors are evaluated as

$$e_{rms}^2 \geq \left[\mathbf{F}^{-1}\right]_{11} + \left[\mathbf{F}^{-1}\right]_{22}, \tag{7.21}$$

187

$$\sigma_{\gamma_k}^2 \geq \left[\mathbf{F}^{-1}\right]_{2+k,2+k}, \tag{7.22}$$

$$\sigma_{L_k}^2 \geq \left[\mathbf{F}^{-1}\right]_{2+K+k,2+K+k}, \tag{7.23}$$

where e_{rms}^2, $\sigma_{\gamma_k}^2$, $\sigma_{L_k}^2$ are the bounds on the location errors, the γ_k and the L_k, respectively. Accordingly, the RMSE on the location is

$$e_{rms} = \sqrt{(x_T - \hat{x}_T)^2 + (y_T - \hat{y}_T)^2}, \tag{7.24}$$

whereas the errors on the PL parameters are $\sigma_{\gamma_k} = |\gamma_k - \hat{\gamma}_k|$ and $\sigma_{L_k} = \left|L_k - \hat{L}_k\right|$.

7.2.4 Performance Analysis by Simulation

The performance of the considered RSS-based position estimation algorithm is evaluated by simulations in terms of achievable accuracy. We impose $\Delta = 1$ m, and the transmitter's position randomly varying around $\pm\Delta/2$ in the horizontal and vertical directions near the search area's center in each trial. M anchor points are then randomly positioned in the area. The corresponding PLs are generated according to a given mean PL log-distance model including shadowing. The simulations are performed according to Table 7.3, and the results are averaged on 1000 trials. We consider the case $K = 2$ and generate half of the PL data per slope for simplicity, and omit the standard deviations (STDs) corresponding to the average errors since in the simulations the STDs are primarily due to the shadow fading, and their values are slightly lower than the average errors themselves. Lastly, to evaluate the CRLB precisely, we avoid anchor points' distributions resulting in badly conditioned or singular FIMs (for example, anchor points along a line or placed on a circle around the target).

7.2.4.1 Comparison with the CRLB

In Fig. 7.4, the average RMSEs returned by the proposed algorithm are compared with the CRLB for two values of σ_S. We randomly generate the anchor points' positions once and keep them fixed to assess the effects of the σ_F on the errors. On average, the algorithm

Table 7.3: Simulation parameters used to generate the PL data for the performance analysis. A square search area having 200 m side and $L_k = L = 30$ dB are considered.

PL model	PL Exponents	σ_S^2[dB]
Single-slope	$\gamma = 2$	$\{3, 12\}$
Dual-slope	$\gamma_1 = 2, \gamma_2 = 4$	3
Two angular sectors	$\gamma_1 = 2, \gamma_2 = 4$	3
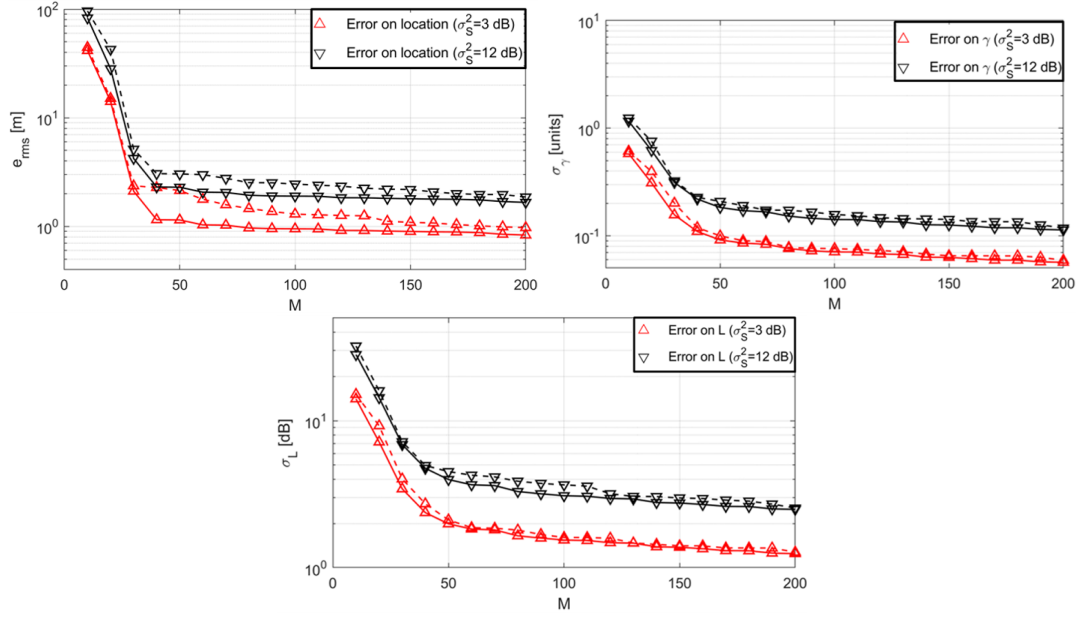
Figure 7.4: Performance of the proposed localization algorithm (dashed lines) compared with the CRLB (continuous lines) for $\sigma_S^2 = 3$ dB and $\sigma_S^2 = 12$ dB.

achieves the CRLB independently from the shadowing, though the noise naturally increases the minimum theoretical achievable errors.

7.2.4.2 Multi-slope PL

We examine the accuracy of the considered algorithm in the case of a dual-slope PL. The anchor's positions are randomly generated at each iteration, and $d_2^{(c)} = 50$ m is set. We give the algorithm firstly the correct value of $d_2^{(c)}$ and, then, a wrong value $d_2^{(c)} = 75$ m as input.

If the algorithm knows the exact $d_2^{(c)}$, it achieves the CRLB (Fig. 7.5). Obliviously, a wrong value of $d_2^{(c)}$ increases the algorithm's errors. In particular, the location error
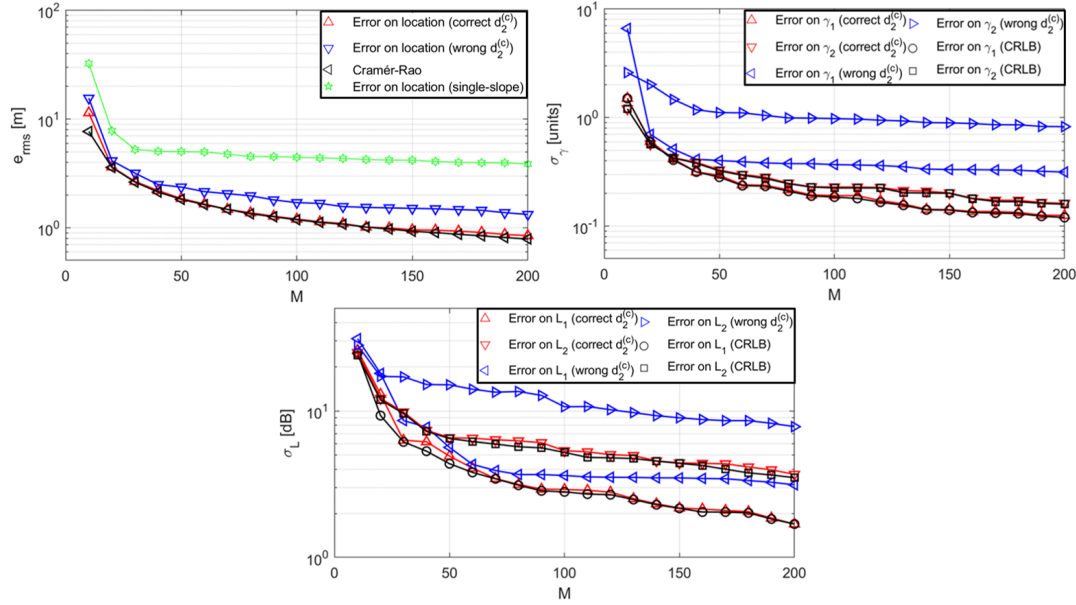
Figure 7.5: Performance of the proposed localization algorithm compared with the CRLB in the dual-slope case when the input $d_2^{(c)}$ value is either correct ($d_2^{(c)} = 50$ m) or wrong ($d_2^{(c)} = 75$ m).

increases significantly if a single-slope is assumed when running the algorithm, remarking the importance of a valid assumption on the radio propagation of the area. Instead, the algorithm is quite robust to errors on the critical distances if the number of measurements is high enough. For instance, the location RMSE is still lower than 1 m for $M \geq 140$.

7.2.4.3 Angular Dependent PL

Finally, the algorithm is tested in the case of an angular dependent PL. We divide the search area into two equal angular sectors, each characterized by a different PLE. The e_{rms} for $M = 100$ and $M = 200$ are compared to the CRLB in Fig. 7.6 when the error on the assumed $\delta_2^{(c)}$ increases up to 15°. Even in this case, the error is similar to the CRLB if the $\delta_2^{(c)}$ is known. Interestingly, an error as low as 2.5^o appears to nullify the benefit of a higher number of collected RSS measurements when $M \geq 100$, and a sectorization error higher than 5° results in the failure of the algorithm. Due to the wrong data partitioning, the

190
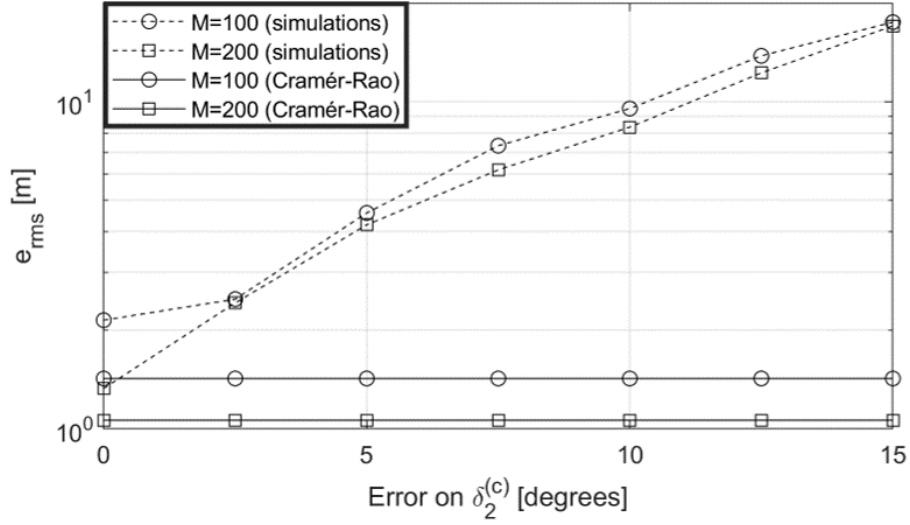
Figure 7.6: Performance of the proposed localization algorithm compared with the CRLB in the case of two angular sectors having different PL when increasing the error on the input $\delta_2^{(c)}$ value.

RSS-based localization in scenarios characterized by an angular dependent PL is thus more critical than in the case of a multi-slope PL since a slightly incorrect $\delta_2^{(c)}$ causes high errors on the target's location. The partitioning precision is expected to be particularly relevant when employing sectorized antennas [246] like those utilized in the base stations for the RSS-based localization.

7.2.4.4 Hierarchical Search Numerical Assessment

The numerical analyses in the previous Subsection and Sub-subsection were performed through direct search, viz. single-step searches. We repeat the same simulations using the hierarchical search to prove its effectiveness in reducing the algorithm's overall computational cost. Based on the project chart in Fig. 7.5, we select $q = m = 10$ and $T = 5$ as hierarchical search parameters, leading to $\alpha \cong 0.02$ from (7.10). The difference in the position estimate with and without hierarchical search is one or more order of magnitude lower than the average value and, thus, negligible, even if 98 % of candidate points were tested. (7.7).
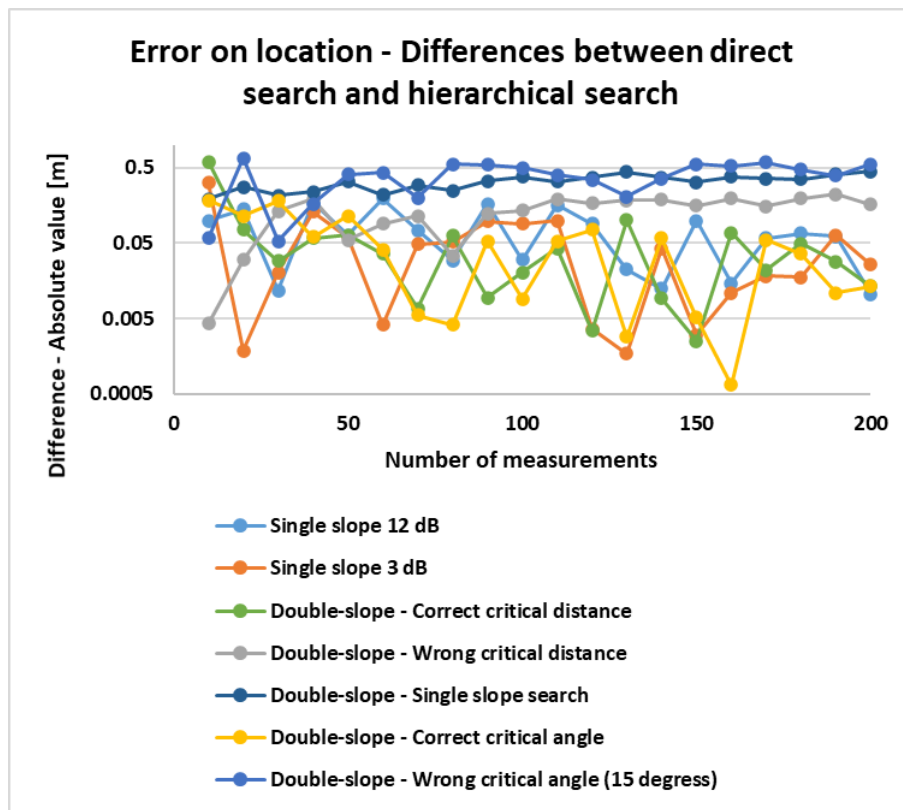
Figure 7.7: Differences in the position estimation between the direct search and a two-step hierarchical search.

7.2.5 Experimentation

The developed algorithm is tested using the LoRa protocol in a real scenario wherein a dual-slope PL model is expected. The transmitting and the receiving radios consist of Arduino Uno boards and Dragino LoRa shields connected to 868 MHz dipoles. The transmitting board is programmed to transmit one LoRa packet every 3 seconds (LoRa transmission parameters as in Chapter 5). Horizontally polarized electromagnetic waves are employed, and the transmitting radio is placed on the ground to avoid ground-bounce reflections. A 62 m × 58 m area, including a building of the University of Rome Tor Vergata, is selected as the test area, as detailed in Fig. 7.8. A network composed of five moving anchor points is then set up. Each receiving board is carried by a volunteer along a straight-line path and sends measured RSSI and SNR to a laptop via Wi-Fi, then the PL is evaluated. Every PL measurement is averaged on three packets so that 200 measurements are collected in 6 minutes. Due to the anchor points positions, a dual-slope PL is experienced, one for the outdoor (receivers 1, 2, 3, and 4) and one for the indoor (receiver number 5) environments.

Based on the search area analysis and the anchor points' topology, given that the indoor area is 16 m × 62 m, the algorithm is set to search for the critical distance between 5 m and 40 m using a step of 5 m. Based on the literature review above and for comparison purposes, the data are given as input to four localization algorithms simultaneously: the proposed algorithm, a DRSS-UDPG ESA estimating (x_T, y_T) and L fixed γ exhaustively searched [247], the GN RSS-UDPG algorithm [234], and a known-PL RSS-based ESA assuming free-space [248]. After 6 minutes, the error on the location returned by the presented algorithm is 5 m, significantly outperforming the other methods that assume a single slope and return errors comprised between 12 m and 47 m (Fig. 7.9). It is worth noting that the experimental data are affected by a very high noise due to misalignments between the transmitting and receiving dipoles, resulting in variable polarization losses and values of the gains; accordingly, the RSS measurement can be considered affected by an extremely high shadow fading. In practical applications, the additional noise can be reduced with near-isotropic antennas and employing linear and circularly polarized electromagnetic waves to make the polarization losses constant and equal to −3 dB. When considering the STDs
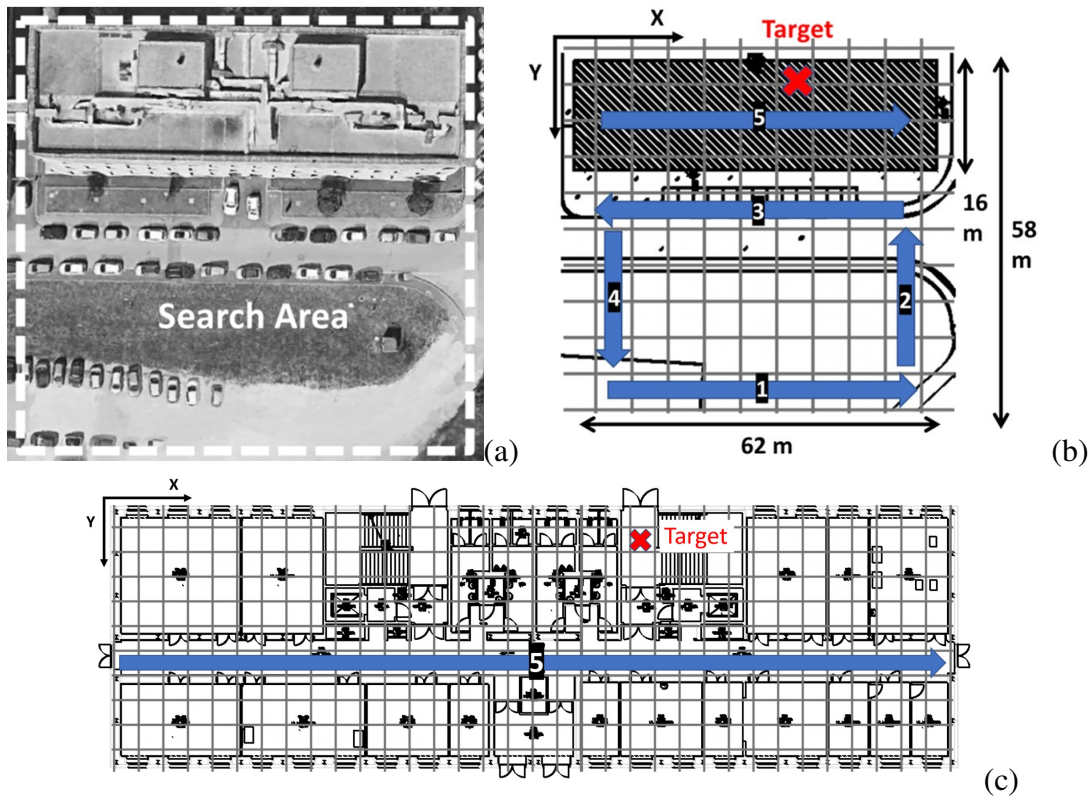
Figure 7.8: Search area and transmitter location selected for the experimentation of the localization algorithms. (a) Satellite image of the search area, (b) sketch of a grid superimposed over the search area, and (c) planimetry of the indoor environment considered. The target position and the paths of the five numbered receivers are shown.

194
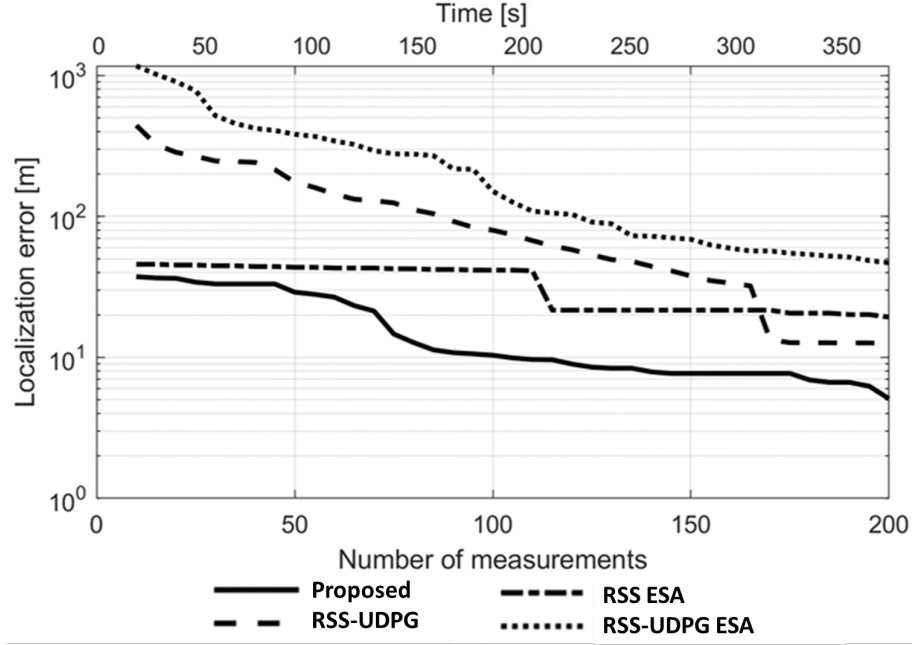
Figure 7.9: Experimental localization errors returned by the four tested algorithms.

numerically evaluated and the uncertainty on the unknown $d_2^{(c)}$, the error is coherent with the simulations shown in the previous Section.

Six minutes could be an excessive long localization time for the most critical SaR operation. This long time is due to the duty cycle imposed by the LoRa protocol [249], which influenced the maximum packet rate achievable by the transceiver used in the experiment. We report the run times of the considered optimization techniques in Fig. 7.10 corresponding to calculations based on experimental data and those obtained by simulation. Data in Fig. 7.10 are obtained considering the hardware/software settings in Table 7.4 and the test area in Fig. 7.8. Naturally, the ESAs' run times are mostly unaffected by the datasets, unlike the GN-based nonlinear technique. The proposed algorithm performed similarly to traditional methods and registered a maximum run time of 600 ms during the experiment. In the case of no exhaustive search over the critical distance, the run time is only slightly higher than the one of the RSS ESA. Therefore, in realistic operative conditions, the localization time is expected to be determined by the measurement period. The measurements can be speeded up by employing a high number of anchor points. If the measurement time is in

Table 7.4: Hardware and software utilized for the run times evaluation.

Central processing unit	Intel® Core i7-9700KF	Processor frequency	3.60 GHz
Random-access memory	16 GB	Software	Matlab® R2019b
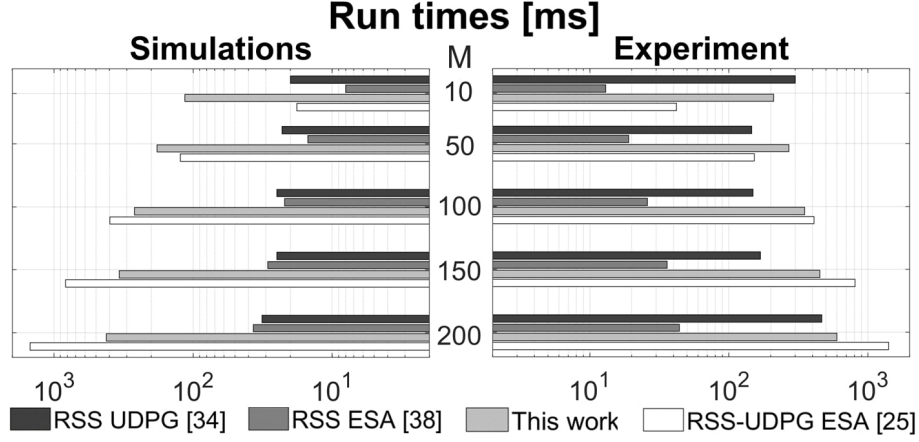
Figure 7.10: Run time of the four tested algorithms when employing simulated or experimental PL values.

the same order of magnitude as the lowest run time of the proposed method in Fig. 7.10, localization with 200 experimental data is carried out in about 20 seconds.

The experimental data used to validate the algorithm in this Subsection are available on the IEEE Dataport [250]. It is worth remarking that the experimental results were obtained through direct search and the transmission parameters detailed in Subsection 4.1.3.1 so that it is possible to observe little variations in the performances of the localization algorithm when changing those main system parameters. However, experiments would not have let us investigate the effects as a theoretical analysis combined with simulations could let us because of the additional noise present in the experimental settings. Instead, we know that when changing the transmission parameters of LoRa, the communications are slower, and so the localization depends merely on the number of measurements collected. On the other hand, the hierarchical search speeds up the localization at the expense of higher localization errors based on the kind of multi-step search chosen (number of steps, type of grid, (m, p, q) settings, et cetera). The possible combinations to experiment are thus unnumerable and,

following the literature on the topic, we assessed the single system parameters based on a combined theoretical and simulative analysis.

7.3 Simulations and Procedures for the Signal-based On-body Transmitter Localization in Mountain SaR Operations

An effective ESA suitable for localization of on-body LoRa transmitter has been developed, analyzed, and tested. The algorithm accounts for the SNR, avoids nonlinear evaluations with the relative conditioning problem, and can manage multi-slope and/or angular-dependent PL models previously unaddressed by the literature on the topic. We show how the off-body LoRa links can be exploited for mountain SaR through the detailed RSS-UDPG ESA in this Section. The effectiveness of the ESA in real scenarios is assessed by simulations using the empirical log-distance model of the mountains area introduced in Chapter 4.

7.3.1 Simulations with Mountain PL Models

The experimental measurement campaigns carried out in mountain areas observed an extremely significant shadow fading due to the irregular terrains and harsh environments. The accuracy of the location estimation algorithm in the presence of such a strong shadowing is assessed by simulation. Synthetic propagation scenarios are generated from the empirical log-distance single-slope models in Chapter 4, which accounts for a body-worn LoRa radio also. In each trial, the transmitter position and the measurement points are randomly generated in the area in accordance with a uniform spatial distribution. The number of PL measurements M is varied between 5 and 300. For each scenario, a number of 10000 trials is performed. The RMSE and the STD of the localization errors are evaluated.

The avalanche scenario with the buried transmitter is considered first. The burial depth is the 1 m estimated median burial depth of avalanche victims [251]. In this case, the search area is a square of 100 m×100 m since the more common human-triggered

avalanches do not exceed said area [252]. The superimposed grid is composed of candidate points at a distance of $\Delta = 1$ m along the x and y axes. We assume a transmitting power $P_{Tx} = -10$ dBm, which is enough to cover the search area according to the models. Since the lower PLs are supposed to be the nearest to the transmitter where the unpredictable effects caused by the wearer's body make the off-body signal strength fluctuating strongly, we weight $w_n = 1/4$ the PLs lower than $T_{PL} = 50$ dB and with $w_n = 3/4$ the PLs higher than or equal to this threshold. Results are reported in Fig. 7.11(a).

From the results, it can be observed that position estimation error rapidly decreases below a few meters for about $M = 100$. In a realistic operational scenario, it is important to achieve good position estimation accuracy in relatively small time and this corresponds to process few measurements. This allows reducing the time required to achieve a first and sufficiently accurate estimate of the transmitter position so to rapidly coordinate rescuers to move towards the estimated position. Naturally, the accuracy in the transmitter position estimation increases with the number of measurements allowing to average the impact of the strong shadow fading. Since the synthetic PL measurements are spatially distributed in accordance with a uniform distribution, the percentage of measurements under the 50 dB PL threshold (i.e., within 7 m of distance from the transmitter) is always about 2 % of M. Thus, as expected, in this case the weighting has a negligible impact over the achievable localization error since the remaining 98 % of the measurements obscure the weighting effects.

To assess the effectiveness of weighting, we consider the possibility of a non-uniform spatial distribution of measurements. In particular, we consider the snow-lying case by including a large percentage of randomly generated PLs values at distances lower than 20 m from the transmitter. The generation range of these PL measurements is set between 20 dB and 130 dB based on the experimental campaign's data. It is observed that when half of the received packets are received at distances lower than 20 m the localization error increases drastically [Fig. 7.11(b)]. In this case, weighting provides some benefits, by increasing the accuracy of more than 20 % as shown in Fig. 7.12. Furthermore, from the simulations, it can be observed that the accuracy gain practically saturates when the number of measurements is $N \geq 200$.
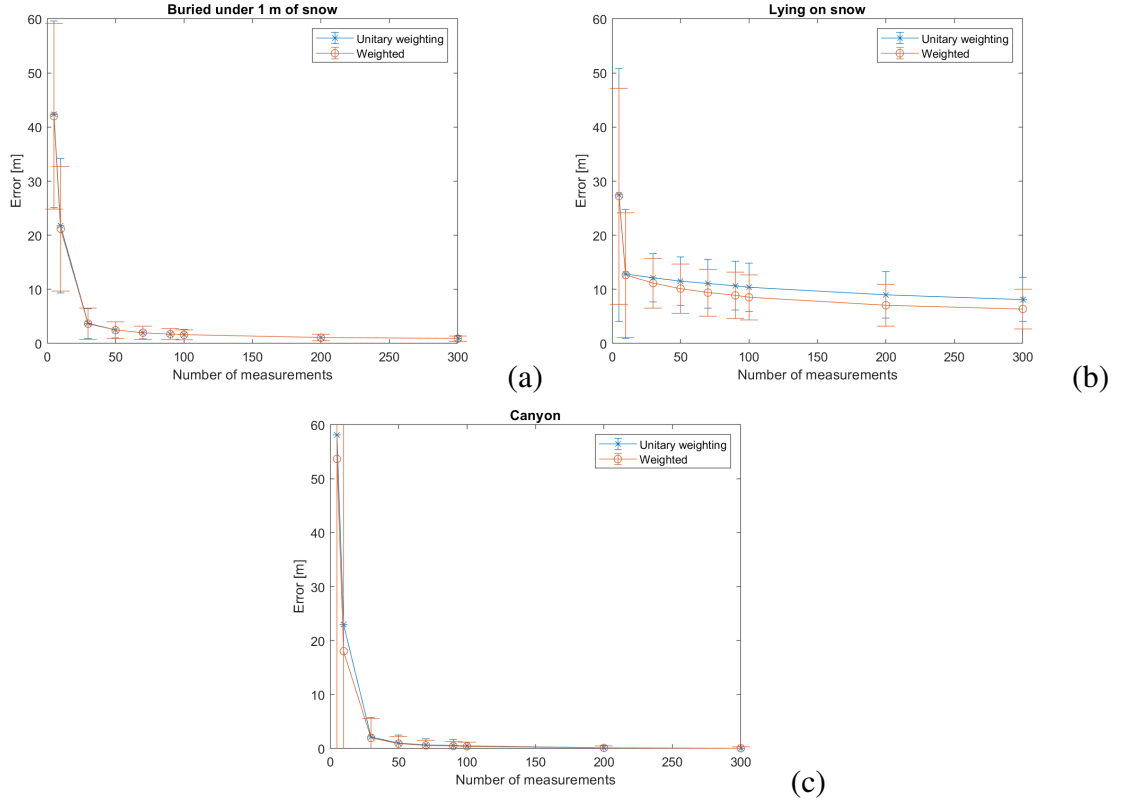
Figure 7.11: RSS-UDPG ESA tested with the experimental PL log-distance models of the LoRa off-body propagation in mountain environments. The localization RMSE error (in m) is computed when the measurements are and aren't weighted (unitary weighting) and M increases. The PL model is of (a) buried transmitter under 1 m of snow, (b) transmitter lying over the snow, and (c) transmitter inside a canyon.

Lastly, since the canyon can be modeled with a one-dimensional problem thanks to the waveguiding effect observed during the measurement campaign inside the Bletterbach canyon, the accuracy of 3 m can be obtained with just $M = 30$ PL measurements, and accuracy of 1 m with $M = 50$ as shown in Fig. 7.11(c).

It can be observed that the algorithm works fine despite the very strong shadowing (standard deviation from 7 to 10 dB) measured in the three scenarios and that the adoption of weighting in the minimization allows improving the results in the worst-case of a high number of inaccurate measurements.
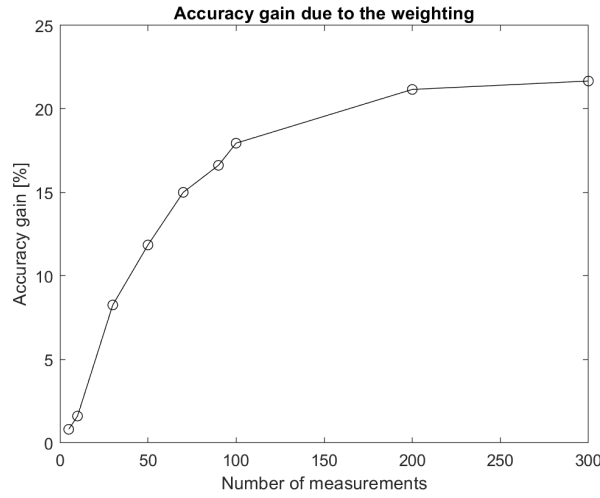
Figure 7.12: Accuracy improvement due to weighting in the case of Fig. 7.11(b) with respect to the non-weighting case.

Overall, the new RSS-UDPG ESA performed satisfactorily with the experimental models of off-body LoRa links in mountain environments. The direct search was preferred over the hierarchical one due to the high shadow fading, which could significantly increase the localization errors.

7.3.2 On-body LoRa-based System and Procedures for Mountain SaR

Thanks to the radio propagation characterization and the ESA, it is possible to perform a high-level design of a LoRa-based system for mountain SaR including the corresponding rescue procedures.

7.3.2.1 Principle Architecture of the System for SaR Operations

In Fig. 7.13(a) the principle scheme of the architecture of a LoRa-based system for supporting mountain SaR operations is depicted. For illustration purposes, the avalanche event is analyzed. Due to the avalanche, one (or more) person(s) can be buried under the snow and they could be also unable to activate their signaling devices (i.e. ARVA or LoRa) to send an alert message. To avoid these problems, we assume the persons involved in the accident

wear devices and sensors on their body so to realize a body area network BAN governed by some intelligence.

During normal conditions, the BAN intelligence continuously monitors through sensors measurements the health status of the person. In the case of an accident or any other dangerous event, data readings from local sensors can be used by the BAN intelligence to assess an abnormal situation affecting the person i.e. the BAN recognizes the imminent or persisting dangerous situation. This information can be used by the BAN intelligence to automatically send help request and (see after) to switch the LoRa transmitter device into the *Emergency Mode*. In Emergency Mode the LoRa transmitter starts to send Help Request Signals (HRSs) with a faster duty cycle than that recommended by regulatory authorities. As observed during the ESA experimentation, this is necessary to efficiently support LoRa-based localization by rescuers of the person involved in the accident or in a critical situation; otherwise, the duty-cycle can hinder the most critical SaR operations. As shown in Fig. 7.13 it is assumed that rescuers moving into the emergency area are equipped with LoRa receivers and are able to (automatically) perform PL measurements. These are forwarded to the CCC (command operation center) and given as input to the RSS-UDPG ESA described above. In particular, the CCC collects PL data to estimate the position(s) of the person(s), which in turn is (are) communicated by the CCC to the rescuers using all the available radio links (see Fig. 7.13) covering the emergency area. As an example, they could use the (available) cellular radio technologies [e.g. 3G, 4G-LTE or the forthcoming 5G - see Fig. 7.13(b)], or they could use the LoRa itself. In Fig. 7.13(c) is indicated one possible end-to-end (i.e. from the rescuer to/from the CCC) protocol stack architecture of the LoRaWAN system, which can be used to practically implement the communication system depicted in Fig. 7.13(b). It is worth noticing that according to the deployed LoRaWAN model the LoRa transmitter, acting as a slave, creates a connection with its network server that can be reached using the IP backhaul link with the LoRa receiver acting as the LoRa gateway. Consequently, the network server in the CCC acts as the master and runs the LoRa app to be used for the processing of the PL data sent by the rescuers.
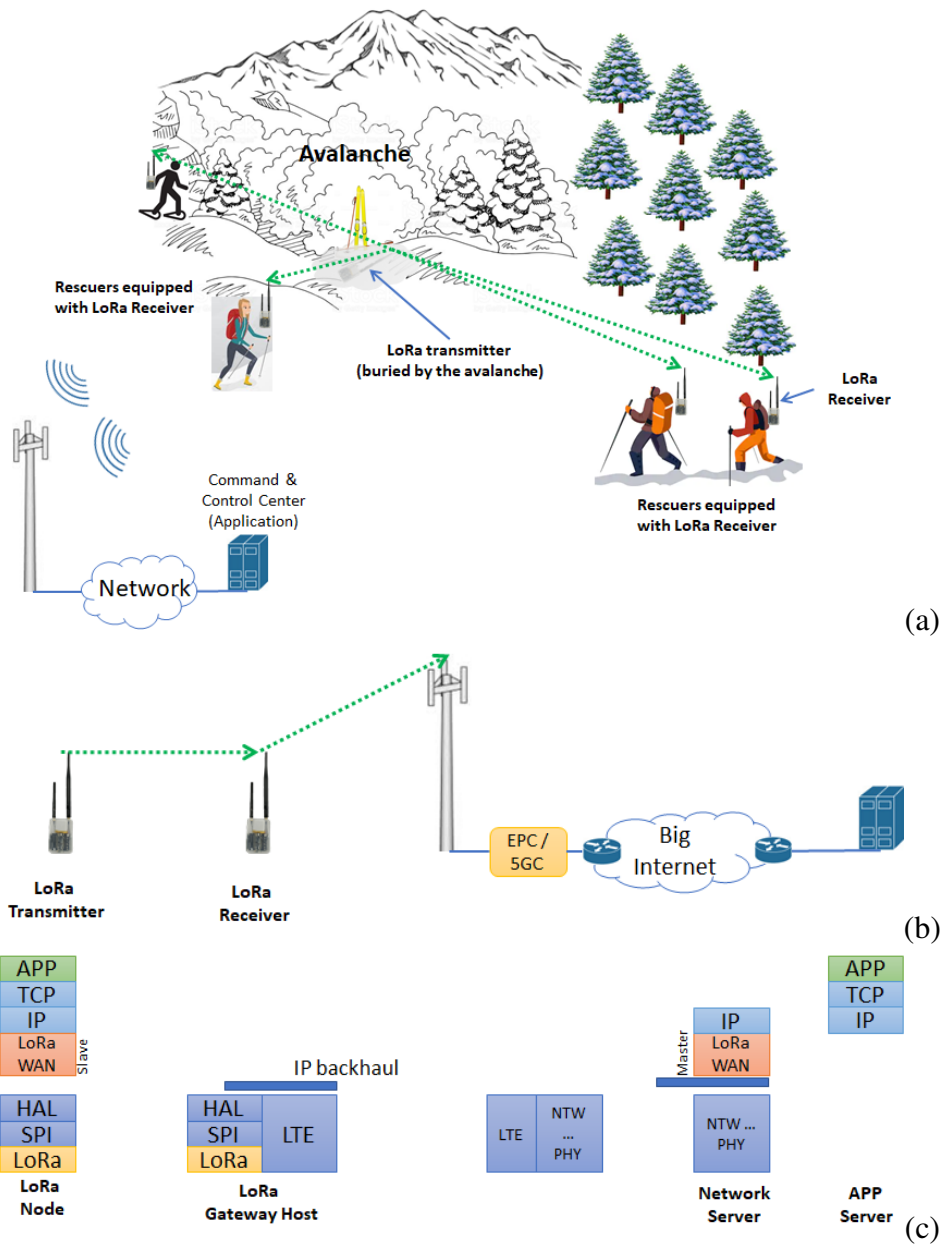
Figure 7.13: (a) Sketch of the avalanche SaR scenario using LoRaWAN system; (b) Principle scheme of the LoRa-based SaR system architecture; (c) Possible LoRaWAN protocol stack for the proposed architecture.

7.3.2.2 Devices and Localization in the Considered LoRa SaR Support System

In this Sub-subsection, a discussion is provided concerning the high-level design, the operational features and additional functionalities of the devices to be integrated into the LoRa based rescue system in Fig. 7.13.

Device design for the user The realization of a device for mountain SaR operations based on LoRa can exploit the great flexibility of LPWAN devices. The dimensions of the commercial ARVA model PIEPS POWDER BT are 118 mm $\times$ 76 mm $\times$ 29 mm and its weight is of 230 g. A LoRa-based transceiver with the same encumbrance can include:

1. *LoRa chip*: e.g. the SX1272 [213];

2. 868 *MHz near-isotropic antenna*: e.g. a turnstile antenna [253];

3. *BAN sensors*: to collect user's data and equipped with an on-board intelligence for making decisions about the health status and orientation of the person;

4. *Screen*: a screen which displays useful feedback to the user, regarding the transmitter status and its current working mode (Normal or Emergency Mode).

Focusing on the BAN, in the simpler case, we can assume it includes the following devices: one GNSS module, sensors for determining the orientation of the human body (i.e. ManDown sensors), sensors for measuring external pressure, temperature and haptic actuators. Even though the BAN is expected to be power consuming, wearable commercial devices integrating the proposed sensors are already available on the market [254]. We assume the BAN is equipped with one Emergency and one Reset Buttons. The pressing of the Emergency Button allows switching the BAN working mode from Normal to the Emergency after a few seconds. The Reset Button is necessary to return to normal mode or to stop sending HRS if the Emergency button has been inadvertently pushed by the BAN's owner, or the Emergency mode has been wrongly activated by the BAN intelligence. The haptic actuators are used to warn the user that the device is switching from Normal to the Emergency Mode.

Additional functionalities of the device for the SaR Rescuer   In our system, we assume the LoRa devices can be classified into two different classes: standard and rescue devices. Only the rescuers involved in the mountain SaR operations can be equipped with LoRa rescue devices. These include all the features of the standard LoRa devices and incorporate some important additional functionalities. During emergency operations, rescuers' LoRa transceivers commonly operate in receiving mode and could be equipped with a directional antenna (e.g. Yagi-Uda or horn antenna), which can be manually (or even automatically) oriented to reveal the direction of the maximum received signal power or RSSI. In addition, we assume the LoRa rescue transceiver should be able to broadcast an Emergency Activation Signal (EAS) to all the LoRa users' transceivers in the area. This can be obtained by means of a dedicated channel, which is used to send a 30 -second long EAS. This signal can force the LoRa standard transceivers in the customers' BAN networks to commute from *Normal* into the *Emergency Mode*. A user needing no help can use the Reset button to switch its transceiver into normal operation mode. This function is necessary to exclude from the rescuers' attention all users needing no help. In fact, the extension of the LoRa area reached by the EAS can be larger than the emergency area. Thus some persons could be reached by the EAS even if they are not involved in the accident.

Detection and localization of persons involved in the accident   After EAS reception and/or after the BAN intelligence has assessed a distress condition of the person, the Emergency Mode is set and LoRa transceiver starts to send the HRS on a properly selected LoRa transmission channel. Rescuers devices continuously monitor for the presence of HRSs in the emergency area. Following the reception of the HRSs, the localization process can start on the basis of the PL measurements sent by the rescuers' moving into the emergency area to the CCC. The LoRa extended radio range allows rescuers to detect the HRS signals even when they are far from the position of the person involved in the accident. The principle of this operating procedure is similar to that based on ARVA. However, ARVA transceivers, characterized by short-range and hard degradation in the signal detection may render difficult the detection of the signal especially when the rescuers are far from the person involved in the accident. Hard degradation in ARVA signal detection is experienced when the received signal power is under the receiver sensitivity level. In this case, the ARVA receiver

declares its impossibility to detect the presence of the signal. Instead, due to the possibility of changing the SF, LoRa can operate with different receiver sensitivities thus enabling for a soft degradation. In the Emergency Mode, the SF= 12 could be used to allow the LoRa receiver to operate at its lowest sensitivity.

The possibility of a random selection of the LoRa transmission channel is helpful to mitigate potential interference among LoRa transceivers belonging to more persons that could be involved in the accident. In principle, all the available LoRa channels in the $865 - 868$ MHz band could be used for supporting HRS transmission. Since up to 47 LoRa channels can be created in the EU 868 MHz unlicensed band using a BW of 125 kHz [153], to simplify the system design and protocol operations one channel can be assigned for the broadcast of the EAS while other channels can be dedicated to the HRSs.

LoRa Message Payload   A proposal for the payload of LoRa packets to be sent by the transmitter in the Emergency Mode is detailed below. The information fields of the considered payload are listed in the following points:

1. *Help Request*: one bit long, with 1 if the transmitter is working in Emergency Mode, 0 otherwise;

2. *Group ID* (optional): a number indicating the group identity of users the single user's transceiver belongs to. This field could be omitted if it is not necessary to identify the group of hikers/tourists visiting the mountain;

3. *Individual ID*: alphanumeric (randomly generated) string. This is the ID of the single LoRa transceiver and it is uniquely associated with its owner. Typically this ID is not displayed on the screen of the device in order to avoid ethical/privacy issues;

4. *GNSS availability status*: one bit, with 1 if the satellite (e.g., GNSS) signal is available and 0 otherwise. A Rescue transceiver can ask for the transceiver to send the GNSS coordinates if they are available. In principle, the BAN could use the unavailability of GNSS signal as additional data to infer on possible dangerous/distress condition of the hiker.

5. *Temperature*: the value of sensed body temperature (in Celsius). This data is retrieved from the corresponding sensor integrated into the BAN;

6. *Pressure*: the value of external pressure (mbar). This data is measured from the sensor in the BAN network;

7. *ManDown*: one (or more) bit(s), in the simple case of one bit, the bit is set to 1 if the ManDown senses the user is fallen for more than 1 minute. In the case of more bits, the remaining bits could be used to indicate the status of gyroscopes in the BAN. These sensors could be used to determine if the person under the snow is in a non-natural position such as upside-down;

8. *WBAN* (optional): one bit, with 1 if the heart rate and the blood pressure sensed by additional BAN sensors (e.g. smartwatch) increases above some thresholds declared to be critical.

7.3.2.3 SaR Procedure and Effectiveness of the Proposed System

In this Sub-subsection, we firstly provide a high-level description of the proposed SaR procedures for the person(s) involved in the accident and for the rescuer(s), and then we estimate the system's effectiveness in terms of end-to-end latency and power consumption.

Procedure: Person involved in the accident side   The diagram in Fig. 7.14(a) indicates the operations required by the user's BAN.

1. *BAN turned on*: it is assumed the person activates the BAN, while starts moving on the mountain. In most parts of Europe it is mandatory to worn and to turn on the ARVA device when skiing and for snowboarding. Similar regulatory rules could be enforced in the LoRa case.

2. *BAN in Normal Mode*: in Normal Mode, the LoRa device in the BAN sends packets 5 bytes long containing user's data in accordance with the duty cycle limitations i.e. the device emits 1 packet every 5 seconds. During the inactivity period, the LoRa device listens to the dedicated channel for the presence of an EAS from rescuers (see
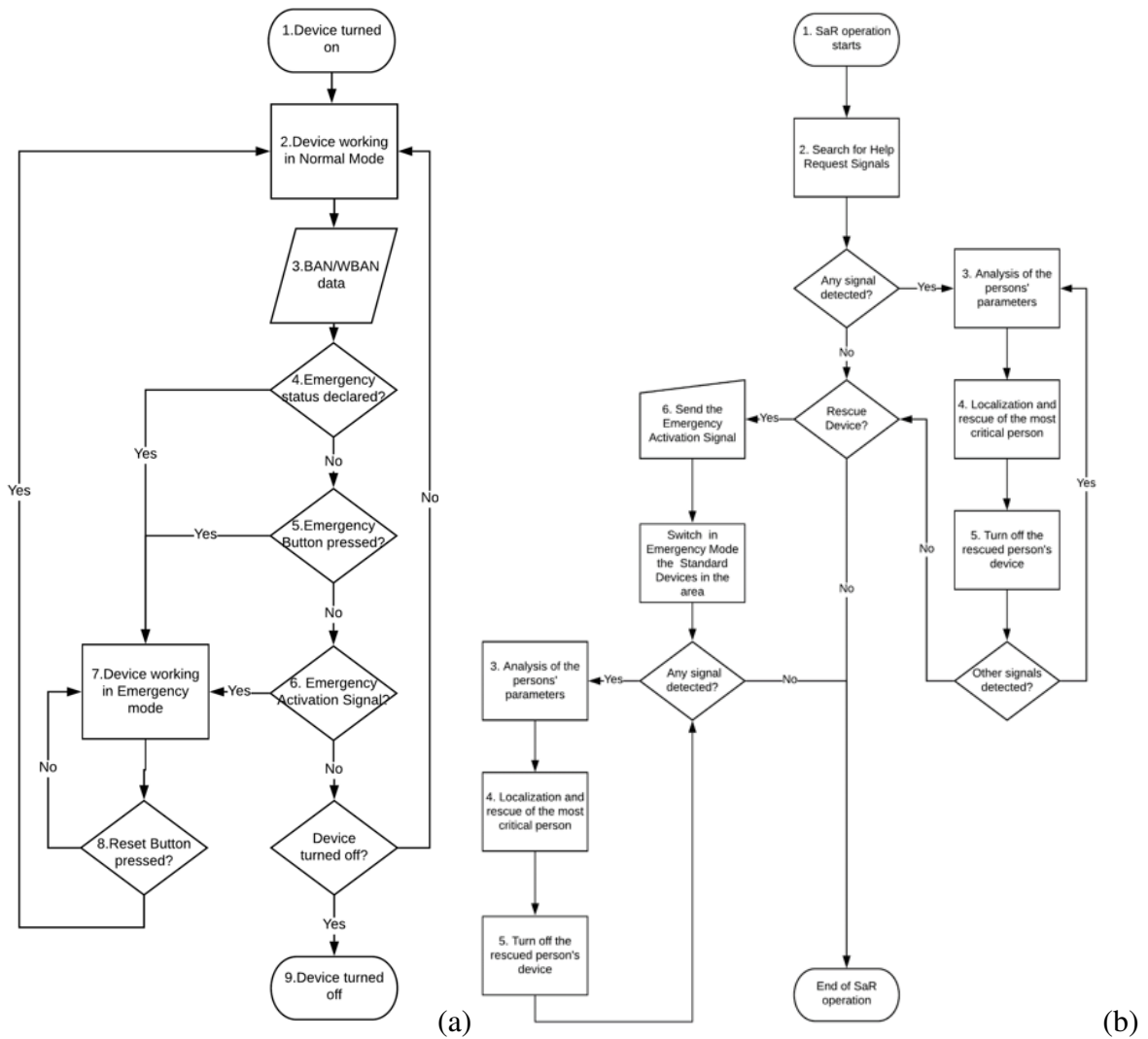
Figure 7.14: SaR procedure: (a) user side, and (b) rescuer side.

after); the reception of an EAS sets the status of the terminal to the Emergency Mode. Users not involved in the emergency can restore the Normal status by pressing the Reset Button. As an alternative, the BAN intelligence can automatically restore the Normal Mode status in the case no anomaly is assessed after a given time.

3. *BAN data*: BAN devices continuously collect data from sensors; BAN intelligence analyzes them to assess for the presence of abnormal conditions. Additional information can optionally be collected from other devices such as the heart rate from a smartwatch. Smartwatches or any other external sensor can communicate with the BAN by means of a local wireless link based for example on BLE.

4. *Declaration of the Emergency status from the BAN without EAS reception*: data from local sensors allow BAN intelligence to assess the presence of anomalous situation and/or ongoing critical situation. If a critical situation is detected, the Emergency Mode status is automatically set by the BAN and a timer starts; if the BAN mistakenly activates the emergency status the user is required to press the Reset Button if he/she needn't help before the timer elapses. If the timer elapses, it is assumed by the BAN intelligence the user is unable to manually activate the Emergency Mode. In this case, the BAN intelligence turns the LoRa transceiver into the Emergency Mode and starts to send the HRS messages.

5. *Emergency Button*: even though an emergency could be not detected by the BAN, the user can always press the Emergency Button to require help.

6. *Emergency Activation Signal from rescuers*: in Normal Mode, when the LoRa transceiver is not transmitting it listens to the dedicated channel for any possible EAS sent by a Rescue transceiver. The reception of the EAS message turns the BAN and the LoRa transceiver into the Emergency Mode.

7. *BAN in Emergency Mode*: in Emergency Mode, the BAN and then the LoRa transceiver operates in a de-regulated mode i.e. by removing the LoRa duty cycle limitation of 1 % so to reach a higher message rate e.g. 1 message every 2 seconds. In this case, the LoRa transmissions follow the protocol described above i.e. random

selection of the transmission channel and, for example, SF set to SF= 12 for the lowest sensitivity.

8. *Reset Button*: under any operating condition, the user can always press the reset button to reset the transceiver into Normal Mode.

9. *BAN turned off*: when the person is not involved in any mountain activity her/his BAN should be turned off so to let the LoRa transmission channels free.

It is useful to point out that the Emergency Mode can be raised by the user himself as well as set automatically by the BAN. This last feature allows launching alarms when the user is unconscious and/or buried in the snow and/or he/she is unable to manually switch the BAN to the Emergency Mode.

Procedure: Rescuer side Rescuers follow the procedure indicated in Fig. 7.14(b). The procedure can vary in accordance with the category of rescuers' equipment, which may consist of a standard transceiver or the rescue transceiver (see Section 7.3.2.2):

1. *Starting of SaR operation*: rescuers moving in the emergency area turn on their LoRa transceivers, which start working in the receiving mode.

2. *Searching for HRS*: the rescuers' transceivers search for the presence of HRSs by rapidly scanning the LoRa channels.

3. *Analysis of the persons' parameters*: the received HRSs contain information on the vital data allowing the rescuers to infer on the clinical status of the person involved in the accident.

4. *Localization of the most critical person*: for each received HRS the corresponding measurements of RSSI and SNR (or equivalently the locally calculated PL) are sent to the CCC to allow the estimation of the position of the person(s) involved in the emergency.

5. *Turn off the BAN LoRa device*: the transceivers of the rescued persons are turned off (eventually by remote action) so to decrease the LoRa channels usage.

6. *Emergency Activation Signal*: if the rescuer is equipped with a rescue transceiver he can emit EASs to automatically turn the standard devices into the Emergency Mode; this option is helpful to assess the presence of injured persons in the emergency area that are unable to manually activate the Emergency Mode and for some unpredictable reasons, the BAN intelligence was unable to set the Emergency Mode.

As outlined in the previous points, the measured RSSI and SNR including the GNSS coordinates of the rescuer are sent to the CCC for the processing required to estimate the position(s) of the person(s) using the new RSS-UDPG ESA discussed in this Chapter. The estimated position could then used by the director of the SaR to coordinate the movements of the rescuers in the area to converge to the estimated point.

Assessment of the end-to-end Latency   To assess the effectiveness of the proposed system it is of interest to evaluate the time taken to detect and localize the person since receiving the first emergency messages until localization by the CCC. We indicate this time as end-to-end latency. To this purpose, we need to evaluate the following three main contributions to end-to-end latency.

1. The time required for the CCC to collect M measurements from rescuers. This number should be selected to guarantee the desired estimation accuracy and it could be inferred for example by the curves depicted in Fig. 7.11(a). In general, in any scenario, it seems $M \geq 50$ can provide an initial acceptable estimation accuracy of the transmitter position that can be improved as the CCC receives new measurements. Indicating with R_m (msg/s) the message generation rate from the transmitter in the Emergency Mode and K_R the number of rescuers receiving the emergency messages, the time $T_m(M)$ required to collect M PL measurements is:

$$T_m(M) = \frac{M}{R_m K_R} \tag{7.25}$$

and $R_m K_R$ is the number of PL data collected by K_R rescuers in the unit of time.

2. The time T_{TX} required to the rescuers to send PL data at the CCC for each received HRS. We assume the transmission capacity of the radio mobile channel is

large enough to allow the rescuers to send PL data to CCC almost simultaneously. From the scheme, in Fig. 7.13 the T_{TX} is the sum of the contributions listed and detailed in Table 7.5.

For this evaluation we considered the maximum serialization delay in LoRa i.e. we assume data are sent to CCC by rescuers using the lowest available bit rate in LoRa $R_b = 300$ bit/s. Obviously, to reduce latency higher bit rates can be considered. The delays for transmissions in the mobile radio network connecting the rescuers to the CCC were taken from [255].

3. The time $T_{P,R_X}(M)$ required for processing the M measurements in the CCC to estimate the position of the transmitter and to return this information to the rescuers in the emergency area. From the definition, $T_{P,R_X}(M)$ is:

$$T_{P,R_X}(M) = T_{srv}(M) + T_{CCC,TX}, \tag{7.26}$$

and $T_{srv}(M)$ is the time required to process M measurements through the RSS-UDPG ESA. To evaluate this delay we refer to the profiling results obtained from the MATLAB implementation of the algorithm. The software runs over the hardware specified in Table 7.4. We obtained the following results: $T_{srv}(M) = 686$ ms for $M = 50$, $T_{srv}(M) = 816$ ms for $M = 100$ and, finally, $T_{srv}(M) = 1020$ ms for $M = 200$. The results are higher to the experimentation discussed before because of differences in the two implementations of the RSS ESA when weighting the data or not. It should be noticed that when $M = 50$ measurements have been collected we obtain a first good estimate of the actual position of the transmitter. This estimate can be immediately sent to rescuers so that they can move toward the target. While the rescuers are moving they continue to transmit PL data to the CCC which uses the new measurements to further refine the position estimate. Finally, the $T_{CCC,TX}$ is the time required by the CCC to send information position to the rescuers. It can be calculated as the sum of the components indicated and detailed in Table 7.6, [255].

Table 7.5: The time required for the rescuers to send data to the CCC.

Contribution	Time [ms]
Tx-Rx LoRa link (for $R_b = 300$ bit/s)	133.3
LoRa GW-to-eNB (eUTRAN)	18.3
Access-to-core	10
Core-to-server (Big Internet)	5
Total	**166.6**

Table 7.6: Time required for the CCC to send the data to the rescuers.

Component	Time [ms]
Server-to-core (Big Internet)	5
Core-to-wireless access	10
BS-to-rescuers	6.5
App processing	4
Total	**25.5**

Summing the three delay components, the overall latency $T(M)$ to obtain a first estimate of the position of the transmitter is:

$$T(M) = T_m(M) + T_{TX} + T_{P,R_X}(M). \tag{7.27}$$

Some results for $T(M)$ have been reported in Table 7.7 for different M, numbers of rescuers K_R and R_m.

Power consumption in the Emergency Mode   To assess the power consumption in the LoPy-4 boards used for the measurement campaigns, we have measured a current of $I_{SB} =$

Table 7.7: Estimated localization latency [s] for some values of M, K_R, and R_m.

Number of rescuers, K	Number of measurements, M					
	50		100		200	
	1 msg/5 s	1 msg/2 s	1 msg/5 s	1 msg/2 s	1 msg/5 s	1 msg/2 s
1	250.88	100.88	501.01	201.01	1001.21	401.21
5	50.88	20.88	101.01	41.01	201.21	81.21
10	25.88	10.88	51.01	21.01	101.21	41.21

105.38 mA in standby condition. It should be remarked that this value refers to the current absorption of the entire device and not of LoRa. This is also in line with the figure reported in the data sheet of the LoPy-4 board [176]. When switching the device in transmission mode with 1 msg every 5 s we measured an average current absorption of $I_5 = 140$ mA. Considering now an increased message rate to 1 msg every 2 s the absorption rises to $I_2 = 192$ mA. From these figures is immediate to evaluate power consumption of the device taking into account that the voltage by the power supply is 5 V. Finally, it is of interest to calculate the battery life when the terminal is in the Emergency Mode. Assuming the device is equipped with a LiPo battery of 1100 mAh, this allows remaining in the Emergency Mode for about 5 h and 45 min.

7.4   Conclusion

In this Chapter, a system for mountain SaR utilizing off-body LoRa links is comprehensively designed and analyzed. To localize the SaR target through off-body links, signal-based localization through LoRa is introduced. Three critical shortcomings in the literature are identified: 1) the neglect of the LoRa SNR, which instead is significant in mountain scenarios, 2) employable algorithm in the literature employ nonlinear techniques that can be ill-conditioned due to harsh radio propagation environments, and 3) said algorithms always assume that a single-slope log-distance model can effectively model the whole search area while it could be not true. A new grid-based ESA is developed to overcome these critical points. The ESA uses the PL measurements, is based on linear systems only, and allows for data partitioning in complicated search areas. Therefore, the new algorithm overcomes the listed shortcomings. Theoretical analyses and experimentation with LoRa radios confirm the algorithm's effectiveness.

Based on the grid-based ESA and the off-body LoRa link model discussed in the previous Chapters, a system for mountain SaR is proposed with a high-level design including the SaR procedures and latency and power consumption evaluations. According to the exposed analysis, the system can effectively support the mountain SaR based on the off-body LoRa terrestrial signals; indeed, the body's shadowing and positioning is usually a relevant effect only up to a few tens of meters wherein the localization is less critical. Instead, at

higher distances, the harsh environment causes extremely high shadow fading, obscuring the body's one, which, thus, does not affect the localization algorithm anymore. However, the use of flying drones is not straightforward for mountain SaR. The body-to-UAV links can be used effectively for the position estimation only if there's LoS between the wearer of the LoRa beacon and the rescuer UAV, viz., when an FS link is given. If the LoS is negated, the PL is angular-dependent and cannot be approximated with simple linear log-distance models, and, consequently, even the sectorizing ESA presented in this Chapter cannot be used. The RSS-range-based position estimation with these links is still an open issue for future research.

Overall Conclusions

Summary and Scientific Contribution of the Work

This thesis investigated the wireless devices and communication working in the body-area to analyze the effects of the human body on the B-IoT communications when considering both local- and remote-processing systems. Two important technologies working in the unlicensed EU UHF band were considered as case-study: passive RFID-based sensors for the local-processing and the LoRa protocol for the remote-processing. Based on a thorough analysis of the literature, the local-processing B-IoT systems to analyze were categorized as (*i*) on-body and (*ii*) off-body sensing, whereas the remote-processing systems were divided depending on the type of the off-body links exploited, i.e. terrestrial or ground-to-air links. Hence, the research carried out in this work enabled new generation RFID sensors based on self-tuning devices and a novel kind of system for mountain SaR operations through the LPWAN technology.

The main achievements can be detailed as follows.

1. *Optimal design of self-tuning sensors and inter- and intra-subject variability quantification.* The de-tuning challenge was overcome by utilizing the recently-introduced auto-tuning RFID ICs. A constrained design technique involving a penalty function was developed and tested to allow the optimal design of this kind of sensor-tags. Local-processing B-IoT systems are currently under research for healthcare applications to sense measurands on the wearer's body itself (on-body sensing) or in the surrounding environment (off-body sensing) through wearable or epidermal antennas. Accordingly, the two identified case studies to validate the design technique concerned the different kinds of sensing and antenna. A wearable tag embedded in a

filtering facepiece respirator was designed as on-body sensing case study to monitor the facemask wetness that could hinder the filtering capability of the mask; instead, epidermal fingertip tags were manufactured to enable dielectric-sensing hand-worn R-FAD systems as a case study for the off-body sensing. The design technique successfully allowed for the creation of new RFID sensor-tags in both cases, confirming its validity.

2. *Off-body LoRa-based B-IoT system for mountain SaR.* The use of off-body links with the LoRa LPWAN protocol for mountain SaR operations was chosen as a remote-processing B-IoT case study unexplored by the literature. The use of a body-worn LoRa transceiver was proved to outperform SoA devices for mountain SaR by an experimental evaluation; then, the links were modeled with measurement campaigns for corroboration. The terrestrial links in the mountain environments followed log-distance PL models, and the body shadowing was the main source of signal's power fluctuations (about 10 dB) up to some tens of meters, after whom the effects of the environment were dominating. Ground-to-air communications were tested successively by assembling radiohelmet prototypes worn by volunteers. By using a helmet antenna, the flying height of the UAV allowed avoiding the body shadowing. However, the eventual presence of a significant ground-bounce multi-path made the body-UAV link more dependent on the posture of the wearer than the terrestrial ones. Moreover, in actual mountain environments, the link model could be angle-dependent. Therefore, for localization purposes in mountain environments using the sole signal strength of a body-worn transmitter, the terrestrial off-body links could exploit the vast literature on the RSS-UDPG localization through log-distance models contrary to the body-UAV links. A new localization ESA working even in environments characterized by multi-slope models was developed accordingly and validated to overcome the limits of the literature on the topic and complete the high-level design of a remote-processing B-IoT system for mountain SaR.

Overall, the B-IoT case studies allowed us to assess the inter- and intra-user variability of the communication degradation in different kinds of links. The inter-subject variability was

negligible in remote-processing B-IoT, whereas the intra-user variability caused by the different positioning of the body-worn antenna and the wearer's posture was always extremely significant. The statistical approach was hence necessary when testing or designing B-IoT systems. Naturally, such a great variability had to be considered when designing both the devices and the system architecture of the B-IoT. Numerical simulations paired with theoretical models could effectively predict B-IoT links' behavior, provided that all the possible configurations were foreseen. Both the kinds of uncertainty depended on the body-antenna distance so that the link of epidermal antennas were much more variable than the wearable ones for the same antenna layout and boundary conditions. However, it is worth remarking that the technological advancement of auto-tuning antennas can significantly reduce these uncertainties so that in the future, the B-IoT communications can become extremely more reliable than SoA links.

Open Issues and Future Directions of Research

Although the body shadowing was comprehensively investigated through local- and remote-processing EM communications, a number of relevant issues are still open to investigation. Firstly, only the links in the European UHF $865 - 873$ MHz band were considered, whereas the intra- and inter-subject variability are expected to be extremely dependent on the considered frequency. More frequency bands and protocols should be experimented with and compared with the same testing conditions consequently while paying attention to the distinction between the local- and remote-processing systems. Moreover, long-range links involving epidermal antennas should be investigated as well to quantify the differences between the wearable and epidermal links. The holistic approach should be further exploited systematically to draw a solid and assessed technique of analysis of bodycentric communications. Such an analysis could allow developing the optimal design workflow for B-IoT systems going from the device manufacturing to the conceptualization of the architecture and procedures. It is of special interest noticing that the remote-processing B-IoT systems also exploiting local-processing have not been considered yet (Fig. 3); instead, this last kind of system can be characterized by challenges different from the ones identified in this doctoral research.

Aside from the holistic approach, many future directions of research can arise from the particular topics addressed as case studies in the present dissertation. The local-sensing by auto-tuning ICs here introduced can be applied to many unsolved problems thanks to the improved reliability of the communication and the minimized number of components. Auto-tuning sensors could be developed for any measurand provided that the antenna's

substrate can produce a permittivity variation proportional to the measurand's one. Moreover, it is worth noting that the whole self-tuning range reported on the Magnus-S3 IC datasheet has never been achieved yet. The use of external electrical components (for instance, diodes) could overcome this issue probably. Similarly, the modeling of the LoRa off-body links can be utilized to merge the extended connectivity with the bodycentric sensing. It is easy figuring the possible benefits, particularly for the poor communities still badly served by the current communication systems; indeed, telemedicine systems could be implemented even in such harsh environments. Finally, the localization based on the RSS through body-UAV links is still an open topic that could significantly empower the system for mountain SaR designed through the second part of the dissertation, empowering a new generation of easily-deployable localization systems.

Appendixes

Appendix A - Low-power Wide-area Networks

The Low-Power Wide-Area Network (LPWAN) technologies have been recently developed to obtain an extremely long communication range while maintaining a low power consumption.

LPWANs' Characteristics

Let us recall the IoT basics to understand why the LPWAN were developed. The IoT paradigm is to make things part of the Internet environment where the "Things" category is a notation used to encompass a generic set of entities, including any object that is aware of its context and is able to communicate with other entities, as smart sensors or human beings [256]. An IoT device can, therefore, be defined as a device capable to connect to the Internet. In order to apply this ambitious paradigm very different technologies are required, such as short-range standards (like RFID, Wi-Fi, Zigbee, Bluetooth) and long-range standards (like 2G, 3G, 4G, LTE). The technology most suited to create an IoT environment depends on the application needed, because one must find the trade-off between at least eight factors.

1. Battery, because it limits the end-devices lifetime.

2. Data rate.

3. Range.

4. Coverage.

5. Network mesh.

6. Node cost.

7. Mobility.

8. Latency.

The LANs *(Local Area Networks)* can communicate up to hundreds of meters with very different power consumption, while the cellular technologies cover wide areas at the cost of high power consumption. The low-power wide-area network (LPWAN) technologies were created to enable long-range connectivity (up to few kilometers) with extremely low power consumption, and this was achieved at the price of a very limited data rate, ranging from 10bps up to a few kbps [257]. Thus the LPWANs emerged as one of the enabling technology of IoT. An LPWAN ensures:

- a communication range of at least few kilometres;

- a low power consumption which enables years of battery lifetime;

- very low sensitivities;

- some form of encryption to protect the data.

Because of the listed requirements, an LPWAN has features different from every other kind of network. In (Fig. A.1) the LPWAN are compared with other communication technologies, as BLE (which is a reference 6LoWPAN [258]) or VSAT (very small aperture terminal*;* a low-cost satellite communication technology).

The most important existing LPWAN technologies are listed below.

- LoRa [259, 260, 140, 257, 261].

- Sigfox [140, 259, 260, 261].

- NB-IoT, also called LTE Cat NB1 [262, 140, 259, 263, 257].

226
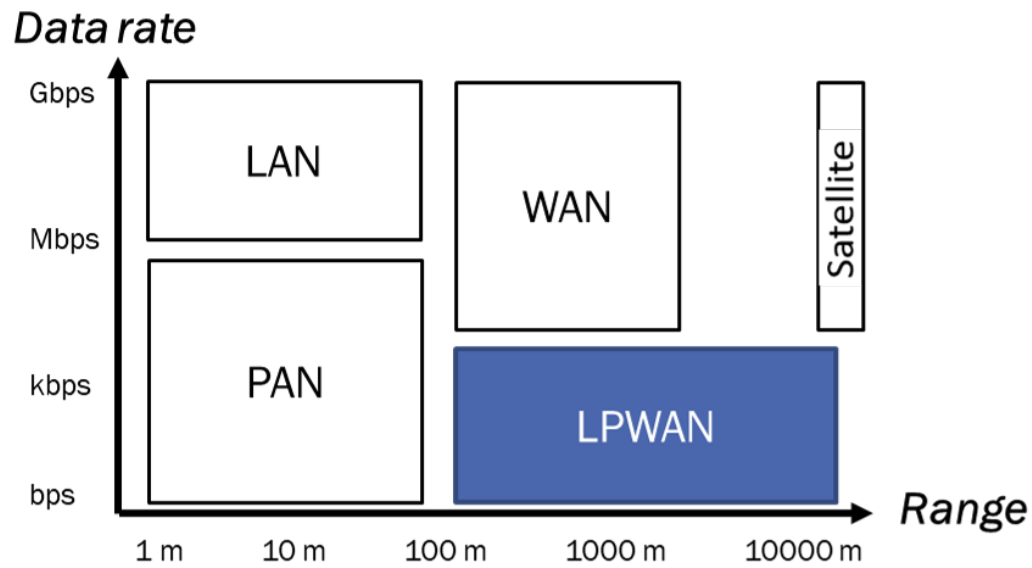
Figure A.1: A comparison between LPWAN and other communication technologies.

- Weightless-N, Weightless-P and Weightless-W [260].

- Ingenu, formerly known as On-Ramp Wireless [260, 264].

- DASH7 [265, 266, 267].

- Nwave [261].

- Neul [261].

- LTE-M, also known as LTE Cat-M1 [259, 268, 269].

Aside from the listed main LPWANs, a lot of less common options are available (e.g.: LTE Cat 0, Wireless-M bus) [270]. The aforementioned technologies are very different from each other: the most of them works in unlicensed sub-GHz bands (LoRa, Sigfox), but some of them work in licensed (NB-IoT) or whitespace (Neul, Weightless-W) bands; they can be either fully bidirectional (Neul, LoRa) or support uplink only (Sigfox, Weightless-N); some can have adaptive data rate (LoRa, Weightless-P), others have a fixed rate (Nwave).

Most of the LPWAN operate using a star topology network, which means that a device called *gateway* collects all the messages from the other devices, called end-devices (ED;
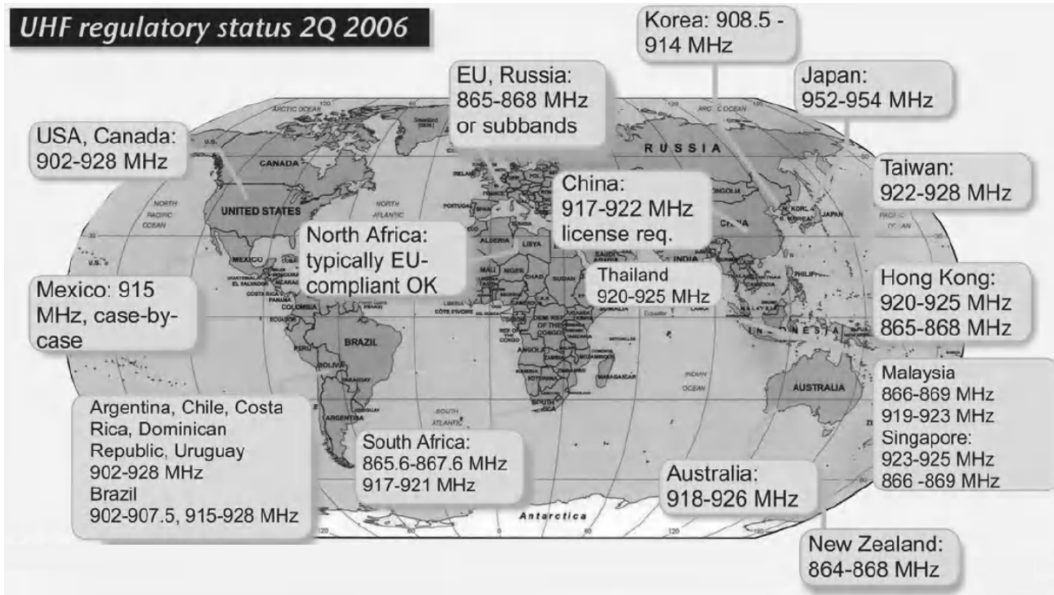
Figure A.2: The UHF bands between 864 and 954 MHz in the world. [272]

also called as *motes* or as *nodes*), and then forwards the messages to a network. In a star topology network, three kinds of links can be distinguished: the uplink, from a mote to the gateway; the downlink, from the gateway to a mote; the backhaul connection, from the gateway to the network. A single gateway can collect messages from thousands of EDs [271] and can use LAN (e.g. Ethernet), WLAN (wireless local area network; e.g. WI-Fi) or LTE (Long Term Evolution) for the back-haul link Although most of the LPWANs are fully bi-directional, as to say the gateway can communicate to every mote, usually the downlink is reserved only for parameters settings controlled by the gateways.

The systems operating in unlicensed bands like the 865.600 - 867.600 MHz and 433.050-434.790 MHz EU bands don't have to pay to use those bands, but the unlicensed bands differ from a country to another, as shown in Fig. A.2. Because of the variation of the bands the hardware can typically be used only in a specific world region. Moreover, the unlicensed bands have harsh limitations of duty cycle and input power: as for example, the ETSI (European Telecommunications Standards Institute) in ETSI[EN300.220] imposes a limitation in most of the EU 863-870 subbands of 1% as maximum duty cycle and a maximum ERP (effective/equivalent radiating power) of 25 mW. Because of the regulations, the LPWAN operating in unlicensed bands have a reduced cost and bitrate respect to those

Table A.1: Frequency bands for non-specific short-range devices in Europe.

Frequency Band	ERP	Duty Cycle	Channel Bandwidth	Remarks
433.05 – 434.79 MHz	+10 dBm	<10%	No limits	No audio and voice
433.05 – 434.79 MHz	0 dBm	No limits	No limits	≤– 13 dBm/10 kHz, no audio and voice
433.05 – 434.79 MHz	+10 dBm	No limits	<25 kHz	No audio and voice
868 – 868.6 MHz	+14 dBm	< 1%	No limits	
868.7 – 869.2 MHz	+14 dBm	< 0.1%	No limits	
869.3 – 869.4 MHz	+10 dBm	No limits	< 25 kHz	Appropriate access protocol required
869.4 – 869.65 MHz	+27 dBm	< 10%	< 25 kHz	Channels may be combined to one high speed channel
869.7 -870 MHz	+7 dBm	No limits	No limits	
2400 – 2483.5 MHz	+7.85 dBm	No limits	No limits	Transmit power limit is 10-dBm EIRP

which work in licensed bands as NB-IoT. In the EU 868-870 MHz unlicensed band, the transmit power and duty cycle limitations change based on the subband used, as in Table A.1.

The LPWANs manage to achieve long ranges thanks to excellent sensitivities which can be lower than -145 dBm. Such a low sensitivity enables to receive a signal also using multipath channels, but, because of this, an evaluation of the position of the target based on the time of arrival is very inaccurate. As an example, a 125 kHz LoRa signal only has a multi-path resolution ability of about 1 km, so if there are any reflected paths with a length of less than one-kilometer different from the direct path, the estimated position of the signal source will be inaccurate [150]. A channel with a higher bandwidth has a better resolution ability, but has also a higher thermal noise and thus a worst link budget; this is why the LPWANs use very narrow channels, as the 100 Hz Sigfox ones. The localization of a source of RF signal will be useful for the LoRa-based B-IoT case study, and it is investigated in-depth in Chapter 7.

The LPWANs use slow modulation rates because of the Shannon-Hartley theorem which states that the energy per symbol (or energy per bit) is the main lever to change the possibility of a message being heard. By slowing the modulation rate by half, you are putting twice as much energy into each symbol; thus, you are increasing the link budget by double (3 dB). As an example, Sigfox has a modulation rate of 300 bps. Another common characteristic of the LPWAN is the use of coding which enables to detect the signals also with SNR (signal noise ratio) as low as -20 dB, thanks to the coding gain. A feature of

coded channels is orthogonality, which is detecting multiple data stream on the same channel and at the same time. This is achieved using different coding for different signals so that the signals appear as noise for each other. Accordingly, the common characteristic of the LPWAN technologies are:

1. long ranges and low power-consumption;

2. star topology networks;

3. slow modulation rates, thus low bit-rate and latency;

4. narrow channels;

5. coding gain;

6. orthogonality;

7. multipath communication channels.

LPWANs QoS (quality of service) can be evaluated based on three factors [218]:

1. packet reception rate (PRR; a.k.a. packet delivery rate, PDR) and packet loss ratio (PLR): percentage of received or lost packets in a transmission;

2. throughput: measured by comparing bit received with the elapsed time;

3. (time) delay: measured by counting the time needed to deliver 1 packet from the client to the gateway.

Cellular LPWAN: NB-IoT and LTE-M

Two of the LPWAN technologies listed in (Section 7.4) operate in the LTE spectrum and are cellular LPWAN technologies: NB-IoT and LTE-M. Respect to non-cellular LPWANs, cellular ones have the following characteristics:

1. higher data rate;

Table A.2: Cost of ED using non-cellular (Sigfox, LoRa) and cellular (NB-IoT) technologies [140].

	Spectrum cost	Deployment cost	End-device cost
Sigfox	Free	>4000€/base station	<2€
LoRaWAN	Free	>100€/gateway >1000€/base station	3-5€
NB-IoT	>500 M€ /MHz	>15000€/base station	>20€

Table A.3: Power consumption of cellular (NB-IoT, LTE Cat-M1) and non-cellular (LoRa) LPWANs [259].

	TX current	RX current	Idle current	Sleep current
Lo Ra	24-44 mA	12 mA	1.4 mA	0.1 μA
NB-IoT	74-220 mA	46 mA	6 mA	3 μA
Cellular LTE cat-M1	100-490 mA	Not specified	9 mA	8 μA

2. higher ED cost;

3. higher power consumption.

Cellular LPWANs have the highest data rate of all LPWANs and operate in licensed spectrum. Because a cellular LPWAN operates using the cellular base stations (BS) they don't need any gateway deployment where there's cellular network coverage, but if there isn't cellular coverage the needed BS deployment is very expensive. Moreover, the cost of an ED using a cellular LPWAN is noticeably higher, up to ten times (Fig. A.2). Cellular LPWANs have also a higher power consumption than non-cellular ones (Fig. A.3). Lastly, because of the licenses, an ED using LTE spectrum needs to pay a network provider in order to use its BS and private network deployment isn't allowed.

Given their characteristics, cellular LPWANs outperform non-cellular LPWANs when:

1. a relatively high data rate is valuable;

2. low latency is required;
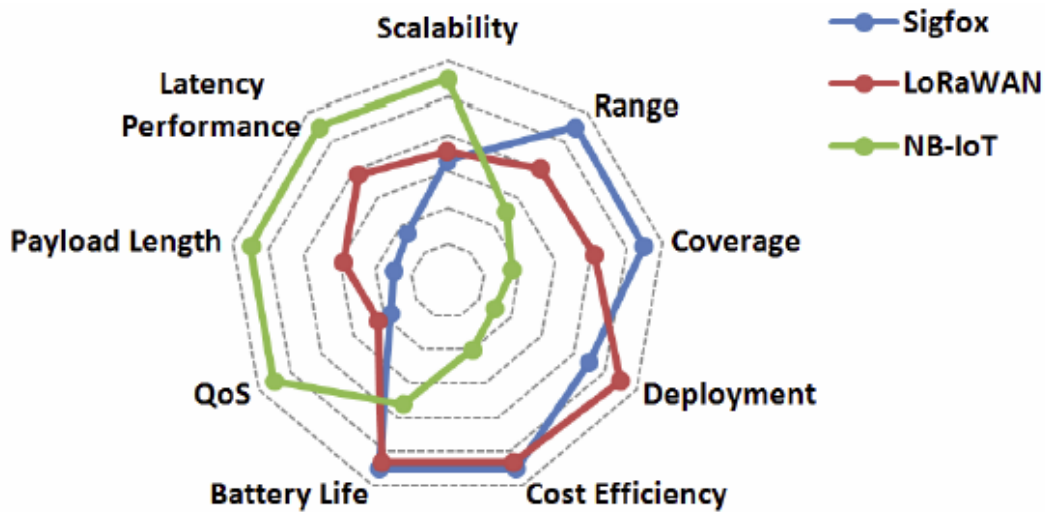
Figure A.3: A graph summing up the differences between cellular (NB-IoT) and non-cellular (LoRa, Sigfox) LPWANs [140].

3. the LPWAN can be more expensive, both because of the network provider subscription and the ED cost;

4. reduced battery life isn't a problem;

5. cellular network coverage is available.

The differences between cellular and non-cellular LPWANs is well represented by the Kiavat diagram in Fig. A.3 which compares the cellular LPWAN NB-IoT with the non-cellular LPWANs LoRa and Sigfox.

Appendix B - Golden Standard of Wireless Devices for Mountain SaR

The mountain SaR operations are very common because of the harsh environment and innumerable mountain activities. For instance, only in France, during the 2012, a number of 5,389 mountain SaR operations was recorded [273] solely for the accidents caused by mountain sports. The golden standard wireless devices widely employed to foster mountain SaR actions are the avalanches beacons and the RECCO® EM system.

Mountain SaR Operations

Mountain SaR operations differ greatly based on the snow presence or absence.

In absence of snow, SaR operation are considerably simpler, and they become usually search-only or rescue-only mission. For example, in Adirondack Park, United States, between years 2008-2009 the 53% of SaR operation carried out were exclusively search, and the 38% were exclusively rescued [274]. Most of the victims are usually hikers [275] and suffer from different kinds of trauma, usually involving the head, or illness [276]. Helicopters are commonly used in mountain SaR operations [277, 278] and camera-equipped UAVs were used for death confirmation in canyons and to explore wide areas [279]. Commonly, helicopters, dogs and cellular systems equipped with GPS if cellular coverage is present are used [280, 281].

The SaR problem in presence of snow is much more complex due to the harsh environmental conditions, especially for the EM power absorption that can jam wireless communications used for the SaR. The most critical scenario is the avalanche one, which is the most

different from the snow-less one. Furthermore, the avalanche death toll is rising around the world in recent years [282] as consequence of the global warming. In [283] the following statistic about avalanche victims are reported.

- More than 150 persons die annually because of avalanches in North America and Europe only.

- The overall survival rate of avalanche victims is approximately 46%.

- Avalanche transceivers and standard rescue equipment (as probe and shovel) increase the chance of survival by reducing the time of extrication.

- In a sample of completely buried avalanche victims, those located via avalanche transceiver had a relative reduction in mortality of 74% (95% confidence interval, 52% to 86%) compared with those located without a transceiver.

- In an in-field survey of back-country users, 75% of mountain recreationists carried an avalanche transceiver and 66% carried standard rescue equipment.

- In another sample of completely buried avalanche victims, 44% of them didn't have a transceiver.

- Off-piste skiers, descend outside the secured ski area, are less frequently equipped with rescue devices.

In addition, a 50x70 m^2 area is the natural deposit of a human-triggered avalanches [284], and the probability of survival is estimated to decrease from 90 to 40 and 30 per cent, if the extrication time is 15, 30 and 60 minutes, respectively [189]. Of 65 avalanche victims dead in Utah between 1989 and 2006, 85.7% of died due to asphyxiation, 8.9% due to a combination of asphyxiation and trauma, and 5.4% due to trauma alone (usually head injuries) [285]. Asphyxia is the commonest cause of death due to the CO_2 concentration. In [251] the median burial depth of 729 avalanche victims who couldn't free themselves is estimated to be 1 m, while the maximum burial depth registered for a survived victim is around 7 meters. The median burial time of those victims who weren't visible nor couldn't free themselves is 60 minutes, but the median burial time of all surviving people is only

11 minutes. Is noticeable that the survival chance of people rescued by companions was evaluated as 71.3%, more than 4 times the survival chance of people rescued by rescue teams (17.7%) because of the significantly faster operation.

Avalanches which cause multiple buried victims, as to say multiple victims without any visible part over the snow, are relatively rare. Of the 432 avalanches reported in the Tyrol region between the years 1997 and 2003, only 8 avalanches caused multiple burial (4.3% of total cases which implied at least one burial) [286] while in Switzerland the multiple burials scenarios between 1970 and 1999 reached 27.4% of the total cases [287].

Current Wireless Devices for Mountain SaR Operations

Due to the mortality because of avalanches, ad-hoc wireless devices were developed to foster SaR missions in the last decades. They most important and common ones are the avalanches beacons and the RECCO®.

Avalanche Beacon: ARVA

Also known as ARTVA (*Apparecchio di Ricerca dei Travolti in VAlanga*; Italian acronym), DVA (*Détecteur de Victime d'Avalanche*; French acronym)*, or more commonly as ARVA (*Appareil de Recherche de Victimes d'Avalanche*; another French acronym), an avalanche beacon is a transceiver which emits low-power pulses at the international standard frequency of 457 kHz ± 80 Hz. The pulse width is in interval 70-900 milliseconds, with a duty cycle in the range 10-69%. The transmitted field power must be in the range $[-6; -7]$ dBµA/m below 30 MHz at a distance of 10 m; even though formulas to evaluate the transmitted power using EIRP were proposed in [288], they are not used for regulations. Frequency, pulse width, duty cycle and transmitted power are regulated by ETSI standard EN 300 718 in the EU [289]. Due to the low frequency, the ARVAs are near-field systems and their pulses can penetrate well the dry snow. even in the case of deep burials, achieving a detection range of around 60 meters. ARVAs are usually modeled as magnetic dipoles which work in near field [290].

An avalanche beacon works in two modes.

1. Transmitting mode: in transmitting mode the ARVA emits the low power pulses until it runs off of the battery.

2. Receiving mode: if an avalanche occurs, the ARVA can be switched to receiving mode. In this mode, the avalanche beacon doesn't transmit and listen to find other ARVA pulses, in order to give to the user feedback about the location of the other ARVAs giving acoustic feedback about the distance from the other ARVA.

Using an avalanche beacon in receiving mode to find a transmitting ARVA can be difficult, and in multiple burial scenarios, a special technique is required to not have the buried ARVAs interfere with each other. The best upside of ARVA is that everyone can use it to transmit and receive; since usually an avalanche doesn't bury an entire group of people, whoever wasn't run over by the avalanche can switch his ARVA to receiving mode and start the rescue operations as soon as possible, and he/she has good probability of saving the avalanche victims in the first critical 30 minutes using the ARVA to localise the victim, a probe to find where to excavate and then a shovel for the extraction.

There are both analogue and digital avalanche beacons. In order to detect multi targets, the modern digital devices use two or three antennas, and by means of digital signal processing they can evaluate the direction and the distance of the buried transmitters. High-class avalanche beacons can use another frequency band in UHF to communicate information as the owner name and his vital signs, such as heartbeat or micro-movements. This optional communication link, named *W-Link*, is strongly criticized for its moral implication (for instance, someone could ignore the nearest victim to find a relative) and was banned in some countries (China, Russia, various countries in Asia and Eastern Europe) [189]. To not create a moral dilemma, the manufacturers excluded the identification through W-link, and no available commercial ARVA allows user identification through RF at the time of writing.

RECCO® system

The RECCO® system is commercially available since 1980 and today is used by more than 700 mountain rescue teams around the world. The system is composed by a wearable passive tag (called the *reflector)* and a portable reader (called the *interrogator*), used by
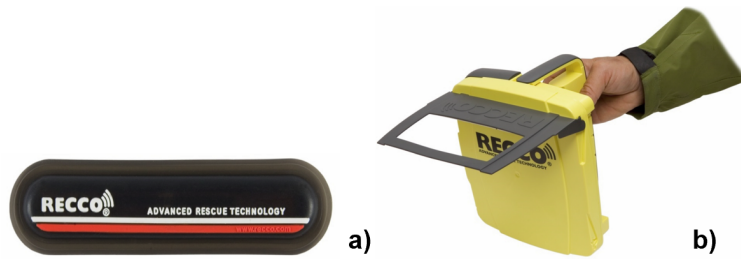
Figure B.1: RECCO® system. (a) Reflector and (b) interrogator (version R9).

the rescuer to localise the tag of the avalanche victims. The interrogator sends to the tag a signal in the unlicensed UHF band using 5 W of power, then the tag receives the signal and double-ups its frequency [291]. When the interrogator receives a signal whose frequency is double than that of the transmitted signal, it gives acoustic feedback through earphones, so that the searcher can find the buried tag. The tag is small and thin and it is usually embedded in clothes Fig. B.1(a). The passive reflector is made of a pair of foil aerials joined by a diode, which doubles up the frequency of the received signal. The size of the aerials makes the unit a tuned circuit resonating at the working frequency and the diode generates harmonics when it is hit by the radar signal. The interrogator is hand-held Fig. B.1(b) and uses a very directive antenna. As an example, the version R9 of the interrogator uses a Yagi-Uda antenna [292]. As ARVAs without W-link, the reflector doesn't communicate any identification signal so the rescue team has to be careful to avoid interference between the buried reflector and reflectors of the rescue team itself. The R9 detector can find a reflector distant up to 120 meters in air and up to 20 meters in dry snow (10 meters in wet snow). The RECCO® system has thus a localization distance of 120 meters in the air, 20 meters in dry snow, 10 meters in wet snow and 0.2 meters when the reflector is underwater [293]. Although high-tier interrogators can theoretically be used from a helicopter, the reading distance is a harsh limitation for the RECCO® system.

Appendix C - Fundamentals of Radiowave Propagation

Path Loss and Attenuation

The large-scale propagation models most used are the *free-space propagation model* and the *log-distance path loss propagation model* (a.k.a. *lognormal model*) [294]. They are based on the Path Loss (PL) L, defined as the dB ratio of the transmitted and received power under the hypothesis of isotropic antennas, null mismatch losses and polarization loss factor equal to zero:

$$L = 10 \cdot \log_{10} \left(\frac{W_T}{W_R} \right) \tag{7.28}$$

where W_T and W_R are the transmitted and received powers in linear scale, respectively. In other words, the PL accounts only for the signal attenuation due to the distances. The attenuation A is defined as the opposite of the path loss in dB scale:

$$A = -L \tag{7.29}$$

so that $L > 0$ and $A < 0$. In particular, the free-space path loss in a weakening of the RF signal due to a broadening of the wave front.

Free-space Propagation and Flat-earth Two-ray Model

It is an ideal model for an LoS path between a T-R unit in free space. In this case, the Friis transmission equation is valid:

$$W_R(d) = W_T \tilde{G}_R \tilde{G}_T \eta_P \left(\frac{\lambda}{4\pi d} \right)^2 \tag{7.30}$$

where W_R is the received power in linear scale, W_T is the transmitted power in linear scale, $\tilde{G}_R$ and $\tilde{G}_T$ are the realized gains of the receiving and the transmitting antenna respectively, η_P is the Polarization Loss Factor (PLF), λ is the wavelength, d is the T-R distance. The *free-space loss L_{fs}* is defined in eq. (7.28), thus from (7.30):

$$L_{fs}\big|_{dB} = 10 \cdot \log \left(\frac{\tilde{G}_R \tilde{G}_T \eta_P W_T}{W_R} \right) = 20 \cdot \log \left(\frac{4\pi d}{\lambda} \right) \tag{7.31}$$

For instance, from eq. (7.31), the $PL(d_0)$ at the LoRa UHF center-band frequency of 868 MHz is equal to 31.24 dB.

However, the free-space propagation discussed above is a single-ray propagation model, i.e. it assumes no copy of the same signal is simultaneously received. In real terrestrial links, this assumption holds rarely, and multiple copies of the signal simultaneously reach the receiver and interfere with the transmitted wave due to the surroundings. The flat-earth two-ray model (FE2R) is the most simple multi-path model, as it assumes the propagation taking place in the free-space aside from a flat infinite earth on whom the antennas are placed. Let's consider the radio-link in Fig. C.1, composed by two directive transceiver antennas with a T-R distance d. Supposing the link reciprocal, we can consider without loss of generality the case in which the antenna 1 is transmitting and the antenna 2 is receiving. Moreover, if D_x is the dominant dimension of the antenna x, is true that $min(h_1, h_2) \gg max(D_1, D_2)$, and that $d \gg max(h_1, h_2)$. We assume that the surface waves propagation is neglectable because $d \gg \lambda$. In order to proceed with the analysis, we assume the following six hypotheses:

1. the terrain reflection is localized in a little zone with respect to d_1 and d_2;

2. because of the length d, $\underline{E}_d$ and $\underline{E}_r$ in Fig. C.1 are both plane waves;
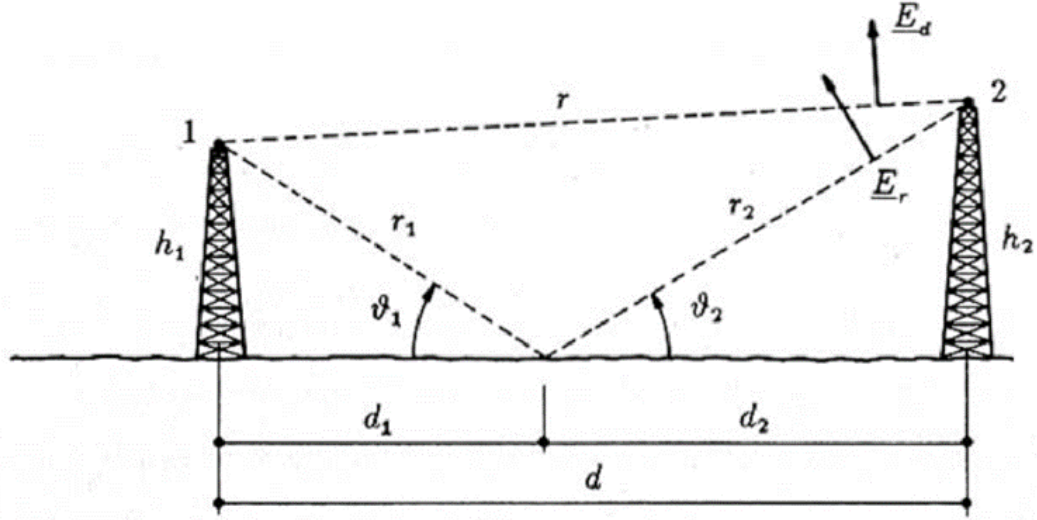
Figure C.1: FE2R model with the direct-ray (ray-path r) and the reflected ray (ray-path $r_1 + r_2$) [295].

3. the terrain is smooth, so $\theta_1 = \theta_2$ and $h_2/d_2 = h_1/d_1$;

4. total reflection, i.e. $q \approx -1$ (this approximation is good when the grazing angle θ is smaller than 1°; for larger angles, the reflection coefficient for the vertical polarization may depart appreciably from -1, whereas for the horizontal polarization the approximation is still good approximately up to 10°);

5. the surface bending along d is neglectable;

6. the atmospheric effects are neglectable.

The total field near the antenna 2 $\underline{E_2}$ can be expressed in vectorial form as:

$$\underline{E_2} = \underline{E_d} + \underline{E_r} \tag{7.32}$$

Considering a vectorial constant $\underline{C_E}$, because of the length of d the angle θ_1 is little and we can write the fields $\underline{E_d}$ and $\underline{E_r}$ as:

$$\underline{E_d} = \underline{C_E} * \exp\left(-j\beta r\right) * r^{-1} \tag{7.33}$$

241

$$\underline{E_r} = q\underline{C_E} * \exp\left[-j\beta\left(r_1 + r_2\right)\right] * \left(r_1 + r_2\right)^{-1} \approx$$
$$\approx -\underline{C_E} * \exp\left[-j\beta\left(r_1 + r_2\right)\right] * \left(r_1 + r_2\right)^{-1} \tag{7.34}$$

where $\beta = 2\pi/\lambda$ is the propagation constant. Supposing d long enough, we can suppose $r \approx r_1 + r_2$, so that $\left|\underline{E_r}\right| = \left|\underline{E_d}\right|$. Regarding the phases, even little differences in the path can correspond to multiple periodicity, since $r_1 + r_2 \gg \lambda$. Therefore, from equations (7.32), (7.33) and (7.34):

$$\underline{E_2} = \frac{\underline{C_E}}{r}\left\{\exp\left(-j\beta r\right) - \exp\left[-j\beta\left(r_1 + r_2\right)\right]\right\} \tag{7.35}$$

from (7.33):

$$\left|\underline{E_2}\right| = \left|\underline{E_d}\right|\left|1 - \exp\left[-j\beta\left(r_1 + r_2 - r\right)\right]\right| \tag{7.36}$$

Since $d \gg max\left(h_1, h_2\right)$, from the Taylor approximation $\sqrt{1 + x} \approx 1 + \frac{x}{2}$:

$$r = \sqrt{d^2 + \left(h_2 - h_1\right)^2} \approx d\left[1 + \frac{\left(h_1 + h_2\right)^2}{2d^2}\right], \tag{7.37}$$

$$r_1 + r_2 = \sqrt{d^2 + \left(h_2 + h_1\right)^2} \approx d\left[1 + \frac{\left(h_1 + h_2\right)^2}{2d^2}\right]. \tag{7.38}$$

From eq. (7.37) and (7.38):

$$r_1 + r_2 - r \approx \frac{2h_1h_2}{d}. \tag{7.39}$$

Therefore, by inserting (7.39) in (7.36) :

$$\left|\underline{E_2}\right| = \left|\underline{E_d}\right|\left|1 - \exp\left[-j\beta\frac{2h_1h_2}{d}\right]\right| = 2\left|\underline{E_d}\right|\left|sin\left(\beta\frac{h_1h_2}{d}\right)\right|. \tag{7.40}$$

Accordingly, the module of the wave near antenna 2 goes from 0 (destructive interference) to $2\left|\underline{E_d}\right|$ (constructive interference) depending on the interference between $\underline{E_d}$ and $\underline{E_r}$. From (7.40), the nulls are equispaced increasing one h, whereas the distance between the nulls increases together with d. The can also eq. (7.40) be written as

$$\left| \underline{E_2} \right| = \left| \sqrt{G_1 \left(\theta_{s,1} \right) G_2 \left(\theta_{s,2} \right)} \frac{e^{-j\beta r}}{4\pi r} \right| F \tag{7.41}$$

where $G_x \left(\theta_x \right)$ are the gain of the antennas in the LoS direction and F is called *path-gain factor*. Accordingly, the general expression of the path-gain factor for the FE2R model is

$$F = \left| 1 + \rho e^{i\phi} \sqrt{\frac{G_1 \left(\theta_{r.1} \right) G_2 \left(\theta_{r.2} \right)}{G_1 \left(\theta_{s.1} \right) G_2 \left(\theta_{s.2} \right)}} e^{-j\beta \left(r - r_1 - r_2 \right)} \right| \tag{7.42}$$

where $\rho e^{j\phi}$ is the *Fresnel's reflection coefficient* determined by the electric characteristics of the ground and the polarization of the electromagnetic wave being reflected . Naturally, (7.42), in the particular case of (7.40), becomes

$$F = 2 \left| \sin \left(\beta \frac{h_1 h_2}{d} \right) \right| . \tag{7.43}$$

Log-distance Path Loss Propagation Model

Theoretical and measurement-based models developed in generic environments indicate that the average received signal power decreases with the distance raised to some exponent [296]. In the log-distance path loss propagation model the average path loss $L_{P,mean} \left(d \right)$ is a function of the distance with a *path loss exponent n*:

$$L_{P,mean} \left(d \right) \propto \left(\frac{d}{d_0} \right)^n \tag{7.44}$$

where d_0 is called the *free space close-in reference distance* [296]. The reference distance should always be in the far-field of the antenna ($d_0 > 2D^2/\lambda$, D largest dimension of the antenna) so that near-field effects can be neglected in the model. Is worth noting that, although in the free-space model $n = 2$, values of n less than 2 were estimated as in [296] ($n = 1.6$ in buildings, LOS) and [141] ($n = 1.76$, the transmitter on a boat, the receiver on a roof, LOS). Values of n between 1.5 and 5 were evaluated for mobile phone links [297]. Some values of n are reported in Table C.1.

The mean path loss value expressed in dB is:

Table C.1: Path loss exponent values for different environments [296].

Environment	Path Loss Exponent, n
Free space	2
Urban area cellular radio	2.7 to 3.5
Shadowed urban cellular radio	3 to 5
In building, line of sight	1.6 to 1.8
Obstructed in building	4 to 6
Obstructed in factories	2 to 3

$$L_{P,mean}\big|_{dB} = L_{fs}(d_0)\big|_{dB} + 10n \cdot \log_{10}\left(\frac{d}{d_0}\right) \tag{7.45}$$

where the reference distance path loss is given by (7.31). The path loss can be expressed in terms of the mean plus a random variable X_σ accounting for the difference between the actual, instantaneous PL and the mean PL [298]:

$$L_P\big|_{dB} = L_{P,mean}\big|_{dB} + X_\sigma\big|_{dB} = L_{fs}(d_0)\big|_{dB} + 10n \cdot \log_{10}\left(\frac{d}{d_0}\right) + X_\sigma\big|_{dB}. \tag{7.46}$$

Lastly, X_σ has two main components [221]:

1. large-scale fluctuations that happens over distances longer than few units of wavelength. These fluctuations are zero-mean Gaussian in the log-distance plane (from whom the alternative name "lognormal PL model"), and are usually attributed to the shadow fading even in LoS conditions [184];

2. small-scale fluctuations, that take place over distances of few wavelengths or shorter, are caused by the interactions between the electromagnetic wave and the surroundings, and can unpredictably vary the signal power level up to 40 dB [221].

The PL at the reference distance given by (7.31) can be substituted by measured values after measurement campaigns, too.
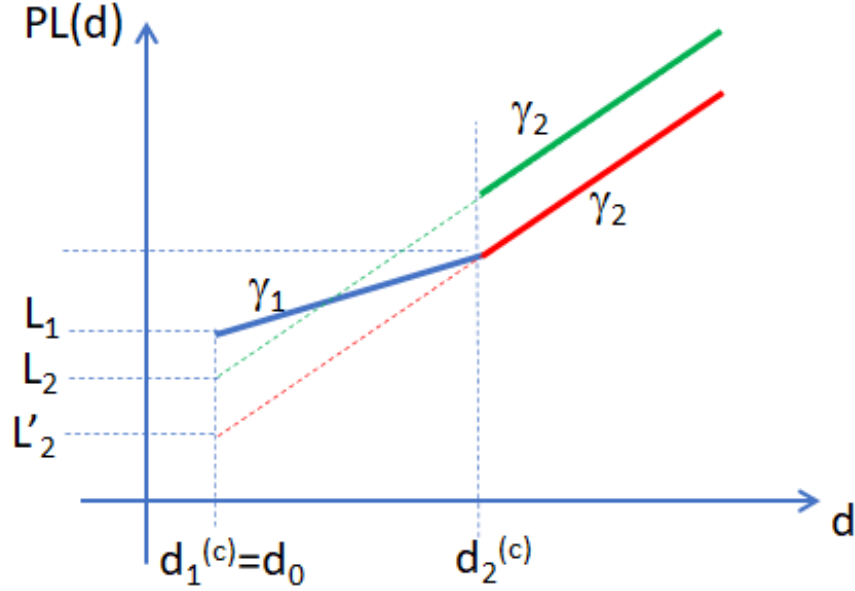
Figure C.2: A pictorial example of dual-slope PL models according to (7.47).

The mean log-distance PL model can be generalized to a multi-slope model including multiple distance-power gradients [299], namely

$$PL_m(d) = \left\{ L_k + 10\gamma_k \cdot \log_{10}\left(\frac{d}{d_0}\right), \ d_k^{(c)} \le d < d_{k+1}^{(c)} \right\} \tag{7.47}$$

and $k = 1, 2, \ldots, K$, where γ_k is the k-th PLE, $d_{K+1}^{(c)} = \infty$, $d_1^{(c)} \ge d_0$, and $\{d_k^{(c)}\}$ are named *critical distances* [237, 300], or breakpoints. In the following, $d_1^{(c)} = d_0$ are assumed to simplify the notation, notwithstanding that d_0 must be longer than the Fraunhofer's limit.

The different PLEs γ_k, $k = 1, 2, \ldots, K$ in (7.47) account for the propagation in various mediums and different configurations of obstacles around the receiver, causing distinct multipath effects. From (7.47), the mean of the PL is expected to follow a piecewise-linear function [301], and the PL slope changes at distances $d_k^{(c)}$, $k = 1, 2, \ldots, K$. With the considered formulation, discontinuous behavior of the mean PL at the critical distances $d_k^{(c)}$ is allowed (Fig. C.2). The model can be further generalized to include the eventual PL's angular dependence by introducing *critical angles* $\delta_k^{(c)}$ similar to the critical distances and

245
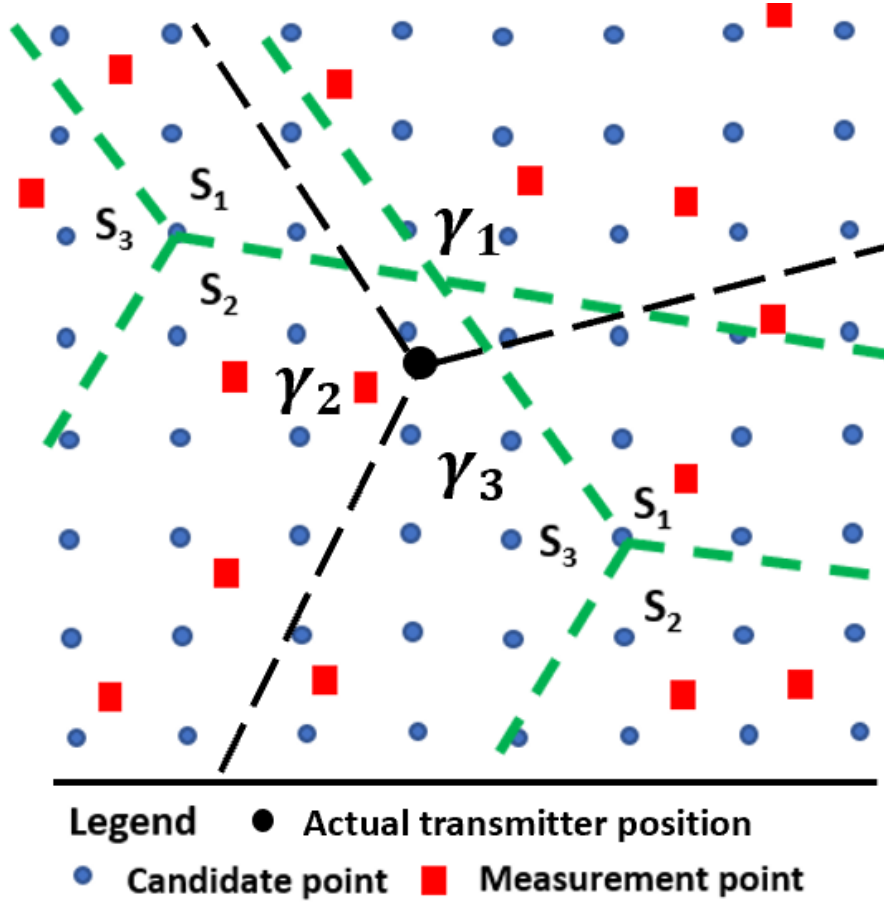
Figure C.3: A scheme of an angular-dependent multi-slope path-loss for two critical angles (120 and 240 degrees by selecting the proper reference null angle)

accounting from different environments (Fig. C.3) [245]. In Table C.2, some references to other works considering empirical multi-slope PL models are reported. All of these models can be re-formulated as in (7.47). From a thorough search of the relevant literature, $K \leq 4$ is found, albeit $K > 4$ is theoretically possible.

In these cases, the EM wave propagates in an environment, then passes through an obstacle, and lastly, it propagates in a new environment. The two environments can be accounted for using a different EPL, whereas the obstacle generates the discontinuity in the PL model named entry loss. A typical example of this condition is an EM wave traveling from a cellular base station to an indoor device.

Table C.2: Selected empirical multi-slope path loss models.

Model	Environment (frequency)	K	Continuous model	Angular dependence
[240]	Indoor (900 MHz)	4	Yes	No
[245]	Urban (900 MHz)	4	No	Yes
[241]	Railway (28 GHz)	3	Yes	No
[242]	Indoor (27.5 GHz)	2	No	No
[244]	Orchad (5.8 GHz)	2	No	No
[243]	Tunnel (900 MHz)	2	No	No

Appendix D - Signal-based Localization and Key Performance Indicators

Signal-based Localization Techniques

The signal-based localization of transmitters (usually called *target*) is a long-researched topic, whose applications are innumerable and origins root in the radar systems and the triangulation algorithms. For example, the signal-based localization of a transmitter was proposed for vehicular localization purposes in 1969 [302] when for the fist time the localization based on the fingerprint (see Section 7.4) was tried at the frequency of 161.49 MHz. Because of its long history and importance, several reviews [303, 304, 305, 306] and books [307, 299, 308] dedicated to comprehensively analyze the topic exist. The signal-based techniques are can be categorized in ToA (time of arrival), TDoA (time difference of arrival), DoA (direction of arrival, also known as AoA, angle of arrival), RSS (received signal strength) and their hybrids [309]. The working principles of the four basic categories are resumed in Fig. D.1.

This Appendix introduces the working principles of signal-based methods and focuses on the RSS techniques that don't require any antenna array nor high-precision synchronization and, thus, are low-requirement candidates for localization [309, 310].

ToA, TDoA, and DoA

The ToA, TDoA and DoA methods usually require either antennas arrays [311], special ad hoc antennas [312], and/or high-precision synchronization [313].
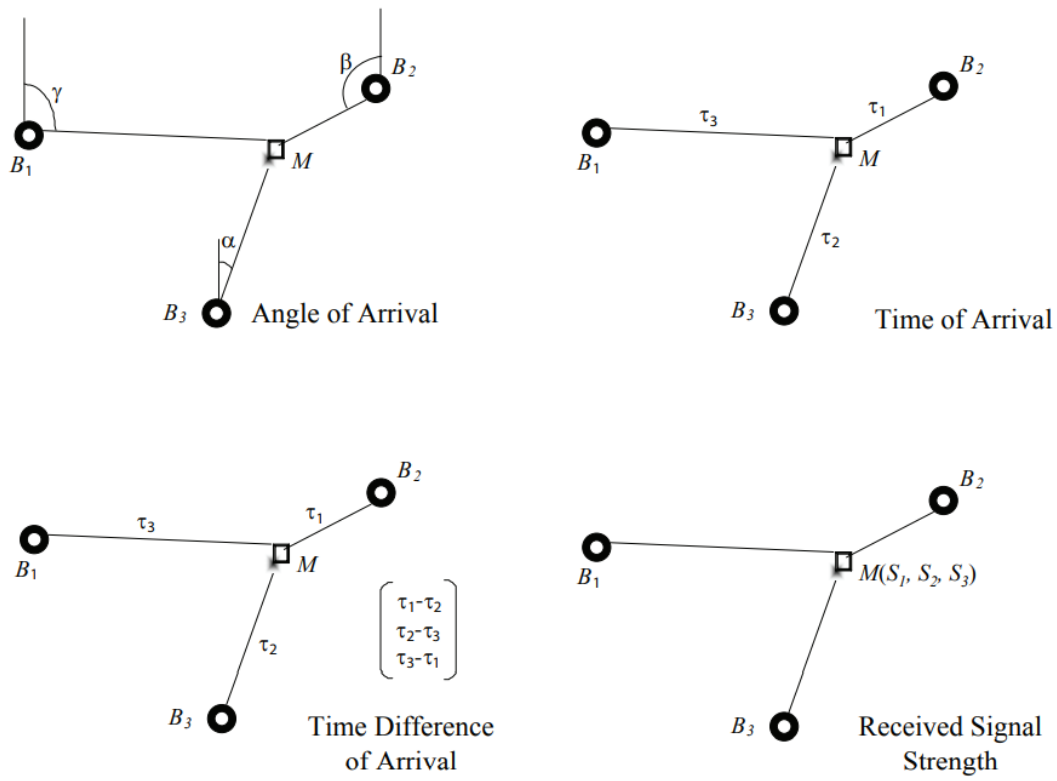
Figure D.1: Principle scheme of AoA, ToA, TDoA, and RSS localization techniques [308].
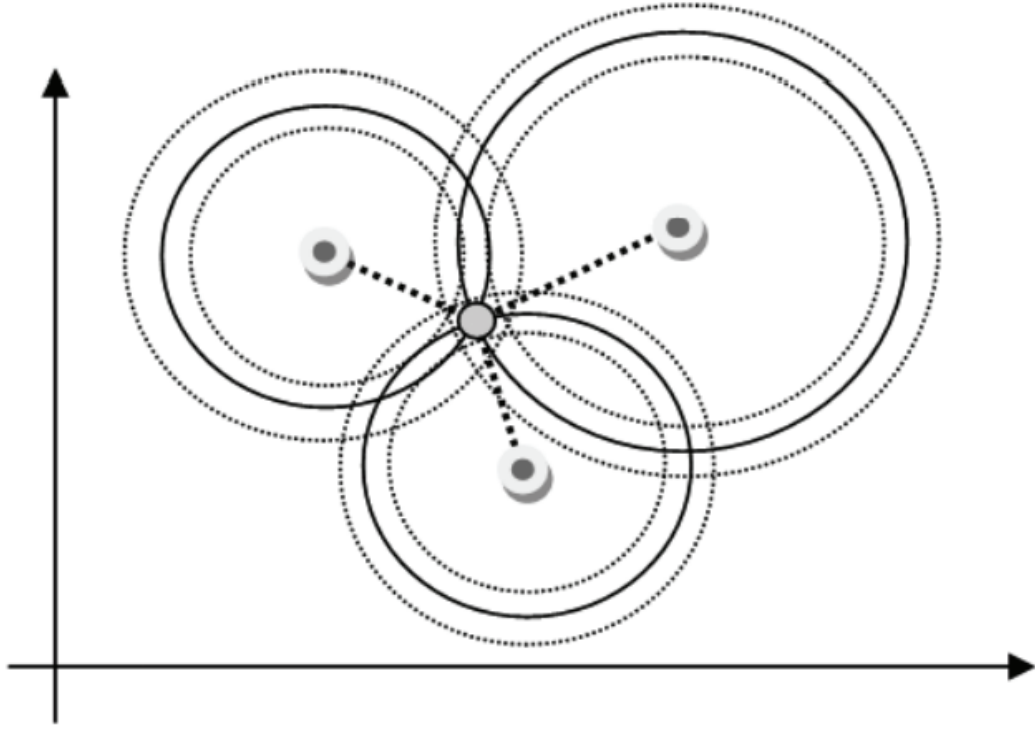
Figure D.2: Position estimation by trilateration [309]. The target node is the gray one, and the intersection between the circles are the indicate the estimated position and the relative uncertainty [308].

Time of Arrival

ToA systems utilize the time the signals spends traveling from the transmitter to the receiver τ_{ToA} to estimate the Tx-Rx distance. From the known speed of the RF signal, the range r from the receiver is evaluated as $r = \tau_{ToA}c$ being c the RF signal speed in the interposed medium. Naturally, only the LoS direct-path ToA is considered in multipath environments [308]. Accordingly, three nodes are sufficient for the localization (Fig. D.2), although additional nodes allows for an increased accuracy. The localization accuracy greatly depend on the clock synchronization, which can be achieved by data exchange or a supplementary, appropriate node. The GPS system uses a fourth node to compensate for the receiver clock bias of the three localizing nodes. Several methods to accurately estimate τ_{ToA} exists, like the inverse Fourier transform, and the maximum-likelihood estimation [308].
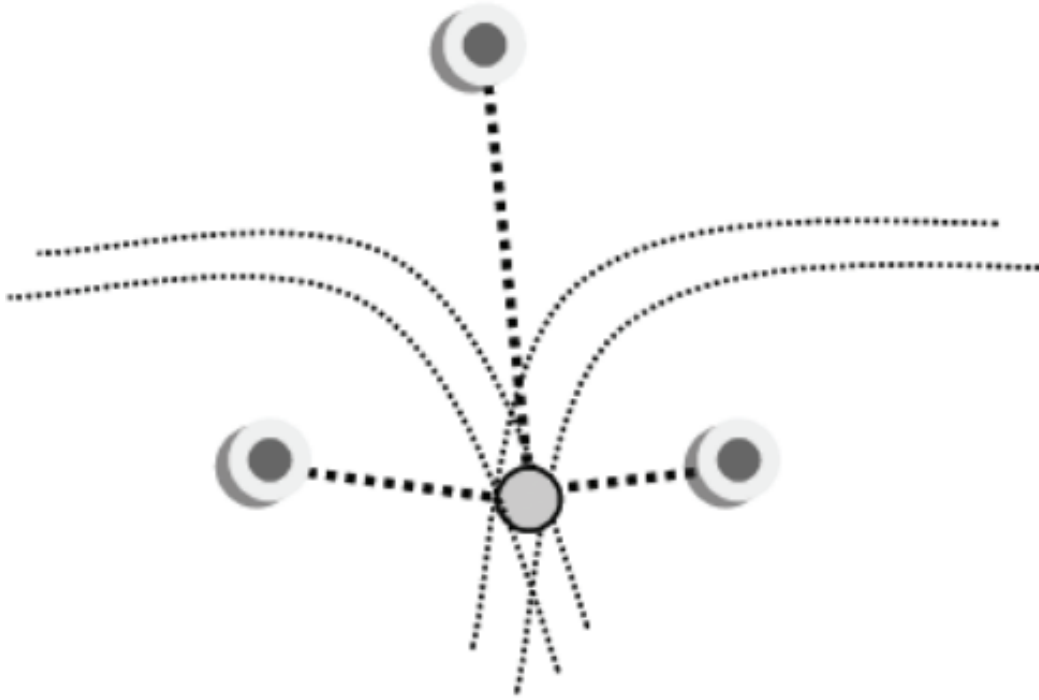
Figure D.3: Hyperbolic localization. The gray circle is the target node to be localized.

Time Difference of Arrival

The TDoA removes the clocks biases by exploiting the difference in the estimated ToA by different receivers. This method is also known as *hyperbolic positioning* for its geometrical interpretation (Fig. D.3) and its estimation is more dependent on the receiver's geometry than the classic ToA [314].

Direction (Angle) of Arrival

DoA localization exploits the received signal angle of arrival, which univocally determines a direction, with respect to a reference direction called orientation [304]. The most common approach consists in placing an array in each sensor node to identify the angular sector of the signal. After the determination of the DoA, the coordinates of the transmitter are estimated by triangulation algorithm as, for instance, [315].

The main DoA limitation is that special antennas are required [304, 305] in each of the anchor nodes, that have to be three or more. As effect of the noise, typical angle measurement errors are comprised between 1° and 25°. Because of the expensive antennas required, DoA is generally used in base station or cell phone towers [304].

RSS-based

The RSS methods can either being *range-free,* namely *fingerprint* or *proximity-based,* or *range-based* [309]. The range-based algorithm can be further partitioned based on the knowledge on the radiopropagation of the area (known and unknown PL) and if the differential RSS (DRSS) is utilized. Among the RSS range-based with unknown distance-power gradient (RSS-UDPG) [234], special attention deserve the grid-based methods thanks to their stability respect nonlinear methods, as detailed next.

Range-free Techniques

Range-free techniques do not require any range estimation since they don't perform any lateration.

Fingerprint   Severe multipath negating the LoS condition can hinder the localization based on lateration and the fingerprint method was developed to overcome this limitation. The fingerprint method is a scene-matching consisting in measuring the RSS on a grid superposed to the search area, and then select the most similar value of the grid as estimated position. This technique was the first proposed as RSS-based localization system [302] and the fingerprint name is documented later [316] when the approach became more common. The main limitation of fingerprint localization is the training phase required for creating the radiomap of the area. Beside being a process more time consuming and memory-expensive the more the search area is wide, it has to be repeated whenever a significant change in the area happens. Because of this reason, fingerprinting is impossible to apply for SaR operation after natural disasters like avalanches.

Proximity-based Proximity-based methods estimate the target position based on which anchors can detect its signal. In other words, it is a connectivity-based technique [309]. Naturally, this approach is effective if many anchor nodes are available in a dense network.

Range-based Techniques

The range-based techniques estimate the distance between the transmitter and some nodes whose positions are known (such nodes are named *anchor points* or *anchors*) to evaluate the target's position by lateration. The range is calculated from the RSS and the PL model of the search area. The PL is usually assumed log-distance. The difference between the mean model and the actual RSS measured is included in the lognormal shadow fading. Aside from the shadow fading, many other factors can cause differences, such as cable losses, deformation in the radiation patterns, and variable polarization losses. These factors added to the shadowing fluctuations can be labeled *additional noise.* Whereas the shadow fading is typical of a search area, the additional noise is for the most part a characteristic of the measurement set-up.

Known PL These algorithms were the first to be developed and exploit the a priori knowledge of the PL model of the search area to localize the transmitter. The PL of the search can be either evaluated right before the search procedure using the links between the anchor points, or evaluated before in a training phase. For example, in [317] and in [248] the anchor nodes estimate the log-distance PL model of the search area, and then the transmitter is localized. This approach can be exploited also with propagation model different from the empirical log-distance one, like, for example, the Okumura-Hata [227, 318].

Unknown PL (UDPG) The hypothesis of good previous knowledge of the area's radio-propagation was removed in the first 2000's. In [234], the RSS-based problem without any knowledge of the PL model in the search areas was formulated and named RSS-UDPG. The RSS-UDPG localization problem is defined as the jointly estimation of the log-distance PL model parameters and the target's position. Therefore, the classic localization problem having only spatial coordinates unknown is generalized to be applied for every search area

254

through an equivalent unknown log-distance model. The RSS-UDPG estimation can remove the uncertainty on the assumed PL model achieving higher accuracy [234].

Several algorithms were proposed to address this localization problem, both when only the PLE is unknown [319, 235, 320, 321, 234] and when also the $PL(d_0)$ is [247, 322]. The latter case is the most interesting one, as it can be employed for non-cooperative localization problem when the transmitting power is unknown. Naturally, in this particular case, the $PL(d_0)$ estimation is inaccurate.

DRSS Like TDoA, DRSS techniques define the measurements through ratios of the measured power respect to a reference node, thus not needing to know in advance the target's transmitting power [309]. Because of this, DRSS methods are prime candidates for non-cooperative localization. Unlikely TDoA techniques, the geometrical representation of the DRSS problem is still a circular localization [309]. The DRSS approach was also proposed for RSS-UDPG problems, bypassing the $PL(d_0)$ estimation [323].

Hybrid Algorithms

The aforementioned techniques can be combined in hybrid algorithms which fuse different kinds of information to achieve more accurate estimates. For instance, reference [246] employ multiple sectorized antennas to fuse DoA and RSS (Fig. D.5), whereas [303] use the RSS to compensate for synchronization errors in ToA localization.

Performance Indicators of RSS-based Localization Algorithms

The signal-based localization algorithms and systems are analyzed in terms of root main square error (RMSE)

$$e_{rms} = \sqrt{(\hat{x} - x_T)^2 + (\hat{y} - y_T)^2}$$

being $(\hat{x}, \hat{y})$ and (x_T, y_T) the estimated and the true transmitter's position, respectively. Less frequently the CEP (circular error probable) used instead, defined as the radius of the circle
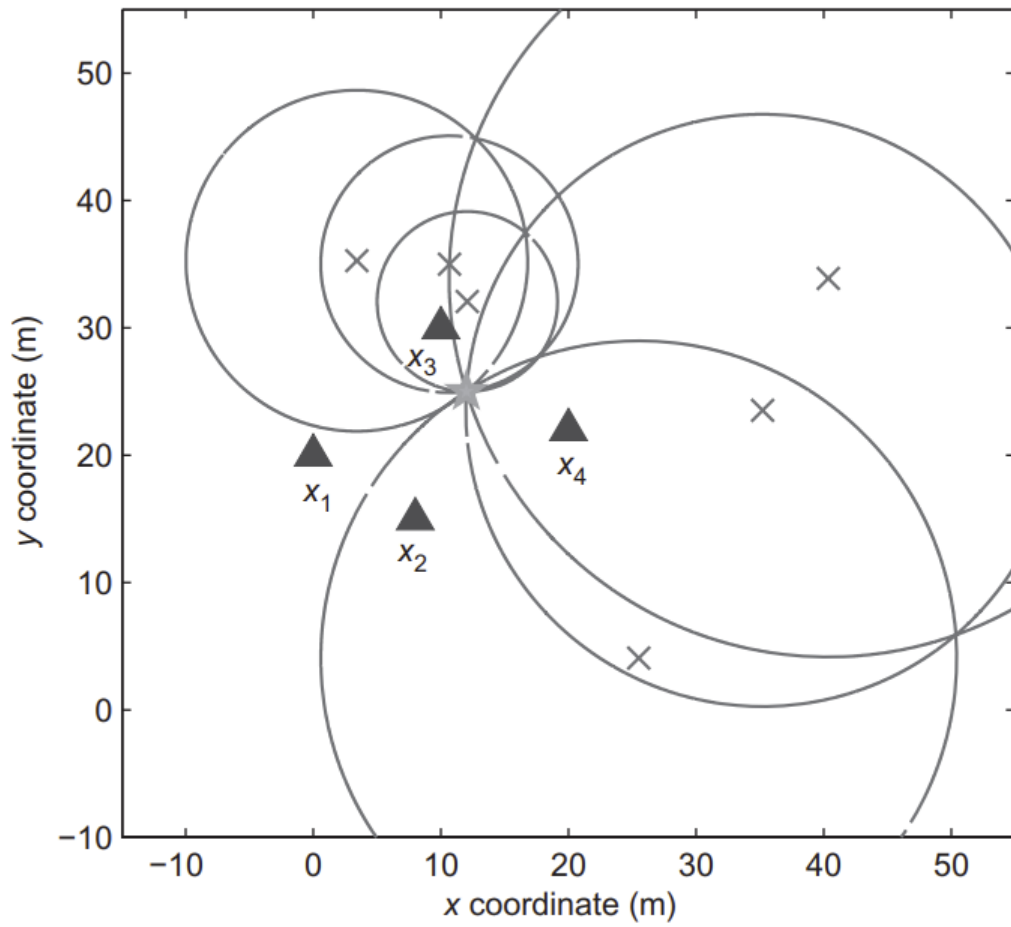
Figure D.4: Geometric interpretation of DRSS lateration [309].
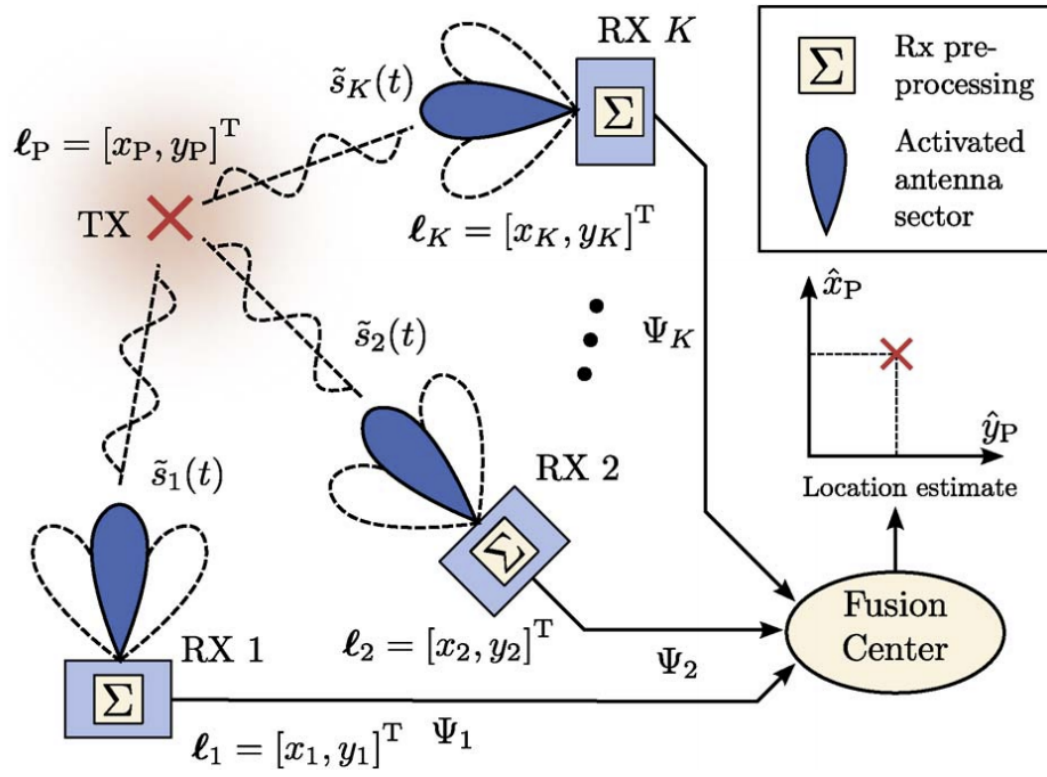
Figure D.5: Scheme of the DoA-RSS localization algorithm in [246].

that has its center at the true location and contains the location estimates with a given probability P_{CEP} [315]. Aside from the position estimation, the impact of wrong input data and the run time are also usually reported. Supplementary performance parameters depend on the specific technique, for example the difference between the estimated and true angle of arrival or PL parameters.

Let us focus on the mountain SaR to restrict the scope of the analysis. ToA, TDoA, and DoA techniques can easily be hindered by the heavy multipath common in mountain scenarios, even more when employing a LPWAN protocol (Section 7.4). As a simple example, the transmitter under a rockfall could not be localized by a DoA-based system due to the multiple reflection near to the transmitter. On the other hand, the range-free RSS-based methods need either an accurate radiomap or a dense network, both absent in most mountain scenarios as mountain canyons. Hybrid techniques are discarded consequently. Moreover, range-based techniques with known PL cannot be used without a reliable model, and all the model's inaccuracies affect the estimated position.

Therefore, UDPG and DRSS techniques based on the log-distance model usually employed for LoRa [219] are promising candidates to solve the mountain SaR problem. Even a single moving anchor node can supply the localization algorithm with hundreds of measurements so to achieve a good target estimation. So, the position estimation is influenced by many factors.

1. PLE n, The higher the PLE, the lower the localization error [324].

2. Number of measurements M. The higher M, the lower the error from the zero-mean lognormal shadow-fading.

3. Topology of the anchors. The topology of the receivers and the corresponding measurements heavily affect the RSS-based methods, and it can be assessed through the dilution of precision [234].

4. Lognormal noise including the additional noise, which is modelled as lognormal shadow fading whose variance is σ_F^2.

5. Other algorithm-specific settings, for example, the weighting of the measurements.

Because of the innumerable combination, the performances of the different algorithms in the literature are extremely difficult or rightly impossible to compare. Indeed, many papers do not explicitly report all the parameters needed to compare the results among the literature's works (see Table 7.1). As a consequence, each algorithm is compared with the corresponding CRLB (Cramér-Rao lower bound) which express the lowest achievable error by unbiased estimators and is derived from the FIM's (Fisher information matrix) inverse [325, 326] (or pseudo-inverse when the FIM is singular [327, 328]) of the formulated problem and data.

List of Abbreviations

ACK: acknowledgment message

ADR: adaptive data rate

AoA: angle of arrival

AoI: area of interest

ARVA: appareil de recherche de victimes d'avalanche; avalanche beacon

BAN: body area network

BAP: battery assisted passive

B-IoT: bodycentric internet of things

BLE: Bluetooth low-energy

BS: base station

BW: bandwidth

CCC: command operation center

CEP: circular error probable

CLA: circular loop antenna

CMOS: complementary metal-oxide semiconductor

COTS: commercial-off-the-shelves

CF: carrier frequency

CP: circularly polarized

CR: coding rate

CRC: cyclic redundancy check

CRLB: Cramér-Rao lower bound

CSS: chirp spread spectrum

DoA: direction of arrival

EAS: emergency activation signal

ECG: electrocardiography or electrocardiogram

ED: end device

EIRP: effective/equivalent isotropic radiated power

EM: electromagnetic or electromagnetism

EMG: Electromyography or electromyograph

EPC: electronic product code

ERP: Effective/equivalent radiating power

ETSI: European telecommunications standards institute

FEC: forward error correction

FFR: facepiece filtering respirator

FIM: Fisher's information matrix

FS: free-space

FSK: frequency shift modulation

GPS: global positioning system

GNSS: global navigation satellite system

GW: gateway

H-IoT: healthcare internet of things

HF: high frequencies

HP: horizontally polarized

HRS: help request signal

IC: integrated circuit

I/O: input-output

IoT: internet of things

ISM: industrial, scientific, and medical

LAN: local area network

LoRa: long-range (the LPWAN protocol)

LoS: line of sight

LHEP: left-hand elliptically polarized

LF: low frequencies

LHCP: left-hand circularly-polarized

LP: linearly polarized

LoRa(WAN): notation to indicate simultaneously LoRa and LoRaWAN

LPWAN: low-power wide-area network

MAC: medium access control

msg: message

NFC: near-field contacting

NLoS: non-line-of-sight

PAN: personal area network

PIFA: planar inverted F antenna

PILA: planar inverted L antenna

PDR: packet delivery ratio

PEC: perfect electric conductor

PET: polyethylene terephthalate

PHY: physical layer

PLE: path loss exponent

PLF: polarization loss factor

PLR: packet loss ratio

PRR: packet reception rate

QoS: quality of service

RF: radiofrequency

RFID: radiofrequency identification

RGB: red-green-blue

RH: relative humidity

RHCP: right-hand circularly-polarized

RHEP: right-hand elliptically polarized

RMSE: root main square error

RSS: received signal strength

RSSI: received signal strength indicator

Rx: receiving (referred to a radio or an antenna)

SAR: specific absorption rate

SaR: search and rescue

SC: sensor code

SF: spreading factor

SIW: substrate-integrated waveguide

SoA: state-of-the-art

STD: standard deviation

TDoA: time difference of arrival

ToA: time of arrival

TP: transmission power

Tx: transmitting (referred to a radio or an antenna)

UAV: unmanned aerial vehicle

UHF: ultra-high frequencies

UNESCO: United Nations educational, scientific and cultural organization

VP: vertically polarized

WAN: wide area network

WLAN: wireless local area network

Bibliography

[1] H. Sundmaeker, P. Guillemin, P. Friess, and S. Woelfflé, "Vision and challenges for realising the internet of things," *Cluster of European research projects on the internet of things, European Commision*, vol. 3, no. 3, pp. 34–36, Mar. 2010.

[2] S. Amendola, *Wireless and battery-less biointegrated sensors for bodycentric Internet of Things*. Rome, Italy: Ph.D. dissertation, Dept. Civil Eng. Comput. Sci. Eng., Univ. Rome Tor Vergata, 2017.

[3] K. Koski, T. Björninen, L. Sydänheimo, L. Ukkonen, and Y. Rahmat-Samii, "A new approach and analysis of modeling the human body in RFID-enabled body-centric wireless systems," *International Journal of Antennas and Propagation*, vol. 2014, 2014.

[4] S. Amudha and M. Murali, "Deep learning based energy efficient novel scheduling algorithms for body-fog-cloud in smart hospital," *Journal of Ambient Intelligence and Humanized Computing*, pp. 1–20, 2020.

[5] J. Gabrys, "Smart forests and data practices: From the Internet of Trees to planetary governance," *Big data & society*, vol. 7, no. 1, p. 2053951720904871, 2020.

[6] C.-C. Chao, J.-M. Yang, and W.-Y. Jen, "Determining technology trends and forecasts of RFID by a historical review and bibliometric analysis from 1991 to 2005," *Technovation*, vol. 27, no. 5, pp. 268–279, Feb. 2007.

[7] H. Habibzadeh, K. Dinesh, O. Rajabi Shishvan, A. Boggio-Dandry, G. Sharma, and T. Soyata, "A survey of healthcare internet of things (HIOT): A clinical perspective," *IEEE Internet Things J*, vol. 7, no. 1, pp. 53–71, 2020.

[8] C. Luo, I. Gil, and R. Fernández-García, "Wearable textile UHF-RFID sensors: A systematic review," *Materials*, vol. 13, no. 15, pp. 2–18, Jul. 2020.

[9] S. Amendola *et al.*, "UHF epidermal sensors: Technology and applications," in *Wearable Sensors*, 2nd ed. Cambridge, MA, USA: Academic Press, 2021, ch. 5, pp. 133–161.

[10] "Regulatory status for using RFID in the EPC Gen2 (860 to 960 MHz) band of UHF spectrum," GS1, Standard, 2021, accessed on: Apr. 29, 2021. [Online]. Available: https://www.gs1.org/docs/epc/uhf_regulations.pdf.

[11] T. Smieszek, S. Castell, A. Barrat, C. Cattuto, P. White, and G. Krause, "Contact diaries versus wearable proximity sensors in measuring contact patterns at a conference: Method comparison and participants' attitudes," *BMC Infectious Diseases*, vol. 16, no. 1, 2016, art. no. 341.

[12] J. Stehlé *et al.*, "Simulation of an SEIR infectious disease model on the dynamic contact network of conference attendees," *BMC Medicine*, vol. 9, 2011, art. no. 87.

[13] C. Cattuto, W. van den Broeck, A. Barrat, V. Colizza, J.-F. Pinton, and A. Vespignani, "Dynamics of person-to-person interactions from distributed RFID sensor networks," *PLoS ONE*, vol. 5, no. 7, 2010, art. no. e11596.

[14] OpenBeacon, https://www.openbeacon.org/source/, 2006.

[15] G. Borelli, P. Orrù, and F. Zedda, "Performance analysis of a healthcare supply chain. a rfid system implementation design," vol. 11-13-September-2013, Senigallia, Italy, Sept 2013, pp. 42–47. [Online]. Available: https://www.scopus.com/inward/record.uri?eid=2-s2.0-84982918598&partnerID=40&md5=c360c6672fa05ec03bac50e8fea8cdc7

[16] X. Qu, L. T. Simpson, and P. Stanfield, "A model for quantifying the value of rfid-enabled equipment tracking in hospitals," *Advanced Engineering Informatics*, vol. 25, no. 1, pp. 23 – 31, 2011, rFID and sustainable value chains. [Online]. Available: http://www.sciencedirect.com/science/article/pii/S1474034610000327

[17] G. Huang, Z. Qin, T. Qu, and Q. Dai, "Rfid-enabled pharmaceutical regulatory trace-ability system," 2010, pp. 211–216.

[18] H. Liu, Z. Yao, F. Chang, and S. Meyer, "An rfid-based medical waste transportation management system: Assessment of a new model on a hospital in china," *Fresenius Environmental Bulletin*, vol. 29, no. 2, pp. 773–784, Feb 2020. [Online]. Available: https://www.scopus.com/inward/record.uri?eid=2-s2.0-85090460619& partnerID=40&md5=f2c3404eabce011699060df790d9b438

[19] H. Liu and Z. Yao, "The research on recycling management model of medical waste based on rfid technology," *Fresenius Environmen-tal Bulletin*, vol. 26, no. 8, pp. 5069–5081, Aug 2017. [Online]. Available: https://www.scopus.com/inward/record.uri?eid=2-s2.0-85050749885& partnerID=40&md5=8e2613f1a05e3a694d2c5fba5602c299

[20] Z. Qi, Y. Zhuang, X. Li, W. Liu, Y. Du, and B. Wang, "Full passive UHF RFID Tag with an ultra-low power, small area, high resolution temperature sensor suitable for environment monitoring," *Microelectronics Journal*, vol. 45, no. 1, pp. 126–131, 2014.

[21] S. Manzari and G. Marrocco, "Modeling and Applications of a Chemical-Loaded UHF RFID Sensing Antenna With Tuning Capability," *IEEE Transactions on An-tennas and Propagation*, vol. 62, no. 1, pp. 94–101, 2014.

[22] R. Colella, L. Catarinucci, and L. Tarricone, "Improved Battery-Less Augmented RFID Tag: Application on Ambient Sensing and Control," *IEEE Sensors Journal*, vol. 16, no. 10, pp. 3484–3485, 2016.

[23] K. Radhakrishna, A. Waghmare, M. Ekstrand, T. Raj, S. Selvam, S. Sreerama, and S. Sampath, "Real-time feedback for improving compliance to hand sanitization among healthcare workers in an open layout ICU using radiofrequency identifica-tion," *Journal of Medical Systems*, vol. 39, no. 6, 2015.

271

[24] A. Decker, G. Cipriano, G. Tsouri, and J. Lavigne, "Monitoring pharmacy student adherence to world health organization hand hygiene indications using radio frequency identification," *American Journal of Pharmaceutical Education*, vol. 80, no. 3, 2016.

[25] D. Wu, W. W. Y. Ng, P. P. K. Chan, H. Ding, B. Jing, and D. S. Yeung, "Access control by RFID and face recognition based on neural network," in *2010 International Conference on Machine Learning and Cybernetics*, vol. 2, 2010, pp. 675–680.

[26] S. Wen, H. Heidari, A. Vilouras, and R. Dahiya, "A wearable fabric-based RFID skin temperature monitoring patch," in *2016 IEEE SENSORS*, 2016, pp. 1–3.

[27] Y.-W. Chen *et al.*, "A RFID model of transferring and tracking trauma patients after a large disaster," Chicago, IL, USA, Jul 2009, pp. 98–101.

[28] Q. Cao, D. R. Jones, and H. Sheng, "Contained nomadic information environments: Technology, organization, and environment influences on adoption of hospital rfid patient tracking," *Information Management*, vol. 51, no. 2, pp. 225 – 239, 2014.

[29] S. Bahri, "Enhancing quality of data through automated SARS contact tracing method using RFID technology," *International Journal of Networking and Virtual Organisations*, vol. 4, no. 2, pp. 145–162, May 2007.

[30] M. Bolic, M. Rostamian, and P. Djuric, "Proximity detection with RFID: A step toward the internet of things," *IEEE Pervasive Computing*, vol. 14, no. 2, pp. 70–76, 2015.

[31] F. Camera, C. Miozzi, F. Amato, C. Occhiuzzi, and G. Marrocco, "Experimental Assessment of Wireless Monitoring of Axilla Temperature by Means of Epidermal Battery-Less RFID Sensors," *IEEE Sensors Letters*, vol. 4, no. 11, pp. 1–4, 2020.

[32] R. Horne, J. Batchelor, P. Taylor, E. Balaban, and A. Casson, "Ultra-Low Power on Skin ECG using RFID Communication," 2020.

[33] C. Miozzi, V. Errico, G. Saggio, E. Gruppioni, and G. Marrocco, "Uhf rfid-based emg for prosthetic control: preliminary results," in *2019 IEEE International Conference on RFID Technology and Applications (RFID-TA)*, 2019, pp. 310–313.

[34] L. Corchia, G. Monti, E. D. Benedetto, and L. Tarricone, "A chipless humidity sensor for wearable applications," in *2019 IEEE International Conference on RFID Technology and Applications (RFID-TA)*, 2019, pp. 174–177.

[35] M. F. Saaid, I. Ismail, and M. Z. H. Noor, "Radio frequency identification walking stick (rfiws): A device for the blind," in *5th International Colloquium on Signal Processing & its Applications*, 2009, pp. 250–253.

[36] R. Buettner, T. Clauà, M. T. Huynh, and D. Koser, "Rfid tracking and localization technologies in healthcare," in *2020 IEEE Symposium on Industrial Electronics Applications (ISIEA)*, Malasya, 2020, pp. 1–5.

[37] M. Haddara and A. Staaby, "Rfid applications and adoptions in healthcare: A review on patient safety," vol. 138, 2018, pp. 80–88.

[38] A. Coustasse, B. Cunningham, E. Willson, P. Meadows, and S. Deslich, "Management Of RDIF Systems in Hospital Transfusion Services," March 2015.

[39] C. Dawson and J. Mackrill, "Review of technologies available to improve hand hygiene compliance - are they fit for purpose?" *Journal of Infection Prevention*, vol. 15, no. 6, pp. 222–228, 2014. [Online]. Available: https://www.scopus.com/inward/record.uri?eid=2-s2.0-84927778025&doi=10.1177%2f1757177414548695&partnerID=40&md5=da27449acf81e8fc9ffb4f68b6201ecc

[40] S. Ajami and M. W. Carter, "The advantages and disadvantages of radio frequency identification (rfid) in health-care centers; approach in emergency room (er)," *Pakistan Journal of Medical Sciences*, vol. 29, no. 1, pp. 443–448, Jan. 2013.

[41] S. Ajami and A. Rajabzadeh, "Radio frequency identification (rfid) technology and patient safety," *Journal of research in medical sciences: the official journal of Isfahan University of Medical Sciences*, vol. 18, no. 9, p. 809, 2013.

[42] S. F. Wamba, "Rfid-enabled healthcare applications, issues and benefits: An archival analysis (1997–2011)," *Journal of medical systems*, vol. 36, no. 6, pp. 3393–3398, 2012.

[43] R. Kalra, P. Shetty, S. Mutalik, U. Nayak, M. Reddy, and N. Udupa, "Pharmaceutical applications of radio-frequency identification," *Systematic Reviews in Pharmacy*, vol. 3, no. 1, pp. 24–30, Feb 2012.

[44] S. Amendola, C. Occhiuzzi, and G. Marrocco, "More than wearable: Epidermal antennas for tracking and sensing," in *Electromagnetics of Body Area Networks – Antennas, Propagation and RF Systems*. Hoboken, NJ, USA: John Wiley and Sons, 2016, ch. 9, pp. 319–348.

[45] R. Dahiya, "Epidermal electronics – flexible electronics for biomedical applications," in *Handbook of Bioelectronics: Directly interfacing Electronics and Biological Systems*. Cambridge, United Kingdom: Cambridge University Press, 2015, pp. 245–255.

[46] S. Amendola *et al.*, "UHF epidermal sensors: Technology and applications," 11 2020, pp. 133–161.

[47] V. Di Cecco, S. Amendola, P. Valentini, and G. Marrocco, "Finger-augmented rfid system to restore peripheral thermal feeling," in *2017 IEEE International Conference on RFID (RFID)*, 2017, pp. 54–60.

[48] C. Occhiuzzi, S. Parrella, F. Camera, S. Nappi, and G. Marrocco, "RFID-based Dual-Chip Epidermal Sensing Platform for Human Skin Monitoring," *IEEE Sensors Letters*, 2020.

[49] C. Miozzi, F. Amato, and G. Marrocco, "Performance and Durability of Thread Antennas as Stretchable Epidermal UHF RFID Tags," *IEEE Journal of Radio Frequency Identification*, vol. 4, no. 4, pp. 398–405, 2020.

[50] C. Miozzi, S. Nappi, S. Amendola, C. Occhiuzzi, and G. Marrocco, "A General-Purpose Configurable RFID Epidermal Board With a Two-Way Discrete Impedance

Tuning," *IEEE Antennas and Wireless Propagation Letters*, vol. 18, no. 4, pp. 684–687, 2019.

[51] C. Miozzi, S. Nappi, S. Amendola, and G. Marrocco, "A General-Purpose Small RFID Epidermal Datalogger for Continuous Human Skin Monitoring in Mobility," in *2018 IEEE/MTT-S International Microwave Symposium - IMS*, 2018, pp. 371–373.

[52] Shang-Wei Wang, Wun-Hwa Chen, Chorng-Shyong Ong, Li Liu, and Yun-Wen Chuang, "RFID Application in Hospitals: A Case Study on a Demonstration RFID Project in a Taiwan Hospital," in *Proceedings of the 39th Annual Hawaii International Conference on System Sciences (HICSS'06)*, vol. 8, 2006, pp. 184a–184a.

[53] C. Miozzi, S. Amendola, A. Bergamini, and G. Marrocco, "Clinical Trial of Wireless Epidermal Temperature Sensors: preliminary results," June 2018, pp. 1041–1044.

[54] C. Miozzi, S. Amendola, A. Bergamini, and G. Marrocco, "Reliability of a re-usable wireless Epidermal temperature sensor in real conditions," in *2017 IEEE 14th International Conference on Wearable and Implantable Body Sensor Networks (BSN)*, 2017, pp. 95–98.

[55] S. Amendola, G. Bovesecchi, A. Palombi, P. Coppa, and G. Marrocco, "Design, Calibration and Experimentation of an Epidermal RFID Sensor for Remote Temperature Monitoring," *IEEE Sensors Journal*, vol. 16, pp. 1–1, October 2016.

[56] T. Adame, A. Bel, A. Carreras, J. Melia-Segui, M. Oliver, and R. Pous, "CUIDATS: An RFID-WSN hybrid monitoring system for smart health care environments," *Future Generation Computer Systems*, vol. 78, December 2016.

[57] S. Milici, S. Amendola, A. Bianco, and G. Marrocco, "Epidermal RFID Passive Sensor for Body Temperature Measurements," October 2014, pp. 140–144.

[58] S. Manzari, S. Pettinari, and G. Marrocco, "Miniaturized and tunable wearable RFID tag for body-centric applications," in *2012 IEEE International Conference on RFID-Technologies and Applications (RFID-TA)*, 2012, pp. 239–243.

[59] X. Chang, J. Dai, Z. Zhang, K. Zhu, and G. Xing, "RF-RVM: Continuous Respiratory Volume Monitoring With COTS RFID Tags," *IEEE Internet of Things Journal*, pp. 1–1, 2021.

[60] C. Miozzi, G. Stendardo, G. M. Bianco, F. Montecchia, and G. Marrocco, "Dual-chip RFID on-skin tag for bilateral breath monitoring," in *15th Annual Conference on RFID*, Apr. 2021.

[61] V. Oliveira, L. Duarte, G. Costa, M. Macedo, and T. Silveira, "Automation System for Six-minute Walk Test Using RFID Technology," 2020.

[62] Y. Wang and Y. Zheng, "TagBreathe: Monitor Breathing with Commodity RFID Systems," *IEEE Transactions on Mobile Computing*, vol. PP, pp. 1–1, February 2019.

[63] Z. Hussain, S. Sagar, W. E. Zhang, and Q. Sheng, "A cost-effective and non-invasive system for sleep and vital signs monitoring using passive RFID tags," November 2019, pp. 153–161.

[64] M. C. Caccami, Y. Mulla, C. Occhiuzzi, C. Natale, and G. Marrocco, "Design and Experimentation of a Batteryless On-skin RFID Graphene-Oxide Sensor for the Monitoring and Discrimination of Breath Anomalies," *IEEE Sensors Journal*, vol. PP, pp. 1–1, August 2018.

[65] C. Occhiuzzi, C. Caccami, S. Amendola, and G. Marrocco, "Breath-monitoring by means of Epidermal Temperature RFID Sensors," in *2018 3rd International Conference on Smart and Sustainable Technologies (SpliTech)*, 2018, pp. 1–4.

[66] M. C. Caccami, M. Y. S. Mulla, C. Di Natale, and G. Marrocco, "Graphene oxide-based radiofrequency identification wearable sensor for breath monitoring," *IET Microwaves, Antennas Propagation*, vol. 12, no. 4, pp. 467–471, 2018.

[67] J. Araujo, S. Morais, G. Serres, C. Albuquerque, A. Serres, D. Santos, and J. Carvalho, "Passive RFID Tag for Respiratory Frequency Monitoring," August 2018, pp. 1–5.

276

[68] X. Hui and E. Kan, "Monitoring vital signs over multiplexed radio by near-field coherent sensing," *Nature Electronics*, vol. 1, January 2018.

[69] P. Sharma and E. C. Kan, "Sleep Scoring with a UHF RFID Tag by Near Field Coherent Sensing," in *2018 IEEE/MTT-S International Microwave Symposium - IMS*, 2018, pp. 1419–1422.

[70] M. C. Caccami, C. Miozzi, M. Y. S. Mulla, C. Di Natale, and G. Marrocco, "An epidermal graphene oxide-based RFID sensor for the wireless analysis of human breath," in *2017 IEEE International Conference on RFID Technology Application (RFID-TA)*, 2017, pp. 191–195.

[71] Y. Hou, Y. Wang, and Y. Zheng, "TagBreathe: Monitor Breathing with Commodity RFID Systems," in *2017 IEEE 37th International Conference on Distributed Computing Systems (ICDCS)*, 2017, pp. 404–413.

[72] X. Hu, K. Naya, P. Li, T. Miyazaki, and K. Wang, "Non-invasive sleep monitoring based on RFID," in *2017 IEEE 19th International Conference on e-Health Networking, Applications and Services (Healthcom)*, 2017, pp. 1–3.

[73] Y. Wang, "Design of the Pulse Oximetry Measurement Circuit and Its Sensing System Based On CMOS," *IOSR Journal of Electrical and Electronics Engineering*, vol. 12, pp. 64–70, March 2017.

[74] C. Wang, L. Xie, W. Wang, Y. Chen, Y. Bu, and S. Lu, "RF-ECG: Heart Rate Variability Assessment Based on COTS RFID Tag Array," *Proceedings of the ACM on Interactive, Mobile, Wearable and Ubiquitous Technologies*, vol. 2, pp. 1–26, July 2018.

[75] Agezo, Zhang, Ye, Chopra, Vora, and Kurzweg, "Battery-free RFID heart rate monitoring system," in *2016 IEEE Wireless Health (WH)*, 2016, pp. 1–7.

[76] S. Vora, K. Dandekar, and T. Kurzweg, "Passive RFID tag based heart rate monitoring from an ECG signal," vol. 2015, August 2015, pp. 4403–4406.

[77] C.-R. Wang, S.-Y. Lee, and W.-C. Lai, "An RFID tag system-on-chip with wireless ECG monitoring for intelligent healthcare systems," *Conference proceedings: Annual International Conference of the IEEE Engineering in Medicine and Biology Society. IEEE Engineering in Medicine and Biology Society. Conference*, vol. 2013, pp. 5489–5492, July 2013.

[78] J. S. Besnoff, T. Deyle, R. R. Harrison, and M. S. Reynolds, "Battery-free multichannel digital ECG biotelemetry using UHF RFID techniques," in *2013 IEEE International Conference on RFID (RFID)*, 2013, pp. 16–22.

[79] V. Mazzaracchio, L. Fiore, S. Nappi, G. Marrocco, and F. Arduini, "Medium-distance affordable, flexible and wireless epidermal sensor for pH monitoring in sweat," *Talanta*, vol. 222, p. 121502, August 2020.

[80] S. Nappi, V. Mazzaracchio, L. Fiore, F. Arduini, and G. Marrocco, "Flexible ph sensor for wireless monitoring of the human skin from the medimun distances," in *2019 IEEE International Conference on Flexible and Printable Sensors and Systems*, 2019, pp. 1–3.

[81] S. Merilampi, Han He, L. Sydänheimo, L. Ukkonen, and J. Virkki, "The possibilities of passive UHF RFID textile tags as comfortable wearable sweat rate sensors," in *2016 Progress in Electromagnetic Research Symposium (PIERS)*, 2016, pp. 3984–3987.

[82] C. Occhiuzzi, C. Vallese, S. Amendola, S. Manzari, and G. Marrocco, "Multi-channel processing of RFID backscattering for monitoring of overnight living," in *2014 XXXIth URSI General Assembly and Scientific Symposium (URSI GASS)*, 2014, pp. 1–4.

[83] C. Occhiuzzi, C. Vallese, S. Amendola, S. Manzari, and G. Marrocco, "NIGHT-Care: A Passive RFID System for Remote Monitoring and Control of Overnight Living Environment," *Procedia Computer Science*, vol. 32, pp. 190–197, December 2014.

278

[84] C. Occhiuzzi and G. Marrocco, "The RFID Technology for Neurosciences: Feasibility of Limbs' Monitoring in Sleep Diseases," *IEEE Transactions on Information Technology in Biomedicine*, vol. 14, no. 1, pp. 37–43, 2010.

[85] C. Miozzi, V. Errico, G. Marrocco, E. Gruppioni, and G. Saggio, "Rfid interface for compact pliable emg wireless epidermal sensor," in *2020 IEEE International Workshop on Metrology for Industry 4.0 IoT*, 2020, pp. 202–206.

[86] D. Shuaib, L. Ukkonen, J. Virkki, and S. Merilampi, "The possibilities of embroidered passive UHF RFID textile tags as wearable moisture sensors," in *IEEE 5th International Conference on Serious Games and Applications for Health*. IEEE, 2017, pp. 1–5.

[87] J. E. Bardram, A. Doryab, R. M. Jensen, P. M. Lange, K. L. G. Nielsen, and S. T. Petersen, "Phase recognition during surgical procedures using embedded and body-worn sensors," in *2011 IEEE International Conference on Pervasive Computing and Communications (PerCom)*, Seattle, WA, USA, Mar 2011, pp. 45–53.

[88] K. Fishkin, M. Philipose, and A. Rea, "Hands-on RFID: wireless wearables for detecting use of objects," in *Ninth IEEE International Symposium on Wearable Computers (ISWC'05)*, 2005, pp. 38–41.

[89] i-Tek - Body Temperature Monitoring System for Employees and Civil Services, https://infoteksoftware.com/rfid-solution/rfid-based-body-temperature-monitoring-for-workers.html?vertical=health-care-vertical.

[90] X. Ni *et al.*, "Automated, multiparametric monitoring of respiratory biomarkers and vital signs in clinical and home settings for COVID-19 patients," *Proc. Nat. Acad. Sciences*, vol. 118, no. 19, Mar. 2021.

[91] C. Massaroni, A. Nicolò, D. Lo Presti, M. Sacchetti, S. Silvestri, and E. Schena, "Contact-based methods for measuring respiratory rate," *Sensors*, vol. 19, no. 4, 2019, Art. no. 908.

[92] Z. Sonner, E. Wilder, J. Heikenfeld, G. Kasting, F. Beyette, D. Swaile, F. Sherman, J. Joyce, J. Hagen, N. Kelley-Loughnane, and R. Naik, "The microfluidics of the eccrine sweat gland, including biomarker partitioning, transport, and biosensing implications." *Biomicrofluidics*, vol. 93, p. 031301, 2015.

[93] C. P. Adans-Dester *et al.*, "Can mHealth Technology Help Mitigate the Effects of the COVID-19 Pandemic? - Supplementary materials," *IEEE Open Journal of Engineering in Medicine and Biology*, vol. 1, pp. 243–248, 2020.

[94] K. Barrell and A. G. Smith, "Peripheral neuropathy," *Medical Clinics of North America*, vol. 103, no. 2, pp. 383–397, 2019.

[95] M. Caccami and G. Marrocco, "Electromagnetic modeling of self-tuning RFID sensor antennas in linear and nonlinear regimes," *IEEE Trans. Antennas and Propag.*, vol. 66, no. 6, pp. 2779–2787, Jun. 2018.

[96] S. Orfanidis, *Electromagnetic Waves and Antennas*, 1st ed. New Brunswick, NJ, USA: Rutgers University Press, 2010.

[97] S. Amendola, V. Di Cecco, and G. Marrocco, "Numerical and Experimental Characterization of Wrist-Fingers Communication Link for RFID-Based Finger Augmented Devices," *IEEE Transactions on Antennas and Propagation*, vol. 67, no. 1, pp. 531–540, Jan. 2019.

[98] M. C. Caccami, C. Miozzi, V. Greco, and G. Marrocco, "Epidermal radio-sensors for wireless detection of physiological parameters and sense augmentation," in *12th European Conference on Antennas and Propagation (EuCAP 2018)*, 2018, pp. 1–5.

[99] "Advice on the use of masks in the context of COVID-19," World Health Organization, Geneva, Switzerland, Standard, Apr. 2020.

[100] National Institute for Occupational Safety and Health, "Recommended guidance for extended use and limited reuse of n95 filtering facepiece respirators in healthcare settings," https://www.cdc.gov/niosh/topics/hcwcontrols/recommendedguidanceextuse.html, 2020.

280

[101] S. Gao *et al.*, "Performance of N95 FFRs against combustion and NaCl aerosols in dry and moderately humid air: Manikin-based study," *Annals of Occupational Hygiene*, vol. 60, no. 6, pp. 748–760, Apr 2016.

[102] A. Pacitto *et al.*, "Effectiveness of commercial face masks to reduce personal PM exposure," *Sci. Total Environ.*, vol. 650, no. 1, pp. 1582–1590, Feb. 2019.

[103] R. J. Roberge, J. Kim, and S. Benson, "N95 filtering facepiece respirator deadspace temperature and humidity," *J. Occup. Environ. Hyg.*, vol. 9, no. 3, pp. 166–171, Mar. 2012.

[104] A. Shwarty *et al.*, "Decontamination and reuse of N95 respirators with hydrogen peroxide vapor to address worldwide personal protective equipment shortages during the SARS-CoV-2 (COVID-19) pandemic," *J. ABSA Int.*, vol. 25, no. 2, pp. 166–171, Jun. 2020.

[105] H. Chan, T. Choi, C. Hui, and S. Ng, "Quick response healthcare apparel supply chains: value of RFID and coordination," *IEEE Trans. Syst., Man, Cybern. Syst.*, vol. 43, no. 6, pp. 887–900, June 2015.

[106] E. M. Amin, M. S. Bhuyian, N. C. Karmakar, and B. Winther-Jensen, "Development of a low-cost printable chipless RFID humidity sensor," *IEEE Sensors J.*, vol. 14, no. 1, pp. 140–149, Jan. 2014.

[107] J. Virtanen, L. Ukkonen, T. Bjurninen, A. Z. Elsherbeni, and L. Syd anheimo, "Inkjet-pronted humidity sensor for passive UHF RFID systems," *IEEE Instrum. Meas.*, vol. 60, no. 8, pp. 2768–2777, Aug. 2011.

[108] G. Marrocco, "The art of UHF RFID antenna design: impedance-matching and size-reduction techniques," *IEEE Antennas Propag. Mag.*, vol. 50, no. 1, pp. 66–79, Feb. 2008.

[109] R. Micron, "Magnus-s3 datasheet," https://pdf1.alldatasheet.com/datasheet-pdf/view/789023/AMSCO/SL900A.html, 2017.

[110] C. Hertleer, *Design of planar antennas based on textile materials*. Ghent, Belgium: Ph.D. dissertation, Dept. Mate., Textiles Chem. Eng., Univ. Ghent, 2009.

[111] J. Hu, L. Zhang, Z. Dang, and D. Wang, "Improved dielectric properties of polypropylene-based nanocomposites via co-filling with zinc oxide and barium titanate," *Composites Sci. Technol.*, vol. 148, pp. 20–26, Aug. 2017.

[112] "IEEE Recommended Practice for Determining the Peak Spatial-Average Specific Absorption Rate (SAR) in the Human Head from Wireless Communications Devices: Measurement Techniques," IEEE Standards Association, Standard, Sep. 2013.

[113] Q. Yang *et al.*, "Study of the micro-climate and bacterial distribution in the deadspace of N95 filtering face respirators," *Scientific Rep.*, vol. 8, no. 1, Nov. 2018, Art. no. 17328.

[114] RF Micron, "RFM3200-AFR," https://axzon.com/rfm3200-wireless-flexible-temperature-sensor/, 2017, (accessed Jan. 31, 2021).

[115] R. J. Roberje, E. Bayer, J. B. Powell, A. Coca, M. R. Roberge, and S. M. Benson, "Effect of exhaled moisture on breathing resistance of N95 filtering facepiece respirators," *Ann. Occup. Hyg.*, vol. 54, no. 6, pp. 671–677, Aug. 2010.

[116] R. J. Roberge, W. J. Coca, A. Williams, P. A. J., and J. B. Powell, "Surgical mask placement over N95 filtering facepiece respirators: physiological effects on healthcare workers," *Respirology*, vol. 15, no. 3, pp. 516–521, Apr. 2010.

[117] "1988 Anthropometric survey of U.S. personnel: summary statistics interim report," U.S. Army Res., Natick, MA, USA, Tech. Rep., Mar. 1989.

[118] W. Yao, C. Chu, and Z. Li, "The Adoption and Implementation of RFID Technologies in Healthcare: A Literature Review," *Journal of medical systems*, vol. 36, pp. 3507–25, October 2011.

[119] N. Panunzio, F. Ciafrei, C. Magnante, G. M. Bianco, and G. Marrocco, "Sensorized facemask with temperature RFID sensor for cough analysis," submitted for publication.

[120] R. Shilkrot, J. Huber, J. Steimle, S. Nanayakkara, and P. Maes, "Digital digits: A comprehensive survey of finger augmentation devices," *ACM Computing Surveys*, vol. 40, no. 2, 2015.

[121] C.-H. Su, L. Chan, C.-T. Weng, R.-H. Liang, K.-Y. Cheng, and B.-Y. Chen, "NailDisplay: bringing an always-available visual display to fingertips," in *Proceedings of Conference on Human Factors in Computing Systems*, Paris, France, 2013.

[122] H.-L. Kao, A. Dementyev, J. Paradiso, and C. Schmandt, "NailO: Fingernails as an input surface," in *Proceedings of Conference on Human Factors in Computing Systems*, Seoul, Republic of Korea, 2015.

[123] P. Sedighi, H. Norouzi, and M. Delrobaei, "An RFID-based assistive glove to help the visually impaired," *IEEE Transactions on Instrumentation and Measurements*, vol. 70, pp. 1–9, 2021.

[124] P. S. Taylor and J. C. Batchelor, "Finger-worn UHF far-field RFID tag antenna," *IEEE Antennas and Wireless Propagation Letters*, vol. 18, no. 12, pp. 2513–1517, 2019.

[125] R.-H. Liang, S.-Y. Yang, and B.-Y. Chen, "InDexMo: exploring finger-worn RFID motion tracking for activity recognition on tagged objects," in *Proc. 23rd International Symposium on Wearable Computers*, London, United Kingdom, 2019.

[126] R. Bainbridge and J. A. Paradiso, "Wireless hand gesture capture through wearable passive tag sensing," in *International Conference on Body Sensor Networks*, Dallas, TX, USA, 2011.

[127] F. Amato, C. Occhiuzzi, and G. Marrocco, "Performances of a 3.6 GHz epidermal loop for future 5G-RFID communications," in *14th European Conference on Antennas and Propagation*, Copenhagen, Denmark, 2020.

[128] G. P. Fettweis, "The tactile internet: Applications and challenges," *IEEE Vehicular Technology Magazine*, vol. 9, no. 1, pp. 64–70, 2014.

[129] R. Shilkrot, *Digital Digits: Designing Assistive Finger Augmentation Devices*. Boston, MA, USA: Massachusetts Institute, 2015, ph.D. dissertation.

[130] G. M. Bianco and G. Marrocco, "Fingertip self-tuning RFID antennas for the discrimination of dielectric objects," in *2019 13th European Conference on Antennas and Propagation (EuCAP)*, Krakow, Poland, March 2019, pp. 1–4.

[131] D. Maberley *et al.*, "The prevalence of low vision and blindness in Canada," *Eye*, vol. 20, no. 3, pp. 341–346, 2005.

[132] V. Svorčík, O. Ekrt, V. Rybka, J. Lipták, and V. Hnatowicz, "Permittivity of polyethylene and polyethyleneterephtalate," *J. Mater. Sci. Letter.*, vol. 19, pp. 1843–1845, Oct. 2000.

[133] C. G. Malmberg and A. A. Maryott, "Dielectric constant of water from 0.0 to 1000 c," *J. Res. Nat. Bur. Standards*, vol. 56, no. 1, pp. 1–8, Jan. 1956.

[134] R. J. Sengwa, "Comparative dielectric study of mono, di and trihydric alcohols," *Indian Journal of Pure & Applied Physics*, 2003.

[135] P. A. Bernard and J. M. Gautray, "Measurement of dielectric constant using a microstrip ring resonator," *IEEE Tran. Microw. Theory Techn.*, vol. 39, no. 3, pp. 592–595, Mar. 1991.

[136] F. Camera and G. Marrocco, "Electromagnetic-based correction of bio-integrated rfid sensors for reliable skin temperature monitoring," *IEEE Sensors Journal*, vol. 21, no. 1, pp. 421–429, 2021.

[137] "Evaluation of measurement data – Guide to the expression of uncertainty in measurements," International Organization for Standardization, Geneva, CH, Standard, Sep. 2008.

[138] S. G. Rabinovich, *Measurement Errors and Uncertainties – Theory and Practice*, 3rd ed. New York, NY, USA: Springer-Verlag New York, 2005.

[139] "LoRaWAN specification," https://lora-alliance.org/resource_hub/ lorawan-specification-v1-1/, 2017, LoRa Alliance. [Online]. Accessed: Aug. 21, 2021.

[140] K. Mekki, E. Bajic, F. Chaxel, and F. Meyer, "Overview of cellular LPWAN technologies for IoT deployment: Sigfox, LoRaWAN, and NB-IoT," in *2018 IEEE International Conference on Pervasive Computing and Communications Workshops (PerCom Workshops)*, 2018, pp. 197–202.

[141] J. Petäjäjärvi, K. Mikhaylov, A. Roivainen, T. Hanninen, and M. Pettissalo, "On the coverage of LPWANs: range evaluation and channel attenuation model for LoRa technology," in *14th Int. Conf. ITS Telecommun.*, 2015, pp. 55–59.

[142] C. A. Trasviña Moreno, R. Blasco, R. Casas, and A. Asensio, "A network performance analysis of LoRa modulation for LPWAN sensor devices," in *Ubiquitous computing and ambient intelligence*. Springer, 2016, pp. 174–181.

[143] P. Jörke, S. Böcker, F. Liedmann, and C. Wietfeld, "Urban channel models for smart city IoT-networks based on empirical measurements of LoRa-links at 433 and 868 MHz," in *IEEE 28th Annual Int. Symp. Personal, Indoor, Mobile Radio Commun.* IEEE, 2017, pp. 1–6.

[144] "Pycom Ation Wi Py 3.0 user guide," https://usermanual.wiki/Document/ Pycom20WiPy203020user20guide.1505216624/html, 2017, Pycom company. [Online]. Accessed: Aug. 21, 2021.

[145] V. Talla, M. Hessar, B. Kellogg, A. Najafi, J. R. Smith, and S. Gollakota, "LoRa backscatter: Enabling the vision of ubiquitous connectivity," *Proc. ACM Interactive, Mobile, Wearable and Ubiquitous Technol.*, vol. 1, no. 3, pp. 1–24, 2017.

[146] T. Attia, M. Heusse, B. Tourancheau, and A. Duda, "Experimental characterization of LoRaWAN link quality," in *IEEE Global Commun. Conf.* IEEE, 2019, pp. 1–6.

[147] M. Bor, J. Vidler, and U. Roedig, "LoRa for the internet of things," in *Proceedings of the 2016 International Conference on Embedded Wireless Systems and Networks*. USA: Junction Publishing, pp. 361–366.

[148] E. D. Ayele, C. Hakkenberg, J. P. Meijers, K. Zhang, N. Meratnia, and P. J. M. Havinga, "Performance analysis of LoRa radio for an indoor IoT applications," in *Int. Conf. Internet of Things for the Global Community*. IEEE, 2017, pp. 1–8.

[149] "An1200.22 lora modulation basics," http://wiki.lahoud.fr/lib/exe/fetch.php?media= an1200.22.pdf, 2015, Semtech corporation. Accessed: Aug. 15, 2021.

[150] "A comprehensive look at low power, wide area networks for internet of things engineers and decision makers," https://cdn2.hubspot.net/hubfs/427771/ LPWAN-Brochure-Interactive.pdf, 2016, Link Labs, White Paper. [Online]. Accessed: Aug. 21, 2021.

[151] M. T. Buyukakkaslar, M. A. Erturk, M. A. Aydin, and L. Vollero, "LoRaWAN as an e-health communication technology," in *IEEE 41st Annual computer software and applications conf.*, vol. 2. IEEE, 2017, pp. 310–313.

[152] N. Abramson, "The ALOHA system: Another alternative for computer communications," in *Proceedings of the November 17-19, 1970, fall joint computer conference*, 1970, pp. 281–285.

[153] K. Mykhaylov, J. Petäjäjärvi, and T. Haenninen, "Analysis of capacity and scalability of the LoRa low power wide area network technology," in *Proc. Eur. Wireless 22th Eur. Wireless Conf.*, Oulu, Finland, 2016, pp. 1–6.

[154] F. Adelantado, X. Vilajosana, P. Tuset-Peiro, B. Martinez, J. Melia-Segui, and T. Watteyne, "Understanding the limits of LoRaWAN," *IEEE Commun. Mag.*, vol. 55, no. 9, pp. 34–40, 2017.

[155] "LoRaTools," https://www.loratools.nl/#/, [Online]. Accessed: Aug. 22, 2021.

[156] J. de Carvalho Silva, J. J. P. C. Rodrigues, A. M. Alberti, P. Solic, and A. L. L. Aquino, "LoRaWAN–A low power WAN protocol for internet of things: A review and opportunities," in *2nd Int. Multidisciplinary Conf. Computer Energy Sci.* IEEE, 2017, pp. 1–6.

[157] D. Bankov, E. Khorov, and A. Lyakhov, "On the limits of LoRaWAN channel access," in *Int. Conf. Eng. Telecommun.* IEEE, 2016, pp. 10–14.

[158] M. Bor and U. Roedig, "LoRa transmission parameter selection," in *13th Int. Conf. Distributed Computing Sensor Syst.* IEEE, 2017, pp. 27–34.

[159] The Things Network, https://www.thethingsnetwork.org/article/lorawan-world-record-broken-twice-in-single-experiment-1, 2020, [Online]. Last accessed on: Apr. 24, 2020.

[160] J. Petäjäjärvi, K. Mikhaylov, M. Hämäläinen, and J. Iinatti, "Evaluation of LoRa LPWAN technology for remote health and wellbeing monitoring," in *10th Int.l Symp. Medical Inf. Commun. Technol.* IEEE, 2016, pp. 1–5.

[161] P. Catherwood, S. McComb, M. Little, and J. A. D. McLaughlin, "Channel characterisation for wearable LoRaWAN monitors," in *Loughborough Antennas & Propagation Conference*. IET, 2017, pp. 1–4.

[162] T. Ameloot, P. Van Torre, and H. Rogier, "Indoor body-to-body LoRa link characterization," in *IEEE-APS Topical Conf. Antennas Propag. Wireless Commun.* IEEE, 2019, pp. 42–47.

[163] ——, "Body-centric LoRa networks based on system-integrated textile SIW antennas," in *XXXIIIrd General Assembly and Scientific Symposium of the International Union of Radio Science*. IEEE, 2020, pp. 1–4.

[164] P. Van Torre, T. Ameloot, and H. Rogier, "Long-range body-to-body LoRa link at 868 MHz," in *13th Eur. Conf. Antennas Propag.* IEEE, 2019, pp. 1–5.

[165] T. Ameloot, P. Van Torre, and H. Rogier, "LoRa base-station-to-body communication with SIMO front-to-back diversity," *IEEE Transactions on Antennas and Propagation*, vol. 69, no. 1, pp. 397–405, 2020.

[166] N. Hayati and M. Suryanegara, "The IoT LoRa system design for tracking and monitoring patient with mental disorder," in *IEEE Int. Conf. Commun. Netw. Satellite*. IEEE, 2017, pp. 135–139.

[167] A. T. Nugraha, R. Wibowo, M. Suryanegara, and N. Hayati, "An IoT-LoRa system for tracking a patient with a mental disorder: Correlation between battery capacity and speed of movement," in *7th Int. Conf. Computer Commun. Eng.* IEEE, 2018, pp. 198–201.

[168] F. Wu, C. Rüdiger, J.-M. Redouté, and M. R. Yuce, "WE-Safe: A wearable IoT sensor node for safety applications via LoRa," in *IEEE 4th World Forum Internet Things.* IEEE, 2018, pp. 144–148.

[169] F. Wu, J.-M. Redouté, and M. R. Yuce, "We-safe: A self-powered wearable IoT sensor network for safety applications based on LoRa," *IEEE Access*, vol. 6, pp. 40 846–40 853, 2018.

[170] "Gper," http://www.gper.me/en/gper_global.php, Accessed: Aug. 22, 2021.

[171] "Lineable," https://www.lineable.net/, Accessed: Aug. 22, 2021.

[172] "Wearloc-2," https://proesystech.com/products/wearloc-2/, Accessed: Aug. 22, 2021.

[173] P. Van Torre, T. Ameloot, and H. Rogier, "Wearable 868 MHz LoRa wireless sensor node on a substrate-integrated-waveguide antenna platform," in *2019 49th European Microwave Conference (EuMC).* IEEE, 2019, pp. 496–499.

[174] T. Ameloot, M. Moeneclaey, P. Van Torre, and H. Rogier, "Characterizing the impact of doppler effects on body-centric LoRa links with SDR," *Sensors*, vol. 21, no. 12, p. 4049, 2021.

[175] S. Agneessens, "Coupled eighth-mode substrate integrated waveguide antenna: Small and wideband with high-body antenna isolation," *IEEE Access*, vol. 6, pp. 1595–1602, 2017.

[176] "Pycom_002_Specsheets_LoPy4_v2," https://docs.pycom.io/gitbook/assets/specsheets/Pycom_002_Specsheets_LoPy4_v2.pdf, 2017, Pycom Company, Guildford, U.K. Accessed: Aug. 15, 2021.

[177] "Manual PIEPS PRO BT/POWDER BT," https://www.pieps.com/sites/default/files/ 2019_08_08_propowderbt_manual_en-en.pdf, 2019, PIEPS GmbH, August 2019. Accessed on: March. 5, 2020.

[178] "Bluetooth Specifications Version 4.2," https://www.bluetooth.org/DocMan/ handlers/DownloadDoc.ashx?doc_id=286439, 2014, Bluetooth SIG, Dec. 2, 2014.Accessed on: March. 5, 2020.

[179] "IEEE standard for information technology—telecommunications and information exchange between systems local and metropolitan area networks—specific requirements - part 11: Wireless LAN medium access control (MAC) and physical layer (PHY) specifications," International Organization for Standardization, Standard, Dec. 2016, in IEEE Std 802.11-2016 (Revision of IEEE Std 802.11-2012).

[180] LoRa (868MHz/915MHz) Sigfox Antenna Kit, https://pycom.io/product/ lora-868mhz-915mhz-sigfox-antenna-kit/, 2017, Pycom Company, Guildford, U.K. Accessed: Oct. 27, 2021.

[181] A. Augustin, J. Yi, T. Clausen, and W. Townsley, "A Study of LoRa: Long Range & Low Power Networks for the Internet of Things, year=2016, volume=16, number=9," *Sensors*.

[182] B. Seye, M. R. Ngom, B. Gueye, and M. Diallo, "A study of LoRa coverage: Range evaluation and channel attenuation model," in *1st Int. Conf. Smart Cities Commun.*, Ouagadougou, Burkina Faso, Jul. 2018, pp. 1–4.

[183] Heino, P. and others, "Deliverable D5.3, WINNER+ Final Channel Models V1.0, CELTIC CP5â026 WINNER+ Project," http://projects.celtic-initiative.org/winner+ /deliverables_winnerplus.html, Jun. 2010.

[184] Z. Cui, C. Briso-RodrÃguez, K. Guan, C. Calvo-RamÃrez, B. Ai, and Z. Zhong, "Measurement-based modeling and analysis of UAV air-ground channels at 1 and 4 GHz," *IEEE Antennas Wireless Propag. Lett.*, vol. 18, no. 9, pp. 1804–1808, Sep. 2019.

[185] R. El Chall, S. Lahoud, and M. El Helou, "LoRaWAN network: Radio propagation models and performance evaluation in various environments in lebanon," *IEEE Internet Things J.*, vol. 6, no. 2, pp. 2366–2378, Apr. 2019.

[186] T. O. Olasupo, "Wireless communication modeling for the deployment of tiny iot devices in rocky and mountainous environment," *IEEE Sensors Letters*, vol. 3, no. 7, pp. 1–4, Jul. 2019, art no. 6001204, doi: 10.1109/LSENS.2019.2918331.

[187] N. Podevijn *et al.*, "TDoA-based outdoor positioning with tracking algorithm in a public LoRa network," *Wireless Communications and Mobile Computing*, vol. 2018, no. 7, pp. 1–9, May 2018, article no. 1864209, . https://doi.org/10.1155/2018/1864209.

[188] T. J. Rouphael, "High-level requirements and link budget analysis," in *RF and Digital Signal Processing for Software-Defined Radio*, 1st ed.   Burlington, Vermont, USA: Elsevier Newnes, 2009, ch. 4, p. 100.

[189] V. Ferrara, "Technical survey about available technologies for detecting buried people under rubble or avalanches," *WIT Transactions on The Built Environment*, vol. 150, pp. 91–101, 2015.

[190] A. Kachroo *et al.*, "Unmanned aerial vehicle-to-wearables (UAV2W) indoor radio propagation channel measurements and modeling," *IEEE Access*, vol. 7, pp. 73 741–73 750, May 2019.

[191] Y. Saita, T. Ito, N. Michishita, and M. Morishita, "Low-frequency inverted-F antenna on hemispherical ground plane," in *Proc. Int. Symp. Antennas Propag. Conf.*, Kaohsiung, Taiwan, 2014, pp. 183–184.

[192] D. Kitching and F. Lalezari, "Low profile helmet mount GPS antenna," in *Proc. Conf. Tactical Commun.*, Fort Wayne, IN, USA, 1990, pp. 661–702.

[193] Y. Ono and Y. Okano, "Development of wearable antenna for VHF-band," in *2013 International Symposium on Intelligent Signal Processing and Communication Systems*.   IEEE, 2013, pp. 622–626.

[194] N. Nishiyama, N. Michishita, and H. Morishita, "Low-frequency inverted-F antenna on annular ground plane," in *Proc. IEEE MTT-S Int. Microw. Workshop Series RF Wireless Technol. Biomed. Healthcare Appl.*, Taipei, Taiwan, 2015, pp. 143–144.

[195] ——, "SAR reduction of helmet antenna composed of folded dipole with slit-loaded ring," in *Proc. Int. Symp. Antennas Propag.*, Hobart, Austrailia, 2015, pp. 1–2.

[196] N. Nguyen-Trong, A. Piotrowski, T. Kaufmann, and C. Fumeaux, "Low-profile wideband monopolar UHF antennas for integration onto vehicles and helmets," *IEEE Transactions on Antennas and Propagation*, vol. 64, no. 6, pp. 2562–2568, 2016.

[197] J. Fortinberry, Z. Hood, and E. Topsakal, "A helmet mounted GPS antenna," in *Mississippi State University, Antennas and Propagation Society International Symposium*, vol. 3, 2005, pp. 471–474.

[198] N. Nomura, N. Michishita, and H. Morishita, "Folded dipole antenna on hemispherical PMC shell for helmet antenna design," in *2017 International Workshop on Antenna Technology: Small Antennas, Innovative Structures, and Applications (iWAT)*. IEEE, 2017, pp. 350–351.

[199] J.-Y. Shin and J.-M. Woo, "Military antennas," in *2018 International Symposium on Antennas and Propagation (ISAP)*. IEEE, 2018, pp. 1–2.

[200] J. Lebaric and A.-T. Tan, "Ultra-wideband conformal helmet antenna," in *2000 Asia-Pacific Microwave Conference. Proceedings (Cat. No. 00TH8522)*. IEEE, 2000, pp. 1477–1481.

[201] R. Sreekrishna, B. Karthikeyan, and G. R. Kadambi, "Design and development of a compact wideband conformal antenna for wireless applications," *SASTech*, vol. 10, 2011.

[202] R. W. Adler, D. S. Gibbs, J. E. Lebaric, and S. S. Schwarz, "Helmet mounted UHF antenna for mobile user objective system (MUOS)," in *MILCOM 2002. Proceedings*, vol. 1. IEEE, 2002, pp. 311–315.

[203] J.-Y. Park, H.-K. Ryu, and J.-M. Woo, "Helmet installed antenna using a half-wavelength circular loop antenna," in *Proc. IEEE Antennas Propag. Soc. Int. Symp.*, Honolulu, HI, USA, 2007, pp. 4176–4179.

[204] J. J. H. Wang, "The physical foundation, developmental history, and ultra-wideband performance of SMM (spiral-mode microstrip) antennas," in *2005 IEEE Antennas and Propagation Society International Symposium*, vol. 3.   IEEE, 2005, pp. 586–589.

[205] H. Goonesinghe, A. Mehta, R. Lewis, and N. Clow, "A conformal pattern adaptive square loop antenna for body and vehicle platforms," in *2014 IEEE Antennas and Propagation Society International Symposium (APSURSI)*.   IEEE, 2014, pp. 1445–1446.

[206] Y. F. Cao, X. Y. Zhang, and T. Mo, "Low-profile conical-pattern slot antenna with wideband performance using artificial magnetic conductors," *IEEE Transactions on Antennas and Propagation*, vol. 66, no. 5, pp. 2210–2218, 2018.

[207] Y. H. Kim, S. W. Chan, J. Ahn, and S. H. Cho, "Studies of the variation in the dielectric constant and unique behaviors with changes in the foaming ratio of the microcellular foaming process," *Polym.-Plastics Technol. Eng.*, vol. 50, no. 8, pp. 762–767, Jun. 2011.

[208] G. Casati *et al.*, "The interrogation footprint of RFID-UAV: electromagnetic modeling and experimentations," *IEEE J. Radio Freq. Identification*, vol. 1, no. 2, pp. 155–162, Jun. 2017.

[209] G. Marrocco, E. Di Giampaolo, and R. Aliberti, "Estimation of UHF RFID reading regions in real environments," *IEEE Antennas and Propagation Magazine*, vol. 51, no. 6, pp. 44–57, 2009.

[210] Keonn Technologies, "Advantenna p11 datasheet, year = 2015, note=Accessed on: June 22, 2020. [Online]. Available: https://www.keonn.com/images/stories/pdf/Keonn-Advantenna-p11-Data_sheet.pdf,."

[211] CAEN RFID srl., "WANTENNAX005 circular polarized antenna datasheet," 2012.

[212] A. A. Khuwaja, Y. Chen, N. Zhao, M.-S. Alouini, and P. Dobbins, "A survey of channel modeling for uav communications," *IEEE Communications Surveys Tutorials*, vol. 20, no. 4, pp. 2804–2821, 2018.

[213] "SX1272/73 Datasheet," https://www.mouser.com/datasheet/2/761/sx1272-1277619.pdf, 2017, Semtech Corporation, Camarillo, CA, USA. Accessed: Aug. 15, 2021.

[214] R. E. Collin, *Radio-Wave Propagation*. New York, NY, USA: Mc-Graw Hill, 1985, ch. 6, sec. 1, pp. 339-349.

[215] Safe operation of drones in Europe, https://www.easa.europa.eu/sites/default/files/dfu/217603_EASA_DRONES_LEAFLET%20%28002%29_final.pdf, 2018, European Union Aviation Safety Agency, April 2018. Accessed: Nov. 5, 2020.

[216] M. Saelens, J. Hoebeke, A. Shahid, and E. De Poorter, "Impact of EU duty cycle and transmission power limitations for sub-GHz LPWAN SRDs: an overview and future challenges," *EURASIP J. Wireless Commun. Netw*, vol. 2019, Sep. 2019, art. no. 219.

[217] Electrical characteristics of the surface of the Earth, ITU-R P.527-4, https://www.itu.int/rec/R-REC-P.527-4-201706-I/en, 2021, International Telecommunication Union Radiocommunication Sector, 2017. Accessed: Feb. 12, 2021.

[218] E. D. Widianto, M. S. M. Pakpahan, A. A. Faizal, and R. Septiana, "LoRa QoS performance analysis on various spreading factor in indonesia," in *Int. Symp. Electronics Smart Devices*, 2018, pp. 1–5.

[219] J. Petajajarvi, K. Mikhaylov, A. Roivainen, T. Hanninen, and M. Pettissalo, "On the coverage of LPWANs: range evaluation and channel attenuation model for LoRa technology," in *2015 14th international conference on its telecommunications (itst)*. IEEE, 2015, pp. 55–59.

[220] A. Al-Hourani and K. Gomez, "Modeling cellular-to-UAV path-loss for suburban environments," *IEEE Wireless Commun. Lett.*, vol. 7, no. 1, pp. 82–85, Feb. 2018.

[221] A. Grami, *Introduction to Digital Communication*, 1st ed.   New York, NY, USA: Academic Press Inc., 2015, ch. 12, pp.493-527.

[222] F. Mira, X. Artiga, I. Llamas-Garro, F. Vázquez-Gallego, and J. S. Velázquez-González, "Circularly polarized dual-band LoRa/GPS antenna for a uav-assisted hazardous gas and aerosol sensor," *Micromachines*, vol. 12, no. 4, p. 377, 2021.

[223] T. Hadwen, V. Smallbon, Q. Zhang, and M. D'Souza, "Energy efficient LoRa GPS tracker for dementia patients," in *2017 39th annual international conference of the IEEE engineering in medicine and biology society (EMBC)*.   IEEE, 2017, pp. 771–774.

[224] M. Aernouts *et al.*, "Combining TDoA and AoA with a particle filter in an outdoor LoRaWAN network," in *2020 IEEE/ION Position, Location and Navigation Symposium*, 2020, pp. 1060–1069.

[225] Y. Lin, W. Dong, Y. Gao, and T. Gu, "SateLoc: A virtual fingerprinting approach to outdoor LoRa localization using satellite images," in *19th ACM/IEEE Int. Conf. Inf. Process. Sensors Netw.*, Sydney, Australia, 2020, pp. 13–24.

[226] H. Zhu, K.-F. Tsang, Y. Liu, Y. Wei, H. Wang, C. K. Wu, and H. R. Chi, "Extreme rss based indoor localization for lorawan with boundary autocorrelation," *IEEE Transactions on Industrial Informatics*, vol. 17, no. 7, pp. 4458–4468, 2020.

[227] T. Janssen, R. Berkvens, and M. Weyn, "Benchmarking RSS-based localization algorithms with LoRaWAN," *Internet of Things*, vol. 11, p. 100235, 2020.

[228] J. Choi, R. Ghaffari, L. Baker, and J. Rogers, "Skin-interfaced systems for sweat collection and analytics," *Science Advances*, vol. 4, p. eaar3921, February 2018.

[229] S. Muekdang and W. San-Um, "Intelligent RF-based indoor localization through RSSI of LoRa communication technology," *International journal of future computer and communication*, vol. 7, no. 4, 2018.

[230] P. Savazzi, E. Goldoni, A. Vizziello, L. Favalli, and P. Gamba, "A Wiener-based RSSI localization algorithm exploiting modulation diversity in LoRa networks," *IEEE Sensors J.*, vol. 19, no. 24, pp. 12 381–12 388, Dec. 2019.

[231] K. Lam, C. Cheung, and W. Lee, "LoRa-based localization systems for noisy outdoor environment," in *Proc. IEEE 13th Int. Wireless Mobil Comput., Netw. Commun.*, Rome, Italy, 2017, pp. 278–284.

[232] ——, "New RSSI-based LoRa localization algorithms for very noisy outdoor environment," in *Proc. IEEE 42nd Annual Computer Software and Applications Conf.*, Tokyo, Japan, 2018, pp. 794–799.

[233] ——, "RSSI-based LoRa localization systems for large-scale indoor and outdoor environments," *IEEE Trans. Veh. Technol.*, vol. 68, no. 12, pp. 11 778–11 791, Dec. 2019.

[234] X. Li, "RSS-based location estimation with unknown pathloss model," *IEEE Trans. Wireless Commun.*, vol. 5, no. 12, pp. 3626–3633, Dec. 2006.

[235] G. Wang, H. Chen, Y. Li, and M. Jin, "On received-signal-strength based localization with unknown transmit power and path loss exponent," *IEEE Wireless Commun. Lett.*, vol. 1, no. 2, pp. 536–539, Oct. 2012.

[236] M. U. Sheikh, K. Hiltunen, and J. Lempiäinen, "Angular wall loss model and extended building penetration model for outdoor to indoor propagation," in *13th Int. Wireless Commun. Mobile Comput. Conf.*, Valencia, Spain, June 2017, pp. 1291–1296.

[237] A. Hrovat, G. Kandus, and T. Javornik, "A survey of radio propagation modeling for tunnels," *IEEE Commun. Surv. Tutor.*, vol. 16, no. 2, pp. 658–669, Oct. 2014.

[238] M. Raspopoulos *et al.*, "Location-dependent information extraction for positioning," in *2012 Int. Conf. Localization GNSS*, Starnberg, Germany, June 2012, pp. 1–6.

[239] N. Salman, A. H. Kemp, and M. Ghogho, "Low complexity joint estimation of location and path-loss exponent," *IEEE Wireless Commun. Lett.*, vol. 1, no. 4, pp. 364–367, Aug. 2012.

[240] D. Åkerberg, "Properties of a TDMA pico cellular office communication system," in *IEEE Veh. Technol. Conf.*, San Francisco, CA, USA, May 1989, pp. 186–191.

[241] J.-J. Park, J. Lee, K.-W. Kim, and M.-D. Kim, "Large- and small-scale fading characteristics of mmWave HST propagation channel based on 28-GHz measurements," in *15th European Conf. Antennas Propag.*, Dusseldorf, Germany, Mar. 2021, pp. 1–5.

[242] P. Zhang, H. Wang, and W. Hong, "Empirical analysis of millimeter-wave propagation in indoor transitional environments," in *IEEE Int. Symp. Antennas Propag. North American Radio Sci. Meeting*, Montreal, Canada, Jul. 2020, pp. 1189–1190.

[243] Y. Zhang, G. Zheng, and J. Sheng, "Radio propagation at 900 MHz in underground coal mines," *IEEE Transactions on Antennas and Propagation*, vol. 49, no. 5, pp. 757–762, May 2001.

[244] K. Nuangwongsa, K. Phaebua, T. Lertwiriyaprapa, C. Phongcharoenpanich, and M. Krairiksh, "Path loss modeling in durian orchard for wireless network at 5.8 GHz," in *6th Int. Conf. Electrical Eng./Electronics, Computer, Telecom. Inf. Technol.*, Chonburi, Thailand, May 2009, pp. 816–819.

[245] M. Babalou, S. Alirezaee, A. Soheili, A. Ahmadi, M. Ahmadi, and S. Erfani, "Microcell path loss estimation using log-normal model in GSM cellular network," in *Int. Symp. Signals, Circuits Systems*, Iasi, Romania, Aug. 2015, pp. 1–4.

[246] J. Werner, J. Wang, A. Hakkarainen, D. Cabric, and M. Valkama, "Performance and Cramer-Rao bounds for DoA/RSS estimation and transmitter localization using sectorized antennas," *IEEE Trans. Veh. Technol.*, vol. 65, no. 3, pp. 3255–3270, May 2016.

[247] Y. T. Chan, B. H. Lee, R. Inkol, and F. Chan, "Estimation of emitter power, location, and path loss exponent," in *Proc. 25th IEEE Can. Conf. Elect. Comput. Eng.*, Montreal, Canada, Apr. 2012, pp. 1–5.

[248] A. J. Weiss, "On the accuracy of a cellular location system based on RSS measurements," *IEEE Trans. Veh. Technol.*, vol. 52, no. 6, pp. 1508–1518, Nov. 2003.

[249] D. Zorbas, "Design considerations for time-slotted LoRa(WAN)," in *Proc. 2020 Int. Conf. Embedded Wireless Systems Netw.*, Lyon, France, Feb. 2020, pp. 271–276.

[250] G. M. Bianco, "Lora (868 MHz) path loss measurements in double-slope environment," 2021. [Online]. Available: https://dx.doi.org/10.21227/agyw-ws11

[251] F. Tschirky, B. Brabec, and M. Kern, "Avalanche rescue systems in Switzerland: Experience and limitations," in *Proc. Int. Snow Sci. Workshop*, Big Sky MT, USA, Oct. 2000, pp. 369–376.

[252] J. Schweizer and G. Krüsi, "Testing the performance of avalanche transceivers," *Cold Regions Sci. Technol.*, vol. 37, no. 3, pp. 429–438, 2003.

[253] S. X. Ta, I. Park, and R. W. Ziolkowski, "Crossed dipole antennas: A review," *IEEE Antennas Propag. Mag.*, vol. 57, no. 5, pp. 107–122, Oct. 2015.

[254] LoRaWAN/GNSS/Biosensor Wearable Tracker WearLOC-2, http://proesystech. com/wp-content/uploads/2018/02/Wearloc-2-datasheet.pdf, 2018, ProEsys s.r.l., Rome, Italy. Accessed: Aug. 15, 2021.

[255] H. Holma, A. Toskala, and T. Nakamura, *5G Technology: 3GPP New Radio*, 1st ed. Hoboken, NJ, USA: Wiley, 2020.

[256] A. Dastjerdi and R. Buyya, *Internet of things: principles and paradigms*, 1st ed. Burlington, MA, USA: Morgan Kaufmann, 2006.

[257] J. Bardyn, T. Melly, O. Seller, and N. Sornin, "Iot: The era of lpwan is starting now," in *42nd European Solid-State Circuits Conference*, Lausanne, Switzerland, 2016, pp. 25–30.

[258] C. Gomez, A. Minaburo, L. Toutain, D. Barthel, and J. C. Zuniga, "Ipv6 over lpwans: Connecting low power wide area networks to the internet (of things)," *IEEE Wireless Communications*, vol. 27, no. 1, pp. 206–213, 2020.

[259] S. C. Gaddam and M. K. Rai, "A comparative study on various lpwan and cellular communication technologies for iot based smart applications," in *2018 International Conference on Emerging Trends and Innovations In Engineering And Technological Research (ICETIETR)*, 2018, pp. 1–8.

[260] E. Kail, A. Banati, E. LÃ¡szlo, and M. Kozlovszky, "Security survey of dedicated iot networks in the unlicensed ism bands," in *2018 IEEE 12th International Symposium on Applied Computational Intelligence and Informatics (SACI)*, 2018, pp. 449–454.

[261] Y. S. Jang, M. R. Usman, M. A. Usman, and S. Y. Shin, "Swapped huffman tree coding application for low-power wide-area network (LPWAN)," in *2016 International Conference on Smart Green Technology in Electrical and Information Systems (ICSGTEIS)*, Bali, Indonesia, 2016, pp. 53–58.

[262] J. Tang, J. Li, A. Zhong, B. Xiong, X. Bian, and Y. Li, "Application of LoRa and NB-IoT in ubiquitous power internet of things: A case study of fault indicator in electricity distribution network," in *2019 4th International Conference on Intelligent Green Building and Smart Grid (IGBSG)*, Hubei, China, 2019, pp. 380–383.

[263] R. S. Sinha, Y. Wei, and S.-H. Hwang, "A survey on LPWA technology: LoRa and NB-IoT," *Ict Express*, vol. 3, no. 1, pp. 14–21, 2017.

[264] M. Centenaro, L. Vangelista, A. Zanella, and M. Zorzi, "Long-range communications in unlicensed bands: the rising stars in the IoT and smart city scenarios," *IEEE Wireless Communications*, vol. 23, no. 5, pp. 60–67, Oct. 2016.

[265] A. D'Elia, L. Perilli, F. Viola, L. Roffia, F. Antoniazzi, R. Canegallo, and T. S. Cinotti, "A self-powered wsan for energy efficient heat distribution," in *2016 IEEE Sensors Applications Symposium (SAS)*, Catania, Italy, 2016, pp. 1–6.

[266] J. Norair, "Introduction to DASH7 technologies," *Dash7 Alliance Low Power RF Technical Overview*, pp. 1–22, 2009.

[267] M. Weyn, G. Ergeerts, R. Berkvens, B. Wojciechowski, and Y. Tabakov, "Dash7 alliance protocol 1.0: Low-power, mid-range sensor and actuator communication," in *2015 IEEE Conference on Standards for Communications and Networking*, Tokyo, Japan, 2015, pp. 54–59.

[268] M. Lauridsen, I. Z. Kovacs, P. Mogensen, M. Sorensen, and S. Holst, "Coverage and capacity analysis of lte-m and nb-iot in a rural area," in *2016 IEEE 84th Vehicular Technology Conference (VTC-Fall)*, Montreal, Canada, 2016, pp. 1–5.

[269] R. Ratasuk, N. Mangalvedhe, A. Ghosh, and B. Vejlgaard, "Narrowband lte-m system for m2m communication," in *2014 IEEE 80th Vehicular Technology Conference (VTC2014-Fall)*, Vancouver, Canada, 2014, pp. 1–5.

[270] S. Barillaro, S. Rhee, G. Escudero, R. Kacker, L. Badger, and D. R. Kuhn, "Low-power wide area networks (lpwan) for communications of mobile sensor data," in *Proceedings of the 2nd ACM/EIGSCC Symposium on Smart Cities and Communities*, New York, NYC, USA, 2019, pp. 1–8.

[271] K.-H. Phung, H. Tran, Q. Nguyen, T. T. Huong, and T.-L. Nguyen, "Analysis and assessment of LoRaWAN," in *2nd International Conference on Recent Advances in Signal Processing, Telecommunications Computing*, 2018, pp. 241–246.

[272] D. M. Dobkin, *The RF in RFID: UHF RFID in Practice*. Elsevier, 2013.

[273] B. Soulé, B. Lefèvre, E. Boutroy, V. Reynier, F. Roux, and J. Corneloup, "Accidentology of mountain sports," *Situation, review & diagnosis. Crolles*, 2014.

[274] R. Sadeghi, J. C. Konwinski, and R. K. Cydulka, "Adirondack park incidents: A retrospective review of search and rescue reports from 2008 and 2009," *Wilderness & environmental medicine*, vol. 26, no. 2, pp. 159–163, 2015.

[275] T. W. Heggie and M. E. Amundson, "Dead men walking: search and rescue in US national parks," *Wilderness & environmental medicine*, vol. 20, no. 3, pp. 244–249, 2009.

[276] S. Hearns, "The Scottish mountain rescue casualty study," *Emergency Medicine Journal*, vol. 20, no. 3, pp. 281–284, 2003.

[277] E. K. Hung and D. A. Townes, "Search and rescue in Yosemite National Park: a 10-year review," *Wilderness & environmental medicine*, vol. 18, no. 2, pp. 111–116, 2007.

[278] F. J. Wild, "Epidemiology of mountain search and rescue operations in Banff, Yoho, and Kootenay National Parks, 2003–06," *Wilderness & environmental medicine*, vol. 19, no. 4, pp. 245–251, 2008.

[279] C. Van Tilburg, "First report of using portable unmanned aircraft systems (drones) for search and rescue," *Wilderness & environmental medicine*, vol. 28, no. 2, pp. 116–118, 2017.

[280] A. Goetz, S. Zorn, R. Rose, G. Fischer, and R. Weigel, "A time difference of arrival system architecture for GSM mobile phone localization in search and rescue scenarios," in *2011 8th Workshop on Positioning, Navigation and Communication*. IEEE, 2011, pp. 24–27.

[281] S. Zorn, M. Gardill, R. Rose, A. Goetz, R. Weigel, and A. Koelpin, "A smart jamming system for UMTS/WCDMA cellular phone networks for search and rescue applications," in *2012 IEEE/MTT-S International Microwave Symposium Digest*. IEEE, 2012, pp. 1–3.

[282] "Avalanche death toll continues to climb," https://planetski.eu/2021/02/01/ avalanche-death-toll-in-the-alps-continues-to-climb/, 2021, Planetsky, Italy. Accessed: Aug. 27, 2021.

[283] K. Grasegger, G. Strapazzon, E. Procter, H. Brugger, and I. Soteras, "Avalanche survival after rescue with the RECCO rescue system: a case report," *Wilderness & environmental medicine*, vol. 27, no. 2, pp. 282–286, 2016.

[284] J. Schweizer and M. Lutschg, "Characteristics of human-triggered avalanches," *Cold Regions Science and Technology*, vol. 33, no. 3, 2001.

[285] S. McIntosh, C. Grissom, C. Olivares, H. Kim, and B. Tremper, "Cause of death in avalanche fatalities," *Wilderness & Environmental Medicine*, vol. 18, no. 4, pp. 293–297, 2007.

[286] D. Stopper and J. Mullen, "How common are multiple burial situations? Avalanche incidents in Tyrol, Austria, 1997-2003," *International Commission for Alpine Rescue ICAR*, 2007.

[287] M. Genswein and S. Harvey, "Statistical analyses on multiple burial situations and search strategies for multiple burials," *ISSW*, 2002.

[288] H. Schantz and A. Nikravan, "Simple Formulas for Near-Field Transmission, Gain, and Fields," in *2013 Antennas Applications Symposium*, 2013.

[289] "ETSI EN 300 718-1 V2.1.0," European Telecommunications Standards Institute, Tech. Rep., 2019.

[290] N. Ayuso, A. J. Cuchi, F. Leral, and J. L. Villarroel, "Avalanche beacon magnetic field calculations for rescue techniques improvement," in *2007 IEEE International Geoscience and Remote Sensing Symposium*, Barcelona, Spain, 2007, pp. 722–725.

[291] M. Stanford, "Use of Recco system to locate buried roads in a winter environment," in *Proceedings of the 1994 International Snow Science Workshop*, Snowbird, Utah, USA, 1994.

[292] O. Bergb, *Advanced rescue detector - Design and development of an improved rescue antenna*. Stockholm, Sweden: KTH Rozal Institute of Technology, 2014, M.Sc. thesis.

[293] R9 quick guide, http://www.recco.com/upload/Global/Images/Downloads/ Training%20materia\/quick_guide/RECCO-R9-quick-guide-v01_ENG_v05.pdf, Available. [Online]. Accessed: Aug. 15, 2021.

[294] Y. Chen and A. Terzis, "On the implications of the log-normal path loss model: an efficient method to deploy and move sensor motes," in *Proceedings of the 9th ACM Conference on Embedded Networked Sensor Systems*, Nov. 2011, pp. 26–39.

[295] P. Ferrazzoli, "Effetti della superficie terrestre," in *Appunti di propagazione di onde elettromagnetiche nei mezzi naturali*, (in Italian,) 1st ed. Roma, Italy: ARACNE ed., 1988, ch. 2, sec. 1, pp. 11-14.

[296] J. P. Linnartz, *Narrowband Land-Mobile Radio networks*. Norwood, MA, USA: Artech house, 1993.

[297] D. Munoz, F. B. Lara, C. Vargas, and R. Enriquez-Caldera, *Position location techniques and applications*. Academic Press, 2009.

[298] J. D. Gibson, *Mobile communications handbook*, 2nd ed. CRC press, 2012.

[299] K. Pahlavan and P. Krishnamurthy, *Principles of Wireless Acess and Localization*. Hoboken, NJ, USA: John Wiley and Sons, 2013.

[300] A. E. Forooshani, S. Bashir, D. G. Michelson, and S. Noghanian, "A survey of wireless communications and propagation modeling in underground mines," *IEEE Commun. Surv. Tut.*, vol. 15, no. 4, pp. 1524–1545, Mar. 2013.

[301] A. Goldsmith, *Wireless Communication*, 1st ed. Cambridge, U.K.: Cambridge University Press, 2005.

[302] W. G. Figel, N. H. Shepherd, and W. F. Trammel, "Vehicle location by a signal attenuation method," *IEEE Trans. Veh. Technol.*, vol. 18, no. 3, pp. 105–109, Nov. 1969.

[303] A. Coluccia and A. Fascista, "Hybrid TOA/RSS range-based localization with self-calibration in asynchronous wireless networks," *Journal of Sensor and Actuator Networks*, vol. 8, no. 2, May 2019.

[304] J. Kuriakose, S. Joshi, R. Vikram Raju, and A. Kilaru, "A review on localization in wireless sensor networks," *Advances in Signal Processing and Intelligent Recognition Systems. Advances in Intelligent Systems and Computing*, vol. 264, 2014.

[305] F. Viani, P. Rocca, G. Oliveri, D. Trinchero, and A. Massa, "âlocalization, tracking, and imaging of targets in wireless sensor networks: An invited review," *Radio Science*, vol. 46, 2011.

[306] C. Savarese, J. M. Rabaey, and J. Beutel, "Location in distributed ad-hoc wireless sensor networks," in *Proc. IEEE Int. Conf. Acoust., Speech, Signal Process.*, vol. 4, Salt Lake City, UT, USA, 2001, pp. 2037–2040.

[307] C. Wu, Z. Yang, and Y. Liu, *Wireless Indoor Localization: A Crowdsourcing Approach*, 1st ed. Berlin, Germany: Springer, 2018.

[308] G. Mao, *Localization Algorithms and Strategies for Wireless Sensor Networks*. Hershey, NY, USA: Information Science Reference, 2009.

[309] J. H. Lee and R. M. Buehrer, "Fundamentals of received signal strength-based position location," in *Handbook of Position Location: Theory, Practice, and Advances*, 1st ed. Hoboken, NJ, USA: John Wiley and Sons, 2012, ch. 11, pp. 359–395.

[310] C. Cavarese, J. M. Rabaey, and J. Beutel, "Location in distributed ad-hoc wireless sensor networks," in *2001 IEEE Int. Conf. Acoust., Speech, Signal Process.*, Salt Lake City, UT, USA, 2001, pp. 2037–2040.

[311] H.-C. Chen, T.-H. Lin, H. Kung, C.-K. Lin, and Y. Gwon, "Determining rf angle of arrival using cots antenna arrays: A field evaluation," in *MILCOM 2012-2012 IEEE Military Communications Conference*. IEEE, 2012, pp. 1–6.

[312] M. R. Kamarudin, Y. I. Nechayev, and P. S. Hall, "Onbody diversity and angle-of-arrival measurement using a pattern switching antenna," *IEEE Transactions on Antennas and Propagation*, vol. 57, no. 4, pp. 964–971, 2009.

[313] C. Steffes, R. Kaune, S. Rau, and F. Fkie, "Determining times of arrival of transponder signals in a. sensor network using gps time synchronization." in *GI-Jahrestagung*. Citeseer, 2011, pp. 481–489.

[314] L. Mailaender, "Comparing geo-location bounds for TOA, TDOA, and round-trip TOA," in *IEEE 18th Int. Symp. Personal, Indoor Mobile Radio Commun.* IEEE, 2007, pp. 1–5.

[315] F. Kong, J. Wang, N. Zheng, G. Chen, and J. Zheng, "A robust weighted intersection algorithm for target localization using aoa measurements," in *IEEE Advanced Inf. Management, Communicates, Electronic and Automation Control Conf.*, 2016, pp. 23–28.

[316] H. Koshima and J. Hoshen, "Personal locator services emerge," *IEEE Spectrum*, vol. 37, no. 2, pp. 41–48, 2000.

[317] N. Saeed, W. Ahmad, and D. M. S. Bhatti, "Localization of vehicular ad-hoc networks with RSS based distance estimation," in *2018 Int. Conf. Comput., Math. Eng. Technol.*, Sukkur, Pakistan, Mar. 2018, pp. 1–6.

[318] A. Medeisis and A. Kajackas, "On the use of the universal Okumura-Hata propagation prediction model in rural areas," in *VTC2000-Spring. 2000 IEEE 51st Vehicular Technology Conference Proceedings (Cat. No. 00CH37026)*, vol. 3. IEEE, 2000, pp. 1815–1818.

[319] N. Salman, M. Ghogho, and A. H. Kemp, "On the joint estimation of the RSS-based location and path-loss exponent," *IEEE Wireless Commun. Lett.*, vol. 1, no. 1, pp. 34–37, Feb. 2012.

[320] Y. T. Chan, B. H. Lee, R. Inkol, and F. Chan, "Received signal strength localization with an unknown path loss exponent," in *Proc. 24th Can. Conf. Elect. Comput. Eng.*, Niagara Falls, Canada, May 2011, pp. 456–459.

[321] J. Shirahama and T. Ohtsuki, "RSS-based localization in environments with different path loss exponent for each link," in *Proc. IEEE Veh. Technol. Conf.*, Singapore, Singapore, May 2008, pp. 1509–1513.

[322] A. Bel, J. L. Vicario, and G. Seco-Granados, "Localization algorithm with on-line path loss estimation and node selection," *Sensors*, vol. 11, no. 7, pp. 6905–6925, Jul. 2011.

[323] S. Uluskan and T. Filik, "A geometrical closed form solution for RSS based far-field localization: direction of exponent uncertainty," *Wireless Netw.*, vol. 25, no. 3, pp. 215–227, July 2019.

[324] Y. Zou and H. Liu, "RSS-based target localization with unknown model parameters and sensor position errors," *IEEE Trans. Veh. Technol.*, vol. 70, no. 7, pp. 6969–6982, Jun. 2021.

[325] G. Palomba, *Elementi di statistica per l'Econometria*, 3rd ed. Ancona, Italy: CLUA edizioni, Oct. 2015, (in Italian).

[326] B.-Z. Bobrovsky, E. Mayer-Wolf, and M. Zakai, "Some classes of global cramér-rao bounds," *The Annals of Statistics*, pp. 1421–1438, 1987.

[327] Y.-H. Li and P.-C. Yeh, "An interpretation of the moore-penrose generalized inverse of a singular fisher information matrix," *IEEE Transactions on Signal Processing*, vol. 60, no. 10, pp. 5532–5536, 2012.

[328] Z. Ben-Haim and Y. C. Eldar, "On the constrained cramér–rao bound with a singular fisher information matrix," *IEEE Signal Processing Letters*, vol. 16, no. 6, pp. 453–456, 2009.

List of Author's Publications

List of Publications and Awards

In this Chapter are listed the publication of the author of this thesis published during his PhD research.

Journal Papers

1. **G. M. Bianco**, A. Mejia-Aguilar, and G. Marrocco, "Numerical and Experimental Characterization of LoRa-based Helmet-to-UAV links on Flat Lands", *IEEE Antennas and Propagation Magazine,* accepted for publication.

2. **G. M. Bianco**, C. Occhiuzzi, N. Panunzio, and G. Marrocco, "A Survey on Radio Frequency Identification as a Scalable Technology to Face Pandemics", *IEEE Journal of Radio Frequency Identification*, vol. 6, pp. 77-96, 2022, doi: 10.1109/JR-FID.2021.3117764.

3. **G. M. Bianco**, R. Giuliano, F. Mazzenga and G. Marrocco, "Multi-slope Path Loss and Position Estimation with Grid Search and Experimental Results", *IEEE Transactions on Signal and Information Processing over Networks*, vol. 7, pp. 551-561, Aug. 2021, doi: 10.1109/TSIPN.2021.3106693.

4. **G. M. Bianco** and G. Marrocco, "Sensorized facemask with moisture-sensitive RFID antenna", *IEEE Sensors Letters*, vol. 5, no. 3, pp. 1-4, March 2021, Art no. 6000604. doi: 10.1109/LSENS.2021.3059348. Scopus code: 2-s2.0-85100944346

5. **G. M. Bianco**, R. Giuliano, G. Marrocco, F. Mazzenga and A. Mejia-Aguilar, "LoRa System for Search and Rescue: Path Loss Models and Procedures in Mountain Scenarios," in *IEEE Internet of Things Journal*, vol. 8, no. 3, pp. 1985-1999, Feb. 2021. doi: 10.1109/JIOT.2020.3017044. Scopus code: 2-s2.0-85100233328

6. **G. M. Bianco**, S. Amendola and G. Marrocco, "Near-Field Constrained Design for Self-Tuning UHF-RFID Antennas," in *IEEE Transactions on Antennas and Propagation*, vol. 68, no. 10, pp. 6906-6911, Oct. 2020, doi: 10.1109/TAP.2020.2995315. Scopus code: 2-s2.0-85092484769

Encyclopedia Entry

1. C. Occhiuzzi, **G. M Bianco**, S. Caizzone and G. Marrocco, "Antennas as Sensors", in *Encyclopedia of Materials: Electronics*, 1st ed. Amsterdam, The Netherlands: Elsevier, to be published.

Book Contributions

1. **G. M. Bianco** and G. Marrocco, "Radiofrequency Finger Augmentation Devices for the Tactile Internet", in *Wearable Antennas and Electronics,* A. Kiourti and J. L. Volakis, 1st Ed., Norwood, MA, USA: Artech House, 2022, ch. 7, pp. 181-202.

2. C. Occhiuzzi, S. Amendola, C. Miozzi, **G. M. Bianco**, S. Nappi, and G. Marrocco, "Bio-Integrated Epidermal Wireless Sensors for Human Health Monitoring and Sensation Recovery", in *Electromagnetic Fields and Health: Safety, Diagnostic, Therapy (CNIT Technical Report-03)*, R. Massa, 1st Ed., Rome, Italy: Textmat, 2019, ch. 12, pp. 137-150.

Conference Papers

1. **G. M. Bianco** and G. Marrocco, "Indirect Propagation of Body-UAV LoRa Links over Wood and Suburb," accepted at the *3rd URSI Atlantic/Asia-Pacific Radio Science Meeting*, May 29- June 3, Gran Canaria, Spain, 2022.

2. C. Occhiuzzi, F. Camera, M. D'Orazio, N. D'Uva, S. Amendola, **G. M. Bianco**, C. Miozzi, L. Garavaglia, E. Martinelli, and G. Marrocco, "Radiofrequency Sensing System for Fruit Quality Evaluation during Forced Ripening Processes," accepted at the *3rd URSI Atlantic/Asia-Pacific Radio Science Meeting*, May 29- June 3, Gran Canaria, Spain, 2022.

3. **G. M. Bianco** and G. Marrocco, "Radio Frequency Identification and Localization by Wearable LoRa for Search and Rescue in Mountains," accepted at the *16th IEEE Internation Conference on RFID*, 17-19 May, Las Vegas, NV, USA, 2022.

4. A. B. Barba, **G. M. Bianco**, L. Fiore, F. Arduini, G. Marrocco, and C. Occhiuzzi, "Design and Manufacture of Flexible Epidermal NFC Device for Electrochemical Sensing of Sweat," accepted at the *IEEE International Conference on Flexible Printable Sensors and Systems,* June 20-23, Vienna, Austria, 2022.

5. **G. M. Bianco**, A. Mejia-Aguilar, and G. Marrocco, "Measurements and Modeling of Radiohelmet-UAV LoRa Links in a Mountain Canyon," presented at *16th European Conference on Antennas and Propagation (EuCAP)*, Mar. 27- Apr. 1, Madrid, Spain, 2022, pp. 1-4.

6. M. Frattaioli, **G. M. Bianco**, S. Nappi, and G. Marrocco, "A Finger-worn Epidermal Antenna for Pressure Sensing", presented at *16th European Conference on Antennas and Propagation (EuCAP)*, Mar. 27- Apr. 1, Madrid, Spain, 2022, pp. 1-4.

7. N. Panunzio, F. Ciafrei, C. Magnante, **G. M. Bianco**, and G. Marrocco, "Sensorized Facemask with Temperature RFID Sensor for Cough Analysis", presented at *16th European Conference on Antennas and Propagation (EuCAP)*, Mar. 27- Apr. 1, Madrid, Spain, 2022, pp. 1-4.

8. **G. M. Bianco**, N. Panunzio, A. Pintaudi, S. Santamaria, F. Faustino, C. Occhiuzzi, and G. Marrocco, "RFID labeling of police equipment," *2021 IEEE International Conference on RFID Technology and Applications (RFID-TA)*, 6-8 Oct., Delhi, India, 2021, pp. 177-180, doi: 10.1109/RFID-TA53372.2021.9617385.

9. **G. M. Bianco**, N. Panunzio, and G. Marrocco, "RFID research against COVID-19 – Sensorized Face Masks," *2021 IEEE International Conference on RFID Technology and Applications (RFID-TA)*, 6-8 Oct., Delhi, India, 2021, pp. 241-243, doi: 10.1109/RFID-TA53372.2021.9617305.

10. N. Panunzio, **G. M. Bianco**, C. Occhiuzzi, and G. Marrocco, "RFID Sensors for the Monitoring of Body Temperature and Respiratory Function: a Pandemic Prospect", *2021 6th International Conference on Smart and Sustainable Technologies (SpliTech)*, Sep. 8-11, Split, Croatia, 2021, pp. 1-5, doi: 10.23919/SpliTech52315.2021.9566334.

11. **G. M. Bianco**, A. Mejia-Aguilar, and G. Marrocco, "Numerical and experimental evaluation of Radiohelmet-to-UAV LoRa Links", *2021 XXXIVth General Assembly and Scientific Symposium of the International Union of Radio Science (URSI GASS)*, Aug. 28 – Sep. 4, Rome, Italy, 2021, pp. 1-4, doi: 10.23919/URSI-GASS51995.2021.9560375.

12. F. Naccarata, **G. M. Bianco**, and G. Marrocco, "Multi-Channel Radiofrequency Finger Augmentation Device for Tactile Internet", *2021 XXXIVth General Assembly and Scientific Symposium of the International Union of Radio Science (URSI GASS)*, Aug. 28 – Sep. 4, Rome, Italy, 2021, pp. 1-4, doi: 10.23919/URSI-GASS51995.2021.9560208.

13. A. Mejia-Aguilar, **G. M. Bianco**, G. Marrocco, A. Voegele, M. van Veelen, and G. Strapazzon, "In-situ and proximal sensing techniques for monitoring naturals hazards to mitigate risk in tourism activities: A case study in the Geoparch Bletterbach, Italy," *2021 IEEE International Symposium on geoscience and remote sensing*, Brussels, Belgium, July 12-16, 2021, pp. 1815-1818, doi: 10.1109/IGARSS47720.2021.9554279.

14. C. Miozzi, G. Stendardo, **G. M. Bianco**, F. Montecchia and G. Marrocco, "Dual-chip RFID on-skin tag for bilateral breath monitoring", *15th Annual IEEE International Conference on RFID (RFID 2021)*, Apr. 27-30, Atlanta, GA, USA, 2021, pp. 1-6, Art. no. 9444377, doi: 10.1109/RFID52461.2021.9444377. Scopus code: 2-s2.0-85107792410.

15. **G. M. Bianco**, C. Vivarelli, S. Amendola and G. Marrocco, "Experimentation and calibration of Near-Field UHF Epidermal Communication for emerging Tactile Internet," *5th International Conference on Smart and Sustainable Technologies (SpliTech)*, Sep. 23-26, Split, Croatia, 2020, pp. 1-4, doi: 10.23919/SpliTech49282.2020.9243753. Scopus code: 2-s2.0-85096722765.

16. **G. M. Bianco**, A. Mejia-Aguilar and G. Marrocco, "Performance evaluation of LoRa LPWAN technology for mountain Search and Rescue," *5th International Conference on Smart and Sustainable Technologies (SpliTech)*, Sep. 23-26, Split, Croatia, 2020, pp. 1-4, doi: 10.23919/SpliTech49282.2020.9243817. Scopus code: 2-s2.0-85096723085.

17. **G. M. Bianco**, S. Amendola and G. Marrocco, "Near-field modeling of Self-tuning Antennas for the Tactile Internet," *XXXIIIrd General Assembly and Scientific Symposium of the International Union of Radio Science*, Aug. 29-Sep. 5, Rome, Italy, 2020, pp. 1-3, doi: 10.23919/URSIGASS49373.2020.9232032. Scopus code: 2-s2.0-85096820731.

18. **G. M. Bianco**, A. Mejia-Aguilar and G. Marrocco, "Radio wave propagation of LoRa systems in mountains for Search and Rescue operations," *XXXIIIrd General Assembly and Scientific Symposium of the International Union of Radio Science*, Aug. 29-Sep. 5, Rome, Italy, 2020, pp. 1-3, doi: 10.23919/URSIGASS49373.2020.9232231. Scopus code: 2-s2.0-85096830150.

19. S. Amendola, V. Greco, **G. M. Bianco**, E. Daprati and G. Marrocco, "Application of Radio-Finger Augmented Devices to Cognitive Neural remapping," *2019 IEEE International Conference on RFID Technology and Applications (RFID-TA)*, Sep.

25-27, Pisa, Italy, 2019, pp. 258-262. doi: 10.1109/RFID-TA.2019.8892012 Scopus code: 2-s2.0-85075764097.

20. **G. M. Bianco** and G. Marrocco, "Fingertip Self-tuning RFID Antennas for the Discrimination of Dielectric Objects", *13th European Conference on Antennas and Propagation (EuCAP)*, Mar. 31- Apr. 5, Krakow, Poland, 2019, pp. 1-4. Scopus code: 2-s2.0-85068477900.

Awards

The author of this thesis won two awards during his PhD research.

1. "Young Scientist Award" by the Union Radio-Scentifique Internationale, in the URSI AT-AP-RASC 2022 conference for the publication "Indirect Propagation of Body-UAV LoRa Links over Wood and Suburb", Commission F (Wave Propagation and Remote Sensing).

2. "Young Scientist Award" by the Union Radio-Scentifique Internationale, in the URSI GASS 2020 conference for the publication "Near-field modeling of Self-tuning Antennas for the Tactile Internet", Commission B (Fields and Waves).

Acknowledgements

I apologize for all the people I fail to mention here. I assure you that the space for thanking you was missed, not the gratitude nor the memory.

Before closing the dissertation, let us indulge for a moment in the art while spending a few lines on the soul of the scientific research. Bruce Sterling, in *Shaping Things* (MIT Press, 2005), imagines the future evolution of human beings that, by the ever-changing technology, become "*a Biot, which we can define as an entity which is both an object and a person*". Basically, a Biot is a cybernetic being able to design and change its own shape, which, in a book analyzing the shapes of the objects as the embodiment of reality, means that a new creating power of humans is obtained. For me here, it is not the place of wondering about the reality of this vision and its philosophical implications. However, dreaming of reaching a new stage of human evolution through technological research is perhaps the single action better explaining what scientific research is or should be. From the B-IoT to the Biot, the truthiness of Goethe's Faust struggling feeling is confirmed. The pact between Faust and Mephistopheles to live the perfect moment is fulfilled when Faust marvels at the human race's labor that beautifies the world and completes human existence. Mephistopheles then claims Faust's soul, but the old man is saved by a chorus of angels. So, the perfect end of this work can only be the words of Goethe-Faust in Act V of the second Part (translation by A. S. Kline, 2003).

"Yes, I've surrendered to this thought's insistence,

The last word Wisdom ever has to say:

He only earns his Freedom and Existence,

Who's forced to win them freshly every day.

Childhood, manhood, age's vigorous years,

Surrounded by dangers, they'll spend here.

I wish to gaze again on such a land,

Free earth: where a free race, in freedom, stand.

Then, to the Moment I'd dare say: 'Stay a while! You are so lovely'"